PhD-FSTC-2017-66
The Faculty of Sciences, Technology and Communication

Fachbereich Bau- und Umweltingenieurwissenschaften

DISSERTATION

Defence held on 17/11/2017 in Luxembourg

to obtain the degree of

DOCTEUR DE L'UNIVERSITÉ DU LUXEMBOURG EN SCIENCES DE L'INGÉNIEUR

AND

DOKTOR-INGENIEUR (DR.-ING.) AT TECHNISCHE UNIVERSITÄT DARMSTADT

by

Yves STAUDT M.Sc.
Born on 17th January 1989 in Esch-sur-Alzette (Luxembourg)

PROPOSAL OF A FAILURE CRITERION OF ADHESIVELY BONDED CONNECTIONS WITH SILICONE

Dissertation defence committee

Dr.-Ing. Christoph Odenbreit, dissertation supervisor
Professor, Université du Luxembourg, Faculté des Sciences, de la Technologie et de la Communication

Dr.-Ing. Jens Schneider, dissertation co-supervisor
Professor, Technische Universität Darmstadt, Fachbereich Bau- und Umweltingenieurwissenschaften

Dr.-Ing. Andreas Zilian, Chairman
Professor, Université du Luxembourg, Faculté des Sciences, de la Technologie et de la Communication

Dr.-Ing. Wilfried Becker, Vice-chairman
Professor, Technische Universität Darmstadt, Fachbereich Maschinenbau

Dr.-Ing. Stephan Marzi
Professor, Technische Hochschule Mittelhessen, Fachbereich Maschinenbau & Energietechnik

Dr. Andreas T. Wolf
A&S SciTech Consulting, Hünstetten

Dr.ir. Eduardus Koenders
Professor, Technische Universität Darmstadt, Fachbereich Bau- und Umweltingenieurwissenschaften

Preface

The present thesis was realised during my time as a research assistant at the ArcelorMittal Chair of Steel and Façade Engineering at the University of Luxembourg in close collaboration with the Institute of Structural Mechanics and Design at Technische Universität Darmstadt.

I would like to express my profound gratitude to my supervisor Prof. Dr.-Ing. Christoph Odenbreit for his continuous guidance, his constructive criticisms and his open ear for personal concerns. I would like to thank him for the pleasant and motivating working environment.

I would also like to express my profound gratitude to my co-supervisor Prof. Dr.-Ing. Jens Schneider for offering me the opportunity to perform parts of my research project at his institute. This continuous exchange was both inspiring and motivating. I would like to thank my co-supervisor for his constructive criticisms and discussions.

I want to express my sincere thanks to Prof. Dr.-Ing. Andreas Zilian from the Research Unit in Engineering Sciences, University of Luxembourg, for his participation as chairman of my defence. My sincere gratitude also to Prof. Dr.-Ing. Wilfried Becker, from the Institute of Structural Mechanics, Technische Universität Darmstadt, for his comments on my work and his willingness to participate as vice-chairman of my dissertation defence committee. I would like to thank Prof. Dr.-Ing. Stephan Marzi from Institute of Mechanics and Materials, Technische Hochschule Mittelhessen, for the opportunity to perform tests in his laboratory, his constructive criticisms and his participation at the defence committee. My sincere thanks also to Dr. Andreas T. Wolf, A&S SciTech Consulting, for his valuable remarks on my work and his willingness to participate as members of my dissertation defence committee. Finally, I would like to thank Prof. Dr.ir. Eduardus Koenders, from the Institute of Construction and Building Materials, Technische Universität Darmstadt, for his participation as a member of my dissertation defence committee.

The research project was performed in close collaboration between the University of Luxembourg and Technische Universität Darmstadt. I would like to thank all my colleagues, who accompanied me during my research work. I really enjoyed the working environments both in Luxembourg and in Darmstadt. In particular, special thanks to my colleagues Michael Weiler, Michael Drass, Maciej Chrzanowski, Sebastian Dietz, Sebastian Nellinger and Mike Tibolt for their willingness to discuss and help.

I express my gratitude to the support team of the laboratory of the University of Luxembourg, without whom the experimental parts of the thesis would not have been possible. Special thanks to Marc Seil, Claude Collé and Vicente Reis Adonis.

I am deeply grateful to Philipp Rosendahl from the Institute of Structural Mechanics, Technische Universität Darmstadt, for the pleasant cooperation, which gave rise to the promising results from Finite Fracture Mechanics. Moreover, I would like to thank him for his valuable

comments and remarks on my thesis.

My thanks are also due to our industrial partners Dow Corning in Seneffe, Belgium, and the Hunsrücker Glasveredelung Wagner in Kirchberg, Germany, for providing silicone.

The circular shear tests have been performed at the Institute of Steel Construction and Materials Mechanics, Technische Universität Darmstadt. I would like to thank Prof. Dr.-Ing. Michael Vormwald and Dr.-Ing. Thomas Beier for the opportunity to use their testing facilities. Special tanks also to Tobias Brehm for his commitment during the tests.

The Double Cantilever Beam tests have been performed at the Institute of Mechanics and Materials, Technische Hochschule Mittelhessen. I would like to thank Christopher Schmandt and Lukas Loh for conducting these tests.

I would like to thank Daniel Bitto, Gregory Mayer and Tony De Jesus, students at University of Luxembourg, for their assistance during the experimental investigations.

At the end, I would like to express my profound gratitude to my family and my girlfriend Katrin Israel for their commendable support and patience.

Luxembourg, in September 2017 *Yves Staudt*

Abstract

In the field of façade engineering, structural silicone sealants have been used in adhesively bonded connections since the 1960s. The low strength and stiffness of silicone rubber compared to other types of adhesives are compensated by the excellent adhesion properties and the good resistance against ageing and environmental influences, like UV radiation. Silicone sealants show a pronounced nonlinear material behaviour. The applicable design concepts in civil engineering propose simplified design equations, which are based on the assumption of a linear material law. Due to the current state of knowledge and to compensate the simplified model assumptions in the design concept, high reduction factors on the material strength and many restrictions on applications are defined. In order to overcome these drawbacks, the stress state within the sealant is increasingly described using the Finite Element Method. Considering the results of these analysis, the assessment of both the complex stress states with a suitable failure criterion and the influence of stress singularities on the failure behaviour constitute inevitable questions.

The present work addresses these two questions. In the first step, the strain magnitude has been determined as a suitable failure criterion for the defect-free bulk material of the considered Dow Corning® 993 structural silicone sealant, subjected to a quasi-static loading. The failure criterion has been calibrated using the results of uniaxial tension as well as circular shear tests and validated with the results of compression tests. The strain magnitude is a strain-based failure criterion, which can be seen as a measure for the distortion of the molecular chains.

In a second step, the stress distribution of the single-lap shear joint has been investigated in detail. For the assessment of the singular stresses and strains at the edge area of the interface between the adhesive and the substrate, referred to as *two-material wedge*, the so-called *coupled stress and energy criterion*, a concept of Finite Fracture Mechanics, was extended to nonlinear elastic material behaviour. Based on results of conduced simple shear tests on small bonded connections with varying adhesive thicknesses and overlap lengths, the coupled criterion was used to predict the crack initiation loads and a good agreement with the experimentally recorded values was obtained. Knowing the strength and the critical energy release rate of the material, the crack initiation load and the corresponding crack length are determined in the coupled criterion by solving an optimisation problem based on a Finite Element Analysis. The stress partial criterion has been modified to consider the strain magnitude as a failure criterion. In order to analyse the energy partial criterion, the critical energy release rate of Dow Corning® 993 structural silicone sealant has been determined in Double Cantilever Beam tests using the evaluation method based on the J-integral approach. Furthermore, concepts of the Theory of Critical Distances were used to determine the failure loads of the small scale tests. Unlike as for the notched circular shear tests and the tension tests on small scale bonded connections, good predictions were found in the Finite Element Analysis for the simple shear specimens, when a constant element size and formulation at the vicinity of the two-material wedge were used. Similar results were obtained with the point method and the control volume approach. These findings indicate that the characteristic

material length for silicone rubber is not constant.

Keywords: Silicone, adhesively bonded connections, experimental investigations, Finite Element Analysis, failure criterion of bulk material, critical energy release rate, Finite Fracture Mechanics, Theory of Critical Distances.

Kurzfassung

Im Bereich Fassadenbau werden Silikone bereits seit den 1960er Jahren in geklebten lastabtragenden Verbindungen eingesetzt. Die im Vergleich zu anderen Strukturklebstoffen geringe Steifigkeit und Festigkeit werden durch die hervorragende Hafteigenschaften sowie die gute Alterungs- und Witterungsbeständigkeit ausgeglichen. Silikone zeigen ein stark nichtlineares Materialverhalten. Das anzuwendende Bemessungskonzept im Bauwesen schlägt vereinfachte Bemessungsformeln vor, die auf der Annahme eines linear elastischen Materialverhaltens beruhen. Aufgrund des aktuellen Wissensstands und zur Kompensation der vereinfachten Modellannahmen bei der Bemessung werden sehr hohe Abminderungsfaktoren auf der Materialfestigkeit sowie Einschränkungen hinsichtlich der Nutzung vorgeschrieben. Um diese Nachteile zu überwinden wird die Beanspruchung des Silikons zunehmend mit der Finite Elemente Methode ermittelt. Die Bewertung sowohl der komplexen Spannungszustände mittels eines geeigneten Versagenskriteriums als auch der Einfluss von Singularitäten auf das Versagensverhalten stellen hinsichtlich der Ergebnisse einer solchen Berechnung unausweichliche Fragestellungen dar.

Die vorliegende Arbeit behandelt diese beiden Fragen. In einem ersten Schritt wurde der Dehnungsbetrag als geeignetes Versagenskriterium für das defektfreie Grundmaterial des Zweikomponentensilikonklebstoffs Dow Corning® 993 unter quasi statischen Belastungen ermittelt. Das Versagenskriterium wurde anhand der Ergebnisse von uniaxialen Zug- sowie Kreisschubversuchen kalibriert und mit den Ergebnissen von Druckversuchen validiert. Der Dehnungsbetrag ist ein dehnungsbasiertes Versagenskriterium, welches als ein Maß für die Verzerrung der Molekülketten gesehen werden kann.

In einem zweiten Schritt wurde die Spannungsverteilung in der einschnittig überlappten schubbeanspruchten Klebeverbindung detailliert untersucht. Zur Bewertung der singulären Spannungen und Dehnungen im Eckbereich der Grenzschicht zwischen Fügeteil und Klebstoff, der sogenannten *Bimaterialkerbe*, wurde das *gekoppelte Spannungs- und Energiekriterium*, eine Methode der Finiten Bruchmechanik, auf nichtlinear elastisches Materialverhalten erweitert. Auf der Grundlage der Ergebnisse von durchgeführten Schubversuchen an kleinen Bauteilproben mit unterschiedlichen Klebschichtdicken und Überlappungslängen wurde die Rissinitiierungslast mithilfe des gekoppelten Kriteriums ermittelt und eine gute Übereinstimmung mit den experimentellen Daten erzielt. Mit Kenntnis der Festigkeit und der kritischen Energiefreisetzungsrate des Materials werden im Rahmen des gekoppelten Kriteriums auf Grundlage von Finite Elemente Berechnungen in einem Optimierungsproblem sowohl die Rissinitiierungslast als auch die entsprechende Risslänge ermittelt. Das Spannungsteilkriterium wurde dabei auf ein dehnungsbasiertes Kriterium, den Dehnungsbetrag, umformuliert. Zur Anwendung des Energiekriteriums wurden *Double Cantilever Beam* Versuche am Dow Corning® 993 durchgeführt und die kritische Energiefreisetzungsrate mit der J-Integral Methode ausgewertet. Darüber hinaus wurden Methoden der Theorie der kritischen Distanzen zur Ermittlung der Rissinitiierungslast bei den Kleinteilversuchen herangezogen. Anders als bei den gekerbten kreisförmigen Schubproben und den Zugproben an geklebten Verbindungen konnte eine gute Übereinstimmung mit den experimentellen Ergebnissen

bei den Schubversuchen festgestellt werden, wenn in der Finite Elemente Simulation eine konstante Elementgröße und Formulierung gewählt wurden. Ähnliche Ergebnisse wurden mit der Punktmethode und dem Ansatz eines Kontrollvolumens erzielt. Die Untersuchungen zeigen, dass der charakteristische Längenparameter keine Materialkonstante ist.

Schlüsselwörter: Silikon, geklebte Verbindungen, experimentelle Untersuchungen, Finite Element Methode, Versagenskriterium des defektfreien Grundmaterials, kritische Energiefreisetzungsrate, Finite Bruchmechanik, Theorie der kritischen Distanzen.

Version abrégée

Dans le domaine de la construction de façades, des silicones ont déjà été utilisés comme matériau de base pour la réalisation d'assemblages collés depuis les années 1960. La résistance et la rigidité du silicone sont relativement faibles comparées à d'autres types d'adhésifs, ce gap de performances étant compensé par une excellente adhésion et une bonne résistance au vieillissement et aux impacts environnementaux. Le comportement mécanique du silicone est fortement non linéaire. Les règlements de dimensionnement en vigueur dans le domaine du génie civil proposent des équations simplifiées, qui sont basées sur l'hypothèse d'un comportement linéaire du silicone. Du fait de l'état de l'art actuel, soit la faible capacité à prédire de façon optimale le comportement de ce matériau et pour compenser les hypothèses simplifiées qui sont à la base du concept de dimensionnement, des facteurs de réduction élevés sur la résistance du silicone et des restrictions concernant son utilisation sont prescrites. Afin de contourner ces défauts, l'étude de la distribution des contraintes dans le silicone est de plus en plus faite par la méthode des éléments finis. Concernant les résultats des simulations numériques, l'évaluation de l'état des contraintes à l'aide d'un critère de rupture approprié et l'analyse de l'influence des singularités sur le comportement de rupture constituent des questions incontournables.

Le présent travail traite ces deux questions. Dans une première étape, l'amplitude de la déformation a été identifiée comme étant un critère de rupture approprié pour la matière brut et exempt de défauts du silicone structurel Dow Corning® 993 soumis à des charges statiques. Le critère de rupture a été calibré avec les résultats d'essais sur des échantillons en traction uniaxiale, ainsi que sur des échantillons circulaires en cisaillement et validé à l'aide des résultats sur des essais de compression sur des échantillons. L'amplitude de la déformation est un critère de rupture basé sur la déformation, cette dernière étant considérée comme une mesure de la distorsion des chaînes polymères.

Dans une deuxième étape, la distribution des contraintes dans un joint de recouvrement en cisaillement a été analysée en détail. Pour l'évaluation des contraintes et des déformations présentant un comportement singulier au coin libre de l'interface entre adhésif et adhérent, appelé *«entaille bi-matière»*, le critère couplé, concept de la méthode connue sous la désignation anglo-saxonne *«Finite Fracture Mechanics»*, a été étendu au comportement hyperélastique. Sur la base de tests de cisaillement sur de petits assemblages collés avec différentes épaisseurs d'adhésif et longueurs de chevauchement, le critère couplé a été utilisé pour prédire la charge à l'apparition de fissure et un bon accord avec les valeurs enregistrées lors des tests a été trouvé. Connaissant la résistance et le taux critique de restitution d'énergie de la matière, la charge à l'apparition de fissure et la longueur correspondante de la fissure initiée sont déterminées avec le critère couplé en résolvant un problème d'optimisation basé sur une analyse des éléments finis. Le critère partiel des contraintes a été modifié pour considérer l'amplitude de la déformation comme un critère de rupture. Afin d'analyser le critère partiel énergétique, le taux critique de restitution d'énergie du silicone structurel Dow Corning® 993 a été déterminée par les essais dits *«Double Cantilever Beam test»* en utilisant la méthode d'évaluation basée sur l'approche du J-intégral. En outre, des

concepts de la théorie des distances critiques ont été utilisés pour déterminer les charges à l'apparition des fissures pour des essais à petite échelle. Contrairement aux essais sur des échantillons circulaires entaillés en cisaillement et aux essais de tension sur les joints adhésifs, de bonnes prédictions ont été trouvées pour les spécimens de cisaillement, lorsque la taille et la formulation des éléments utilisées dans l'analyse par éléments finis ont été choisies de façon constante à proximité de la singularité. Des résultats similaires ont été obtenus avec la méthode ponctuelle et l'approche du volume de contrôle. Ces résultats indiquent que la longueur caractéristique du silicone n'est pas constante.

Mots clés: Silicone, connections collées, études expérimentales, éléments finis, critère de rupture, taux critique de restitution d'énergie, «Finite Fracture Mechanics», théorie des distances critiques.

Kuerzfaassung

Am Beräich Fassadenbau gëtt Silikon schonns säit den 1960er Joren an geklieften laaschtofdroenden Verbindungen agesaat. Déi am Vergläich zu aneren Kollen geréng Steifegkeet an Festegkeet ginn duerch déi exzellent Adhäsiounseegeschaften souwéi déi gudd Alterungs- an Witterungsbeständegkeet ausgeglach. Silikon weist e staark netlineart Materialverhalen op. Dat z'applizéiernd Bemiessungskonzept am Bauwiesen proposéiert vereinfacht Bemiesssungsformeln, déi e linear elastescht Materialverhalen unhuelen. Opgrond vum aktuellen Wëssensstand an fir déi vereinfacht Hypothesen vum Bemiessungskonzept ze kompenséieren ginn héich Ofminderungsfaktoren op der Materialfestegkeet an Aschränkungen hisiichtlech der Notzung virgeschriwwen. Fir déi Nodeeler z'iwwerwannen gëtt d'Beusprochung vum Silikon ëmmer méi heefeg mat der Finite Elemente Method ermëttelt. D'Bewäertung souwuel vun de komplexen Spannungszoustänn mat engem gëeegenten Versoenskritär wéi och den Afloss vun Singularitéiten op d'Versoensverhalen stellen hisiichtlech vun den Resultater vun esou enger Berechnung onauswäichlech Froen duer.

Déi virleiend Aarbecht behandelt dës zwou Froen. An engem éischten Schrëtt gouf den Dehnungsbetraag als e gëeegenten Versoenskritär fir dat defektfräit Grondmaterial vum Zweekomponentensilikon Dow Corning® 993 ënner quasi stateschen Belaaschtungen ermëttelt. De Versoenskritär gouf op der Basis vun Versich un eenaxeschen Zug- an kreesfërmegen Schubprouwen kalibréiert an mat den Resultater vun Drockversich validéiert. Den Dehnungsbetraag ass en dehnungsbaséierte Versoenskritär, dat als eng Mooss fir d'Verzerrung vun den Moleküllketten kann gesinn ginn.

An engem zweete Schrëtt gouf d'Spannungsverdeelung an enger eenschnëtteg iwwerlappeten schubbeusprochten geklieften Verbindung am Detail ënnersicht. Fir d'Evaluatioun vun den singulären Spannungen an Dehnungen um fräien Enn vun der Grenzfläch tëschent dem Fügedeel an dem Koll, dem sougenannten *Bimaterialkrack*, gouf den *gekoppelten Spannungs- an Energiekritär*, e Konzept aus der Finiten Brochmechanik, erfollegräich op netlinear elastescht Material erweidert. Op der Grondlag vun duerchgefouerten Schubversich u kléngen Baudeelprouwen mat ënnerschiddlechen Schichtdéckten vum Koll an ënnerschiddlechen Iwwerlappungslängten gouf d'Rëssinitiéierungslaascht mat dem gekoppelten Kritär ermëttelt an en gudden Accord mat den experimentellen Miessdonnéeën erzielt. Mat der Kenntnes vun der Festegkeet an der kritescher Energiefraisetzungsrat ginn am Kader vum gekoppelten Kritär op Basis vun Finite Elemente Berechnungen an engem Optimiséierungsproblem souwuel d'Rëssinitiéierunglaascht wéi och d'Längt vum entspriechenden Rëss ermëttelt. De Spannungsdeelkritär gouf dobäi an en dehnungsbaséierten Kritär ëmformuléiert. Fir den Energiekritär kënnen z'applizéieren, goufen *Double Cantilever Beam* Versich um Dow Corning® 993 duerchgefouert an d'kritesch Energiefraisetzungsrat mat der J-integral Method ausgewäert. Doriwwer eraus goufen Methoden vun der Theorie vun den kriteschen Distanzen fir d'Ermëttlung vun der Rëssinitiéierungslaascht bei den klengen Baudeelprouwen applizéiert. Anescht wéi bei den kreesfërmegen Schubprouwen mat engem Krack an den Zugversich un den geklieften Prouven konnt e gudden Accord mat den experimentellen Resultater bei den Schubversich festgestallt ginn, wann an der Finite Element Simulatioun

eng konstant Elementgréisst an eng konstant Elementformuléierung gewielt goufen. Ähnlech Resultater goufen mat der Punktmethod an dem Usaatz vun engem Kontrollvolumen erzilt. D'Enquête huet gewisen, dat den charakteristeschen Längtenparamter fir de Silikon keng Materialkonstant ass.

Schlësselwieder: Silikon, geklieft Verbindungen, experimentell Enquêten, Finite Element Method, Versoenskritär vum defektfräit Grondmaterial, kritesch Energiefraisetzungsrat, Finite Brochmechanik, Theorie vun den kritischen Distanzen.

Contents

List of Figures

List of Tables

Nomenclature

Abbreviations

2D	Two-dimensional
3D	Three-dimensional
ASTM	American Society for Testing and Materials
BEM	Boundary Element Method
cf.	"*confer*" - compare with
CZM	Cohesive Zone Modelling
DC	Dow Corning®
DCB	Double Cantilever Beam
DIC	Digital Image Correlation
DOF	Degree of freedom
e.g.	"*exempli gratia*" - example given
ETAG	European Technical Application Guideline
FDM	Finite Difference Method
FEM	Finite Element Method
FFM	Finite Fracture Mechanics
i.e.	"*id est*" - in other words / that is
IGU	Insulation glass unit
N/A	Not available
PE	Polyethylene
PIB	Polyisobutylene
PTFE	Polytetrafluoroethylene
SSG	Structural Sealant Glazing
Std. dev.	Standard deviation
TCD	Theory of critical distances
TSSA	Transparent Structural Silicone Adhesive
XFEM	Extended Finite Element Method

Symbols

Mathematical operators

$\det(\cdot)$	Determinant of a matrix
$\mathrm{tr}(\cdot)$	Trace of a matrix
$(\cdot)^T$	Transpose of a matrix
$(\cdot)^{-T}$	Inverse of the transpose of a matrix
$\dot{(\cdot)}$	Time derivative
$\cdot$	Inner scalar product

Greek letters

α_i	Coefficient of *Ogden* hyperelastic material law
α_{MD}	Coefficient of *Drass* hyperelastic material law
β_{MD}	Coefficient of *Drass* hyperelastic material law
Γ	Path
γ_{e}	Engineering shear strain
$\dot{\gamma}_{\mathrm{e}}$	Engineering shear strain rate
Δ	Change, difference
Δa	Crack length
ΔA	Crack surface
$\Delta a_{\max}$	Upper bound for the crack length
$\Delta a_{\min}$	Lower bound for the crack length
$\Delta\varepsilon$	Strain offset
Δh	Change of height
Δl	Change of length of a material line
Δl_{th}	Differential thermal expansion
δ	Separation
δ_{c}	Separation at crack propagation
δ_{ext}	Starting point for extrapolation of the crack opening displacement
$\delta_{\max}$	Maximum crack opening displacement
δ_{MD}	Coefficient of *Drass* hyperelastic material law
$\boldsymbol{\varepsilon}$	Infinitesimal strain tensor
ε	True or logarithmic strain
ε_1	First or maximum principal strain (true strain)
ε_2	Second or mid principal strain (true strain)
ε_3	Third or minimum principal strain (true strain)
ε_x	True or logarithmic strain in x-direction
ε_y	True or logarithmic strain in y-direction
ε_z	True or logarithmic strain in z-direction
$\varepsilon_{\mathrm{corr}}$	Corrected engineering compression strain
ε_{e}	Engineering strain
$\varepsilon_{\mathrm{e,UC}}$	Engineering strain in compression
$\varepsilon_{\mathrm{e,UT}}$	Engineering strain in uniaxial tension
$\varepsilon_{\mathrm{e},x}$	Engineering strain in x-direction
$\varepsilon_{\mathrm{e},y}$	Engineering strain in y-direction
$\varepsilon_{\mathrm{e},z}$	Engineering strain in z-direction
$\varepsilon_{\mathrm{e,l}}$	Engineering strain longitudinal in uniaxial tension
ε_{ij}	Components of the true strain tensor
ε_{M}	Strain magnitude
$\varepsilon_{\mathrm{raw}}$	Engineering compression strain calculated from the raw test data
$\varepsilon_{\mathrm{r,UC}}$	Remaining engineering compression strain after unloading
$\dot{\varepsilon}_{\mathrm{e,UC}}$	Engineering strain rate in load direction for the compression test
$\dot{\varepsilon}_{\mathrm{e,UT}}$	Engineering strain rate in load direction for the uniaxial tension test
$\varepsilon_{\mathrm{UT}}$	Uniaxial tensile strength (true strain)
η	Relative ordinate
ϑ	Angle, or ordinate of a polar coordinate system
ϑ_i	Angle characterising the two-material-wedge
ϑ_{R}	Rotation of the adherends at the loading point
λ	Order of a singularity

λ_i	Principal stretch in i-direction, $i = 1, 2, 3$
λ_m	Limit extension in *Arruda-Boyce* hyperelastic material law
λ_UT	Uniaxial tensile stretch in direction of principal stretch
$\lambda_\mathrm{UT}^\mathrm{eq}$	Equivalent uniaxial tensile stretch in direction of principal stretch
μ	Friction coefficient or coefficient of *Arruda-Boyce* material law
μ_i	Coefficient of *Ogden* hyperelastic material law
ν	*Poisson* ratio
ν_a	*Poisson* ratio of the adhesive layer
ν_s	*Poisson* ratio of the adherend
ξ	Relative ordinate
Π	Potential
ρ	Density
$\boldsymbol{\sigma}$	Stress tensor
σ	True stress
σ_1	First or maximum principal stress (true stress)
σ_2	Second or mid principal stress (true stress)
σ_3	Third or minimum principal stress (true stress)
σ_∞	Design value of the tensile strength according to ETAG 002 for long term loads
$\sigma_{\mathrm{AL},x}$	Stresses in overlap direction according to the *Allman* model
$\sigma_{\mathrm{AL},y}$	Peel stresses direction according to the *Allman* model
σ_c	Tensile strength
σ_des	Design value of the tensile strength according to ETAG 002
σ_E	Acting tensile stress according to ETAG 002
σ_e	Engineering stress
σ_{ij}	Components of the true stress tensor
σ_iso	Isochoric stress
σ_LM	True stress for *Line Method*
σ_max	Mode I strength in the traction-separation law
σ_Mises	*Von Mises* equivalent stress
$\sigma_{r\vartheta}^m$	Stress at a two-material wedge
σ_PM	True stress for *Point Method*
σ_UC	Uniaxial compression strength (true stress)
σ_UT	Uniaxial tensile strength (true stress)
τ	Shear stress
τ_∞	Design value of the shear strength according to ETAG 002 for long term loads
$\tau_{\mathrm{AL},xy}$	Shear stresses according to the *Allman* model
τ_des	Design value of the shear strength according to ETAG 002
τ_e	Average shear stress or engineering shear stress
τ_E	Acting shear stress according to ETAG 002
$\tau_{r\vartheta}^m$	Shear stress at a two-material wedge
τ_VK	Shear stress according to *Volkersen*
Φ_i	Stress functions in the *Allman* model
φ	Angle
χ	Vector field linking reference and current configuration
χ_MD	Coefficient of *Drass* hyperelastic material law
ω_AL	Coefficient defined for the *Allman* equation
ω_VK	Coefficient defined for the *Volkersen* equation
Ω_c	Set

Latin letters

$\boldsymbol{a}$	*Euler-Almansi* strain tensor
a	Crack length
A	Cross-sectional area
$\boldsymbol{b}$	Left *Cauchy-Green* tensor
B	Body in the current configuration
B_0	Body in its reference configuration
$\boldsymbol{C}$	Right *Cauchy-Green* tensor
C	Compliance
C_i	Coefficients of *Arruda-Boyce* hyperelastic material law
c_i	Coefficients of *Dias* hyperelastic material laws
C_{ij}	Coefficients of polynomial hyperelastic material laws
da	Infinitesimal surface element
dC	Change in compliance
$d\varepsilon$	Infinitesimal amount of true strain
dl	Infinitesimal amount of length change of a material line
ds	Infinitesimal element of path
du	Deformation of the infinitesimal line element dx
d_{UC}	Diameter of the compression test specimen
$d_{\mathrm{UC},0}$	Initial diameter of the compression test specimen
$d\varphi$	Infinitesimal angle
dx	Infinitesimal line element
e	Silicone thickness
$\boldsymbol{E}$	*Green-Lagrange* strain tensor
E	*Young*'s modulus
E_{a}	*Young*'s modulus of the adhesive layer
$\vec{e_i}$	Unit basis vectors of the current configuration
$\vec{E_i}$	Unit basis vectors of the reference configuration
E_{s}	*Young*'s modulus of the adherend
$\boldsymbol{F}$	Deformation gradient
$\overline{\boldsymbol{F}}$	Deviatoric part of the deformation gradient
F	Force
$\vec{f}$	Body force
$f(\cdot)$	Function
$f^m_{r\vartheta}$	Function describing a stress field
F_{FEA}	Load
F_{u}	Failure load
$\mathcal{G}$	Energy release rate
$\mathcal{G}_{\mathrm{c}}$	Critical energy release rate
$\bar{\mathcal{G}}$	Incremental energy release rate
G_{a}	Adhesive's shear modulus
G_{Pane}	Weight of a glass pane
$\boldsymbol{H}$	Displacement gradient
H	Free edge stress intensity factor
h_{c}	Silicone bite
H_{c}	Critical free edge stress intensity factor
H_i	Free edge stress intensity factors $i = 1..2$
H_{FEA}	Free edge stress intensity factors for a given load
h_{UC}	Height of the compression test specimen

$h_{\mathrm{UC},0}$	Initial height of the compression test specimen
h_{v}	Length of the vertical silicone bead
i	Index
$\boldsymbol{I}$	Unit tensor
$\tilde{I}_1$	Given value for the first invariant of the left *Cauchy-Green* tensor
I_i	i^{th} invariant, $i = 1, 2, 3$
j	Index
J	J-integral or determinate of the deformation gradient
J_{c}	Critical value for the J-integral
J_{m}	Limit extension in *Gent* material law
K_{c}	Critical energy release rate
L	Length parameter for the *Theory of Critical Distances*
l	Length in the deformed configuration
l_0	Initial or undeformed length
l_{a}	Smaller dimension of a rectangular glass pane
l_{adh}	Adhesive overlap length
l_{b}	Larger dimension of a rectangular glass pane
m	Material index
M	Moment
$\vec{n}$	Normal vector
o	Origin of the current configuration
O	Origin of the reference configuration
p	Hydrostatic pressure
$\vec{p}$	Surface load
P	Material point of a body in its current configuration
P_0	Material point of a body in its reference configuration
$\boldsymbol{P}_1$	1^{st} *Piola-Kirchhoff* stress tensor
$\boldsymbol{P}_2$	2^{nd} *Piola-Kirchhoff* stress tensor
p_{d}	Acting surface load
r	Length of the position vector in a polar coordinate system, radius
$\boldsymbol{R}$	Rotational tensor
r_{c}	Radius of the control volume
$\boldsymbol{s}$	Deviatoric stress tensor
$\vec{t}$	Force vector
t	Time or thickness
$\vec{T}$	Traction vector
T	Traction
t_{a}	Adhesive layer thickness
t_{s}	Adherend thickness
$\vec{u}$	Displacement vector
u	Displacement
$\boldsymbol{U}$	Right stretch tensor
$\vec{u}$	Displacement vector
u_x	Displacement in x-direction
u_y	Displacement in y-direction
u_z	Displacement in z-direction
$\boldsymbol{V}$	Left stretch tensor
V	Volume
V_{c}	Control volume
v_{UC}	Loading speed for the compression test

V_{UC}	Volume of the compression test specimen
$V_{\mathrm{UC},0}$	Initial volume of the compression test specimen
w	Crack opening displacement
W	Strain energy potential
$\overline{W}$	Strain energy density averaged within a control volume
$\overline{W_{\mathrm{c}}}$	Strain energy density averaged within a control volume at failure
W_{dev}	Deviatoric part of the strain energy potential
W_{vol}	Volumetric part of the strain energy potential
$\vec{X}$	Position vector referring to a material point in its undeformed state
$\vec{x}$	Position vector referring to a material point in its deformed state
x	x-coordinate (abscissa)
$x_{0,j}$	Abscissa of point j in its reference configuration
x_j	Abscissa of point j
y	y-coordinate (ordinate)
$y_{0,j}$	Ordinate of point j in its reference configuration
y_j	Ordinate of point j
z	z-coordinate

1 Introduction

1.1 Motivation

In construction industry, silicones have already been used for more than half a century. Due to their high elasticity and good resistance against environmental impacts, silicones were first employed as sealants, such as in façade engineering. In the 1960s, large curtain wall systems became popular in the United States. The glass panes used were clamped at the top and bottom edge. The size of the glass elements was limited and thick glass panes were required to avoid excessive deflections under wind and gravity loads. In parallel, silicone weather seals exhibited excellent adhesion properties on glass and a good resistance against UV radiation. From these considerations, the idea was arising to structurally bond vertical glass fins with silicone sealants as bracing elements to the glass panes and the first adhesively bonded connection of glass panes with silicone was realised (Klosowski and Wolf, 2016). An example of this so-called *total vision system*, dating back from 1964, is shown in figure 1.1a.

(a) Total vision system, picture from Klosowski and Wolf

(b) Burj Khalifa, picture from Dow Corning Corporation (2011a)

Figure 1.1: Examples of Structural Sealant Glazing systems

In the following years, silicones have also been successfully used in two and later in four-sided applications, where the glass pane was bonded to the metallic substructure. An example of such an application is shown in figure 1.1b. In the field of façade applications, adhesive connections show a number of advantages, starting at the large bonding area, which creates a uniform load transfer and thus reduces stress concentrations in the adherends. In addition, with no mechanical components penetrating the building skin, an architectural attractive, easy to maintain and energetically optimised façade is obtained.

Regarding the verification of the load bearing capacity of structurally bonded glass com-

ponents, the design guidelines ETAG 002 (2012) and ASTM C1401 (2002) define design equations, which are based on simplified assumptions, such as a linear elastic material behaviour. Since the material behaviour and the required structural modelling are not fully understood, high design factors on the material strength and restrictions in use, such as regarding the dead load transfer, are defined.

Silicone exhibits a nonlinear elastic and quasi-incompressible material behaviour. Due to the high deformations which can occur in the adhesive joint, bonded connections are increasingly analysed with the Finite Element Method, a numerical approximation tool, with the sealant being typically modelled with solid elements. The results of these numerical simulations need to be assessed regarding two issues. First of all, the three-dimensional stress states need to be compared with the strength values, which are generally determined in simple uniaxial material tests. This comparison is usually done assuming a suitable failure criterion. For silicone sealants, only a few works deal with the definition of a failure criterion for bulk material. Apart from the definition of a failure criterion, stress singularities can arise in the numerical simulation, which cause the stresses in the vicinity of the singularity to become dependent on the chosen size of the Finite Element used. Therefore, the results of these stresses and strains become into a certain extend arbitrary and need to be assessed.

In the present work, the definition of a failure criterion for silicone bulk material and the assessment of the stresses in the vicinity of a singularity, the two-material wedge, for standard linear bonded connections are addressed. In a first part, failure of the defect-free bulk material is investigated based on simple characteristic stress states with the objective to identify a suitable failure criterion for simple linearly bonded joints. In the second part of this thesis, different methods, based on Finite Fracture Mechanics and the Theory of Critical Distances are considered to describe failure initiation in the vicinity of the two-material wedge.

1.2 Objectives

For the verification of the load bearing capacity of adhesively bonded connections with silicone, the load or displacement at which failure occurs, needs to be determined. Due to the highly nonlinear material behaviour of the structural sealant, these structures are increasingly analysed using the Finite Element Method. Both the complex three-dimensional stress state and the non-converging stresses in the vicinity of a singularity need to be assessed. The present work focus on these two aspects.

In a first step, failure of defect-free bulk material is analysed. A failure criterion allows to compare complex stress states, which can be found in structural elements, with results from simple material tests, as the uniaxial tensile strength. With the two fundamental stress states uniaxial tension and shear, a suitable failure criterion is identified for a quasi-static loading under laboratory conditions. The proposed failure criterion is validated using the results of compression tests. The knowledge of a failure criterion is a fundamental requirement to understand the failure behaviour of a material.

In the second step, the stresses in the vicinity of the edge region of the interface between the adhesive and the adherend are analysed. Due to the sharp change of the elastic constants and the geometry, the stress field at this so-called two-material wedge is singular. As a consequence, the stresses become dependent on the chosen size of the Finite Elements

and therefore into some extend arbitrary. Methods from Finite Fracture Mechanics and the Theory of Critical Distances are presented and implemented to predict the failure loads and displacements of small scale tests on bonded connections, which exhibit a stress singularity.

1.3 Contents and structure of the thesis

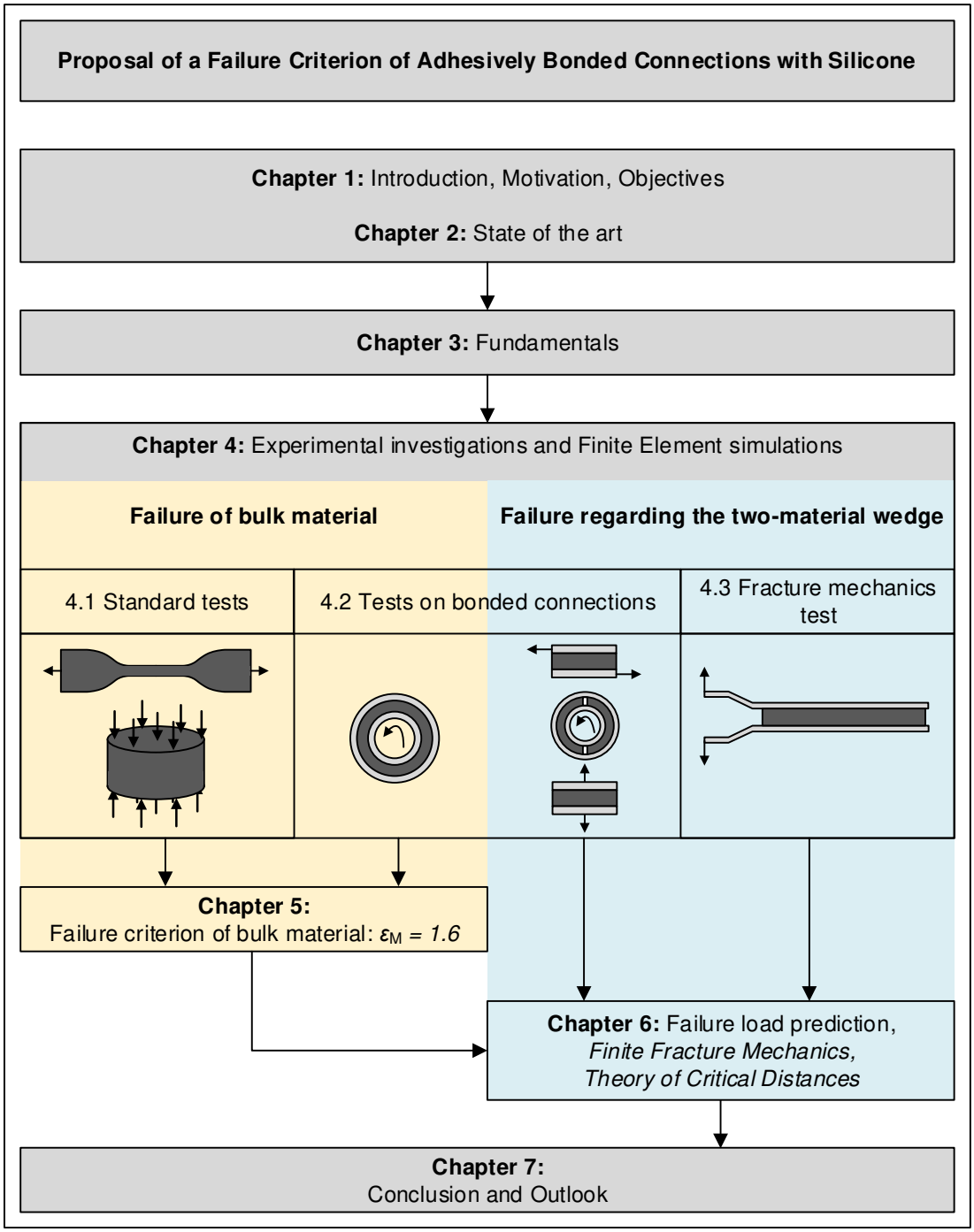

Figure 1.2: Structure of the thesis

The structure of the thesis is shown in figure 1.2. After a short **introduction** in **chapter 1**,

the **state of the art** in the field of the failure load analysis of adhesively bonded connections is given in **chapter 2**. This chapter focus on the different aspects discussed in the thesis and summarises in a concise way important findings and recent developments.

Chapter 3 introduces the **relevant concepts** used in the thesis, starting at the material properties of cross-linked silicones and the basic equations from continuum mechanics. The Finite Element Method is briefly presented with a focus on singularities. In addition, various simple failure criteria from literature are given. The **stress field in the vicinity of the two-material wedge** is discussed in **section 3.5**. Some analytical solutions, like the *Volkersen* equation, are shown and their limitations discussed. The singular behaviour of the stress field at the corner edge of the interface between the adhesive and the adherend is illustrated with own examples. Finally, methods to assess the stresses in the vicinity of the two-material wedge are presented. Apart from Finite Fracture Mechanics and the Theory of Critical Distances, advanced numerical modelling techniques are briefly introduced.

In the following, a differentiation between failure of the defect-free bulk material and failure regarding the two-material wedge is made. Both cases have been investigated for one temperature.

For the **failure of defect-free bulk material**, test results of **standard experimental investigations**, i.e. tension and compression tests are given in **section 4.1**. In addition, the test results of circular shear specimens with a continuous joint, presented in **section 4.2** were used to calibrate the **failure criterion for silicone bulk material**, which is proposed in **chapter 5** and which focus on linearly bonded joints.

Failure regarding the two-material wedge is analysed on the basis of the tests on bonded connections, described in **section 4.2**. Since the failure load prediction based on Finite Fracture Mechanics requires the knowledge of the critical energy release rate, **Double Cantilever Beam tests**, described in **section 4.3**, were performed. With these results, the tests documented in section 4.2 were analysed. The **results of this failure load discussion** are given in **chapter 6**.

Chapter 7 summarises the main **conclusions** and gives an **outlook on further research work**.

2 State of the art

Silicone was developed in the early 20th century by the US chemist *Kipping*, when he performed experiments on silicone-oxygen chemical bonds (Reller et al., 2000). *Kipping* did not recognise the huge field of applications of this new material. After the successful development of the methods for a production of silicone in an industrial scale in the 1940s, companies like *Dow Corning* or *Wacker* were founded (Thomas, 2010). The production process of silicone is described in detail in Schliebs and Ackermann (1987) and Ackermann and Damrath (1989). Silicone is a rubber-like material, composed of cross-linked molecular chains. The chemical backbone of the molecular chains are silicon-oxygen bonds. Amongst others, due to the high strength of this bond, silicone exhibits a very good resistance against environmental influences, like UV-radiation and ageing. In addition, it shows excellent adhesion on many materials, especially glass. The material properties are subject in a number of publications, e.g. Gutowski et al. (1993) (adhesion), Beers and Klosowski (1990), De Buyl (2001), Wolf and Cleland-Host (2004) and Habenicht (2009). Due to their exceptional properties, silicones are used in many industrial fields. A good overview on the different applications of silicone is given in Andriot et al. (2007).

In construction industry, crosslinked silicones were first employed as sealants because of their high elasticity and excellent ageing resistance. Only after the development of silicones with higher strength, they have been used in load bearing connections (Tock et al., 1988). In 1965, glass fins were structurally bonded with silicone as bracing elements on glass panes. In the 1970s, glass panes have been adhesively bonded on the building's substructure (Clift et al., 2014). Since the 1990s, silicone is increasingly used for façade applications in regions with high seismic activity or wind loads (Dow Corning Corporation, 2006). Apart from these applications, innovative adhesive connections are subject to recent research activities, like in Dias (2013), where silicone was used as shear connector in steel to glass composite beams, or concerning the geometry of the bondline as investigated in Hagl (2006), Hagl (2008a), Richter et al. (2014) and Scherer (2014). Apart from façade engineering, the strength of adhesively bonded connections with silicones has also been investigated in Banea and da Silva (2010) for aerospace applications.

The **mechanical material behaviour of crosslinked silicones** has been investigated in a number of research works, e.g. Hagl (2006), Brendler and Haufe (2007), Dias (2013), Staudt (2013) and Scherer (2014). Considering typical applications with simple geometries, silicone is generally described with a nonlinear elastic, so-called *hyperelastic*, material behaviour assuming nearly or full incompressibility. Hyperelastic material laws generally describe a functional expression for the strain energy density using the invariants of the deformation gradient. Marckmann and Verron (2006) give a good overview on the large number of hyperelastic material laws. The simplest functional expressions are given by *Neo-Hooke* and *Mooney-Rivlin*, which are both phenomenological models. There are as well micro-mechanically based models, like *Arruda-Boyce* and the *Extended-Tube* model, or models, using experimental data without a definition of a functional expression, like the model according to Marlow (2003). Although silicones are not fully incompressible (e.g. Wolf and

Descamps (2002) and Dias (2013)), a *Poisson* ratio of 0.5 is assumed for many applications (e.g. Hagl (2016)).

For the **verification of the load bearing capacity of a structure**, the acting stress state needs to be compared to an upper limit, which is generally determined in a simple material test, like the uniaxial tension test (Mang and Hofstetter, 2013). In order to allow for this comparison, the stress states need to be transformed into a scalar value. This is usually done assuming a failure criterion. According to Naït-Abdelaziz et al. (2012), the failure assessment can be done following three different concepts. In a first approach, the material is assumed to be defect-free and the stress state can be assessed with a classic failure criterion, like *Rankine* for brittle materials or *von Mises* as yield criterion for ductile materials. In a fracture mechanics approach, the presence of a pre-crack is assumed. Finally, failure can also be covered by the constitutive modelling of the material in a damage mechanics approach.

Failure of rubber-like material is often associated with internal growth of voids or cavities. A first work on the so-called *cavitation* was presented by Gent and Lindley (1959). Butt bonded specimens with different adhesive layer thicknesses under tensile forces were considered. A threshold value for cavitation was determined and experimentally validated. Cavitation however was only observed for specimens with high hydrostatic tensile stresses. Similar results were found in Aït-Hocine et al. (2011), where only the specimens with thin adhesive layers exhibited the typical failure pattern observed with cavitation. Research is currently performed on silicone adhesive in point-wise connections, e.g. Dispersyn et al. (2014) and Drass and Schneider (2016). For the failure of rubber-like material with a dominant dependence on deviatoric stresses, Kawabata (1973) proposed a principal stretch criterion, which was validated on plane stress specimens. In Zine et al. (2011), the maximum principal strain was referred to as a typical failure criterion for rubber. Apart from this, the strain magnitude was proposed in Molls (2013). Failure of silicone sealants in bonded connections with complex geometry was investigated in Hagl (2009) and Scherer (2014). Hagl (2009) considered the distribution of first principal stresses and in Scherer (2014), the strain energy density was identified as a possible failure criterion, but further research was recommended to confirm this finding.

Apart from a failure criterion on bulk material, the **critical energy release rate** is an essential parameter for the assessment of fracture mechanics problems. For the determination of the critical energy release rate of an adhesive, the Double Cantilever Beam test is often used. The evaluation of this test can be done following two concepts, one based on linear elastic fracture mechanics using the *Irwin-Kies* equation (Blackman et al., 1991) and one based on the J-integral (Li and Ward, 1989). The method based on linear elastic fracture mechanics works with the compliance of the adherends with a restriction of the material behaviour of both substrate and adhesive to linear elastic. The second method, which was developed to determine the post peak tensile behaviour of concrete in tension, is based on the J-integral (cf. (Rice, 1968)) to determine the critical energy release rate of the material and can be used with non-linear elastic materials. The Double Cantilever Beam test is typically used for thin adhesive layers and stiff adhesives (e.g. Biel (2005)). Only a few works deal with thick adhesive layers with soft material properties, e.g. Biel et al. (2012a) and Campilho et al. (2015). In Banea et al. (2010), Double Cantilever Beam tests on a thin silicone adhesive layer were performed to quantify the temperature dependence of the adhesive's cohesive properties.

In façade engineering, for the design of bonded connections, the so-called ***structural sealant glazing kits***, guidelines like the ETAG 002 (2012) in Europe or the ASTM C1401 (2002) in the United States define the requirements and design equations. For both guidelines, only silicone sealants are allowed to be used and the design equations are based on similar assumptions, like a uniform stress distribution within the sealant, a linear elastic material behaviour and a simplified load distribution. As a result of these simplifications, high reduction factors on the material strength and restrictions in use are defined. The accurate determination of the acting stresses and the detailed knowledge about the failure mechanism are inevitable to calculate the failure probability of a given structure.

In order to overcome the restrictions defined in the design guidelines, the **Finite Element Method** is increasingly used to describe the stress and strain distributions taking account of the nonlinear material behaviour of the silicone sealant. The Finite Element Method is a numerical approximation tool to solve partial differential equations. The designation *Finite Element Method* has been introduced by *Clough* in the 1960s (Klein, 2007). The Finite Element Method is a numerical approximation tool, which is based on the principle of partitioning a given structure in small parts, the so-called *Finite Elements*. The elements are defined by their nodes and each node has a defined number of degrees of freedom. Consequently, a whole structure can be described with a delimited number of degrees of freedom (Da Silva and Campilho, 2012). Due to the continuous development of the method and the availability of ever more powerful hardware, the Finite Element Method has become a standard tool for the prediction of the behaviour of complex structures for which no closed-form analytical solutions are available.

The stiffness of an **adhesively bonded connection with silicone** can be accurately predicted using a nonlinear Finite Element Analysis, as shown in Brendler and Haufe (2007), Dias (2013), Scherer (2014) and Descamps et al. (2017). These works mainly cover the prediction of the stiffness of the bonded connections, but do not analyse in detail the stress or strain distributions at failure initiation. Dias (2013) and Staudt (2013) highlight the observation that the stresses at the interface between the adhesive layer and the substrate depend on the chosen size of the Finite Elements. According to Alfredsson (2003), the full potential of adhesively bonded joints cannot be used because of the lack of reliable methods for the strength prediction. The lack of a reliable failure criterion for the use in the numerical simulation of adhesively bonded joints is also discussed in Banea and da Silva (2009). Clift et al. (2014) compares in a Finite Element Analysis the first principal stress distribution in a small scale specimen under the nominal strength as defined by the standard with the stresses in a structural component in order to optimise the shape of the adhesive joint.

There are a number of **analytical solutions for adhesively bonded connections**. In automotive and aeronautic industry, adhesively bonded connections, especially loaded in shear, constitute an important joining technology. According to Habenicht (2009), compared to butt bonded connections, lap shear joints show the advantage that both adhesive and adherends can be economically used. Da Silva et al. (2009a) give an overview on closed-form solutions for the stress distribution in the adhesive for single-lap shear joints. The earliest work was done by Volkersen (1938), originally intended to describe the force distribution in riveted joints. The *Volkersen* equation only considers shear stresses. Apart from the constant shear stress due to the applied load, the deformation of the adherends is taken into account as well. Additional closed-form solutions were proposed by Goland and Reissner (1944), as well as by Hart-Smith (1973). These equations also take into account for the rotation of

the adherends. Most of these analytical solutions are restricted to linear elastic material behaviour. In Da Silva et al. (2009a), additional equations are presented, which deal with elastic-plastic material behaviour. Recently, a new general computational framework for the analysis of ductile adhesives was proposed in Stein et al. (2017b). Non-linear elastic material behaviour has not been considered yet. Moreover, the equations generally fail in the stress-free edge condition. Allman (1977) proposes a solution, which predicts zero shear stresses at the corner edge of the interface. A common point for many of the analytical solutions is the assumption of a constant stress distribution over the adhesive thickness, as only very thin adhesive layers are considered. This assumption corresponds to considering the stresses in the adhesive layer at mid-height (Weißgraeber, 2014).

The previously described non-converging behaviour of the stresses in the numerical simulation (cf. Dias (2013) and Staudt (2013)) is due to the stress singularity of the **two-material wedge** (Weißgraeber, 2014). In the framework of the elasticity theory, stress singularities describe stresses with infinitely high values. A classic example are the stresses at the tip of a sharp crack (Gross and Seelig, 2011). The stress singularity at the two-material wedge is subject to a number of publications. Bogy (1968) and Hein and Erdogan (1971) give the theoretical background for the description of the stresses at the two-material wedge. Penado (2000) considers the stress singularity in the context of an adhesively bonded connection. Chen et al. (2011) classify the singularities, which arise at the corner edge of a bonded connection, by distinguishing between strong and weak singularities. In Gleich (2002), the so-called *adhesive thickness effect* was investigated. The adhesive thickness effect describes that starting from an optimal bondline thickness, the strength of a bonded connection decreases for an increasing adhesive layer thickness. Most stress-based failure criteria fail in the prediction of the adhesive thickness effect. Gleich (2002) however did not consider the *average stresses* at the mid-height of the adhesive layer, but the stresses at the interface. Considering these stresses and adopting concepts from linear elastic fracture mechanics, Gleich (2002) predicted the failure load of shear loaded bonded connection and a good agreement was obtained. The adhesive thickness effect has also been investigated in Banea et al. (2015) for a two-component polyurethane adhesive. Although the failure load was influenced by the adhesive thickness, the overall stiffness was constant.

For the **prediction of crack onset at a weak singularity**, like the two-material wedge, concepts from classic fracture mechanics cannot be used, since the energy release rate evaluated locally at the singular point gives zero for weak singularities like a notch (Weißgraeber, 2014). For the prediction of crack onset at a weak singularity, different methods can be used. Taylor (2008) gives an overview on methods, which are generically referred to as the *Theory of Critical Distances*. A common point of these theories is the usage of a length scale parameter, which is considered as a material constant. Concepts assuming a characteristic length scale parameter have been proposed first by Neuber (1936) and Whitney and Nuismer (1974). In the framework of a Finite Element Analysis, the advantage of these methods consists in evaluating the stresses at a certain distance from the notch tip, where the stresses give convergent results when a reasonably refined mesh is employed. In Waddoups et al. (1971), a crack with a constant length is assumed at a weak singularity, thus enabling the use of classic fracture mechanics concepts. In Schaaf et al. (2015), the strain energy density was averaged in a certain control volume, which was calibrated using experimental data. An engineering approach, which is used in the context of the Theory of Critical Distances consists in selecting a constant element size and element formulation in the numerical simulation. Although the Theory of Critical Distances accurately predicts crack

onset at weak singularities for a given configuration, the material length parameter is missing a physical basis (Taylor, 2008) and is often found to depend on the geometry or loading (Chaves et al., 2014). For the concept of Fracture Mechanics, crack onset is a continuous process. Hashin (1996) proposes the concept of Finite Fracture Mechanics in which, the crack onset is considered as a *fracture event* with development of a crack with a finite length (Weißgraeber et al., 2016). In Taylor (2008), Finite Fracture Mechanics is considered as the theoretical basis for the Theory of Critical Distances. Apart from this, advanced numerical modelling techniques, as the *Extended Finite Element Method* or *Cohesive Zone Modelling*, have been reviewed in Da Silva and Öchsner (2008). These methods are promising tools to predict crack propagation.

In the field of Finite Fracture Mechanics, a criterion for the onset of a crack at a weak singularity, referred to as the **coupled stress and energy criterion**, has been proposed by Leguillon (2002). A crack in the vicinity of a weak singularity will develop, if two partial criteria are simultaneously satisfied. The coupled criterion has been successfully employed in Weißgraeber (2014) to calculate the failure load of single-lap shear joints with an epoxy-based adhesive. The coupled criterion is an optimisation problem, since the crack initiation load and the initiated crack length are both unknown. The stress partial criterion gives an upper boundary for the crack length, as the crack length is limited to the region, where the acting stresses exceed the material strength. The energy criterion gives a lower boundary, as only cracks can develop, which release enough energy for their creation. Regarding the coupled criterion, there is no inherent limitation to linear elastic material (Leguillon, 2002). In order to employ the coupled criterion, the critical energy release rate and the strength of the considered material have to be known.

The material behaviour of silicone has been extensively investigated. Adhesively bonded connections with silicone are increasingly numerically reproduced using the Finite Element Method in an attempt to overcome the restrictions defined by the technical applications guidelines and to generate a better understanding of the material. Although the material behaviour of the silicone sealant can be accurately simulated, there are still aspects, which require additional research work, starting at the definition of a failure criterion for bulk material. In addition, stress singularities, which arise at discontinuities as sharp edges, hamper the assessment of these stress peaks. The present work focus on these two aspects.

3 Fundamentals

3.1 Material properties of silicone

The classification of adhesives can be done according to their chemical basis, their molecular structure or their evolution reaction. Considering the chemical basis, silicone neither belongs to the group of adhesives with an organic carbon based structure nor to the group of inorganic chemicals. Silicone elastomer exhibits an organic-like structure but the molecular chain is based on the inorganic components silicon and oxygen, which form the molecular backbone (Habenicht, 2009).

Concerning the molecular structure of polymers, *thermoplastics*, *thermosets* and *elastomers* are generally distinguished, as shown in figure 3.1. Thermoplastics are composed of linear or branched molecules, which have no connection points between each other. Therefore, thermoplastics liquefy at high temperatures. Thermosets are composed of densely linked molecules. Thermosets are hard and brittle, even at high temperatures. Finally, elastomers show widely-meshed connections of the molecules (Habenicht, 2009).

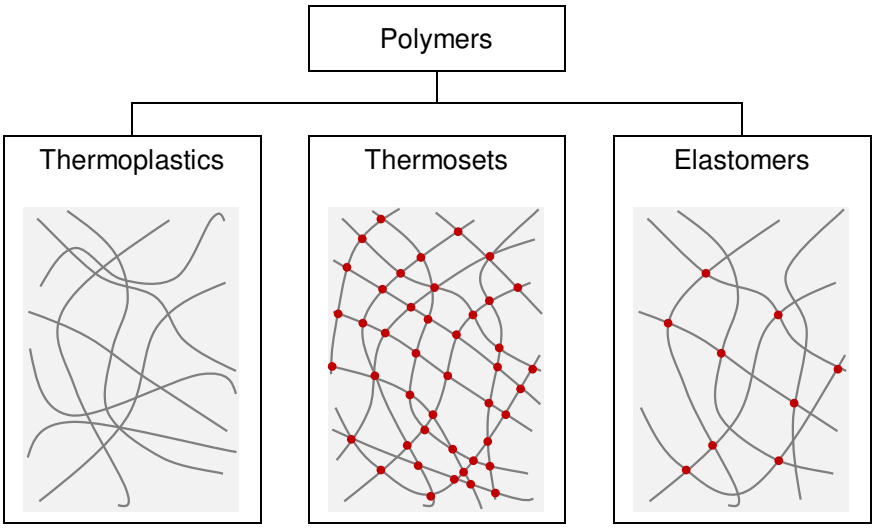

Figure 3.1: Characterisation of the adhesives according to their molecular structure (Habenicht, 2009)

The evolution reaction is another criterion for the characterisation of polymers. During the evolution reaction of *polymerizates*, several monomers containing double or triple bonds connect to each other by splitting up a double or triple bond. In a second step, the split bond can connect to another split bond thus creating a new single bond. For *polyadducts*, no double or triple bonds are split. Two and more monomers are able to connect because of hydrogen atoms leaving the monomer. The monomer with the free valence electron can form

a simple connection with another monomer having as well one free valence electron. The same holds true for *polycondensates*, but unlike for polyadducts, by-products, like water or alcohol, are created. Silicone elastomer can be classified in the group of polyadducts and polycondensates depending on the type of silicone considered (Habenicht, 2009).

Silicone is a synthetic rubber-like material having the structure of an elastomer, as it is composed of molecular chains with widely-meshed cross-linkings. As aforementioned, it is based on a silicon-oxygen molecular chain. Regarding the curing process, two types of silicones are distinguished. The curing process denotes the process during which the cross-links between the molecules are created. The curing process of *one component silicones* mostly needs air moisture. Therefore, this type of silicone is not suited for joints with large bite, as the curing process would require a long time. Amongst the one component silicones, there are neutral and acid curing systems. For these systems, different by-products are created during the curing process. For the *two component silicones*, a differentiation between condensation cure and addition cure silicones is made. The first ones produce by-products leading to some shrinkage. The curing process however is less vulnerable regarding the environmental conditions than for addition cure silicones (Habenicht, 2009), (Brockmann et al., 2005). The mechanical properties of both are similar (Ackermann and Damrath, 1989). There are a number of additional curing processes possible for silicones, which will not be further exposed here. Apart from silicones behaving like rubber-like materials, different formulations, like gels or liquids, exist. The length of the molecular chains and the density of cross-links are different for these products (Kurzweil and Scheipers, 2012).

The raw materials for silicone are quartz sand, coal, methane and salt. First of all, the quartz sand is reduced to silicon using coal and the salt is dissociated in sodium and chlorine in an electrolysis. In a second step, chlorine and methane form methyl chloride. Methyl chloride, silicon and water are the base components of silicone (Reller et al., 2000). These materials react in several steps in the presence of catalysts (Beers and Klosowski, 1990).

Apart from the polymer, reinforcing and non-reinforcing fillers are added to the elastomer. Reinforcing fillers lead to interactions between the polymer chain and the filler, thus increasing the strength by a factor of 10 to 30. Adding a filler has the same effect than increasing the density of cross-linking, as additional links between filler and filler or filler and polymer chains are formed. Examples of reinforcing fillers are pyrogenic and precipitated silica (Domininghaus et al., 2008). Furthermore, non-reinforcing fillers are used as an in-fill for bulking up (Ackermann and Damrath, 1989). Apart from those fillers, only a few additives are used when compared to other elastomers, because of the exceptional properties of silicone (Wacker Chemie AG, 2007).

Silicone elastomers can experience large deformations without failure. This behaviour can be observed from very low temperatures to their decomposition temperature (Eyerer et al., 2008). The glass transition temperature, i.e. the temperature at which the material behaviour changes from rubber-like to brittle, can be at -120°C for some silicone elastomers. Furthermore, silicone has stable properties and keeps its rubber-like behaviour for temperatures up to 200°C. The very strong silicon-oxygen molecular chain, which is moreover screened by nonpolar methyl-groups, is the reason for this exceptional behaviour (Habenicht, 2009). In addition to the stable rubber-like properties in the significant temperature range for civil engineering applications, silicone shows a pronounced resistance against ageing, weather impact and solar radiation. The reason for this is again the stable molecular chain, which has

only single bonds (Beers and Klosowski, 1990). Silicone is resistant against weak acids and basic solutions. In case of fire impact, a layer of silicon oxide is formed on the surface, which protects the material underneath (Schliebs and Ackermann, 1987). In addition, silicones show a very good wettability and excellent adhesion properties on many materials, especially on glass, due to silicone's chemical resemblance to glass (both are basically composed of silicon and oxygen) (Gutowski et al., 1993). Silicone can enter a chemical compound with glass (Hagl, 2006).

Elastomers generally show nonlinear material behaviour. The material properties can no longer be described by the linear elasticity, except for small deformations. Instead the nonlinear elasticity or hyperelasticity, which is introduced in section 3.3.1, is applied. Apart from the physical nonlinearities, geometric nonlinearities must be considered as well, due to the soft material behaviour and the large deformations that occur. Hyperelasticity can be described as an *entropy-elastic* material behaviour (Bormann, 2005). The entropy is a measure for the internal disorder. When a strain is applied to an elastomer, the molecules will become aligned. This constitutes a state of lower entropy than the initial tangled configuration. When unloading the elastomer, the molecules will return into their tangled configuration, which is a more favourable energetic state. According to the entropy-elastic model, the distance between two adjacent atoms is constant, the deformation is mainly due to the displacement of the whole molecular chain (Rinnbauer, 2006).

Apart from a highly nonlinear elastic material behaviour, silicone sealants also exhibit time dependent material behaviour, like creep and relaxation, as well as a strain rate dependency. These phenomena have been considered in Dias (2013) and Staudt (2013). Rubber-like materials show in addition a so-called *stress-softening* effect, called *Mullins* effect (Mullins, 1948). The *Mullins* effect is a change of the mechanical properties after the first stretching of the material with the unloading path being softer than the initial loading path. When stretching the material again, the reloading path is between the unloading and initial loading path or coincident with the unloading path for the ideal *Mullins* effect. Most of the softening occurs after the first unloading, reaching a stable material response, if fatigue is disregarded. If the material is extended beyond the preloaded range, the stress-strain curve will follow the initial stiffness or *virgin* curve.

The *Mullins* effect (Mullins, 1948) has already been investigated for some decades, but no consensus has been found yet for the underlying physical mechanism. Initially, the stress-softening effect was referred to the presence of fillers. For an applied stretch, the bonds to the polymeric matrix fail thus leading to a softer material behaviour. Other interpretations assume bond rupture of molecules or molecular slippage. Finally, the rearrangement of molecules and the change in the density of entanglement of the molecules is supposed to cause the *Mullins* effect. Assuming these mechanics, a thermal exposure of the material could lead to a new entanglement of the molecular chains and thus to a recovery of the initial stiffness. Experimental investigations have shown a limited recovery for samples exposed to high temperatures or solvents. A detailed review of the *Mullins* effect is given in Diani et al. (2009). For silicone materials, the stress-softening effect was investigated in Machado et al. (2010) and Dias (2013).

3.2 Structural Sealant Glazing Applications

3.2.1 Glass and its connections

Glass has been used increasingly over the past decades in façade applications in order to create both an architectural attractive façade and a highly transparent building skin, allowing for the usage of natural illumination in the building (Overend et al., 2011), (Tibolt and Odenbreit, 2014). Since glass is a brittle material (Schneider et al., 2016), the question of its connection to the mostly metallic substructure becomes crucial. Three types of connections are possible: mechanical, adhesive or a combination of both (Dias, 2013). For *mechanical connections*, glass can be linearly supported or point-wise by bolted (Dispersyn et al., 2014) or clamped connections (Drass et al., 2016). Whereas linear connections reduce the transparency of the building and promote thermal bridges (De Buyl, 2001), bolted connections significantly weaken the glass pane as boreholes are drilled. This treatment creates scratches and flaws, which reduce the strength of glass (Schneider et al., 2012). Moreover the loads are transferred on a very small area between the bolt and the borehole (Dispersyn et al., 2014).

Glass can also be *adhesively bonded* to the building's substructure. Although other adhesives like polyurethanes, which are used in automotive industry, have higher strength and stiffness (Richter et al., 2014), only soft silicone structural sealants can be used for façade applications, as prescribed by ETAG 002 (2012) and discussed later. For adhesively bonded connections, linear and point-wise applications of the sealant can be envisaged. Especially for linear applications, the main advantage of bonded connections is the uniform load transfer due to the large bonding area and the capability of the adhesive to compensate differences in thermal or structural movements of the adherends. In addition, silicones can absorb a significant amount of energy, which is important for regions with high seismic activity or high wind loads. Finally, the smooth building skin, with no mechanical fixation devices penetrating the building skin, is both energy efficient and architectural attractive (Descamps et al., 1996), (De Buyl, 2001), (Ihara et al., 2014).

Due to restrictions in current regulations, a *combination of mechanical and adhesive connections* is often used, as in the building shown in figure 3.2. For this building, two sides have been conventionally (mechanically) glazed and the two other sides with structural silicone. Depending on the country, applications with all four edges adhesively bonded can also be found (Descamps et al., 1996).

3.2.2 Insulation glass units

Extensive curtain walls are used to benefit from natural light, thus reducing the need for artificial lighting. To ensure the thermal performance of the building, insulation glass units (IGU), shown in figure 3.3, are used. Insulating glass units are composed of two or more similar or dissimilar glass panes. The distance between the panes is kept constant at their edges. The separated space is called *cavity* and the connection between the glass panes *edge bond*. The edge bond has a structural function as it connects the two glass panes and it guarantees the tightness of the cavity. The cavity is an enclosed unit and filled with air or special gases. The thermal performance of the IGU depends on the width of the cavity. To increase the thermal insulation performance of the assembly, inert gas can be used instead of air in the cavity. In order to reduce the heat transfer due to radiation, low emissivity coatings are applied on the glass panes (Sedlacek et al., 1999).

Figure 3.2: Example of a two-sided structural glazing system: Kastor (middle) and Pollux tower (right) in Frankfurt/Main (Germany), picture from Dow Corning Corporation (2010a)

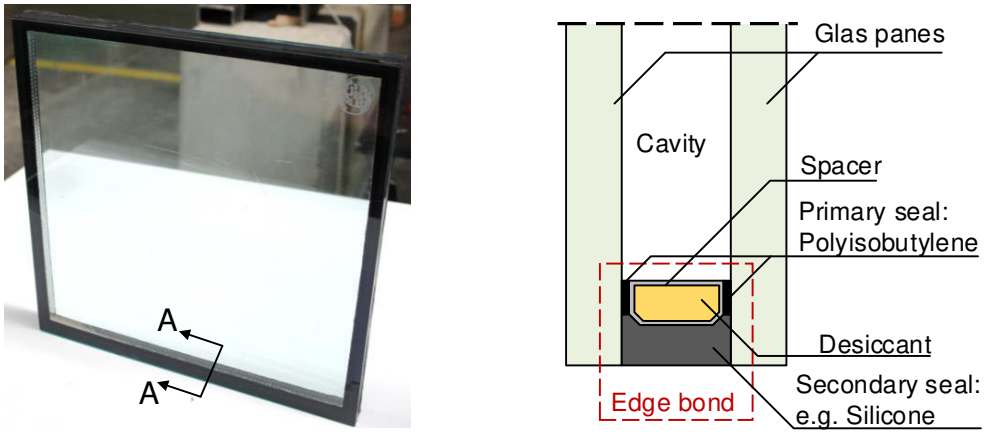

(a) Small insulation glass unit

(b) Section A-A

Figure 3.3: Example of a small insulation glass unit

A typical assembly is composed of two glass panes separated by an aluminium, galvanised steel or plastic spacer. The spacer is bonded on the glass panes with polyisobutylene (PIB), which is used due to its low permeability of water and its high elasticity. The spacer is a perforated hollow section filled with a desiccant to absorb any humidity, which diffuses through the edge bond, in order to prevent fogging. The assembly spacer and PIB is called *primary seal*, responsible for the tightness of the cavity. Furthermore, a second edge seal is applied. For this, polysulfide, polyurethane or silicone elastomer is used. This seal is called *secondary seal*. It has a structural function (Sedlacek et al., 1999).

3.2.3 Structural applications of silicone sealants

As mentioned before, silicone sealants can be used to adhesively bond glass to the metallic structure of a building. Figure 3.4 shows a typical example of a structural edge bond, which transfers wind loads. The insulation glass unit itself is as well adhesively bonded to the substructure. For this example, the dead load is mechanically transferred to the building's structure.

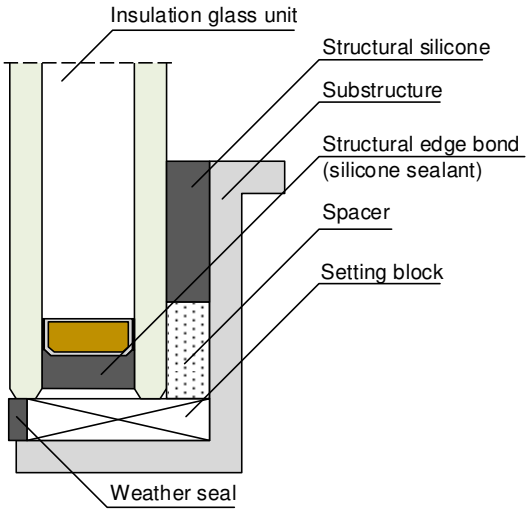

Figure 3.4: IGU with structural edge bond and adhesive connection to the building

Figure 3.5 shows a restaurant in Austria with a structural sealant glazing (SSG) façade. The façade is composed of a triple IGU (3 glass panes and 2 cavities), which is four-sided bonded to the substructure with Dow Corning® 993 structural silicone. The façade is inclined to the outside with an angle of 8 degrees. Retaining devices reduce the danger in case of an adhesive bond failure and the dead loads are transferred mechanically to the building's substructure (Wolf, 2010), (Weller et al., 2011).

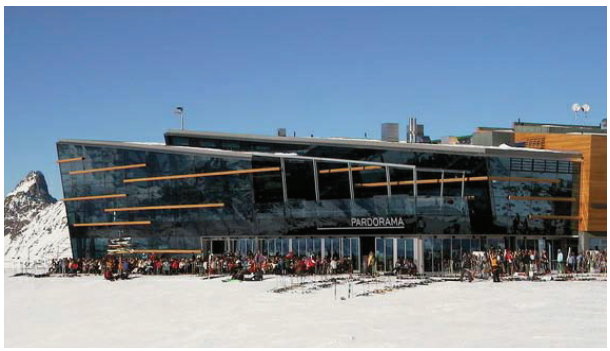

Figure 3.5: SSG façade of a restaurant in Austria, picture from Wolf (2010)

Figure 3.6 shows a second example of a SSG façade. The façade of the Zeppelin University in Friedrichshafen (Germany) is a double skin façade with mechanically fastened IGUs as inner skin and a SSG façade as outer skin. The outer skin is a laminated glass, which is four-sided structurally bonded with Dow Corning® 993 structural sealant to the substructure. A special approval from the upper construction authority was required for this project as the dead load is not mechanically transferred to the substructure (Dow Corning Corporation, 2010b).

Figure 3.6: SSG façade of the Zeppelin University in Friedrichshafen, Germany, picture from Dow Corning Corporation (2010b)

3.2.4 Current research work

Apart from the above mentioned applications of structural silicone adhesives, there is a number of research projects dealing with innovative connection types. To increase the transparency of the façade while avoiding the inconveniences of drilled-through bolts, adhesively bonded point-fixings, as shown in figure 3.7, are subject to research activities. While in Hagl (2006) the standard black structural silicone adhesive (Dow Corning® 993) was investigated, Drass et al. (2016) worked with Dow Corning® TSSA (Transparent Structural Silicone Adhesive), a thin transparent structural silicone adhesive with higher strength and stiffness compared to the standard formulations. This adhesive however is only available as thin sheets, which are curing under pressure and heat (Dow Corning Corporation, 2013).

(a) DC 993 (Hagl, 2006)

(b) TSSA (Dias, 2013)

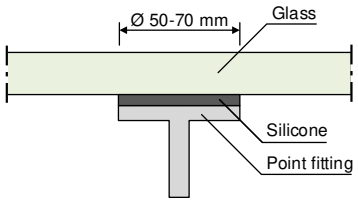

(c) Side view

Figure 3.7: Adhesive point fittings using silicone adhesives

Other researchers deal with linear or point-wise joints of more complex geometries (e.g. Hagl (2008a) or Richter et al. (2014)), as shown in figures 3.8 and 3.9. The U-type bonding shown in figure 3.8b has been used in the Herz-Jesu church in Munich, Germany, to connect horizontal and vertical glass fins with steel stringers. These steel stringers were fixed to the façade stringers using bolts (Hagl, 2008b).

At the University of Luxembourg, steel to glass composite beams using Dow Corning® 993 structural silicone adhesive have been developed and tested in 4-point bending (see figure 3.10). The shear connection between the steel beam and the glass pane has been realised

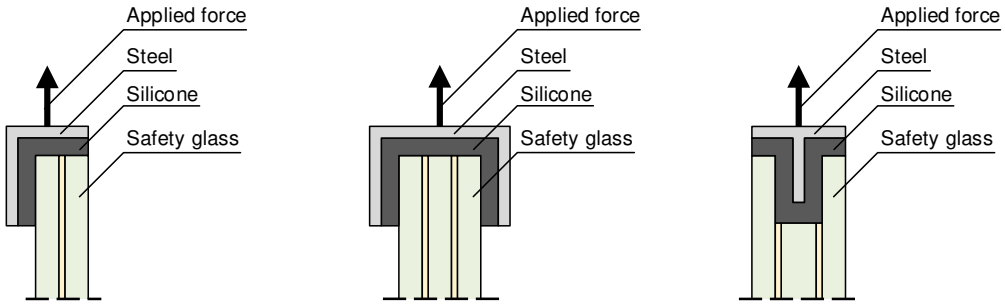

(a) L-type (b) U-type (c) T-type

Figure 3.8: Steel to glass adhesive connections with complex geometries (Hagl, 2007)

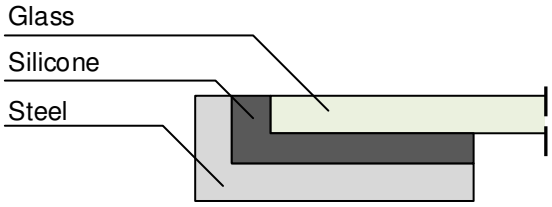

Figure 3.9: L-shaped connection (Richter et al., 2014)

using the previously mentioned structural silicone adhesive. The tests have been numerically reproduced and a hyperelastic material law has been developed for the silicone adhesive (Dias, 2013).

Figure 3.10: Steel to glass composite beam, developed and tested at the University of Luxembourg, picture from Dias (2013)

3.2.5 Normative background - ETAG 002 and ASTM C1401

In Europe, design guidelines for Structural Sealant Glazing Systems are defined in the European Technical Approval Guideline ETAG 002 (2012). In the United States, the American Society for Testing and Materials (ASTM) published as well a "Standard Guide for Structural Sealant Glazing", labelled ASTM C1401 (2002). The current section will explain the design concept of these standards and focus on their limitations and assumptions.

European Technical Approval Guideline ETAG 002

ETAG 002 (2012) covers façades with glazing at an angle between vertical and 7° above horizontal. Glass, either uncoated or with hard inorganic (pyrolytic) coatings, anodised aluminium or stainless steel can be used as substrate with special requirements defined for glass with organic coatings, aluminium with a coating other than anodising or thermal breaks used in SSG framing systems. Due to their exceptional adhesion performance and durability, only silicone adhesives are authorised to be used as structural sealants. The 4 types of structural glazing systems, shown in figure 3.11, are defined in ETAG 002 (2012), depending on the support of the dead load and on the presence of mechanical retaining devices. For type I, the dead load is transferred mechanically to the substructure. Moreover, retaining devices are used to reduce the danger in case of a failure of the adhesive. Type II is similar to type I, except that no retaining devices are used. For type III, all loads including dead load are transferred by the adhesive. Retaining devices however reduce the danger in case of bond failure. For type IV, all actions are transmitted through the adhesive. No retaining devices are used.

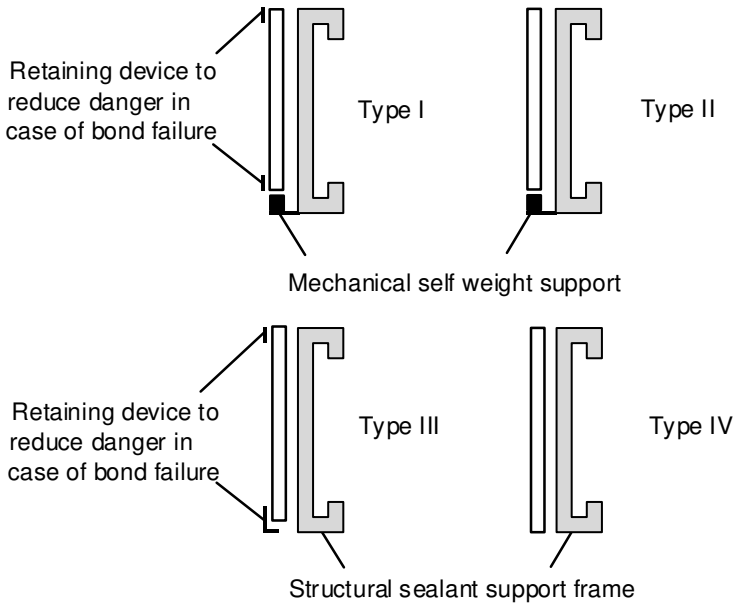

Figure 3.11: Different types of Structural Sealant Glazing Systems (ETAG 002, 2012)

Due to the state of current understanding, several restrictions are defined. The structural bond must be in the form of a linear silicone bead. Discontinuities in the structural bond are allowed, but no edge is allowed to be free, except if it is mechanically fastened. The structural

sealant must to be factory applied and adhesion of the sealant on more than two surfaces is not allowed. The adhesion of the secondary seal on the edge bond spacer is not considered as contributing towards three-side adhesion in this context. For insulation glass units with a mechanically fastened interior pane and only the exterior pane structurally bonded, the present specifications do not apply. Type III and IV are only applicable for monolithic glass. For IGU and laminated glass, each pane of glass must be supported.

ETAG 002 defines experimental methods to assess the applicability of a given silicone based adhesive for usage in a structural sealant glazing system. Testing methods for the mechanical properties and performance of the adhesive are detailed. The material properties and the material performance have to be determined both in tension and shear immediately after the curing period and after artificial ageing. The specimen detailed by the ETAG 002 is shown in figure 3.12. Testing procedures regarding various physical properties (gas inclusion, elastic recovery, shrinkage, tear resistance, mechanical fatigue, UV resistance, elastic (*Young's*) modulus, creep) are defined as well. Considering long-term loads, the design values of the tensile and shear strength are reduced by a factor of 10. ETAG 002 requires a minimal thickness of the structural sealant e of 6 mm and a bite dimension h_c between 6 and 20 mm. The definition of bite (effective structural contact dimension) and thickness of the structural sealant are given in figure 3.12.

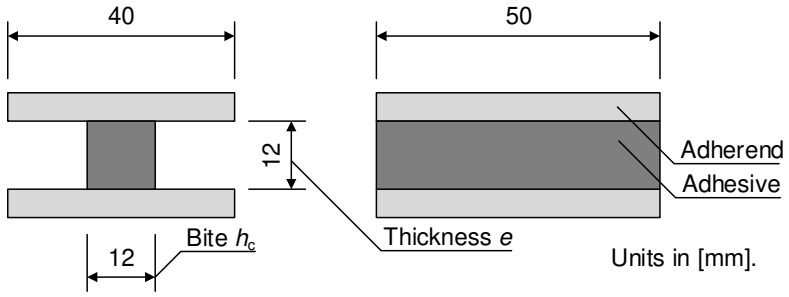

Figure 3.12: Specimen detailed by ETAG 002 (2012)

ETAG 002 foresees two methods of calculation. Apart from the design formulas presented below, a method of calculation *"based on simulation test or results of research"* can be envisaged (ETAG 002, 2012). The design formulas are based on two fundamental assumptions, beginning at a trapezoidal surface load distribution and a uniform distribution of the stresses within the sealant. For supported systems, the bite can be calculated as

$$\sigma_\mathrm{E} = \frac{l_\mathrm{a}\, p_\mathrm{d}}{2\, h_\mathrm{c}} \leq \sigma_\mathrm{des} \implies h_\mathrm{c} = \frac{l_\mathrm{a}\, p_\mathrm{d}}{2\, \sigma_\mathrm{des}}. \tag{3.1}$$

In equation 3.1, l_a is the shorter dimension of a rectangular glass pane, h_c the bite, p_d the acting surface load and σ_des the engineering tensile strength as defined in ETAG 002 (2012). For supported systems, the required thickness of the structural sealant depends on the differential thermal expansion Δl_th of the assembly with the shear stress given as

$$\tau_\mathrm{E} = \frac{E\, \Delta l_\mathrm{th}}{3\, e} \leq \tau_\mathrm{des} \implies e = \frac{E\, \Delta l_\mathrm{th}}{3\, \tau_\mathrm{des}} \geq 6\,\mathrm{mm}. \tag{3.2}$$

In equation 3.2, E is *Young*'s modulus of the sealant. The adhesive bite dimension should not be smaller than the adhesive thickness and not larger than 3 times the adhesive thickness. For unsupported systems, the same equations apply, but for the thickness, shear stresses

$$\tau_{\mathrm{E}} = \frac{G_{\mathrm{Pane}}}{2\, h_{\mathrm{c}}\, h_{\mathrm{v}}} \leq \tau_{\infty} \tag{3.3}$$

from the dead load must be considered only for the vertical silicone beads. In equation 3.3, G_{Pane} is the weight of the glass pane, h_{v} the length of the vertical silicone beads and τ_{∞} the design shear stress for long term loads. The tensile strength σ_{des} is the ratio of maximum applied force and the initial cross sectional area, as determined on the H-specimen shown in figure 3.12. An analogous procedure on the same specimen is described to determine the shear strength τ_{des}. The design values for both stresses are obtained, taking the 5% fractile of the obtained test results and dividing it with a design factor of 6. For long term loads, the design stresses σ_{des} and τ_{des} are divided in addition with a factor of 10.

American Society for Testing and Materials ASTM C1401-02

The ASTM C1401 (2002) focusses on bonded connections, which have a slope of not more than 15° from vertical. Only silicone adhesives are accepted for use in structural sealant applications. A differentiation between structural loads and movements is made. Structural loads are dead loads, wind, snow, life (maintenance) and seismic loads as well as missile impact. The application of a structural sealant for unsupported systems must be approved by the manufacturer. However, the value for the dead load stress is limited to 7 kPa. Movements from building motion, thermal movements, deflections of the supporting frame, creep, shrinkage and seismic movements have to be considered. The uncertainty over the long-term durability and the compatibility with other materials, such as setting blocks or gaskets, are taken into account. Moreover, bonded connections are considered less redundant than a mechanically attached system.

ASTM C1401 (2002) basically considers two systems: two- and four-sided SSG systems. For the two-sided systems, the structural sealant is applied at two opposite sides of a panel, the other sides are mechanically fastened. These systems are suited both for construction-site or shop glazing. Four-sided SSG systems are very energy efficient, as no metal parts are exposed to the outer building surface. Moreover, there are no components, which overcome the plane of the glass and thus acting like a dam, which collects dirt. However, four-sided systems exhibit a higher risk than two-sided SSG systems. Four-sided SSG systems are only applicable to shop glazed systems. For the metal framing system, only aluminium, steel and stainless steel should be used. For the glass pane, monolithic, insulating and strengthened glass are allowed. If laminated glass is used, compatibility tests are required. For coated glass, adhesion tests must be performed. Apart from glass, many other materials can be used in structural sealant application. Amongst them, stainless steel is a very good adherend, because of its good corrosion resistance (ASTM C1401, 2002).

Only silicone elastomer fulfils the requirements for structural sealant glazing use. ASTM C1401 (2002) defines a minimum tensile strength of 0.345 MPa after exposure to several conditions, like heat, water immersion and weather impact. The test specimen is detailed in ASTM C1135. It is similar to the specimen detailed by ETAG 002 (2012), which is shown in figure 3.12. A transparent structural sealant is not recommended. Pigments should be

added to block UV radiation affecting the adhesion performance of the adhesive-adherend interface. Single component and multicomponent silicones can be used. For compatibility reasons, non-structural weather sealants should as well be silicone sealants.

ASTM C1401 (2002) defines design factors according to the principle *"the less engineering knowledge available and the higher the degree of risk, the larger the design factor"*. As aforementioned, the minimum tensile strength is set to 0.345 MPa. The maximum design strength however is set to 0.139 MPa, which gives a design factor of 2.5. Bite and thickness are defined in the same way as in ETAG 002 (2012). A minimum value of 5 mm is required for the adhesive thickness of shop glazed assemblies and 6 mm for construction site glazed façades. ASTM C1401 (2002) differentiates between primary loads, like wind and secondary loads, like differential thermal and building movement or dead load and seismic events.

For the structural sealant joint design, ASTM C1401 (2002) proposes several design methods. The trapezoidal method is based on the assumption that a glass panel deflects in tributary areas under a load normal to the panel. It is a method for the primary load transfer, the maximum value occurring at the centre point of the glass pane's short dimension. This method corresponds to the equation given in ETAG 002 (2012) and discussed in the previous section. The rigid plate method assumes the glass pane to be rigid and the stresses

$$\sigma_{\mathrm{E}} = \frac{l_{\mathrm{a}}\, l_{\mathrm{b}}\, p_{\mathrm{d}}}{2\ (l_{\mathrm{a}} + l_{\mathrm{b}})\ h_{\mathrm{c}}} \leq \sigma_{\mathrm{des}} \tag{3.4}$$

as uniformly distributed. In equation 3.4, σ_{E} is the acting stress, p_{d} the acting surface load, h_{c} the adhesive bite and σ_{des} the design value of the tensile strength. l_{a} and l_{b} are the dimensions of the rectangular glass pane.

The Finite Element Method can, similarly as in ETAG 002 (2012), be used to calculate the stress distribution (normal and shear stresses) occurring under primary and secondary loads. The Finite Element Method allows to take into account physical and geometrical nonlinearities. As primary and secondary loads can occur simultaneously, their combined effect should be evaluated. Generally speaking, the secondary loads should not cause more than an additional stress of 0.021 MPa to 0.035 MPa. Moreover, the sum of tensile and shear stresses should not exceed 0.139 MPa. Alternatively, the effect of combined loads can be assessed with the elliptical interaction equation

$$\left(\frac{\sigma_{\mathrm{E}}}{\sigma_{\mathrm{des}}}\right)^2 + \left(\frac{\tau_{\mathrm{E}}}{\tau_{\mathrm{des}}}\right)^2 = 1. \tag{3.5}$$

In equation 3.5, σ_{E} is the acting tensile stress, τ_{E} the acting shear stress, σ_{des} the design value for the tensile strength and τ_{des} the design value for the shear strength. The same formula applied for long term loads by using the respective long term strengths. The maximum value for the dead load stress must be limited from 7 kPa to 3.5 kPa. The transfer of dead loads must be approved by the manufacturer. Dead loads of insulating glass panels are usually transferred by setting blocks, but the edge bond can also be designed for a dead load transfer, following

$$\tau_{\mathrm{E}} = \frac{G_{\mathrm{Pane}}}{2\ h_{\mathrm{c}}\ (l_{\mathrm{a}} + l_{\mathrm{b}})} \leq \tau_{\infty}. \tag{3.6}$$

In equation 3.6, τ_{E} is the acting shear stress, G_{Pane} the dead load of the glass pane, h_{c} the adhesive bite, l_{a} the pane's shorter dimension, l_{b} the pane's larger dimension and τ_{∞} the design value of the shear strength for long term loads.

The calculation of the stresses induced by a differential thermal movement depends on the type of structural sealant glazing system considered. Depending on the location of an adhesive joint undergoing a differential thermal movement, tensile, shear or compressive stresses can be caused. The acting stresses are determined from the stress-strain graph, knowing the value for the differential movement. It should be limited to 0.139 MPa for tension. When shear stresses are induced, the acting shear stress can be obtained from the stress-strain graph in shear, knowing the induced shear angle, or from the tension stress-strain graph, if no values for shear are available. The combined action of these stresses as well as the interaction with other loads should be considered.

3.3 Modelling of silicone sealants

3.3.1 Basics of continuum mechanics

In the present section, the basic concepts of continuum mechanics are introduced. Since silicone elastomer exhibits a nonlinear elastic material behaviour, this section focuses on hyperelastic material laws. Hyperelastic material laws are mostly based on a strain energy potential. Some commercial Finite Element software codes offer in addition a material model, which uses experimental data directly without an explicit definition of a strain energy potential to determine the material's response (e.g. Marlow (2003)). A basic assumption of hyperelastic, i.e. nonlinear elastic theory is that the current stress state is only dependent on the current deformation. Time and load history dependencies are not considered (Altenbach, 2012). In the following, most equations are based on the publication of Dorfmann (2009).

Kinematics

Generally speaking, a body can be represented as a set of material points, which can be considered in a three dimensional *Euclidian* space. Considering a body (shown in figure 3.13) in its undeformed configuration (reference configuration) B_0 and in its deformed state B, the boundaries of these bodies in the two states are denoted ∂B_0 and ∂B respectively. The coordinate system of the reference configuration is given by the origin O and the base vectors $\vec{E_1}$, $\vec{E_2}$, $\vec{E_3}$. The coordinate system of the deformed state is defined by the origin o and the base vectors $\vec{e_1}$, $\vec{e_2}$, $\vec{e_3}$. A point P_0 of the body in the reference configuration can thus be described by a vector $\vec{X}$ and the point P its deformed state by a vector $\vec{x}$.

There is a vector field χ that describes the deformation of the body. This vector field is a one-to-one invertible orientation preserving mapping. The vector field is independent of the deformation history (Altenbach, 2012).

$$\vec{x} = \chi\left(\vec{X}\right) \qquad \text{and} \qquad \vec{X} = \chi^{-1}\left(\vec{x}\right). \tag{3.7}$$

The deformation gradient $\boldsymbol{F}$ is a measure of the deformation of the body. It is a tensor, which

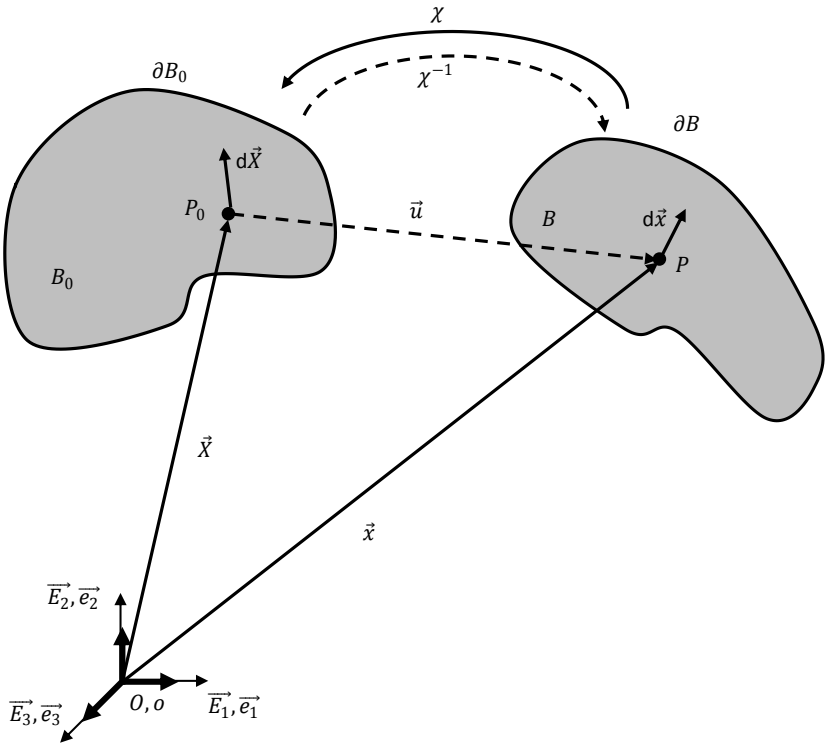

Figure 3.13: Deformation of a body from the reference in the current configuration (Dorfmann, 2009)

maps the reference and current configuration. It is defined as

$$\boldsymbol{F} = \frac{\partial \vec{x}}{\partial \vec{X}} = \frac{\partial}{\partial \vec{X}} \left(\vec{X} + \vec{u} \right) = \boldsymbol{I} + \frac{\partial \vec{u}}{\partial \vec{X}} = \boldsymbol{I} + \boldsymbol{H}. \tag{3.8}$$

In equation 3.8, $\boldsymbol{H}$ is the displacement gradient and $\boldsymbol{I}$ the unit tensor. Physically, the deformation gradient $\boldsymbol{F}$ transforms a line segment $d\vec{X}$ from the reference configuration to the deformed configuration $d\vec{x}$. According to the polar decomposition theorem, the deformation gradient can be decomposed into a proper orthogonal tensor and a symmetric tensor

$$\boldsymbol{F} = \boldsymbol{R}\,\boldsymbol{U} = \boldsymbol{V}\,\boldsymbol{R}. \tag{3.9}$$

$\boldsymbol{R}$ is the rotational tensor, $\boldsymbol{U}$ is the right stretch tensor and $\boldsymbol{V}$ the left stretch tensor. Physically, these tensors represent a pure stretch of the body without rotation. Considering the equation above, it can be seen that the body can first be turned into the current configuration and then be stretched or it can be stretched in the reference configuration and then turned. The deformation gradient is defined in both the reference and current configuration and is not necessarily symmetric. Moreover, it contains both a stretch and rotation part. The left and right *Cauchy-Green* tensors describe deformations without being influenced by a pure rotation. Moreover, they are only defined in one basis, either the reference configuration for the right *Cauchy-Green* tensor $\boldsymbol{C}$ or the current configuration for the left *Cauchy-Green* tensor $\boldsymbol{b}$.

$$\begin{aligned} \boldsymbol{C} &= \boldsymbol{F}^T\,\boldsymbol{F} = \boldsymbol{U}^T\,\boldsymbol{U} = \boldsymbol{U}^2, \\ \boldsymbol{b} &= \boldsymbol{F}\,\boldsymbol{F}^T = \boldsymbol{V}\,\boldsymbol{V}^T = \boldsymbol{V}^2. \end{aligned} \tag{3.10}$$

The invariants of both tensors are equal as they only depend on the principal stretches λ_i,

$$\begin{aligned} I_1(\boldsymbol{b}) = I_1(\boldsymbol{C}) &= \operatorname{tr}(\boldsymbol{C}) = \lambda_1^2 + \lambda_2^2 + \lambda_3^2, \\ I_2(\boldsymbol{b}) = I_2(\boldsymbol{C}) &= \frac{1}{2}\left[(\operatorname{tr}(\boldsymbol{C}))^2 - \operatorname{tr}(\boldsymbol{C}^2)\right] = \lambda_1^2\,\lambda_2^2 + \lambda_1^2\,\lambda_3^2 + \lambda_2^2\,\lambda_3^2, \\ I_3(\boldsymbol{b}) = I_3(\boldsymbol{C}) &= \det \boldsymbol{C} = J^2 = \lambda_1^2\,\lambda_2^2\,\lambda_3^2. \end{aligned} \tag{3.11}$$

J is the determinate of the deformation gradient and is a measure of the volume change. If an incompressible material is considered, $J = 1$. When considering compressible material behaviour, the deformation gradient can be split into a deviatoric and volumetric component,

$$\boldsymbol{F} = \left(J^{1/3}\,\boldsymbol{I}\right)\,\overline{\boldsymbol{F}}. \tag{3.12}$$

In equation 3.12, $J^{1/3}\,\boldsymbol{I}$ is the volumetric part ($\boldsymbol{I}$ is the unity tensor) and $\overline{\boldsymbol{F}}$ the deviatoric part. The same method applies to the left and right *Cauchy-Green* tensor. Further strain tensors are defined in table 3.1. The infinitesimal strain tensor is considered, if the displacement gradient is small, i.e. if the difference between the reference and the current configuration can be neglected.

Table 3.1: Strain tensors

Strain tensor	Definition
Green-Lagrange strain tensor	$\boldsymbol{E} = \frac{1}{2}\left(\boldsymbol{U}^2 - \boldsymbol{I}\right)$
Euler-Almansi strain tensor	$\boldsymbol{a} = \frac{1}{2}\left(\boldsymbol{I} - \boldsymbol{b}^{-1}\right)$
Infinitesimal strain tensor	$\boldsymbol{\varepsilon} = \frac{1}{2}\left(\boldsymbol{H} + \boldsymbol{H}^T\right)$

Stress tensors

Consider a body under given loads in equilibrium in its deformed configuration, as shown in figure 3.14. When this body is cut into two pieces, these pieces are no longer in equilibrium. According to *Cauchy*'s stress principle, equilibrium will be fulfilled when assuming the existence of a vector of internal forces acting on the cutting plane. For a given normal vector $\vec{n}$, the stress vector $\vec{t}$ is given by

$$\vec{t} = \boldsymbol{\sigma}^T\,\vec{n}, \tag{3.13}$$

where $\boldsymbol{\sigma}$ is the *Cauchy* stress tensor, a second order tensor, which is defined in the current configuration. Considering equilibrium of moments, it can be shown that the *Cauchy* stress tensor is symmetric.

There are more stress tensors, like the nominal stress tenor and the *Piola-Kirchhoff* tensor. Table 3.2 summarises the stress tensors with their definitions, their properties and their work conjugate.

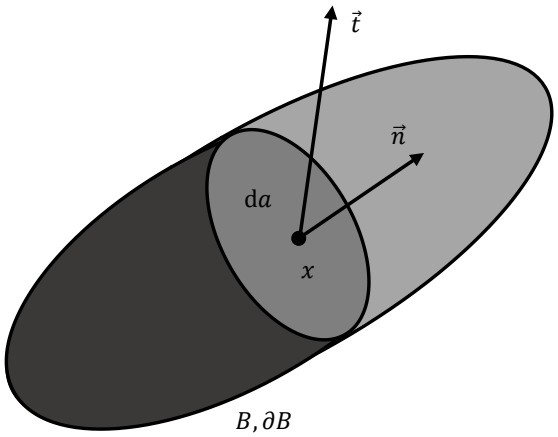

Figure 3.14: Free-body principle on a solid under loads in its deformed configuration

Table 3.2: Different definitions for stress tensors

Stress tensor	Equation	Properties	Work conjugate
Cauchy stress tensor	$\boldsymbol{\sigma}$	Current configuration, symmetric	*Euler-Almansi*
1^{st} *Piola-Kirchhoff* stress tensor	$\boldsymbol{P}_1 = J\ \boldsymbol{\sigma}\ \boldsymbol{F}^{-T}$	not symmetric	Deformation gradient
2^{nd} *Piola-Kirchhoff* stress tensor	$\boldsymbol{P}_2 = J\ \boldsymbol{F}^{-1}\ \boldsymbol{\sigma}\ \boldsymbol{F}^{-T}$	Reference configuration, symmetric	*Green-Lagrange*

Equation of equilibrium

Considering body forces $\vec{f}$, defined per unit mass and acting throughout the body (e.g. gravitational forces), equilibrium in the deformed configuration requires that both the sum of all body forces and the sum of surface tractions vanish, i.e.

$$\int_B \rho \vec{f} dv + \int_{\partial B} \vec{t} da = \vec{0}. \tag{3.14}$$

In equation 3.14, ρ is the density of the material of the body, $\vec{f}$ the body forces per volume dv and $\vec{t}$ the surface tractions per area da. Considering equation 3.13, the equilibrium equation can be written as a function of the *Cauchy* stress tensor,

$$\int_B \rho \vec{f} dv + \int_{\partial B} \boldsymbol{\sigma}^T\ \vec{n} da = \vec{0}. \tag{3.15}$$

Finally, using the divergence theorem, equation 3.15 can be rewritten in its local form,

$$\mathrm{div}\ \boldsymbol{\sigma} + \rho \vec{f} = \vec{0}. \tag{3.16}$$

Boundary conditions

The general field equations are completed by boundary conditions, which are applied to the considered body (Altenbach, 2012). Three types of boundary conditions can be distinguished:

- prescribed surface displacements,
- prescribed surface forces and
- a combination of the prescribed surface loads and displacements.

For a number of problems, analytical solutions for the stress distribution or the displacements can be found, especially if symmetry or plane strain and plane stress conditions are assumed.

Constitutive equations

For a hyperelastic material, it is postulated that a *Helmholtz* free-energy function W, defined per unit volume exists. If W is a function of the deformation gradient or some other strain tensors, it is referred to as strain energy function (Holzapfel, 1996). For homogeneous materials, the strain energy potential only depends on the deformation gradient,

$$W = W\left(\boldsymbol{F}\right). \tag{3.17}$$

The relation between the *Cauchy*-stress tensor and the strain energy potential is given by

$$\boldsymbol{\sigma} = J^{-1}\ \boldsymbol{F}\ \frac{\partial W}{\partial \boldsymbol{F}}. \tag{3.18}$$

For isotropic materials, the strain energy potential can also be expressed as functions of the invariants of the left or right *Cauchy-Green* tensors.

$$W = W\left(I_1(\boldsymbol{C}), I_2(\boldsymbol{C}), I_3(\boldsymbol{C})\right) = W\left(I_1(\boldsymbol{b}) I_2(\boldsymbol{b}), I_3(\boldsymbol{b})\right). \tag{3.19}$$

For this case, the *Cauchy* stress tensor can be written as follows

$$\boldsymbol{\sigma} = 2\ J^{-1}\ \left[I_3\ \frac{\partial W}{\partial I_3}\ \boldsymbol{I} + \left(\frac{\partial W}{\partial I_1} + \frac{\partial W}{\partial I_2} I_1\right)\ \boldsymbol{b} - \frac{\partial W}{\partial I_2}\ \boldsymbol{b}^2\right]. \tag{3.20}$$

Incompressible hyperelasticity

When an incompressible material behaviour is considered, the above shown equations simplify considering that the ratio of current volume to initial volume, defined by J gives

$$J = \det\left(\boldsymbol{F}\right) = \lambda_1\ \lambda_2\ \lambda_3 = 1. \tag{3.21}$$

Therefore, the third invariant of the left and right *Cauchy-Green* tensors gives

$$I_3(\boldsymbol{C}) = I_3(\boldsymbol{b}) = J^2 = 1. \tag{3.22}$$

The strain energy potential can now be written independently of the third invariant. In order to account for the hydrostatic pressure, the following expression is postulated

$$W = W(\boldsymbol{F}) - p(J-1). \tag{3.23}$$

In equation 3.23, p is the hydrostatic pressure, known as the undetermined *Lagrange* multiplier. The hydrostatic pressure cannot be determined by the constitutive equation, it has to be found through consideration of equilibrium or the boundary conditions. The *Cauchy* stress tensor reduces to

$$\boldsymbol{\sigma} = 2\left(\frac{\partial W}{\partial I_1} + \frac{\partial W}{\partial I_2} I_1\right)\boldsymbol{b} - \frac{\partial W}{\partial I_2}\boldsymbol{b}^2 - p\,\boldsymbol{I}. \tag{3.24}$$

Compressible hyperelasticity

For the consideration of compressible hyperelasticity, the strain energy potential can be split into volumetric and deviatoric part

$$W = W_{\mathrm{dev}} + W_{\mathrm{vol}}. \tag{3.25}$$

Again, the strain energy potential can be expressed in terms of the invariants of the left or right *Cauchy-Green* tensor if isotropic material behaviour is considered. As introduced before, a multiplicative split of the invariants of the left or right *Cauchy-Green* tensor is performed.

Strain energy potentials

Up to this point, the strain energy potential was not described in detail. For rubber-like materials, a number of strain energy potentials are available. There are two main categories of material laws: micro-mechanically based and phenomenological models. Moreover, some material laws are only based on the first invariant of the left *Cauchy-Green* tensor, whereas others also take into account the second invariant. A good overview of hyperelastic material laws is given in Marckmann and Verron (2006).

Table 3.3 gives the functional expression of some material models, which are generally available in commercial Finite Element software codes. For the basic *Neo-Hookean* model, the parameter C_{10} corresponds to half of the initial shear modulus of the material. The *Yeoh* model additionally takes into account terms of higher order and the *Mooney-Rivlin* model the influence of the second invariant. These models are phenomenological and their coefficients are typically determined in a curve fitting process using experimental test results of characteristic stress states (uniaxial tension, pure shear, etc.). The curve fitting process is based on a least square optimisation algorithm to determine the set of coefficients, which best reproduces the experimental data (Dassault Systèmes, 2014).

The models of *Gent* and *Arruda-Boyce* include a limiter for the extensibility of the molecular chains of the considered material (Marckmann and Verron, 2006). For silicone adhesives, a phenomenological material law based on the first and second invariant has been developed

Table 3.3: Strain energy potentials for modelling hyperelastic material behaviour

Strain energy potential	Parameters	Deviatoric part
Neo-Hooke	C_{10}	$W = C_{10}\,(I_1 - 3)$
Mooney-Rivlin	C_{ij}	$W = \sum_{i,j=0}^{n} C_{ij}\,(I_1 - 3)^i\,(I_2 - 3)^j$
Yeoh	C_{i0}	$W = \sum_{i=1}^{n} C_{i0}\,(I_1 - 3)^i$
Ogden	μ_i, α_i	$W = \sum_{i=1}^{n} \frac{\mu_i}{\alpha_i}\ (\lambda_1^{\alpha_i} + \lambda_2^{\alpha_i} + \lambda_3^{\alpha_i} - 3)$
Gent	μ, J_m	$W = -\frac{\mu}{2} J_m \ln\left[1 - \frac{I_1 - 3}{J_\mathrm{m}}\right]$
Arruda-Boyce	$\mu, C_i, \lambda_\mathrm{m}$	$W = \mu \sum_{i=1}^{5} \frac{C_i}{\lambda_\mathrm{m}^{2i-2}}\,(I_1^i - 3^i)$
Dias	c_i	$W = c_1\,(I_1 - 3) + c_2\,(I_1 - 3)^2 + c_3\,(I_2 - 3) + -\frac{c_4}{I_2 - 3 + c_5} + \frac{c_4}{c_5}$
Drass	$\alpha_\mathrm{MD}, \beta_\mathrm{MD}, \chi_\mathrm{MD}, \delta_\mathrm{MD}$	$W = \frac{(I_1 - 1)}{\alpha_\mathrm{MD} + \beta_\mathrm{MD}\,(I_1 - 3)} + \frac{(I_2 - 3)}{\chi_\mathrm{MD} + \delta_\mathrm{MD}\,(I_2 - 3)}$
Marlow	Test data	$W = \int_0^{\lambda_\mathrm{UT}^\mathrm{eq} - 1} \sigma_\mathrm{e}\,(\varepsilon_\mathrm{e})\,\mathrm{d}\varepsilon_e$, see equation 3.36

in Dias (2013) and more recently for transparent structural silicone adhesive by Drass et al. (2017b). There are also material laws, which are not based on a functional expression of the strain energy density (e.g. Marlow (2003)). More details are given in section 3.3.3.

3.3.2 Definition of true and engineering strains

Silicone sealants exhibit large deformations. Therefore, true strains and engineering strains as well as true stresses (*Cauchy*) and engineering stresses are discussed in this section.

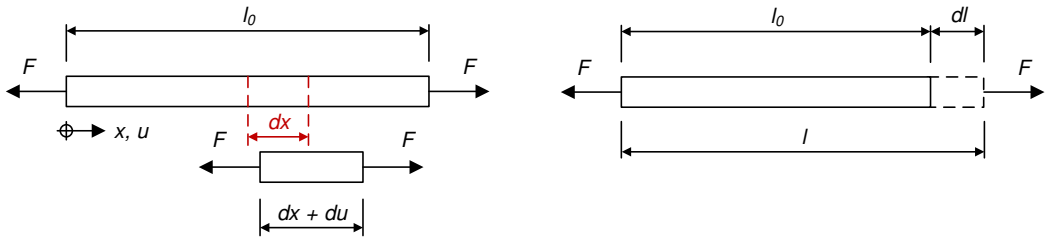

(a) Engineering strains

(b) True strains

Figure 3.15: Difference between true strains and engineering strains

Consider the one-dimensional line element shown in figure 3.15a with an initial length l_0 under a tensile force F and the infinitesimal segment with a length dx. Due to the force F, the material segment exhibits a change of length du. The *engineering strain* is defined as the ratio of the change of length over the initial length (Altenbach, 2012) with

$$\varepsilon_\mathrm{e} = \frac{du}{dx} \Leftrightarrow du = \varepsilon_\mathrm{e}\, dx. \tag{3.26}$$

For the determination of the total elongation Δl of the material line, the changes in length of each segment are summarised

$$\Delta l = \int du = \int_0^{l_0} \varepsilon_\mathrm{e}\, dx. \tag{3.27}$$

If the cross section stiffness is constant (constant cross sectional area and *Young*'s modulus), then the strain ε_e is constant along the ordinate x and equation 3.27 simplifies to

$$\Delta l = \varepsilon_\mathrm{e} \int_0^{l_0} dx = \varepsilon_\mathrm{e}\, l_0 \Leftrightarrow \varepsilon_\mathrm{e} = \frac{\Delta l}{l_0}. \tag{3.28}$$

An inconvenience of the engineering strains is that for large deformations, the sum of engineering strains of two consecutively applied length changes does not equal the strain of the total applied elongation. Therefore, it can be useful to define an additional measure for strains (Altenbach, 2012). Consider the line element in figure 3.15b with an initial length l_0 under a tensile force F. An infinitesimal amount of *true strain* $d\varepsilon$ is defined as the ratio of an infinitesimal length change dl over the current length l,

$$d\varepsilon = \frac{dl}{l}. \tag{3.29}$$

The total amount of true strain for a finite elongation Δl of the material line is obtained by integration of equation 3.29,

$$\varepsilon = \int_{l_0}^{l} \frac{d\hat{l}}{\hat{l}} = \ln l - \ln l_0 = \ln \frac{l}{l_0} = \ln \lambda. \tag{3.30}$$

True strains are also called *Hencky strains* or *logarithmic strains*, which becomes evident regarding their definition. In equation 3.30, λ is referred to as *stretch*. Finally, considering 3.30, a relationship between true and engineering strains can be found,

$$\varepsilon = \ln \frac{l}{l_0} = \ln \frac{l_0 + \Delta l}{l_0} = \ln \left[1 + \varepsilon_\mathrm{e}\right]. \tag{3.31}$$

In an analogous way, a difference can be made between true and engineering stresses. True stress is the ratio between the acting force on the area of a cutting plane in the deformed configuration (*Cauchy* stress), whereas for engineering stresses, the acting force is divided by the area of the cutting plane in the undeformed or reference configuration (2. *Piola-Kirchhoff*

stress). The difference between true and engineering or nominal stresses is negligible for small strains. The relation between true and engineering stresses in the one-dimensional tension bar is given in Schneider et al. (2016) as

$$\sigma = \sigma_{\mathrm{e}} \ (1 + \varepsilon_{\mathrm{e,l}})^{2\nu} \, . \tag{3.32}$$

In equation 3.32, σ are true stresses, σ_{e} engineering stresses, $\varepsilon_{\mathrm{e,l}}$ the longitudinal engineering strain and ν is the actual *Poisson* ratio. Considering a one-dimensional bar loaded in tension, equation 3.32 allows to determine the distribution of true stresses in the bar, provided that the strain distribution and the value of *Poisson*'s ratio of the material are known. If *Poisson*'s ratio is assumed as $\nu = 0.5$ for quasi-incompressible materials, equation 3.32 can be simplified to

$$\sigma_{\mathrm{iso}} = \sigma_{\mathrm{e}} \ (1 + \varepsilon_{\mathrm{e,l}}) \, , \tag{3.33}$$

with σ_{iso} referred to as *isochoric stress*.

3.3.3 Selected material law and chosen assumptions

In Finite Element Analysis, the nonlinear elastic material behaviour of silicone sealants is generally reproduced assuming hyperelastic material laws (e.g. Dias (2013)). In this section, the chosen material law for the considered Dow Corning® 993 structural silicone sealant (Dow Corning Corporation, 2001) is presented and the basic assumptions are discussed.

First of all, the considered silicone material is assumed to be fully incompressible, since the bulk modulus is much higher (factor 600) than the shear modulus of the sealant (Dias, 2013). Wolf and Descamps (2002) have shown with ultrasonic measurements that *Poisson's* ratio of silicones are close to 0.5. Values between 0.4957 and 0.4979 have been found for different sealants. In addition, as mainly linear silicone beads are considered, the deviatoric part of the stress tensor is judged dominant. Apart from the assumption of incompressibility, a quasi-static loading is assumed and the initial stiffness is considered regarding the *Mullins* effect.

In section 3.3.1, different strain energy potentials have been introduced. They have all been based on a functional expression using the invariants of the left *Cauchy-Green* strain tensor. Investigations in Staudt (2013) have shown that the response function gives a good agreement between the conducted shear tests and their numerical simulation. The response function or *Marlow* hyperelastic material law is not based on a functional expression for the strain energy density. The material behaviour is assumed to depend only on the first invariant of the left *Cauchy-Green* tensor. With this assumption, the material response can directly be derived from uniaxial tensile test data. In the following, a simplified analysis is given to explain the continuum mechanics basis of the *Marlow* model. The experimental data consists in uniaxial tensile stress-strain curves from section 4.1.1.

An incompressible material point under a given deformation state is considered. Knowing that for incompressible material behaviour, $\lambda_1 \ \lambda_2 \ \lambda_3 = 1$, the first invariant of the left *Cauchy-*

Green tensor gives

$$I_1(\boldsymbol{b}) = \lambda_1^2 + \lambda_2^2 + \lambda_3^2 = \lambda_1^2 + \lambda_2^2 + \frac{1}{(\lambda_1\,\lambda_2)^2} = \tilde{I}_1. \tag{3.34}$$

In equation 3.34, $I_1(\boldsymbol{b})$ is the first invariant of the left *Cauchy-Green* tensor and λ_i are the stretches in the three directions of the *Euclidean* space. With this given value for the first invariant $\tilde{I}_1$, an equivalent stretch λ_{UT} for a material point in uniaxial tension, i.e. $\lambda_2 = \lambda_3$, can be found, which leads to the same value of the first invariant

$$\tilde{I}_1 = \lambda_{\mathrm{UT}}^2 + \frac{2}{\lambda_{\mathrm{UT}}} \implies \lambda_{\mathrm{UT}}^3 - \tilde{I}_1\,\lambda_{\mathrm{UT}} + 2 = 0. \tag{3.35}$$

It can be shown that the third order equation given in equation 3.35 has exactly one root $\lambda_{\mathrm{UT}}^{\mathrm{eq}} > 1$. This root corresponds to the equivalent uniaxial stretch, which leads to the same value of the first invariant of the left *Cauchy-Green* tensor $\tilde{I}_1$ compared to the initially given deformation state. With this equivalent stretch, the experimental data can be used to determine numerically the strain energy density with

$$W\left(\tilde{I}_1\right) = \int_0^{\lambda_{\mathrm{UT}}^{\mathrm{eq}}-1} \sigma_{\mathrm{e}}(\varepsilon_{\mathrm{e}})\,\mathrm{d}\varepsilon_{\mathrm{e}}. \tag{3.36}$$

In equation 3.36, W is the strain energy density of the material point considered, σ_{e} the experimental engineering stress and ε_{e} the corresponding engineering strains.

3.3.4 Finite Element Method

The *Finite Element Method* (FEM) is a numerical approximation method to solve partial differential equations. In this section, the basic concepts of this method are presented. The designation "Finite Element Method" was first introduced by *Clough* in 1960, describing the essence of this method, which consists in dividing the continuum in small partitions, the so-called *Finite Elements* (Zienkiewicz and Taylor, 2000). The continuous development of the method and the availability of more and more powerful computers in the past years allowed the Finite Element Method to become a powerful predictive tool for complex engineering processes. Modelling of complex experiments and nonlinear problems, for which no closed-form solutions exist, can be handled. Several types of nonlinearities can be included in an analysis, beginning with geometrical (large displacements but small strains) and physical (nonlinear material response) nonlinearities. Furthermore finite deformations with large strains, stability problems and nonlinear boundary conditions can be treated in many commercial Finite Element software codes (Ogden, 2005).

As already mentioned before, the essence of the Finite Element Method consists in a discretisation of the continuum in various sub-domains, called elements. These elements are defined by nodes. Each node has a limited number of degrees of freedom. Therefore, the continuum can be represented by a finite number of degrees of freedom (DOF). DOF are independent quantities, which determine the spatial variation of a field. The number of DOF of a given structure depends on the number of elements, the number of nodes per element and the number of DOF per node. The arrangement of the Finite Elements is called *mesh*.

The FEM allows to determine an approximate numerical solution for a given field problem, in which the spatial distribution of a given variable (e.g. displacements in elasticity problems) has to be determined. For elasticity problems in a displacement-based formulation, the DOF are displacements, whose values are calculated at the nodes by solving a system of algebraic equations. Within an element, the distribution of the considered variable is interpolated from the values at the nodes. For high order elements, additional nodes are placed between the edges of an element allowing for a more accurate distribution of the field quantity without changing the size of the finite element. For the determination of the spatial distribution of the variable within the continuum, the weighted residual method is used to find the solution for the governing differential equations (e.g. equilibrium of stresses in elasticity problems). The variational method consists in finding a minimum for the functional used and respecting internal compatibility and boundary conditions. In elasticity problems, the functional used is the total potential energy (Cook et al., 2002). Furthermore, for elasticity problems, the described optimisation problem leads to a system of equations of the form *force = stiffness x deformation* (Klein, 2007). This equation is solved for the unknown deformation vector, which contains the displacements of the nodes. Some of these displacements can already be known by applied boundary conditions. The initial partial differential equation (equilibrium condition in elasticity) is replaced by a system of linear algebraic equations (Klein, 2007). The force vector is generally known and composed of the external loads. Finally, the stiffness matrix includes the properties of the elements. A numerical integration procedure is used for the determination of the stiffness matrix. The accuracy of the stresses is limited by both the mesh refinement and the degree of the Ansatz function used. From the deformations of nodes, the stresses and strains are calculated at the integration points, the so-called *Gauss points*, and extrapolated to the nodes and if necessary averaged with the values of the nodes of neighbouring elements.

The elements used can be characterised by 5 aspects: family, degrees of freedom (DOF), number of nodes, formulation and integration. Continuum, shell, beam, rigid or connector elements are commonly used element families. For the modelling process, the choice of the appropriate element family depends on many parameters, as the idealisation of the reproduced "real" structure or the problem classification. The degrees of freedom (DOF) are fundamental variables of the analysis. Basically, they denote translations and rotations of the nodes. The number of nodes and the order of interpolation are additional characterising values. For elements, which only have nodes at their corners, the displacements at any other point are obtained by a linear interpolation of the values at the corners. These elements are called first-order or linear elements. Elements, which have additional nodes between the corners use a quadratic interpolation. They are called second order or quadratic elements. The formulation of the elements refers to the mathematical theory used. Two formulations are used: the *Eulerian* and *Lagrangian* method. The *Eulerian* method is used in fluid dynamics problems. For this method, elements are fixed in space and material flows through them. On the contrary, for the *Lagrangian* formulation, the deformation of a material point is described. This formulation is used in stress/displacement based problems. When considering nearly or fully incompressible material behaviour, elements with a hybrid formulation must be used. In elasticity problems, the finite elements used generally have displacement degrees of freedom. If an incompressible material behaviour is assumed using these elements, an arbitrary hydrostatic pressure can be added without influencing the displacements. On the other hand, for nearly incompressible material behaviour, the results of the hydrostatic pressure are very sensitive towards small changes of the displacements, as they are found within the round-off error. *Hybrid* elements can be used to overcome these issues. These elements have a mixed formulation, i.e. they have, apart from the displacements, additional degrees of freedom,

such as the hydrostatic pressure. The hydrostatic pressure is coupled with the displacement solution using compatibility condition and the constitutive theory. Concerning the integration, the numerical technique of the *Gaussian* quadrature is used for most elements. The material response is evaluated at each integration point. A reduced integration is available (Dassault Systèmes, 2014), which means that less integration points are employed.

3.3.5 Singularities in a Finite Element Analysis

The Finite Element Method has become a powerful tool to analyse complex stress states. Since it is a numerical approximation method, it is important to check if sufficiently accurate stresses are obtained from such an analysis. It is essential to know, if the results for stresses in a given model are converging or not and if they converge to a sufficiently accurate approximation of the stresses in the real structure (Zienkiewicz and Taylor, 2000).

If the model exhibits a stress *singularity*, the values of the diverging stresses increase for an increasing mesh density. The numerical results thus depend on the arbitrary choice of the structure's discretisation (Gleich, 2002). According to Sinclair (2004), *"stress singularities are not of the real world. Nonetheless, they can be a real fact of a stress analysis"*. The challenge consists in the identification of singular points. Either, the model is improved in a way that the singularity vanishes or the results have to be interpreted and assessed for singularities that persist.

For problems in elasticity, singularities at concentrated loads and singularities away from concentrated loads can be distinguished. Singularities at concentrated loads can arise if a load or support condition is defined on an infinitesimal small area, like for a point or line load on solid elements. These singularities are also called *singular loads*. Singularities away from concentrated loads arise from discontinuities in the model, like sharp edges (re-entrant corner), wedges or cracks and an offset in the elastic constants between two or more materials. These discontinuities show stress concentrations, which are potential sources of fatigue or failure, even if the stress singularities, which are results of the elastic analysis, are physically unrealistic (Sinclair, 2004).

Stress singularities can lead to major problems in the assessment of the results computed in a Finite Element analysis. A decreasing element size or increasing order of integration of the elements will cause the integration points to move towards the origin of the singularity, thus increasing the stress values. Thus, for the same element size, the higher order element will give a higher peak value. There are special elements, so-called *Barsoum* elements, which are able to represent singularities, but only for singularities such as cracks. In the case of notches, these elements are not helpful since the order of singularity of a crack is different from that of a wedge (Weißgraeber and Becker, 2013). For an elastic-plastic material law, the stress singularity disappears, as yielding occurs, but a strain singularity remains (Gleich, 2002).

3.4 Failure criteria

3.4.1 Objectives of failure criteria and concepts

For a structural engineer, the key task consists in the verification of the load bearing capacity of a structure. For this verification, the acting stress state in the structure is compared to an allowable upper limit, the material strength. As discussed in section 3.1, silicone sealants exhibit a pronounced nonlinear material behaviour and experience large deformations. In order to capture these physical and geometrical nonlinearities, the stresses in silicone sealants are often analysed using a Finite Element Analysis. As the result of these analysis are generally triaxial stress states (Stommel and Korte, 2011) and as the material strength is often determined in uniaxial tensile tests on dog bone specimens due to their simplicity (Mang and Hofstetter, 2013), a method is needed to compare the complex stress state with the results obtained from the simple material tests. Alternatively, the ultimate load bearing capacity can be assessed with component tests. These component tests however are time consuming and thus expensive.

According to Naït-Abdelaziz et al. (2012) and Banea and da Silva (2009), the assessment of complex stress states can be performed following the three concepts given in figure 3.16. In a first method, a perfect bulk material without defects or flaws is assumed. The complex stress state is assessed using a fracture criterion, which is based on a mathematical function using as input mechanical quantities, like stresses or strains, as determined on the perfect flawless material. On the other hand, a fracture mechanics approach assumes the existence of a pre-crack. Fracture mechanics concepts are used to evaluate the crack propagation. Finally, due to the availability of more and more powerful computers and the continuous development of numerical methods, the failure point is included in the constitutive material laws and the failure process is thus modelled in the numerical simulation in a damage mechanics approach. In Grandcoin et al. (2014), a micro-mechanically based constitutive damage model of a silica-filled silicone rubber was formulated to assess fatigue. Damage initiation of this model is based on the decohesion between filler and polymeric matrix.

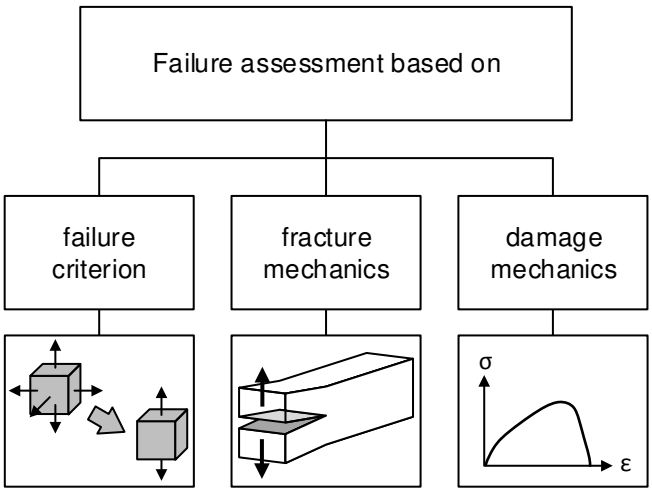

Figure 3.16: Overview of concepts to assess failure

In the following investigations, simple failure criteria on defect-free rubber-like bulk material are

investigated for the case of a static loading with the assumptions given in section 3.3.3. For failure criteria based on the assumption of a flawless bulk material, three different concepts can be adopted: stress-, strain- or energy-based formulations. Whereas stress-based criteria take into account the hydrostatic stress state, which can be relevant for rubber-like materials (Ayoub et al., 2010), strain-based criteria use displacements as directly measurable values (Zine et al., 2006).

3.4.2 Types of fracture

The present section gives a short overview about the definitions of the term *brittle* in the context of elastomer failure. Generally speaking, the fracture process is considered as completed, if crack growth comes to an end or if there is a complete break-through of the body with a distinction between *brittle* and *ductile* failure (Gross and Seelig, 2011).

In the field of elasticity, brittleness is defined as the opposite of plasticity. Brittle materials exhibit very small deformations before rupture, as opposed to ductile materials, which show large deformations prior to failure (e.g. Thrower (1986), Habenicht (2009)). In addition, failure of brittle materials is governed by the acting normal stresses, as described in Beer et al. (2009) in the context of tensile specimens. The same approach is adopted in the field of structural sealant glazing systems. Here, the term *brittle* is defined as the opposite of elasticity (AAMA, 2014), which is defined as the ability of a material to take extension and compression. Thus, a brittle material behaviour is related as well to small deformations.

Gross and Seelig (2011) consider the occurring plastic deformations to define brittle or ductile failure. For ductile fracture, large inelastic deformations are observed prior to failure and brittle failure is characterised by the absence of a significant amount of plastic deformation prior to failure.

For polymers, the question about brittle or ductile failure is often answered with a visual assessment of the fracture surfaces, but no quantitative measure is given for brittleness (Brostow and Lobland, 2010). In Trapper and Volokh (2008), cracks in rubber were investigated and brittleness was defined as the ratio of the shear modulus to the average bond energy. Furthermore, brittle materials were found more sensitive to cracks than soft materials. This finding was explained with the large deformations, soft materials can undergo.

For soft and highly deformable elastomers, Williams (1984) reported about brittle-like fracture behaviour. In a similar way, Boué et al. (2015) described the failure behaviour of highly deformable materials, like elastomers, as brittle, since they show only very small inelastic deformations. In these cases, the bulk dissipation can be neglected, i.e. the material remains elastic, even at high strains. Finally, Brighenti et al. (2017) presented investigations on a hyperelastic silicone polymer. Pre-cracked specimens were tested in tension. The crack tip was found to blunt due to the high deformations of the material, but the observed failure mechanism was described as brittle with instantaneous rupture of the specimens.

Concluding, the question of brittle or ductile failure can either be assessed considering the deformations of a material or considering the amount of inelastic deformation prior to failure. In this context, it is noticed that brittle or ductile behaviour is not a pure material property, but also depends on the stress state, the temperature or the loading rate (Gross and Seelig, 2011). Regarding the influence of the stress state, a hydrostatic stress state, which causes

an elastic deformation for many plastically deformable materials, can lead to brittle failure of the material, i.e. showing small amount of inelastic deformations. Apart from the stress state, many materials behave brittle at sufficiently low temperatures, i.e. below the transition temperature. The same effect can be observed when the loading rate is sufficiently high.

3.4.3 Stress-based criteria

The well-known and simple *principal stress hypothesis* has been introduced by *Rankine*, *Lamé* and *Navier*. It is generally used for brittle materials, like glass. Failure is observed, when either the maximum principal stress exceeds the tensile strength or when the minimum principal stress exceeds the compression strength (Gross and Seelig, 2011),

$$\sigma_1 = \sigma_{\mathrm{UT}} \vee \sigma_3 = \sigma_{\mathrm{UC}}. \tag{3.37}$$

In equation 3.37, σ_1 is the maximum principal stress, σ_{UT} the tensile strength, σ_3 the minimum principal stress and σ_{UC} the compression strength. As failure of polymers in compression is considered as unlikely, the second condition in equation 3.37 is often omitted.

The failure process of quasi-incompressible rubber-like materials is often related to an internal creation and growth of voids and cavities. The phenomenon of void nucleation, called *cavitation*, can be related on a macroscopic scale to a significant change of slope in the stress-strain diagram (Gent and Lindley, 1959). Cavitation is observed for specimens exhibiting high values of hydrostatic tension. These stresses can be found in so-called *pancake* specimens under tensile forces. Pancake specimens are butt bonded cylinders with small adhesive thickness compared to the cylinder's diameter, or cylinders bonded on flat surfaces (Drass and Schneider, 2016). The influence of the adhesive thickness on cavitation has been investigated in Aït-Hocine et al. (2011) on a filled rubber, similarly as in Gent and Lindley (1959). In both investigations, the fracture pattern of the specimens with small thickness clearly showed small bubbles coming from cavitation. Furthermore, a significant change of slope in the stress-strain diagram was observed for these specimens. For the thick adhesive layers, no change of slope in the stress-strain diagram was observed and the failure pattern did not show small air bubbles. The failure process of these specimens was controlled by crack propagation. The threshold value for void nucleation

$$p = -\frac{1}{3}\, I_1\left(\boldsymbol{\sigma}\right) < \frac{5}{6}\, E \tag{3.38}$$

was derived and validated on pancake specimens in Gent and Lindley (1959) for a *Neo-Hookean* material. In equation 3.38, p is the hydrostatic pressure, $I_1\left(\boldsymbol{\sigma}\right)$ the first invariant of the *Cauchy* stress tensor and E Young's modulus of the considered sealant at small strains.

The *von Mises* criterion was originally developed as a yield criterion for ductile materials, like steel. This criterion does not take into account the hydrostatic stress state (Gross and Mendelson, 1970). But as discussed previously, the failure of rubber-like material depends on the hydrostatic stress state (Gent and Lindley, 1959). As the *von Mises* criterion is implemented in many commercial Finite Element software codes, it is often accepted to assess failure of polymers (Kolupaev et al., 2003). The *von Mises* stress is given as

$$\sigma_{\mathrm{Mises}} = \sqrt{3\, I_2\left(\boldsymbol{s}\right)}. \tag{3.39}$$

In equation 3.39, σ_{Mises} is the equivalent stress according to *von Mises*, $I_2\left(\boldsymbol{s}\right)$ the second invariant of the deviatoric stress tensor $\boldsymbol{s}$, which is defined as: $\boldsymbol{s} = \boldsymbol{\sigma} - p\,\boldsymbol{I}$, where p is the hydrostatic pressure and $\boldsymbol{I}$ the unit tensor.

3.4.4 Strain-based criteria

A criterion, similar to the *Rankine* maximum principal stress criterion is available for strains. The *maximum principal strain* hypothesis was introduced by *Saint-Venant* and *Bach*. Failure occurs if the maximum principal strain

$$\varepsilon_1 = \varepsilon_{\mathrm{UT}} \tag{3.40}$$

exceeds an upper limit (Gross and Seelig, 2011). In equation 3.40, ε_1 is the first principal strain and $\varepsilon_{\mathrm{UT}}$ the ultimate strain. For rubbers, the maximum principal strain criterion has been used by Kawabata (1973) and validated performing tests on rubber sheets. The maximum principal strain is amongst others widely used in fatigue life analysis of rubber (Zine et al., 2011).

The maximum principal strain only considers one component of the three dimensional principal strain tensor. The *strain magnitude* can be physically seen as a measure for the stretch of the molecular chains (Molls, 2013), with

$$\varepsilon_{\mathrm{M}} = \sqrt{\varepsilon_1^2 + \varepsilon_2^2 + \varepsilon_3^2}. \tag{3.41}$$

In equation 3.41, ε_{M} is the strain magnitude and ε_i are the three principal true strains. The strain magnitude is used with true strains. The strain magnitude has been employed in Molls (2013) to assess failure in elastomeric parts in technical applications. In the space of true principal strains, equation 3.41 describes a sphere with the centre at the origin of the coordinate system.

3.4.5 Energy-based criteria

In addition to the maximum principal strain criterion, the *strain energy density*, referred to as the failure criterion according to *Beltrami* (1889) (Lazzarin and Berto, 2005), is as well widely used to assess fatigue of rubber-like material (Zine et al., 2011). Since the constitutive laws for rubber-like materials are generally based on a functional expression for the strain energy density, it can also be used a limiter to reproduce the failure process in numerical simulations (Volokh, 2010).

The strain energy density approach has been identified in Scherer (2014) as a potential failure criterion for silicone sealant. However, additional investigations were recommended to validate this failure criterion.

3.5 Considerations on the stress field in a single-lap shear joint

In this section, a literature review on single-lap shear joints is given. Single lap shear joints are used in many industrial applications, like aerospace industry. The literature review focus on the stress distribution in the adhesive and examples are given to illustrate the different aspects discussed. In contrast to civil engineering, a thin adhesive layer thickness and stiff adhesives are generally used. As the analytical solutions discussed in the following usually deal with linear elastic and stiff adhesives, two cases are considered. A linear elastic adhesive is considered in a thin lap shear joint, as well as the soft silicone adhesive in form of a thick silicone bead as used in the specimen detailed by ETAG 002 (2012). Special attention will be put on the singularities, which can be found at the corner edges of the adhesive. Several assessment techniques are introduced and discussed.

3.5.1 Analytical models - *Volkersen* and *Allman* solution

In the current section, some analytical solutions for the stress distribution in a single-lap shear joint are presented and their results are compared to the stress distributions obtained from a Finite Element Analysis. For simplicity, the same thickness is defined for both adherends. Furthermore, a linear elastic material behaviour is assumed for the adherends and the adhesive. In the following, two cases are distinguished, starting with a thin and stiff adhesive and in a second step, with rigid adherends and a thick and soft adhesive layer. Figure 3.17 shows the considered single-lap shear joint and table 3.4 gives the elastic constants and dimensions of the bonded connection.

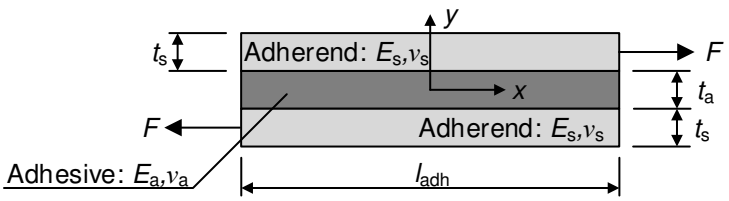

Figure 3.17: Single lap-shear joint

Table 3.4: Elastic constants and dimensions of the single-lap shear joint

Nomenclature		Stiff adhesive	Soft adhesive
t_s	Adherend thickness	5 mm	5 mm
t_a	Adhesive thickness	1 mm	12 mm
E_s	Adherend *Young*'s modulus	70 000 MPa	70 000 MPa
E_a	Adhesive *Young*'s modulus	1000 MPa	2.4 MPa
ν_s	Adherend *Poisson* ratio	0.34	0.34
ν_a	Adhesive *Poisson* ratio	0.35	0.5
F	Applied force	480 N	480 N
h_c	Adhesive width	12 mm	12 mm
l_{adh}	Adhesive overlap length	50 mm	50 mm

The simplest form of the shear stress distribution in the single-lap shear joint assumes a constant shear stress over the adhesive thickness and overlap length. It can be physically

interpreted as an average or engineering shear stress. Equation 3.42 gives the expression for the average shear stress (Da Silva et al., 2009a)

$$\tau_{\mathrm{e}} = \frac{F}{h_{\mathrm{c}}\, l_{\mathrm{adh}}}. \tag{3.42}$$

In equation 3.42, τ_{e} is the average shear stress, F the applied force, h_{c} the adhesive width (bite) and l_{adh} the adhesive overlap length.

The earliest closed form solution for the shear stress distribution was given by Volkersen (1938). Compared to the concept of average stresses, given in equation 3.42, the *Volkersen* solution is based on a concept of differential shear, where the adherends are considered elastic, not rigid. The additional differential shear deformation, which causes additional shear stresses in the adhesive, is taken into account in the *Volkersen* solution. The *Volkersen* equation only considers shear stresses, assuming a simple shear stress state. The shear stresses are constant through the thickness of the adhesive. Bending of the adherends due to the eccentric loading situation is not considered (Weißgraeber and Becker, 2013). Equation 3.43 gives the *Volkersen* equation for a symmetric single-lap shear joint as

$$\begin{aligned} \tau_{\mathrm{VK}}(\xi) &= \frac{F}{h_{\mathrm{c}}\, l_{\mathrm{adh}}}\, \frac{\omega_{\mathrm{VK}}}{2}\, \frac{\cosh(\omega_{\mathrm{VK}}\, \xi)}{\sinh(\omega_{\mathrm{VK}}/2)},\ \text{with}\ \frac{1}{2} \leq \xi = \frac{x}{l_{\mathrm{adh}}} \leq \frac{1}{2}\ \text{and} \\ \omega_{\mathrm{VK}}^2 &= 2\, \frac{G_{\mathrm{a}}\, l_{\mathrm{adh}}^2}{E_{\mathrm{s}}\, t_{\mathrm{s}}\, t_{\mathrm{a}}}. \end{aligned} \tag{3.43}$$

In equation 3.43, τ_{VK} is the shear stress according to *Volkersen*, ξ the relative ordinate, E_{s} *Young*'s modulus of the adherend and G_{a} the shear modulus of the adhesive.

The *Volkersen* equation was published in 1938 and originally used for the calculation of the force distribution in the bolts of riveted joints (Volkersen, 1938). Since then, many closed form solutions were found, including effects like the bending of the adherends, or considering elastic-plastic material behaviour for the adhesive, e.g. Hart-Smith (1973). These solutions usually take into account peel stresses as well, like the solution of Goland and Reissner (1944), which considers the opening stress in the joint. Peel stresses are the stresses perpendicular to the plane of the adhesive layer, which are caused by the eccentricity of the applied tensile force (Allman, 1977). More analytical solutions can be found in Da Silva et al. (2009a) and Da Silva et al. (2009b) as well as in Gleich (2002).

A basic property of the analytical models is their so-called *weak interface formulation* with adherends considered as beams and the adhesive as smeared springs. The condition of traction free surfaces in the adhesive is generally not fulfilled (Weißgraeber et al., 2014). As mentioned before, only average stresses are considered over the height of the adhesive and almost all solutions predict the maximum stress to occur at the edge of the adhesive area, which violates the shear stress-free condition. This is a result of ignoring the normal stresses in the adhesive (Gleich, 2002).

The analytical solution of *Allman* fulfils the free edge condition. The general form of *Allman*'s

solution is given in equation 3.44 (Allman, 1977) with the components

$$\begin{aligned} \sigma_{\mathrm{AL},x} &= 0 && \text{normal stress,} \\ \tau_{\mathrm{AL},xy} &= -\frac{1}{t_\mathrm{a}}\,\frac{d\Phi_1}{dx} + \frac{F}{t_\mathrm{s}\,l_\mathrm{adh}} && \text{shear stress and} \\ \sigma_{\mathrm{AL},y} &= -\frac{t_\mathrm{s}}{2\,t_\mathrm{a}}\,\eta\frac{d^2\Phi_1}{dx^2} + \frac{d^2\Phi_2}{dx^2} && \text{peel stress.} \end{aligned} \tag{3.44}$$

In equation 3.44, $\eta = 2\,y/t_\mathrm{s}$ is the relative ordinate normal to the interface. $\Phi_1\,(x)$ and $\Phi_2\,(x)$ are two unknown stress functions. These stress functions are determined by minimizing the strain energy. Due to the complexity of the stress functions, only the special case of rigid adherends is considered here. This case corresponds to bonded connections with silicone, as the elastic modulus of glass or aluminium is much higher than the elastic modulus of the sealant. For this case, the distribution of the stress components are given as

$$\begin{aligned} \sigma_{\mathrm{AL},x} &= 0 && \text{normal stress,} \\ \tau_{\mathrm{AL},xy} &= \frac{F}{h_\mathrm{c}\,l_\mathrm{adh}}\left[1 + \frac{1 - l_\mathrm{adh}/2\,\omega_\mathrm{AL}\,e^{-\omega(l_\mathrm{adh}/2-x)}}{l_\mathrm{adh}/2\,\omega_\mathrm{AL} - 1}\right] && \text{shear stress and} \\ \sigma_{\mathrm{AL},y} &= \frac{F\,t_\mathrm{a}\,\omega_\mathrm{AL}^2}{4\,h_\mathrm{c}\,(l_\mathrm{adh}/2\,\omega_\mathrm{AL} - 1)}\,e^{-\omega_\mathrm{AL}(l/2-x)} && \text{peel stress.} \end{aligned} \tag{3.45}$$

In equation 3.45, $0 \leqslant x \leqslant l_\mathrm{adh}/2$ and $\omega_\mathrm{AL} = \frac{2}{t_\mathrm{a}}\left(\frac{3\,E_\mathrm{a}}{G_\mathrm{a}}\right)^{1/2}$.

A major limitation of the analytical models is the basic assumption of constant shear stress distributions over the adhesive thickness. This assumption is commonly used as mainly very thin adhesive layers are investigated. From the analytical models, an increase of the adhesive's thickness leads to a decrease of the stresses and thus to a higher load bearing capacity. Experimental investigations however show that the load bearing capacity decreases for an increasing adhesive layer thickness. This phenomenon is called *adhesive thickness effect*. Considering the average shear and peel stress distributions, the adhesive thickness effect cannot be explained. However, taking into account the stresses at the interface of the adhesive, shear and peel stresses are found to increase for an increasing thickness, thus leading to a decreased load bearing capacity, as observed in the tests (Gleich, 2002). A consideration of the stresses at the interface of the adhesive seems essential, as the most common type of failure is cohesive failure close to the bondline interfaces (Weißgraeber and Becker, 2013). As mentioned before, the middle layer of the adhesive is typically modelled. As the adhesive is represented as smeared springs, the two-dimensional elastic continuum is not fully represented. Therefore, these weak interface solutions do not represent stress singularities at the bi-material points, thus predicting finite stresses instead of infinite stresses (Weißgraeber et al., 2014).

The adhesive thickness effect was investigated in Banea et al. (2015) and Campilho et al. (2015). Potential interpretations were given for the decreasing adhesive strength with increasing thickness. The presence of defects were judged more likely in thick adhesive layers. Another explanation states that yielding of an adhesive can develop faster in a thick joint. Gleich (2002) refers to the stress distribution with increasing stresses at the interface for a higher thickness. Finally, due to the increasing distance between the applied forces with

an increasing adhesive layer thickness, the acting bending moment increases as well. For silicone sealants, single-lap shear joint tests have been performed in Banea and da Silva (2010) on a one-component room temperature vulcanising silicone adhesive. The failure load was found to increase with increasing adhesive thickness. A silicone sealant with a shear modulus around 0.6 MPa was tested in shear in a single-lap shear joint. Specimen with a bondline thickness of 0.5 mm and 1 mm were produced and tested. The width of the specimens was approximately 25 mm. In chapter 4.2.1, bonded connections with silicone sealant were tested in simple shear and the strength was found to decrease with increasing adhesive thickness. Layers from 6 to 24 mm were tested. In this context, it should be noted that an optimum bondline thickness can be identified for adhesive layers, such as in Gleich (2002), where the strength of the single-lap shear joint was found to increase with decreasing adhesive thickness up to a certain point at which, the strength decreased again. Finally, in Weißgraeber (2014), the adhesive thickness effect was related to the energy release rate. A higher amount of strain energy, which can be released in case of crack onset, is stored in thick adhesive layers for the same applied load compared to thin layers.

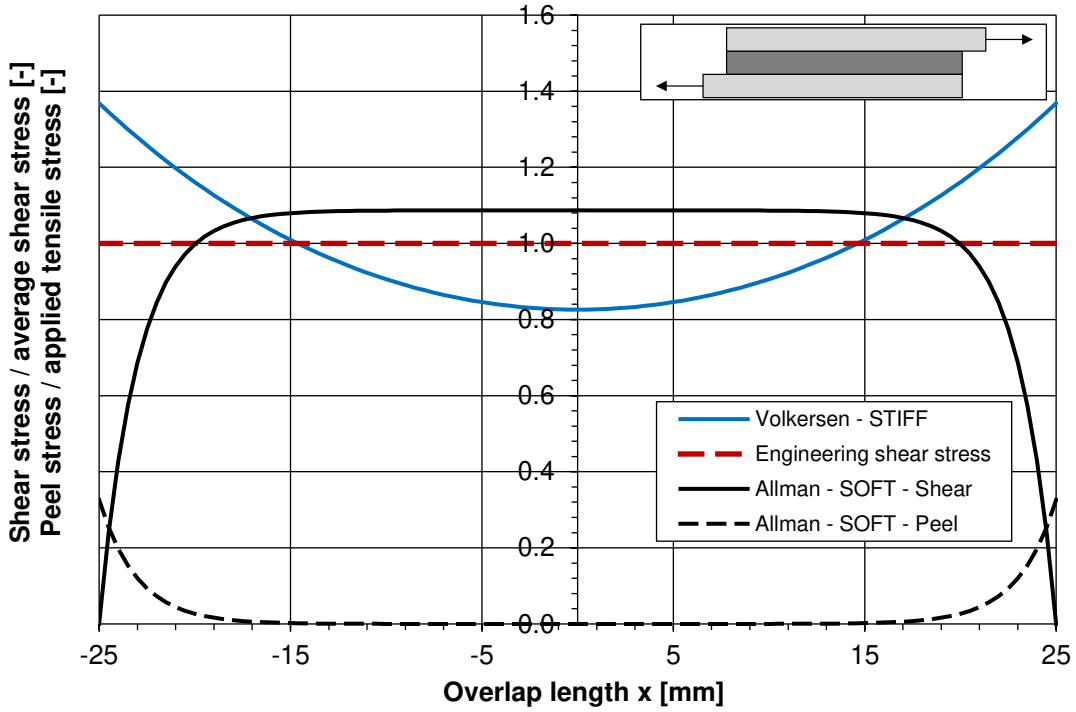

Figure 3.18: Stress distribution along the interface of a single-lap shear joint. *Volkersen* and *Allman* solution considered.

To illustrate the previously given equations, the shear and peel stress distributions are given for both cases of the *stiff* and *soft* connection defined in table 3.4. Figure 3.18 displays the shear stress distribution according to *Volkersen* for the stiff connection and both shear and peel stresses according to *Allman* for the soft connection. In addition, the engineering shear stresses following equation 3.42 are given. The ratio between the shear stresses and the average shear stress as well as the ratio between the peel stress and the acting tensile stress $(F/(h_c\, t_s))$ are plotted against the overlap length. The *Volkersen* model predicts stress peaks at the free edges of the adhesive joint, which are due to the elastic adherends. The *Allman* model satisfies the stress free edge condition. Therefore, the constant shear stress in the middle area is higher in order to satisfy global equilibrium.

In a second step, the stress distributions obtained from the previously presented analytical solutions are compared with the stress distributions from a Finite Element Analysis. Special attention will be devoted to the convergence behaviour of the stresses at the edge area of the adhesive. The assumed boundary conditions of the numerical model are given in figure 3.19. The upper and lower supports in y-direction were used to avoid rotation of the adherends thus better fulfilling the boundary conditions assumed by *Volkersen*. The commercial Finite Element software code ABAQUS® (Dassault Systèmes, 2014) was used for the numerical simulation of the single-lap shear joint. The dimensions and elastic constants are given in table 3.4. 8-node biquadratic plane strain quadrilateral elements were selected in the geometric linear analysis. For the simulation of the bonded connection with the stiff adhesive, three different element sizes were considered: 0.5 mm, 0.1 mm and 0.01 mm.

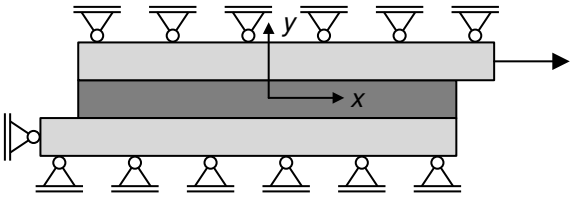

Figure 3.19: Boundary conditions for the single-lap shear joint

Figure 3.20 shows the result for the stress distribution at the interface between the stiff adhesive and the adherend (values for $-25 \leq x \leq 0$) and at the centreline of the adhesive (values for $0 \leq x \leq 25$). The shear stress distribution was determined using ABAQUS® (Dassault Systèmes, 2014) for the three aforementioned element sizes. Furthermore, the stress distribution obtained from the *Volkersen* equation is plotted. A good correlation between the *Volkersen* equation and the numerical simulation is found for both centreline and interface path. For the centreline path, the shear stresses tend to zero at the edge areas, thus fulfilling the stress free edge condition. For the interface path in the numerical simulation, stress peaks appear with increasing values for a decreasing element size, thus indicating the singular behaviour of the edge area.

Figure 3.20 shows the convergence of the different stress components. Both the centreline and the interface between adherend and adhesive are considered. The centreline values are dashed. The stress components of the interface do not converge for a refined mesh, whereas the centreline values converge, even when a coarse mesh of 0.5 mm (which corresponds to 2 elements over the adhesive thickness) is used. This behaviour was as well observed in Weißgraeber et al. (2014), where the stresses at the mid-plane of the adhesive were selected for further investigations. In general, taking the stress values at the centreline is the most common way to handle the singularity at the interface.

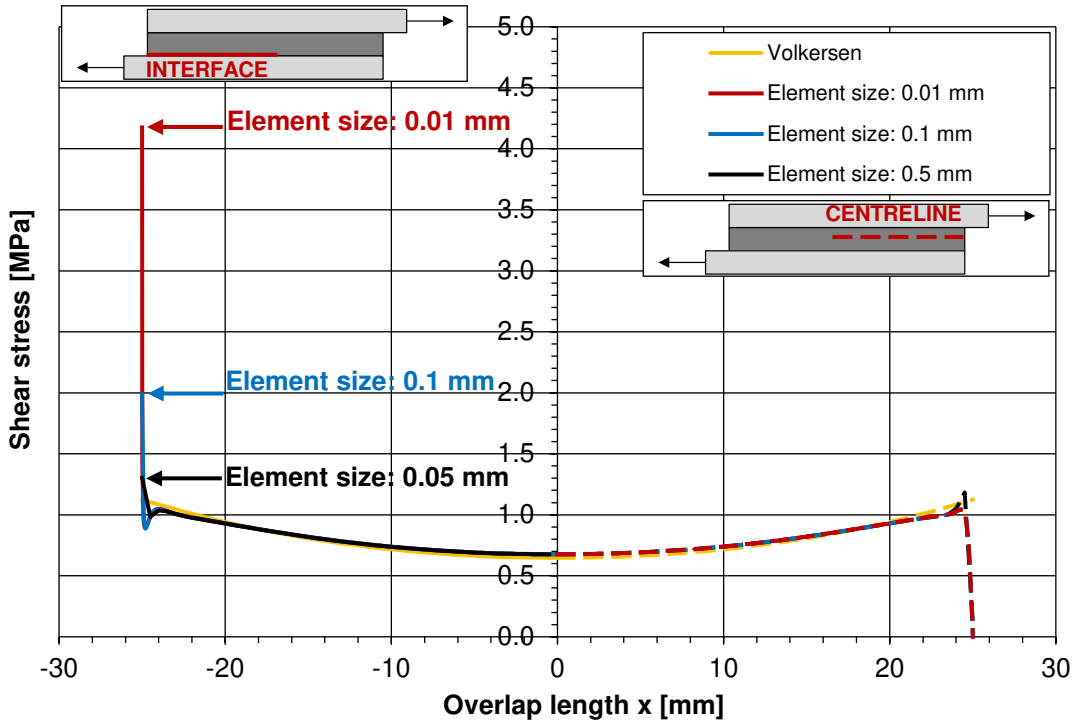

Figure 3.20: Shear stress distribution at the interface (left) between the stiff adhesive and adherend and the centreline (right) - comparison between *Volkersen* and FEA

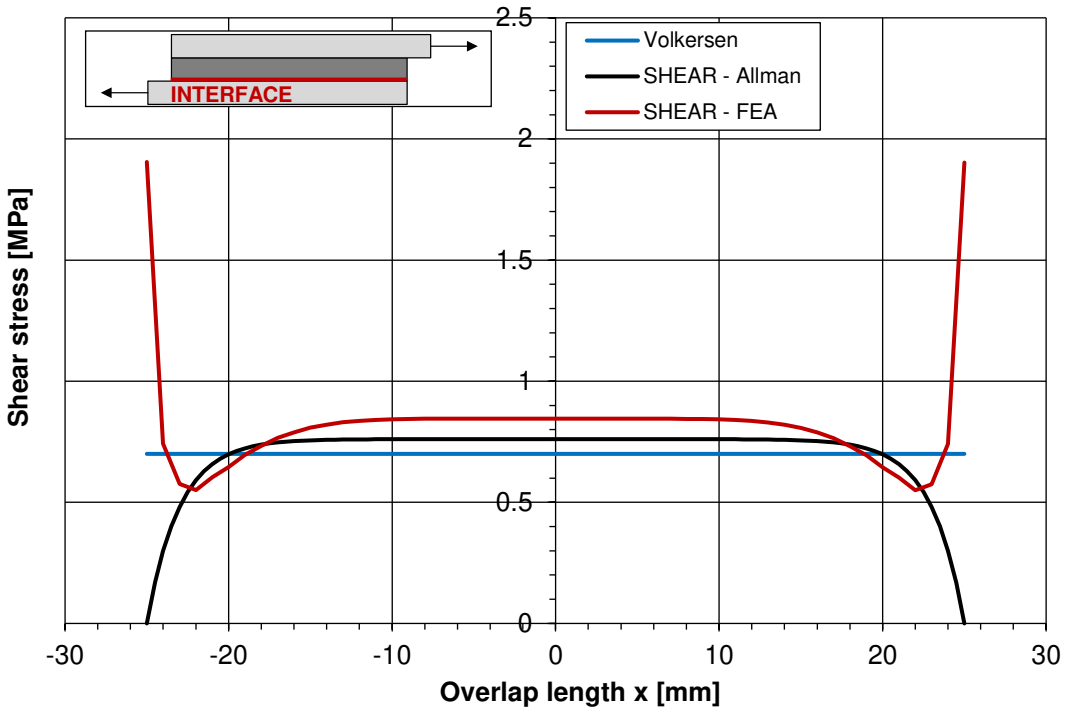

Figure 3.21: Shear stress distribution for the stresses at the interface of the soft adhesive - comparison between the values from FEA, the *Volkersen* equation and the *Allman* equation

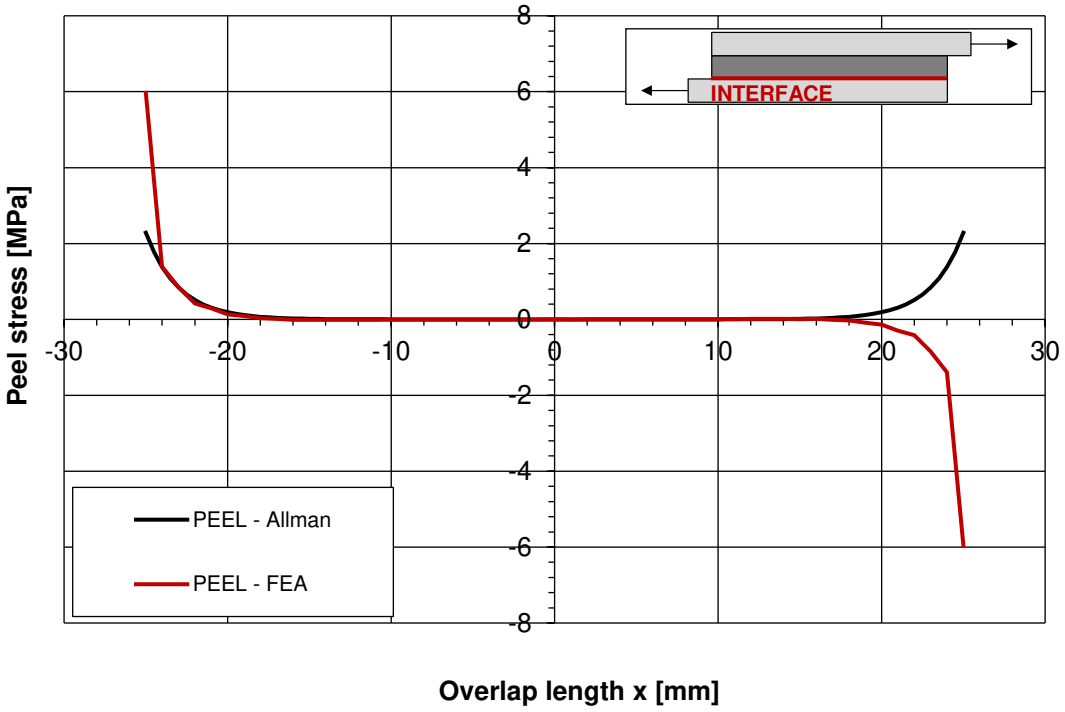

Figure 3.22: Peel stress distribution for the stresses at the interface of the soft adhesive - comparison between the values from FEA and the *Allman* equation

Figure 3.21 shows the shear stress distribution for the soft adhesive as defined in table 3.4. The values obtained from the linear analysis using the commercial Finite Element software code ABAQUS® (Dassault Systèmes, 2014) (linear elastic material law, plane strain conditions, CPE8H quadratic elements with hybrid formulation due to the incompressible material behaviour) were compared with the analytical solutions of *Volkersen* and *Allman*. A good agreement was found except at the edge areas, where stress peaks appear in the numerical simulation. For a soft adhesive, the stress distribution according to *Volkersen* corresponds to a constant value, like the average shear stress.

Figure 3.22 shows the peel stress distribution obtained from the numerical simulation and from the *Allman* solution. It shows very good correlation with the numerical simulation, except for the peak value at the corner edges. Moreover, the analytical solution only predicts positive peel stresses.

3.5.2 Stress singularities at single-lap shear joints

In the previous section, the stresses at the interface between adhesive and adherend were found not to converge to a constant value, when the Finite Element mesh is refined. This indicates the presence of a singular point. Stress singularities exist at the bi-material interface in bonded joints due to the sharp change of the geometry and the material properties (Gleich, 2002). According to Chen et al. (2011), the singularity problem at the interface corner in adhesive joints in Finite Element Analysis is mentioned, but often ignored.

The presence of stress singularities at the edge areas of bonded connections is subject of a number of publications. The stress singularity at the two-material wedge has been

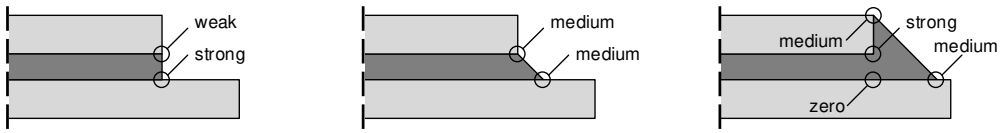

(a) No fillet (b) 45°fillet (c) Full 45°fillet

Figure 3.23: Singularities in a single-lap shear joint - consideration of different fillets, from Chen et al. (2011)

investigated by Bogy (1968) and the highest stress concentrations were found for the combination between a soft and a stiff material. Similar results were obtained in Hein and Erdogan (1971), where a more general overview on singularities in two-material wedges was given. In Altus et al. (1986), the question of assessing the stresses in vicinity of the singularity was addressed. The singularity was explained with geometrical and material discontinuities. Since the stresses could not be properly assessed, a failure envelope in terms of allowable deformations was envisaged and finally, a failure envelope, based on the strains in the substrates next to the two-material wedge, was proposed. Reedy (1993) considered a two-material wedge under normal and shear loading. Penado (2000) performed an analysis of singular regions in bonded connection, for which stress intensity factors were given for different joint configurations. Similar investigations were presented in Wang and Rose (2000). Chen et al. (2011) proposed a classification of the singularities, which is shown in figure 3.23. Finally Van Tooren and Krakers (2006) propose a stress singularity approach for material failure prediction for bonded connections.

In Cognard and Créac'hcadec (2009), the presence of stress singularities was explained as well by the sharp change of material properties and geometry. Experimental investigations and numerical analysis were performed on single-lap shear joint specimens with an epoxy-based adhesive. To obtain a more homogeneous stress state and to avoid the influence of edge effects, the geometry of the single-lap shear joint was modified. A Finite Element Analysis was performed to verify the influence of the proposed changes. Fillets in both adhesive and adherends were introduced, leading to a complex geometry of both substrate and adhesive layer.

3.5.3 Description of the stress singularity for a two-material wedge

Due to the singular behaviour of the stresses at the edge of the interface of bonded connections, the stress values obtained from a Finite Element Analysis are highly mesh dependent. Therefore, the peak values obtained from the numerical analysis are arbitrary into some extend. The stress state in the vicinity of a crack can be analytically described using a fracture mechanics approach. The edge point of the interface between adhesive and adherend can be seen as a *two-material wedge*. Figure 3.24 shows a two-material wedge.

The stress field around the two-material wedge can be described using a series expansion (Williams, 1952). In this series expansion, the first term is singular and dominant in the vicinity of the crack. Therefore, the stress field can be described with good accuracy at the vicinity of the crack, when only this singular term is considered. For larger distances from the singularity, more terms have to be taken into account in order to describe the stress field.

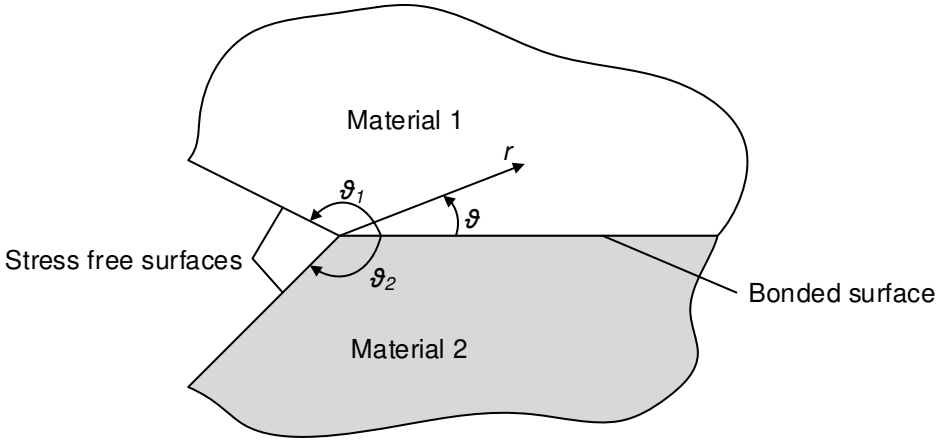

Figure 3.24: Two-material wedge, from Gleich (2002) - the polar coordinate system with its origin at the tip of the wedge is shown in the figure

These additional terms are no longer singular (Weißgraeber and Becker, 2013). The stresses in the vicinity of the singular point can be accurately described with

$$\sigma_{r,\vartheta}^{m} = H\, r^{\lambda-1}\, f_{r,\vartheta}^{m}\left(\lambda,\vartheta\right). \tag{3.46}$$

In equation 3.46, m is the material index ($m = 1, 2$) , H is the free edge stress intensity factor, $f_{r,\vartheta}^{m}\left(\lambda,\vartheta\right)$ are known angular functions describing the stress field and λ is order or strength of the singularity. The order of the singularity describes the shape of the stress field and the stress intensity factor its magnitude. r and ϑ are polar coordinates having their origin at the singularity. The free edge stress intensity factor H depends on the geometry, the elastic constants of the materials and the applied load. The order of the singularity depends on the angles ϑ_1 and ϑ_2 as well as the elastic constants of the materials involved. The order of the singularity is independent of the loading conditions. Only the first singular term of the stress function is shown, thus reducing the validity of equation 3.46 on the region close to the singular point.

Focussing on one material and combining the stress intensity factor with the known angular functions describing the stress field, equation 3.46 can be rewritten as

$$\begin{aligned} \sigma_{r,0}^{m=1}\left(r\right) &= H_1\, r^{\lambda-1} \qquad \text{peel stresses and} \\ \tau_{r,0}^{m=1}\left(r\right) &= H_2\, r^{\lambda-1} \qquad \text{shear stresses.} \end{aligned} \tag{3.47}$$

Applying the logarithm on both sides of equation 3.47 gives

$$\begin{aligned} \log\left[\sigma_{r,0}^{m=1}\left(r\right)\right] &= \log\left(H_1\right) + \left(\lambda-1\right)\log\left(r\right) \qquad \text{peel stresses and} \\ \log\left[\tau_{r,0}^{m=1}\left(r\right)\right] &= \log\left(H_2\right) + \left(\lambda-1\right)\log\left(r\right) \qquad \text{shear stresses.} \end{aligned} \tag{3.48}$$

Considering equation 3.48, it can be concluded that both the stress intensity factors and the order of the singularity can be evaluated from a logarithmic plot of the stress distribution on a path on the interface, which can be obtained from a Finite Element Analysis. In order

to capture the singularity, a very fine mesh is required. Due to the basic assumption that equation 3.46 is only valid in the vicinity of the singularity, only the region close to the singularity must be considered. For the stress plot, this means that only the linear part of the curve is to be considered.

Using a linear elastic material

The order of the singularity depends on the stiffness ratio of the adherends and the adhesive. For the configuration of a rigid adherend and a soft adhesive, an order of singularity of $\lambda = 0.7$ is given in Weißgraeber and Becker (2013). To illustrate this, the single-lap shear joint presented in section 3.5.1 is modelled in a plane strain linear Finite Element Analysis using the elastic constants and dimensions defined for the case "soft adhesive" in table 3.4. Figure 3.25 displays the focussed mesh used with a minimum element size at the corner edge point of $0.5\ \mu m$.

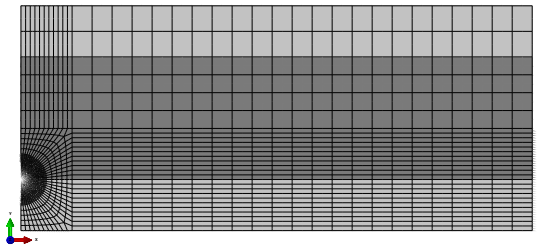

Figure 3.25: Focussed mesh used in the FE model of the single-lap shear joint

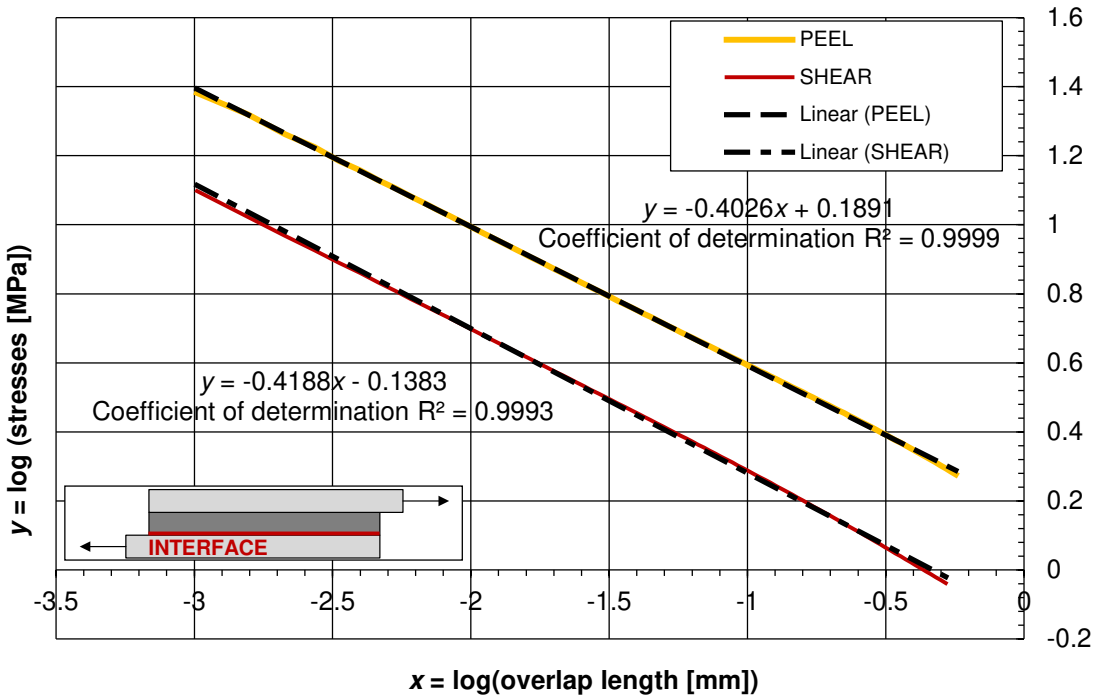

Figure 3.26: Double logarithmic plot of the stress distribution in the soft adhesive for the single-lap shear joint at the vicinity of the singular point - linear regression indicated

Figure 3.26 shows the result of this simulation. A double logarithmic diagram gives the stress distribution plotted against the interface paths. As explained in section 3.5.3, the slope of the line corresponds to the order of the singularity $\lambda - 1$. In the case of figure 3.26, $\lambda - 1 = -0.4$, which means $\lambda = 0.6$. This result shows good agreement with the values given in Weißgraeber and Becker (2013).

Using a soft hyperelastic material

Up to this point, the stresses have been determined assuming a linear elastic material law with the elastic constants given in table 3.4. In the second example presented below, the *Marlow* hyperelastic material law, described in section 3.3.3, calibrated on uniaxial tension test data on Dow Corning® 993 structural silicone sealant (Dow Corning Corporation, 2001), was used to describe the adhesive layer. The geometry of the lap shear joint and the elastic constants of the adherends are given in table 3.4. The boundary conditions shown in figure 3.19 were chosen as in the preceding example. The stresses and strains were determined in a nonlinear Finite Element Analysis using the commercial software code ABAQUS® (Dassault Systèmes, 2014). 2D plane strain conditions were assumed and quadratic, fully integrated hybrid elements were chosen due to the incompressible material behaviour of the adhesive.

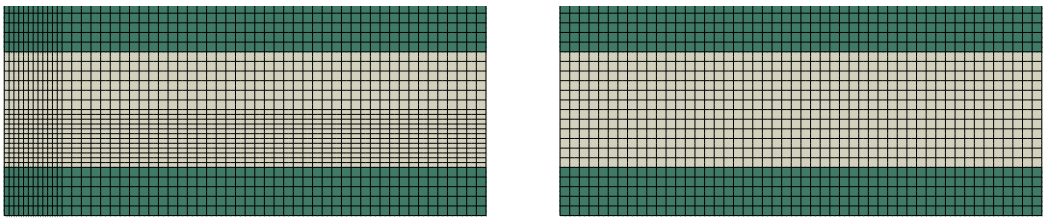

(a) 0.5 mm element size at the corner edge (b) 1 mm element size at the corner edge

Figure 3.27: Numerical model for the mesh study on the stresses and strains for a single-lap shear joint assuming a hyperelastic material

In order to visualise the influence of the chosen element dimensions on the results, the values for the first principal stress and the first principal strain were determined for 5 different element edge dimensions: 0.1 mm, 0.5 mm, 1 mm, 2 mm and 3 mm. For computational efficiency, a fine mesh was only inserted at the area in the vicinity of the two-material wedge, as shown in figure 3.27a.

The results of the mesh study on the first principal stress and strain at the notch tip of the two-material wedge are shown in figure 3.28. The results were evaluated at the nodes. The non-converging behaviour is clearly observable both for stresses and strains.

Stress intensity factor

A design approach for adhesively bonded connections based on a stress intensity factor has been proposed by Gleich (2002), considering a linear elastic material behaviour. In the design process, the stress intensity factor, determined at the two-material wedge using a Finite Element Analysis, is compared to a critical stress intensity factor, which is considered as a material property. According to Gleich (2002), both the stress intensity factor and the order

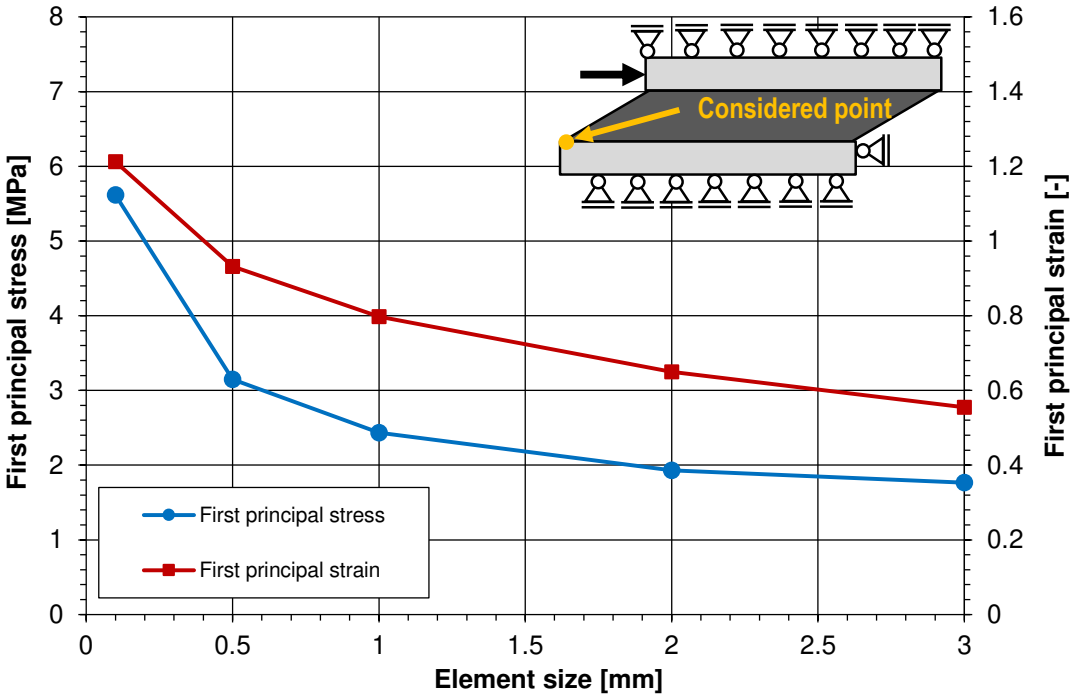

Figure 3.28: Mesh study on the stresses and strains for a single-lap shear joint assuming a hyperelastic material

of the singularity are convergent values, provided that a reasonably refined mesh is used. This method has already been applied by Groth (1988), but considering only peel stresses. Failure of bonded connections with large overlap lengths was well predicted, in contrast to small overlap lengths, for which shear stresses were supposed to be dominant (Gleich, 2002). In the work of Gleich (2002), the above mentioned design approach was used for single-lap shear joints. Peel and shear stresses were investigated separately for the prediction of the failure load and fair results were obtained. The procedure is based on two fundamental assumptions. The critical stress intensity factor at the corner edge was considered to be independent of the bondline thickness and a linear relationship was supposed between the failure load and the free edge stress intensity factor

$$F_{\mathrm{u}} = F_{\mathrm{FEA}} \frac{H_{\mathrm{FEA}}}{H_{\mathrm{c}}}. \tag{3.49}$$

In equation 3.49, F_u is the predicted failure load, F_{FEA} the load for a given bonded connection leading to the free edge stress intensity factor H_{FEA} and H_{c} critical stress intensity factor. In contrast to the analytical approaches, like the *Volkersen* equation, the stress intensity approach takes into account the stress state at the interface, where crack onset is observed. Gleich (2002) investigated thin adhesively bonded connections loaded in shear and an optimum bondline thickness was identified, which was as well approved by tests. Similar investigations using a stress intensity factor were performed in Berto (2015) on the stress distribution in the vicinity of a V-notch for an incompressible *Mooney-Rivlin* hyperelastic material.

3.5.4 Advanced numerical modelling

Cohesive zone modelling

In the numerical simulation of adhesively bonded connections, *Cohesive Zone Modelling - CZM* can be used to reproduce the progressive damage and failure of an interface or a region. According to Campilho et al. (2012), CZM modelling describes the elastic behaviour, the damage initiation and the propagation of a crack on a given path in a bulk material or at an interface between two materials. The basic concepts of CZM were proposed independently by Dugdale (1960) and Barenblatt (1962). The description of this behaviour is based on the relation between stresses and the relative displacement of a defined interface. A Cohesive Zone Model can be used in a continuum based Finite Element simulation. In Campilho et al. (2012), the CZM was investigated in the context of a Finite Element Analysis and the results on a single-lap shear joint were found to be mesh independent. In the field of adhesively bonded connections, two approaches are currently adopted, depending on the nature of the problem. In a *local approach*, the behaviour of the interface between adhesive and adherend (with zero thickness) is simulated, whereas in a *continuum approach*, the whole adhesive is replaced by a layer of cohesive elements. The latter method is adopted for adhesive joints with small adhesive layer thickness.

A cohesive element can either connect two coincident nodes (in the local approach) or two distant nodes (in the continuum approach). The mechanical behaviour is defined using so-called *traction-separation laws* (cf. section 3.9), which define the stress components (three modes according to fracture mechanics approach cf. figure 3.29) as a function of the displacement between the two interfaces. The traction-separation law contains three characteristic parts: elastic behaviour until damage initiation, damage evolution and complete failure (Da Silva and Campilho, 2012). Different shapes of the cohesive laws are available in commercial Finite Element software codes, like ABAQUS® (Dassault Systèmes, 2014).

Cohesive Zone Modelling is often used for thin adhesive layers and stiff adhesives. In Piculin et al. (2016), this concept has been employed in the context of bonded connections between timber frames and glass panes. The epoxy-based adhesive with a layer thickness of 3 mm and *Young*'s modulus (at the origin of the stress-strain curve) of 10 MPa was modelled with a linear visco-hyperelastic compressible material law. The interface behaviour between adhesive and adherend was numerically reproduced with cohesive elements, since adhesive failure of the epoxy was observed in the tests.

In contrast to the epoxy-based adhesive, cohesive failure (i.e. rupture within the adhesive layer) was observed in different tests (tension, shear) of adhesively bonded connections with silicone, e.g. Hagl (2007), Dias (2013) and chapter 4.

Extended Finite Element Method

The *Extended Finite Element Method - XFEM* is another advanced numerical modelling tool, which has been used in Campilho et al. (2011) for the simulation of adhesively bonded connections. It is an extension of the Finite Element Method, based on the concept of partitioning elements. Damage initiation is generally based on the bulk strength of the material and failure on strains. Crack onset and crack growth are independent of the chosen mesh, as elements can be split in two parts due to enrichment functions for the nodal displacements. Unlike for

CZM, a crack can grow in an arbitrary direction. Furthermore, no remeshing is required after an onset of a crack. XFEM is available in commercial Finite Element software codes, like ABAQUS® (Dassault Systèmes, 2014).

For the elements, enrichment functions are defined, which allow for the representation of the displacement jump between two initially coincident nodes, which are separated by the onset of the newly created crack or the propagation of an existing crack (Campilho et al., 2011). As implemented in ABAQUS® (Dassault Systèmes, 2014), crack propagation will occur perpendicular to the direction of maximum principal stress or strain. Crack propagation is supposed to be relatively mesh independent, when the crack initiation is based on an energetic criterion. In Campilho et al. (2011), single and double-lap shear joints with a brittle adhesive have been numerically reproduced. The results however were found to be mesh dependent and a crack propagation starting at the adhesive interface and running into the adherend was observed. The latter problem has been fixed recently by Stein et al. (2017a).

Boundary Element Method

The *Boundary Element Method* is an efficient tool to describe stress fields in regions of large stress gradients. In Gaul and Fiedler (2013), a general description is given and in Vable (2008), the application of the BEM in the field of adhesively bonded connections is discussed. Although the BEM exhibits a number of advantages compared to the widely used Finite Element Method, only very few applications of the BEM in the field of adhesive joints are available (cf. Da Silva and Campilho (2012)).

Gaul and Fiedler (2013) explain the major differences between the Finite Element and the Boundary Element Method. For the FEM, the continuum is divided into small partitions, the Finite Elements. For the BEM, only the boundary is divided into small partitions. As a consequence, the dimension of the problem is reduced by one dimension. For example, a 2D plate is represented with 1D line elements at the boundaries. As the stresses are computed at the boundary and not at the integration points, as for the FEM, large stress gradients in the vicinity of a crack can be accurately represented.

According to Vable (2008), the BEM is not straightforward to implement. Moreover, the reduced size of the stiffness matrix due to the small number of elements compared to the FEM is partially compensated by its complexity. As a consequence, some highly efficient equation solvers cannot be used.

Finite Difference Method

The *Finite Difference Method - FDM* is a numerical technique to approximate the solution of differential equations. Unlike as for the Finite Element Method, a given structure is not subdivided in elements, which are delimited by nodes, but in a uniform grid of points. The results in terms of stresses are obtained in these points. Whereas in the FEM, the values computed at the integration points are extrapolated and averaged between neighbouring nodes, the results of the grid points are not averaged. According to Da Silva and Campilho (2012), the FDM is mainly used for very simple geometries, for complex geometries and nonlinear material behaviour, a Finite Element Analysis is generally preferred.

3.6 Basics on fracture mechanics

3.6.1 Griffith criterion

In section 3.5.2, the singular behaviour of the stresses at the corner edge of the single-lap shear joint specimen has been discussed. The corner edge exhibits a discontinuity regarding both the material properties and the geometry. It has been referred to as a *two-material wedge*. The two-material wedge can be seen as a special case of the bi-material crack, i.e. a crack going through the interface of two materials. According to Gross and Seelig (2011), a *crack* is a cut in a body, as shown in figure 3.29a. The boundaries of the crack are called *crack surfaces*. The crack surfaces are assumed to be traction-free. The crack ends at the so-called *crack front* or *crack tip* (in 2D considerations).

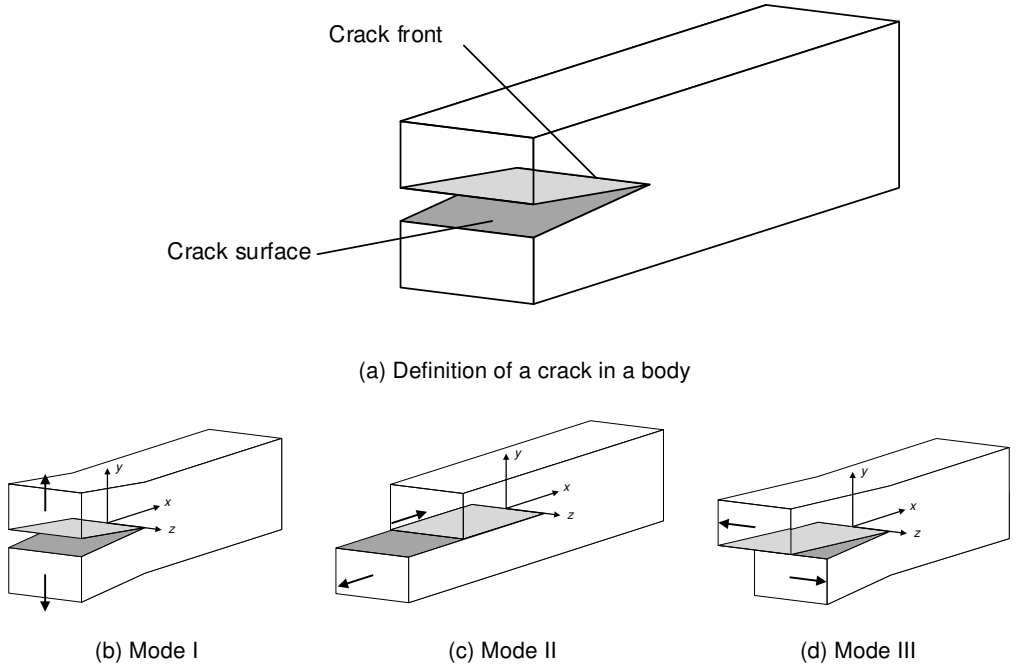

(a) Definition of a crack in a body

(b) Mode I (c) Mode II (d) Mode III

Figure 3.29: Crack definition and crack opening modes, from Gross and Seelig (2011)

For cracks, the three deformation modes, shown in figure 3.29, are generally distinguished. *Mode I* describes a crack opening, which is symmetric to the $x - z$ plane. *Mode II* describes a crack opening, where the crack surfaces are deformed in a direction normal to the crack front. Finally, *mode III* describes a crack opening, where the crack surfaces deform in a direction tangential to the crack front.

For a given structure exhibiting a crack, the crucial question consists in assessing, whether the crack propagates under given loads and boundary conditions or not. This assessment is performed with methods from *fracture mechanics*. A criterion for crack propagation was developed by Griffith (1921). It states that crack can only grow, if the energy released by the propagation of the crack is sufficient to create the new surfaces. The "force" required to allow for crack propagation is referred to as *critical energy release rate*. The criterion according to

Griffith can be written as

$$\mathcal{G} = \lim_{\Delta A \to 0} -\frac{\Delta \Pi}{\Delta A} \geq \mathcal{G}_{\mathrm{c}}. \tag{3.50}$$

In equation 3.50, $\mathcal{G}$ is the energy release rate, ΔA the newly created crack surface, $\Delta \Pi$ the change of potential energy due to the onset of the new crack surface ΔA and $\mathcal{G}_{\mathrm{c}}$ the critical energy release rate.

For weak singularities such as notches, the concepts from fracture mechanics, e.g. classic *Griffith* energy criterion, cannot be used without the assumption of a pre-existing crack or flaw (Weißgraeber, 2014). The differential energy release rate $\mathcal{G}$ can be calculated with the virtual crack closure integral. The virtual crack closure integral denotes the energy required to close a virtual crack. It is the product of the stress field at the vicinity of the notch tip with the displacement of the virtual crack faces, integrated over the whole crack surface. Evaluating the integral shows that the differential energy release rate $\mathcal{G}$ vanishes at weak singularities, where $\lambda \geq 1/2$, i.e. for notches. This would mean, that a notch can resist infinitely high loads, which is in contradiction with test results.

3.6.2 J-integral

Apart from stress intensity factors or the concept of energy release rate as proposed by Griffith (1921), Rice (1968) introduced a path independent contour integral, the so-called *J-integral*. In contrast to the previously mentioned concepts, the use of the J-integral is not restricted to elastic material behaviour. The J-integral is a path independent contour integral surrounding a singularity. Typically, contour integrals are employed when the exact shape of a field quantity cannot be determined in the vicinity of a singular point. The contour integral is computed using the far field values, which can be accurately determined.

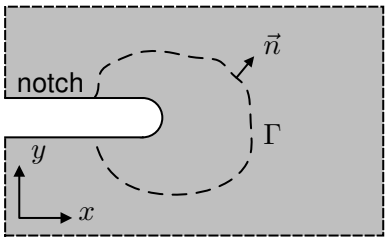

Figure 3.30: Definition of a path around a notch for the evaluation of the J-integral, from Rice (1968)

Figure 3.30 shows a two-dimensional body with a notch. A path Γ, surrounding the notch, is defined. The normal vector $\vec{n}$ is defined on the path Γ. According to Rice (1968), the J-integral is defined as

$$J = \int_{\Gamma} \left(W dy - \vec{T} \cdot \frac{\partial \vec{u}}{\partial x} ds \right). \tag{3.51}$$

In equation 3.51, Γ a path surrounding the notch tip, W is the strain energy density, $\vec{T}$ the traction vector defined according to the outward normal $\vec{n}$, $\vec{u}$ the displacement vector and ds

an element of the path Γ. For linear elastic materials, the J-integral is equivalent to the stress intensity factors concept. For cracks in elastic materials, the value of the J-integral equals the energy release rate as defined by Griffith (1921).

3.7 Finite Fracture Mechanics

3.7.1 The coupled stress and energy criterion by *Leguillon*

For weak singularities such as notches, the classic fracture mechanics approach cannot be used to assess crack initiation. In order to allow for an assessment for these kind of notches, Leguillon (2002) proposed a *hybrid criterion*, which is based on both a *stress criterion* and on an *energy criterion*. The fundamental difference regarding *Griffith's* approach is that an onset of a crack with finite length is considered, instead of a continuous crack growth (cf. Hashin (1996)). Therefore, the method is referred to as *Finite Fracture Mechanics*. Crack initiation with a length Δa (respectively with the surface ΔA for 3D problems) is assumed, if both criteria are simultaneously fulfilled for the same crack length. The fracture mechanics or energy criterion gives a lower bound of possible crack lengths and the stress criterion an upper boundary for crack lengths. Since both the crack length and the crack initiation load are unknown, the coupled criterion is an optimisation problem.

For the energy or fracture mechanics criterion, the potential energy in the body is considered for the state without crack and after the initiation of a crack with the finite length Δa following the concept of *Griffith* (see equation 3.50). According to Leguillon (2002), the fracture mechanics criterion, or energy criterion, can be written as

$$-\frac{\Delta \Pi}{\Delta A} \geq \mathcal{G}_{\mathrm{c}}. \tag{3.52}$$

In equation 3.52, $\Delta \Pi$ is the change in potential energy of the system, ΔA is the created crack surface and $\mathcal{G}_{\mathrm{c}}$ the critical energy release rate. As explained in section 3.6.1, the fracture energy per unit surface vanishes if $\Delta A \to 0$.

The stress criterion corresponds to a comparison between the acting stresses and the bulk material strength on the area of the newly created crack, i.e.

$$\sigma \geq \sigma_{\mathrm{c}}. \tag{3.53}$$

In equation 3.53, σ is the acting stress and σ_{c} the material strength. The stress criterion claims that a crack with the length Δa or the surface ΔA can develop, if the acting equivalent stress exceeds the bulk material strength over the whole area of the crack surface. In Leguillon (2002), stresses are considered, but in general, any suitable failure criterion could be used, such as strains or the strain energy density. Consequently, in order to use the coupled criterion, the critical energy release rate and the failure criterion of the considered material must be known.

In order to illustrate the necessity of both criteria, two examples, from Leguillon (2002), as shown in figure 3.31, are investigated. In a continuum mechanics approach for the notched

bar under a tensile force, the stresses are found to be infinitely high at the notch tip. Therefore, the bar fails for an infinitely small load, which contradicts observations from material tests. The stress criterion alone is therefore not sufficient to explain the failure process observed in this case. On the other hand, when a straight bar of a material with *Young*'s modulus E, a cross sectional area A and a length l_0, subjected to a tensile force F is assumed, the energy criterion alone is not sufficient to predict failure. For this example, the fracture energy is evaluated as

$$-\Delta\Pi = \Pi = \frac{1}{2}\, A\, l_0\, \frac{\sigma^2}{E}. \tag{3.54}$$

In equation 3.54, σ is the tensile stress in the bar. Π is the product of the strain energy potential of the bar with the volume V of the considered bar. At failure, the initiated crack surface equals the total surface of the cross section. Thus, the change in potential energy corresponds to the potential energy stored in the bar before complete failure.

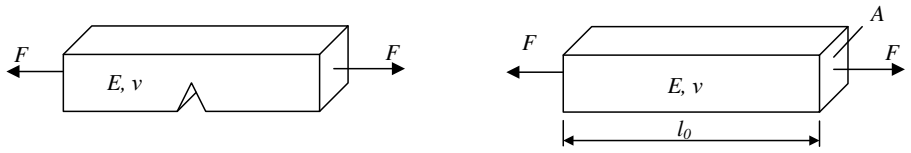

(a) Notched bar under tensile force (b) Defect-free bar under tensile force

Figure 3.31: Examples illustrating the coupled stress and energy criterion

Assuming that failure occurs, when the energy criterion given in equation 3.52 is fulfilled, inserting equation 3.54 in equation 3.52 gives

$$\frac{1}{2}\, A\, l_0\, \frac{\sigma^2}{E} \geq \mathcal{G}_c \Rightarrow \sigma \geq \sqrt{\frac{2\, E\, \mathcal{G}_\mathrm{c}}{l_0}}. \tag{3.55}$$

Consequently, regarding equation 3.55, a sufficiently long bar already fails at low applied tensile stresses. In that case, the stress criterion is needed to compute the real failure load.

The coupled stress and energy criterion has been applied in Weißgraeber (2014) to predict the failure in adhesively bonded single-lap shear joints. For the stress partial criterion, *Rankine*'s failure hypothesis was employed, as the investigated adhesive exhibited a brittle material behaviour. The fracture mechanics criterion was evaluated using the incremental or average energy release rate, which is defined as

$$\bar{\mathcal{G}} = \frac{1}{\Delta A} \int_0^{\Delta A} \mathcal{G}(\hat{a})\, d\hat{a} = -\frac{\Delta\Pi}{\Delta A}. \tag{3.56}$$

With equation 3.56, the coupled stress-energy criterion can be rewritten as

$$f(\sigma_{ij}(x)) \geq \sigma_\mathrm{c} \qquad \forall x \in \Omega_\mathrm{c}(\Delta A) \qquad \wedge \qquad \bar{\mathcal{G}} \geq \mathcal{G}_\mathrm{c}. \tag{3.57}$$

In equation 3.57, f is an equivalent stress depending on the chosen failure criterion, x is a point in the Euclidian space and Ω_c is the surface of the crack ΔA. The coupled criterion of equation 3.57 is satisfied, if both partial criteria are simultaneously fulfilled for the same crack length. The equivalent stress (e.g. *von Mises* stress for steel or the first principal stress for glass) must be higher than the material strength for all points on the crack surface (or crack edge for 2D considerations) with length Δa. In addition, the average energy release rate must be higher than the critical energy release rate for the crack of the length Δa or the surface ΔA, in order to allow for the initiation of a crack. Consequently, the load at crack initiation and the crack length are unknown at the beginning.

A similar criterion was proposed by Cornetti et al. (2006). In contrast to equation 3.57, the averaged equivalent stress over the crack length Δa is considered,

$$\frac{1}{\Delta A}\int_0^{\Delta A} f(\sigma_{ij}(\hat{x}))d\hat{x} \geq \sigma_{\mathrm{c}} \qquad \forall x \in \Omega_{\mathrm{c}}(\Delta A) \qquad \wedge \qquad \bar{\mathcal{G}} \geq \mathcal{G}_{\mathrm{c}}. \tag{3.58}$$

The stress criterion gives an upper boundary for the possible crack surface ΔA, as a crack can only appear on the surface on which the acting stress exceeds the material resistance. Longer cracks are only possible if the load is increased and thus the acting stress exceeds the strength of the material over a larger area. In other words, only cracks smaller than ΔA are possible. On the other hand, the energy criterion gives a lower boundary for the crack length, as only cracks longer than the lower boundary release enough energy for crack initiation. The solution of the optimisation problem is found, when the upper boundary meets the lower one.

3.7.2 Illustrating example

In order to illustrate the optimisation problem of the coupled criterion, the following example of a single-lap shear joint, shown in figure 3.32 and taken from Weißgraeber (2014), is presented. The single-lap shear joint is considered in a two-dimensional analysis. For simplicity reasons, only interface cracks are considered, i.e. $\varphi = 0$, in figure 3.32. The crack surface ΔA simplifies to $h_c\,\Delta a$ with h_c, the width (bite) of the adhesive joint.

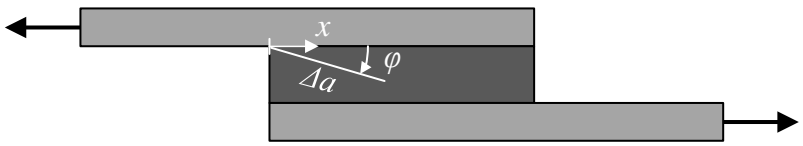

Figure 3.32: Single-lap shear joint under applied loads

For the given example, the stress distribution is plotted in figure 3.33 against the interface path x shown in figure 3.32 for the three load levels: (1) Applied force smaller than the crack initiation load (figure 3.33b), (2) applied force equals the crack initiation load (figure 3.33a) and (3) applied force exceeding the crack initiation load (figure 3.33c). Apart from the stresses, the incremental energy release rate is plotted against the developed crack length Δa in dashed lines for the three load cases.

Consider figure 3.33b for the given load case (1). The predicted crack lengths for both criteria correspond to the distances between the notch tip and the intersection point, where the

acting stresses $f(\sigma_{ij})$ meet the bulk material strength σ_c, respectively where the incremental energy release rate $\bar{\mathcal{G}}$ meets the critical energy release rate $\mathcal{G}_c$. The predicted crack length from the stress criterion Δa_{max}, which corresponds to the upper limit for possible cracks, is smaller than the predicted crack length Δa_{min} from the energy criterion. Therefore, the given load is too small for crack initiation. The energy released by a crack with the length Δa_{max} is not sufficiently high for crack initiation, as the incremental energy release rate for a crack with a length Δa_{max} is smaller than the critical energy release rate of the material. If the load corresponds to the failure load, both crack lengths are equal as shown in figure 3.33a. The last case, which is shown in figure 3.33c, corresponds to the case where the applied force exceeds the failure load. Here, both criteria are fulfilled, the crack length predicted by the stress criterion releases enough energy for crack initiation. However, crack initiation would also be possible for a smaller load level.

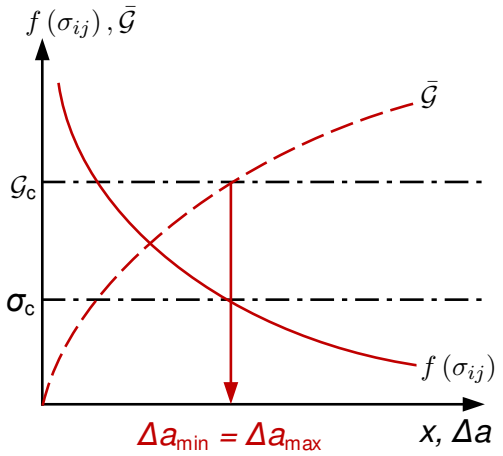

Legend:

$f(\sigma_{ij})$	Failure criterion (stress or strain based)
$\bar{\mathcal{G}}$	Incremental energy release rate
$\mathcal{G}_c$	Critical energy release rate
σ_c	Strength of the bulk material
x	Path starting at the singularity
Δa	Finite crack length
Δa_{min}	Lower boundary for Δa
Δa_{max}	Upper boundary for Δa

(a) Applied force equals the crack initiation load

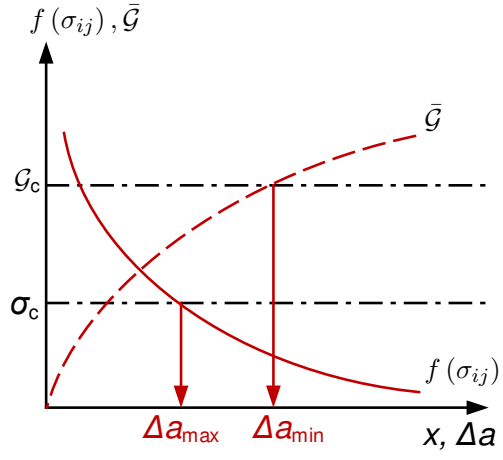

(b) Applied force below the crack initiation load

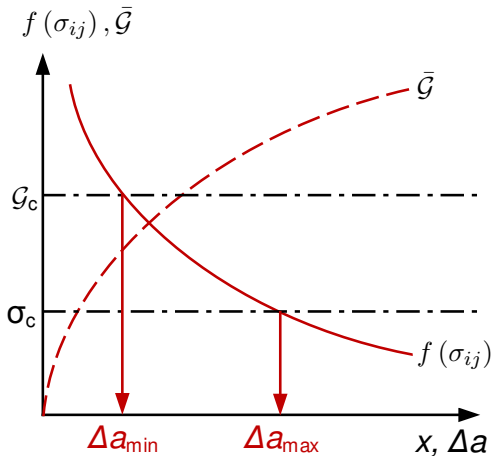

(c) Applied force exceeding the crack initiation load

Figure 3.33: Illustration of the evaluation of the coupled criterion

The curve for the incremental energy release rate exhibits a monotonically increasing behaviour. This behaviour has been chosen for clarity reasons. In Weißgraeber (2014), the influence of a non-monotonic behaviour for the incremental energy release rate is discussed. A non-monotonic behaviour of the incremental energy release rate leads to ranges of possible

crack lengths and allows for crack arrest after crack initiation.

The concepts of Finite Fracture Mechanics, which have been presented in this section, avoid the question of the mesh dependency observed in a Finite Element Analysis in the vicinity of the two-material wedge, as the stresses or strains are not considered at the origin of the singularity, but in a certain distance away. Therefore, the results obtained from the numerical simulation give convergent values, provided that a sufficiently refined mesh has been selected. The energy partial criterion is much less affected from the stress singularity as it is based on the global behaviour of the specimen. An inconvenience of the method proposed by Leguillon (2002) is the high computational effort required. Since both crack length and orientation are unknown, a number of Finite Element calculations is needed, as well as a refined mesh to capture the stress distribution in the vicinity of the notch in an accurate way, unless closed-form solutions are available.

3.8 Theory of Critical Distances

3.8.1 Point method, line method and imaginary crack method

The name *Theory of Critical Distances* (TCD) has been introduced by Taylor (2008). It includes methods, which predict the effect of notches. These methods work with a characteristic length parameter, which is considered as a material constant. According to Taylor (2008), four different methods can be distinguished: the *point method*, the *line method* (both as proposed by Whitney and Nuismer (1974)), the *imaginary crack method* (cf. Waddoups et al. (1971)) and the *Finite Fracture Mechanics - FFM*. The FFM has already been introduced in the previous section. In Taylor (2008), FFM is considered as a potential scientific basis for the Theory of Critical Distances, which was referred to as an approximation of the Finite Fracture Mechanics approach.

A first approach working with a length parameter to predict the effect of notches was already introduced by Neuber (1936). Sharp notches in linear elastic materials were investigated and the stress intensity factor was found to depend not only on the shape of the notch, but also on an elementary particle. This elementary particle was considered as new material constant, which quantifies the notch sensitivity of the material. Following this concept, a large number of different structural components has been analysed in Neuber (1958), including the effect of yielding of metallic materials.

A simple engineering approach for the prediction of the uniaxial tensile strength of laminated composites containing stress concentrations has been proposed by Whitney and Nuismer (1974). The concept was based on the two parameters unnotched tensile strength of the laminate and a characteristic dimension. This dimension was considered as a material property. Two concepts have been proposed. According to Whitney and Nuismer (1974), failure occurs, when the acting stresses exceed the strength over a certain distance (*point method*). Alternatively, failure occurs, when the acting stress averaged over a given distance exceed the strength of the bulk material (*line method*). In order to illustrate these methods, the example of a body with a round notch under an arbitrary load is given in figure 3.34. The stress distribution is plotted over a horizontal path starting from the root of the notch. For the point method, the stresses are evaluated at a distance $L/2$ from the notch tip. For the line

method, the stresses are averaged over the distance $2\,L$ from the notch tip,

$$\sigma_{\mathrm{LM}} = \frac{1}{2\,L}\int_0^{2\,L} \sigma\,(r)\,\mathrm{d}r. \tag{3.59}$$

In equation 3.59, σ_{LM} is the stress evaluated according to the line method. In this example, stresses are considered, but the method is not restrained to stresses.

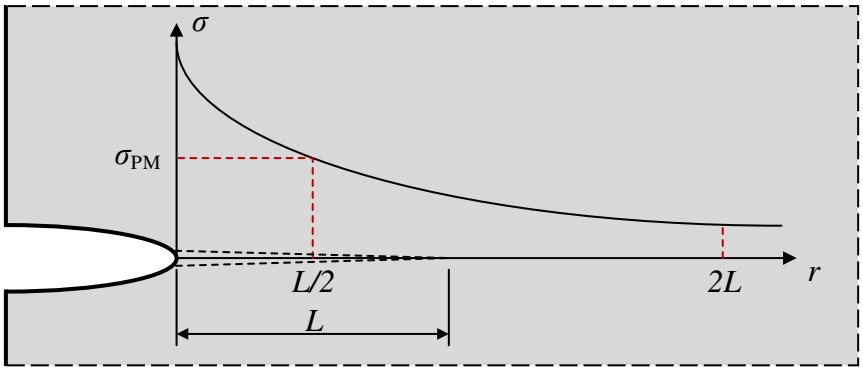

Figure 3.34: Methods from Theory of Critical Distances - point method, line method and imaginary crack method, from Taylor (2013)

The *imaginary crack method*, as proposed by Waddoups et al. (1971), assumes the presence of a sharp crack with the length L at the tip of the considered notch. With this assumed crack, concepts from fracture mechanics can be used to determine the load at which crack propagation will occur (cf. *Griffith*). A commonly used value for the length scale is the so-called *Irwin-length*, which was originally defined to describe the size of a plastic zone at the crack tip (Weißgraeber, 2014). The *Irwin*-length is given as

$$L = \frac{1}{\pi}\left(\frac{K_{\mathrm{c}}}{\sigma_{\mathrm{c}}}\right)^2. \tag{3.60}$$

In equation 3.60, L is the characteristic length scale, K_{c} fracture toughness of the considered material and σ_{c} the tensile strength of the material. For some materials, the parameter L is related to a microstructural dimension, like the grain size of steel. For many other cases, the physical relation between the characteristic length and material properties remains unclear (Weißgraeber, 2014). In many cases, the characteristic length has to be determined empirically.

Although the length parameter is considered as a material property in the framework of the TCD, there are a number of works, which observe some variations. Pipes et al. (1979) considered the two-parameter methods (characteristic dimension and unnotched tensile strength) proposed by Whitney and Nuismer (1974) and Waddoups et al. (1971), which assume that the characteristic dimension is a material constant. They showed that this assumption is invalid and proposed a three-parameter model to evaluate the notched strength of composite materials. Awerbuch and Madhukar (1985) reviewed a large set of experimental data dealing with the notched strength of composite materials and several failure models. For

the two-parameter models proposed by Waddoups et al. (1971) and Whitney and Nuismer (1974), it was concluded that the constant characteristic dimension strongly depends on the laminate configuration investigated. For one specific configuration, the models were found to give good results. Comparable results were found in Tan (1987) for the fracture strength of composite laminates with elliptical holes.

The previously described point and line method are very straightforward to use in the post-processing of a Finite Element Analysis. According to Weißgraeber (2014), the TCD is implicitly used in some engineering applications, when the element size is kept constant in the vicinity of the notch. This requires the chosen Finite Element mesh to be calibrated for each numerical analysis using experimental data. Another method to avoid the singularity, which is discussed in Gleich (2002), consists in considering the stress values at a small distance from the interface corner, such as the third node from the singular point. This method however also requires a constant element size and a calibration using experimental data, as mentioned before.

3.8.2 Control volume approach

For the line method, the stresses are averaged over a path of a length of $2\,L$, where L is the length scale parameter. This approach can also be extended to a three-dimensional stress analysis, in which the acting stresses, strains or strain energy are averaged within a volume, called *control volume*.

This control volume approach was used in Schaaf et al. (2015) for the life estimation of a short fibre reinforced polymer. The strain energy density was used as failure criterion for the material and was averaged within the structural or control volume. Failure in terms of crack onset at a notch occurred, when the average strain density in the control volume reached a critical value. The control volume was defined through a radius, which was considered as material property.

The same approach was used in Berto (2015). The fracture assessment was based on the local strain energy density averaged over a spherical control volume with a given radius, which was considered as a characteristic parameter of the material. The fracture behaviour of notched plates of natural rubber was predicted in a Finite Element Analysis assuming a *Mooney-Rivlin* incompressible material law and good agreement was found with the experimental data. A focussed mesh was used at the notch tip. Since the strain energy density was averaged over a finite volume, the results found did not depend on the chosen size of the Finite Elements, provided that a reasonably refined mesh was built.

The control volume approach was reviewed and extended in the work of Schaaf et al. (2015) and implemented using a Finite Element Analysis. Instead of defining a constant volume with a fixed radius, the so-called V_{90}*-concept* was adopted. V_{90} is the volume, in which the stresses are higher than 90% of the maximum stress at the notch tip. The basic idea is, that the smaller the highly stresses volume, the lower the failure probability of the considered notch. In Schaaf et al. (2015), this concept was combined with the control volume approach. Instead of averaging the strain energy density over a spherical control volume, the strain energy density was averaged over the V_{64}-volume. The threshold value was lowered to 64% to reduce the requirement for a refined mesh.

3.9 Determination of the critical energy release rate

3.9.1 Double Cantilever Beam test

The objective of a Double Cantilever Beam test is the determination of the cohesive properties, like the cohesive law and the critical energy release rate of an adhesive. Two different approaches can be used to evaluate the DCB test. The first approach is based on linear elastic fracture mechanics and considers the compliance of the adherends (Blackman et al., 1991). The second methods works with the J-integral, thus allowing for nonlinear elastic behaviour of the adhesive.

Generally speaking, cohesive laws give the relationship between the stresses across the interface zone and the separation distance of the crack faces, prior to the real crack opening (Li and Ward, 1989). The stresses decrease to zero for a critical local displacement, which corresponds to the actual crack initiation (Sorensen and Jacobsen, 2003). Figure 3.35 shows the representation of cohesive behaviour and two possible shapes for the cohesive law, the so-called *traction-separation law*. A typical application of cohesive zone modelling are thin adhesively bonded connections, where the adhesive layer is replaced with cohesive elements instead of solid elements representing the bulk material (Da Silva and Campilho, 2012).

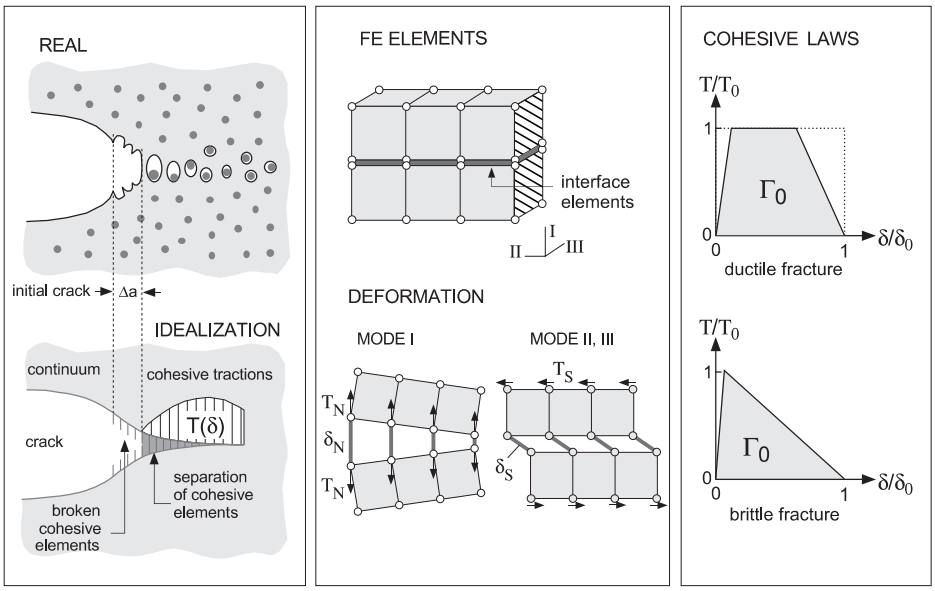

Figure 3.35: Representation of the ductile failure process by cohesive modelling, picture taken from Cornec et al. (2003)

3.9.2 Method based on linear elastic fracture mechanics

As mentioned before, if the adhesive and the adherends show a linear elastic behaviour, methods from linear elastic fracture mechanics can be used to determine the critical energy release rate of the adhesive. In Blackman et al. (1991), several of these methods are presented, beginning at the "area" method, for which the energy release rate $\mathcal{G}$ is calculated from the change of potential (area under the load-displacement curve) $\Delta\Pi$ for a given

increase of the crack length Δa, with

$$\mathcal{G} = -\frac{\Delta \Pi}{h_\mathrm{c}\, \Delta a}. \tag{3.61}$$

In equation 3.61, h_c is the specimen width. Another method is based on the *Irwin-Kies* equation, in which the fracture energy is evaluated from the change of compliance of the specimens with increasing crack length. In this case, the energy release rate

$$\mathcal{G} = \frac{F^2}{2\, h_\mathrm{c}}\, \frac{dC}{da} \tag{3.62}$$

is given as a function of the applied load F and the measured compliance C. The compliance can also be determined analytically from the simple beam theory. Correction factors are given in Blackman et al. (1991), which take into account the low shear modulus of the adhesive as well as effects arising from the large deflections of the beams.

3.9.3 Method based on nonlinear elastic fracture mechanics

Apart from the restriction of linear elastic material behaviour, the second disadvantage of the compliance method is the accurate measurement of the crack propagation (Biel, 2005). Therefore, a second method, based on the path independent J-integral, introduced by Rice (1968), was developed by Anthony and Paris (1988) to experimentally determine the post peak tensile behaviour of cementitious composites. A compact tension specimen was used for the experimental investigations. The J-integral can be evaluated for a path in the cohesive zone, given as

$$J_\mathrm{c} = \int_0^{\delta_\mathrm{c}} \sigma\left(\delta\right) d\delta. \tag{3.63}$$

In equation 3.63, σ is the stress acting normal to the crack face, labelled as T in figure 3.35, J_c is the critical value of the J-integral at crack onset and δ_c is the displacement at which the traction vanishes, i.e. the displacement at which the crack is fully developed. In Leffler et al. (2007), the fracture energy J_c is considered as a material property. In an analogous way as described in section 3.6.1 for linear elastic materials, if the energy released by crack propagation exceeds the critical energy release rate, the crack will be able to propagate. According to Rice (1968), the J-integral can also interpreted as

$$J = -\frac{\Delta \Pi}{\Delta A}. \tag{3.64}$$

In equation 3.64, $\Delta\Pi$ is the change in potential energy due to the change of the crack surface ΔA. Since the accurate measurement of the crack propagation is very challenging, Li and Ward (1989) used pre-notched specimens with different notch lengths. For the evaluation, the differences in the potential energy $\Delta\Pi$ (area under the force-deformation curve) were considered for a given displacement u. The J-integral in this case is given as

$$J\left(u\right) = -\frac{\Delta \Pi\left(u\right)}{h_\mathrm{c}\, \Delta a}. \tag{3.65}$$

In equation 3.65, Δa is the difference of the length of the pre-notches. Knowing $J(u)$, the traction σ can be obtained by differentiating equation 3.63. In Olsson and Stigh (1989), a closed form solution based on the application of the *Euler-Bernoulli* beam theory for the adherends was given for the evaluation of the DCB specimen loaded under a force by solving an inverse problem between the crack opening displacement and the applied force. Andersson and Stigh (2004) gives

$$\sigma\left(w\right) = \frac{dJ\left(w\right)}{dw} \qquad \text{with } J = 2\frac{F\,\vartheta}{h_{\mathrm{c}}}. \tag{3.66}$$

In equation 3.66, F is the applied force, ϑ the rotation of the loading point and w the crack opening displacement, as shown as well in figure 3.36. Sorensen and Jacobsen (2003) proposed a double cantilever beam specimen with a bending moment applied on the boundaries. For this loading, the J-integral can be determined in closed form. Alternatively, in the case of an applied force at the boundaries, the rotation of the load application point has to be measured. A detailed derivation of equation 3.66 is given in Andersson and Stigh (2004), where Double Cantilever Beam tests were conducted on thin adhesive layers (0.2 mm). The evaluation of the Double Cantilever Beam test using the J-integral concept allows to take into account nonlinear material behaviour, but a basic assumption is the elastic material behaviour of both adhesive and adherends.

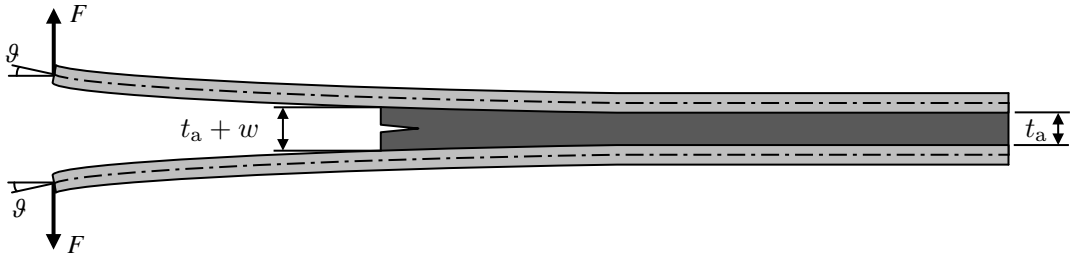

Figure 3.36: Definition of the quantities for the evaluation of the Double Cantilever Beam test

As shown in equation 3.63, the traction-separation law can be calculated by differentiation of the product of the experimentally record force with the rotation angle of the load application point. As a differentiation of experimentally recorded data can lead to important scattering, the values of the J-integral versus the crack opening displacement obtained from the experimental investigations (equation 3.66) are approximated by a *Prony* series (e.g. Leffler et al. (2007)). The critical energy release rate $\mathcal{G}_{\mathrm{c}}$ is defined as the value obtained for the deformation, for which the traction σ drops to zero. This corresponds to a maximum in the J-integral versus crack opening displacement curve. In the actual evaluation process, the value of 5% of the maximum traction is taken as a threshold for the determination of the critical energy release rate (e.g. Marzi et al. (2011)).

The presented J-integral based evaluation has been employed in a number of research projects, focussing initially on thin and stiff adhesives. In Biel (2005), the influence of the specimen geometry and the loading rate was investigated on a thin layer of an epoxy resin (Young's modulus of 2900 MPa) using the J-integral approach. Whereas the adhesive layer thickness was constant (0.2 mm), different geometries and cross sections were selected for

the adherends. No influence was found on the cohesive properties as long as no plastic deformation of the adherends occurred. The critical energy release rate was found to increase with an increasing loading rate.

A comparison between the method based on linear elastic fracture mechanics and the J-integral approach for the evaluation of the cohesive properties of an epoxy adhesive is presented in Biel et al. (2012a). A stiff epoxy adhesive with a nominal thickness of 1 mm was tested, as well as a soft polyurethane based adhesive with a nominal thickness of 3 mm. Both adhesives were evaluated using the two methods. Whereas a good agreement between the two methods was found for the thin adhesive, the differences found were larger for the polyurethane adhesive. This result showed well that the method based on linear fracture mechanics was invalid for the nonlinear material behaviour of polyurethane.

The influence of the layer thickness on the cohesive properties of a stiff epoxy adhesive was investigated in Marzi et al. (2011). Different layer thickness from 0.2 mm-4 mm have been tested. An unstable crack growth was observed with the most flexible adhesive layer, i.e. the adhesive with 4 mm layer thickness. These curves were cut at the first sign of instability. Unstable crack growth means that the fracture energy is not fully consumed at the crack tip before the crack propagates. This leads to lower fracture energies, but the difference is not expected to be large. The specimens used were not pre-cut, neither using a razor blade nor a sharp PTFE inlay, since crack onset at the interface of the adherend was judged of larger engineering interest as crack propagation. The test results of the different DCB test were compared to specimens produced from bulk material, i.e. without adherends. The critical energy release rate was found to be strongly dependent on the adhesive thickness. A plateau was reached for 1 mm, after which the values were decreasing again. Unlike for the thick adhesive layers, the results between the linear elastic fracture mechanics and the J-integral approach do not differ for thin adhesive layers. It is assumed that thick adhesive layers violate the assumption of a rigid adhesive in the linear elastic fracture mechanics approach. The results for the critical energy release rate of the bulk specimens were found to be significantly higher. It is assumed that this is due to the different stress conditions in the specimens. Whereas a plane stress condition dominates in the bulk specimen, the DCB specimen rather shows a plane strain condition.

The effect of the adhesive thickness on the cohesive properties was investigated in Banea et al. (2015) as well for a two-component structural polyurethane adhesive with Young's modulus of 2530 MPa. The layer thickness was varied from 0.2 mm to 2 mm. The evaluation has been done using the J-integral approach. The critical energy release rate was found to increase with the layer thickness, as opposed to the lap shear strength. For the thick layers, the increase of the critical energy release rate was less pronounced. It is assumed that the values reach a constant plateau corresponding to the critical energy release rate of bulk material. Unlike as in Marzi et al. (2011), a sharp pre-crack was inserted at mid-thickness in the adhesive using a razor blade. Similar investigations were carried out by Campilho et al. (2015). A polyurethane-based adhesive (Young's modulus of approximately 500 MPa) was tested with DCB specimens of different adhesive layers (from 0.1 to 2 mm). The critical energy release rate in peel was found to increase almost linearly with the adhesive thickness.

The effect of the lateral free edges was investigated in Biel et al. (2012b) for a thick polyurethane based adhesive (Young's modulus 31.9 MPa) with a constant layer thickness of 3 mm. Three different joint widths have been tested: 10.6 mm, 25.6 mm and 40.6 mm. The

fracture energy was found to be almost independent of the joint width with values of 11.8 kN/m for the narrow specimens to 12.9 kN/m for the large specimens. Concerning the maximum traction, it has been found to increase with the joint width (from 5 MPa to 7 MPa).

In Banea et al. (2010), DCB tests have been performed on a thin (adhesive layer thickness of 1 mm) room temperature moisture curing silicone at different temperatures. The adhesive engineering tensile strength showed a value of 2.6 MPa at 400% elongation. A pre-crack has been inserted in the adhesive layer at mid-thickness and the tests have been evaluated using the J-integral concept. It has been found that the cohesive properties were temperature dependent. At 100 °C, the peak stress decreased with an increasing crack opening displacement compared to the results at room temperature. At 200 °C, both the peak stress value and the crack opening displacement were found to be significantly lower than at room temperature. At room temperature a value of 2.73 kJ/m^2 was found for the mode I critical energy release rate with a maximum cohesive strength of 2.08 MPa at an end-opening of 2.12 mm.

4 Experimental investigations and Finite Element simulations

4.1 Standard experimental investigations on bulk material

4.1.1 Uniaxial tensile tests

Uniaxial tensile tests on Dow Corning® 993 structural silicone sealant (Dow Corning Corporation, 2001) are presented. These tests have been subject to the master thesis of Staudt (2013) and some results have been published in Staudt et al. (2017). In the original work, several parameters of influence were investigated. Here, only the tensile stress and strain at failure for a quasi-static loading are considered. In addition, the uniaxial stress-strain curve is used to characterise the selected hyperelastic material model of the sealant.

i Specimens and test setup

In order to evaluate the material properties in uniaxial tension of a material, so-called *dumbbell* or *dog-bone* shaped specimens, are typically used. For the silicone sealant, specimens according to ASTM D412 (2013) have been produced in two steps. After a sheet of nominal thickness of 2 mm was poured on a polyethylene foil, the specimens were stored for one week, before the final samples were punched out using an appropriated punching tool. The specimens were stored in controlled conditions after the production. The geometry of the specimens is shown in figure 4.1a.

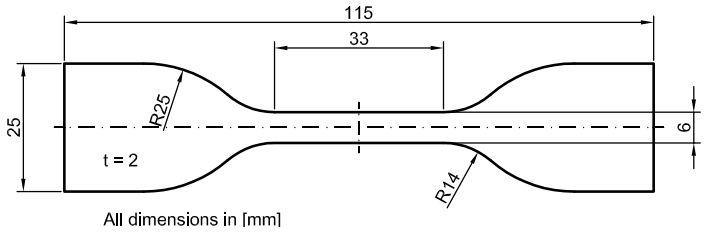

(a) Dimensions in mm of the tensile test specimen

(b) Picture of the tensile test specimen

Figure 4.1: Uniaxial tensile test specimen according to ASTM D412 (2013)

In total, a number of 5 specimens was tested for the considered test series at low velocities.

Details about the manufacturing process can be found in annex B. The material behaviour is assumed to be homogeneous, isotropic and independent regarding the manufacturing and curing conditions.

The tests have been performed using a tensile testing machine with electronic drive and a capacity of 50 kN, shown in figure 4.2a, in an air-conditioned laboratory with 23 °C and 50 % relative humidity. Due to the soft material and the small cross sectional area, only small forces were expected. Therefore, an additional external load cell with a maximum capacity of 500 N was used, in order to record values with high accuracy. The loading rate was set to 6 mm/min.

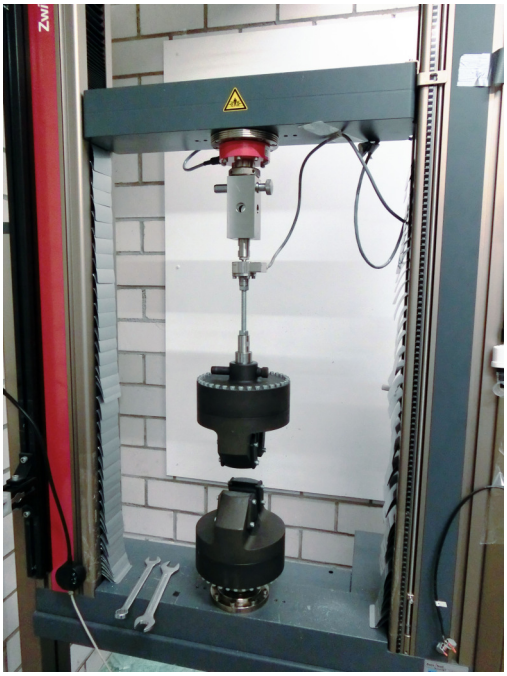

(a) 50 kN Zwick tensile testing machine

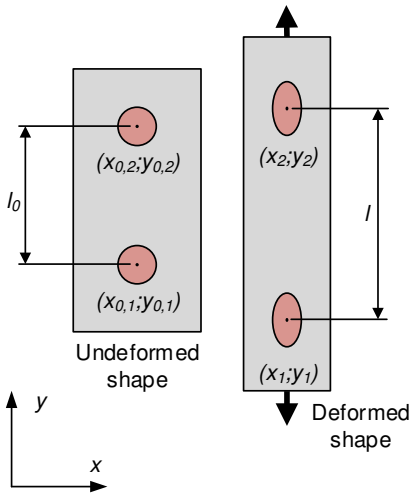

(b) Video-extensometry

Figure 4.2: Test setup and measurement method

The deformations of the region with parallel edges of the specimens were measured locally on the surface using video-extensometry. For the video-extensometry, the deformations of red marks, which are shown on the dumbbell specimens (see figure 4.1b), were measured by analysing each frame of the video file with a *Matlab*® script. In this script, for each video frame, the parts of the picture, which fulfil a given condition concerning the colour, as "red" for example, are selected. For each set of red pixels, the centre is determined and its position within the considered picture is saved. This method is visualised in figure 4.2b and the algorithm is described in detail in Franz (2015). Finally, with the assumption of a homogeneous strain distribution within the region with parallel edges, the engineering strains are calculated for each time step using

$$\varepsilon_{\mathrm{e,l}} = \frac{\Delta l}{l_0} = \frac{l - l_0}{l_0} = \frac{y_2 - y_1}{y_{0,2} - y_{0,1}} - 1 \tag{4.1}$$

and the obtained strain channel was synchronised with the force channel from the load cell. In equation 4.1, $\varepsilon_{\mathrm{e,l}}$ is the longitudinal engineering strain at the considered time step, l_0 the initial distance between the two red marks for the unloaded configuration, l the distance between

the two red marks for the deformed shape and y_j the ordinate of the red point's (j) centre at the respective time step. The initial ordinates of the undeformed points are denoted by $y_{0,j}$. The red points had a diameter of 2 mm and a thickness of less than 0.5 mm. One-component neutral curing silicone sealant with red colour was used for this purpose, since no other material adhered on the silicone specimens and was able to perform engineering strains larger than 200 %. Due to their low thickness and the soft material behaviour of the sealant used, the influence of these red marks on the stress-strain behaviour was judged negligible.

The engineering strain, measured locally using video-extensometry, is given in figure 4.3. An almost linear curve can be observed. One representative specimen was selected. The engineering strain rate is obtained by evaluating the slope of the curve, which is a linear function of the time.

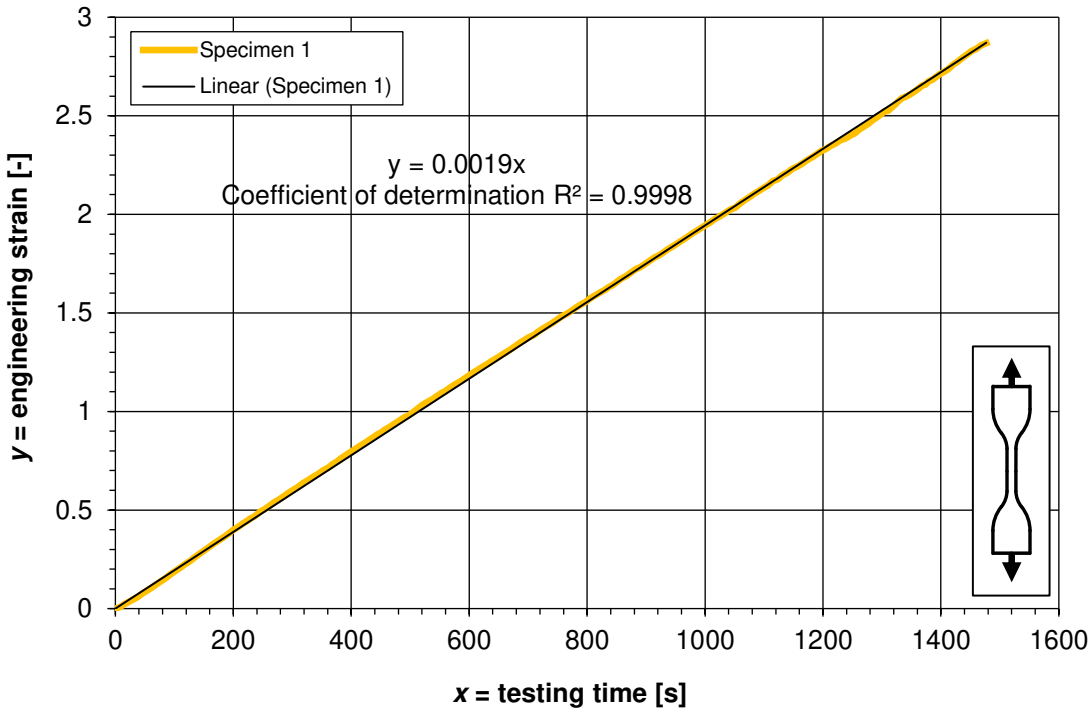

Figure 4.3: Average engineering strain rate measured in the uniaxial tensile test

ii Test results

Figure 4.4 shows the engineering stress-strain relationship of the test specimens and the numerically obtained stress-strain curve, which will be detailed in the following section. A very low scattering regarding the stress-strain curve was obtained. The specimens failed after showing a uniform extension without visible local necking of the material at high strains. As displayed in figure 4.5, failure occurred in the region of parallel edges without being influenced by the location of the red marks. The specimens recovered their initial shape. No significant remaining deformation was recorded. The crack surfaces did not show any air voids or defects.

The stresses and strains at failure recorded in the uniaxial tensile tests are given in table 4.1.

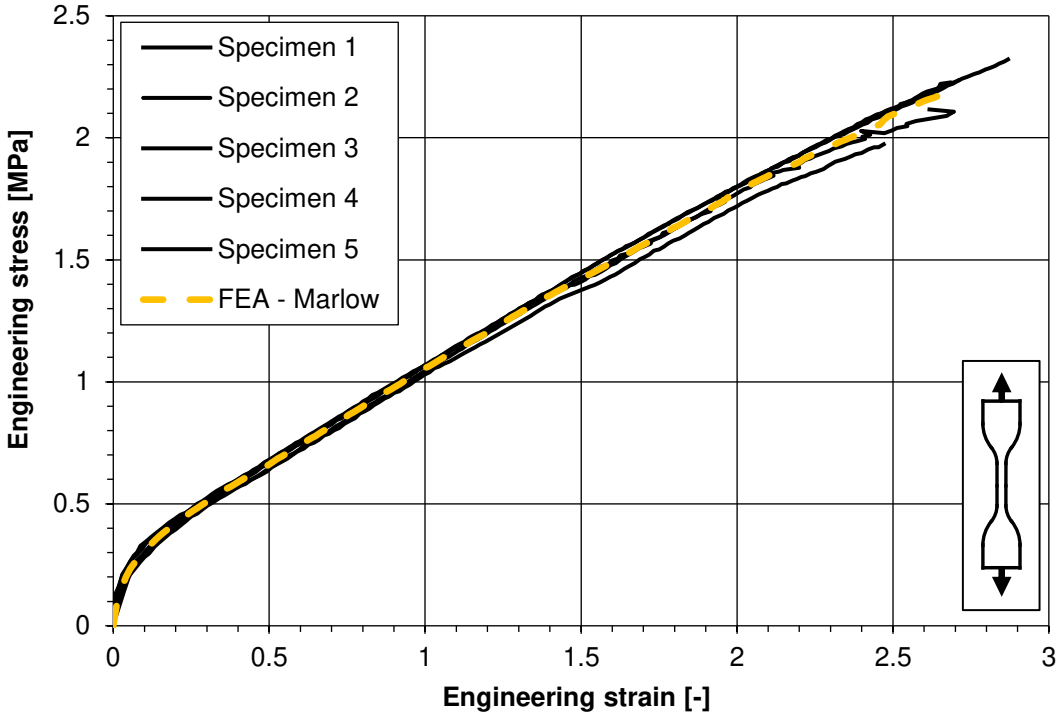

Figure 4.4: Results of the uniaxial tension tests

The values of the engineering stresses and strains at failure are listed for the 5 specimens tested.

Table 4.1: Stresses and strains at failure for the uniaxial tensile test

Specimen	Engineering stress [MPa]	Engineering strain [-]	True strain [-]
Specimen 1	2.321	2.869	1.353
Specimen 2	2.227	2.686	1.304
Specimen 3	2.235	2.709	1.311
Specimen 4	2.116	2.696	1.307
Specimen 5	1.973	2.470	1.244
Mean	2.174	2.686	1.304
Standard deviation	0.134	0.142	0.039

iii Numerical simulation

The engineering stress-strain curve in tension has been selected to characterise the Marlow (2003) hyperelastic material law. In order to verify the numerical model, the uniaxial tensile tests have been reproduced using the commercial Finite Element software code *ABAQUS*® (Dassault Systèmes, 2014). The silicone sealant was modelled using the *Marlow* hyperelastic material law, as detailed in section 3.3.3. 20 node fully integrated hybrid solid elements (C3D20H) were used in the geometrical nonlinear analysis. Convergent results were obtained even for a coarse mesh.

Figure 4.5: Failure pattern of the uniaxial tensile test specimens

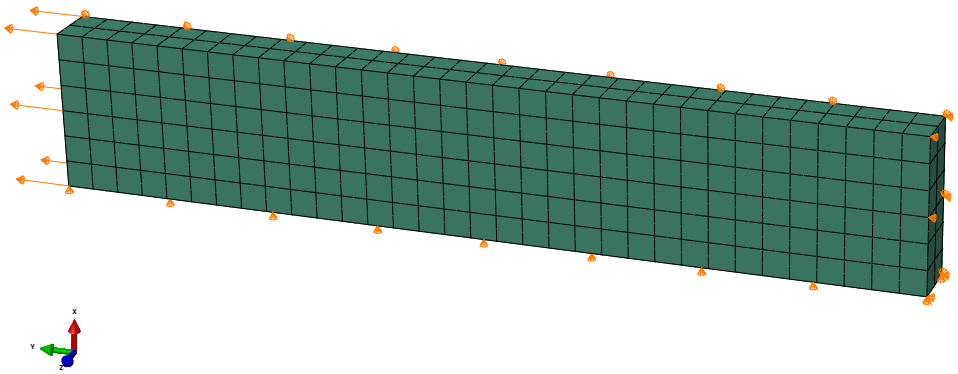

Figure 4.6: Numerical model of the uniaxial tension test

For the numerical model, only the region with parallel edges was modelled since the deformations have been measured in this area. Symmetry in all directions was used as shown in figure 4.6. An excellent agreement between the numerical and the experimental stress-strain curves was obtained (figure 4.4), since the experimental stress-strain relation in uniaxial tension was used to characterise the material law. With the uniform loading and boundary conditions, a Finite Element model consisting of only one element would have been sufficient as well.

4.1.2 Uniaxial compression tests

Uniaxial compression tests were carried out on Dow Corning® 993 structural silicone sealant, in order to obtain the material response and the failure load in uniaxial compression. The selected specimens consisted of small silicone cylinders, according to ISO 7743 (2008). Unlike as for the tensile and shear specimens, a remaining deformation was measured after unloading the compression test specimens. This remaining deformation even occurs for small applied deformations. Failure in terms of rupture of the test specimens was only observed for deformations, which are much higher than the deformations at failure onset. The permanent

deformation is assumed to be associated with damage of the material. Therefore, the failure initiation point is referred to as the load or displacement, for which the amount of remaining or plastic deformation significantly increases.

i Specimens and test setup

As mentioned before, the specimens consist of small silicone cylinders (shown in figure 4.7b) with a diameter of 12 mm and a height of 12 mm. The silicone sealant used was Dow Corning® 993 structural silicone adhesive (Dow Corning Corporation, 2001). The adhesive has been poured using a professional mixing plant. After pouring of the silicone, the specimens have been stored at ambient conditions at the manufacturer. Detailed information about the boundary conditions of the manufacturing process can be found in annex B. For the pouring of the sealant, a mould, shown in figure 4.7a, made of polytetrafluoroethylene (PTFE), has been manufactured. It is composed of a block of PTFE with the cavities for the specimens and a cover with holes for pouring the silicone. The same manufacturing process, but with different geometry has already been presented in Dias (2013). The material behaviour of the specimens is assumed to be homogeneous, isotropic and independent regarding the manufacturing conditions.

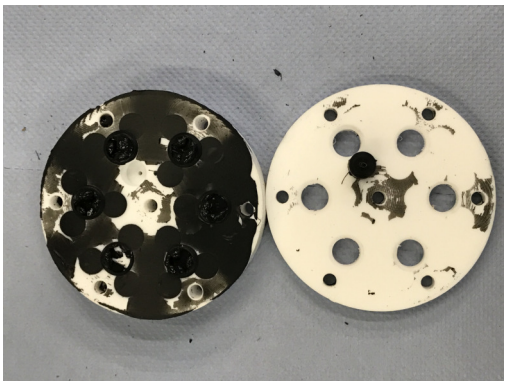

(a) PTFE mould used

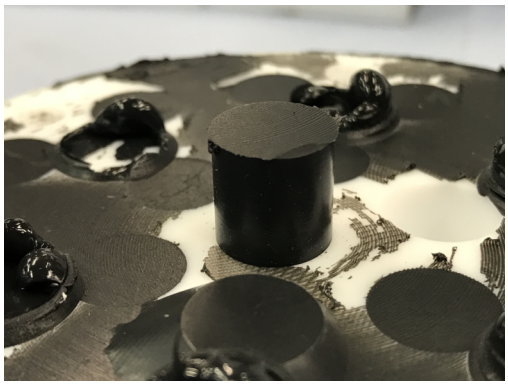

(b) Compression test specimen

Figure 4.7: Compression test specimen

A 10 kN hydraulic tensile testing machine was used in a displacement controlled mode. The test setup consisted of two thick polished plates, as shown in figure 4.8a. A load cell was inserted between the upper plate and the transversal beam of the test frame. The relative displacement between the two compression plates was measured, using two linear inductive displacement transducers, fixed on the upper plate with magnetic stands, as shown in figure 4.8b. The tests have been carried out under ambient conditions. Due to the interdisciplinary use of the laboratory, the conditions could not be maintained at a constant level. Since these variations were small and since the sealant exhibits stable properties over a wide temperature range, the effect of these conditions was judged negligible.

Preliminary tests have shown that friction between the compression plates and the specimen can be reduced using lubricant, but not be fully eliminated. As a lubricant is supposed to affect the recorded load-displacement behaviour, it was not used for the tests. The loading speed was not chosen in accordance with ISO 7743 (2008). It was determined in a way to obtain the same average engineering strain rate in load direction, as for the uniaxial tensile

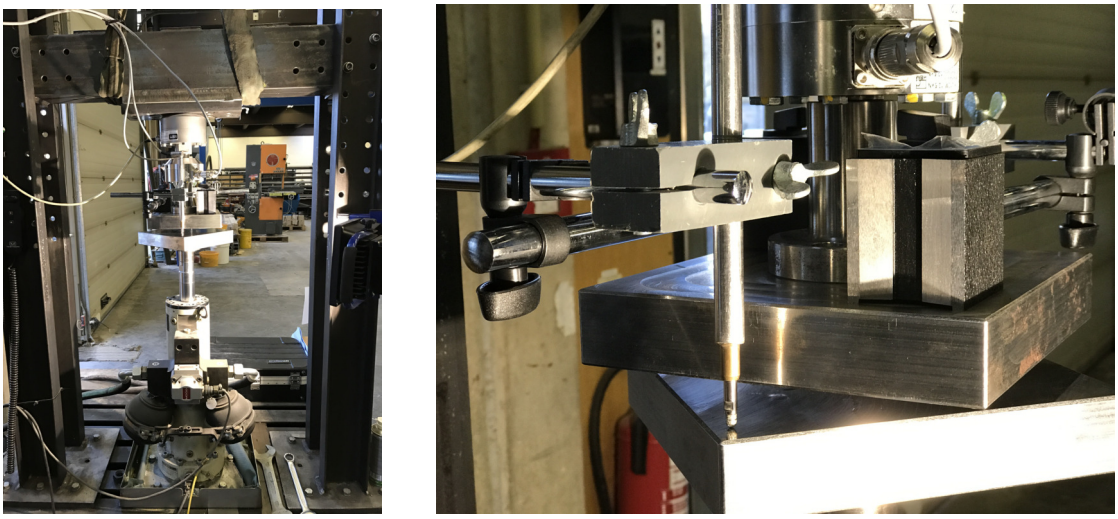

(a) Compression test setup

(b) Detailed view on the compression test setup

Figure 4.8: Compression test setup

test. Thus,

$$v_{\mathrm{UC}} = \dot{\varepsilon}_{\mathrm{e,UC}}\, h_{\mathrm{UC}} = \dot{\varepsilon}_{\mathrm{e,UT}}\, h_{\mathrm{UC}}. \tag{4.2}$$

In equation 4.2, v_{UC} is the average loading rate in uniaxial compression, $\dot{\varepsilon}_{\mathrm{e,UT}}$ the strain rate measured in the uniaxial tensile tests and h_{UC} the thickness of the compression specimen. With a strain rate of 0.002 s^{-1}, measured in the uniaxial tensile tests (cf. figure 4.3), a loading rate of 1.44 mm/min is obtained for the compression test. The determination of the loading rate according to the principle of constant energy input, described in Scherer (2014) and applied in Drass et al. (2016), was not used, since a very small value was obtained for the loading rate, leading to tests of about 1 hour.

Table 4.2: Conducted compression tests series

Test series	Test routine
UC-DC-17-1.1 to 1.3	Load specimen in displacement control to 90% engineering compression strain.
UC-DC-17-2.1 to 2.3	Load specimen in displacement control to 90% engineering compression strain in steps of 10 %. Unloading after each step and measuring of the remaining height.
UC-DC-17-3.1 to 3.5	Load specimen in displacement control to 5% engineering compression strain, unload and reload to a defined strain.

Three different test series have been conducted. Table 4.2 gives an overview on the defined test routines. In series 1 (3 specimens), the specimens have been loaded in displacement control until 90% applied engineering compression strain in one step. As mentioned before, the rupture of the specimens was not used as a failure initiation point, but the load at which a remaining deformation strongly increased. In order to determine this point, the specimens of series 2 (3 specimens) were loaded (in displacement control) in steps of 10% engineering compression strain. After each load step, the specimens were unloaded and their dimensions

(a) Thickness gauge to determine the remaining thickness of a specimen

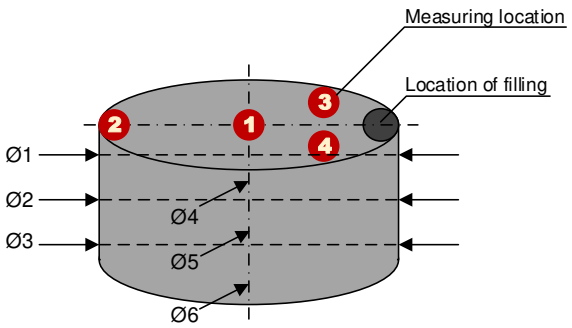

(b) Measuring points for the specimens

Figure 4.9: Measuring the height of a compression test specimen

immediately measured using the thickness gauge shown in figure 4.9a. Finally, in test series 3 (5 specimens), the specimens were loaded in displacement control to a defined level of compression strain. The remaining compression strain has been measured as well for these specimens.

The definition of zero displacement is not straightforward, since imperfections lead to some difficulties in the interpretation of the test start. In fact, it is not possible to precisely adjust the tensile testing machine to a level, where the gap between the machine and the specimen is closed, but no force on the specimen is applied. Figure 4.10 shows the stress-strain curve in compression for very low strains.

In figure 4.10, the curve starts almost horizontally, which shows that a displacement of the machine is performed without being in contact with the material. Once the gap between the rigid plate and the specimen is completely closed, the force increases significantly. In order to define a suitable correction procedure for the stress-strain data, the slope of the curve at the origin is considered. For the tensile and compression curves, the slopes of the curves at the origin must be equal. From this consideration, the compression curve is translated horizontally up to the point, where the tangent at the origin of the tensile part is coincident with the tangent at the origin of the compression part. In other words, the strain is modified as

$$\varepsilon_{\mathrm{corr}} = \varepsilon_{\mathrm{raw}} + \Delta\varepsilon. \tag{4.3}$$

In equation 4.3, $\varepsilon_{\mathrm{corr}}$ is the corrected strain, $\varepsilon_{\mathrm{raw}}$ the strain calculated from the raw data and $\Delta\varepsilon$ the defined offset. The stresses remain unchanged. The strains $\varepsilon_{\mathrm{corr}} > 0$ are not considered for further analysis. The part of the compression curve, where the slope changes

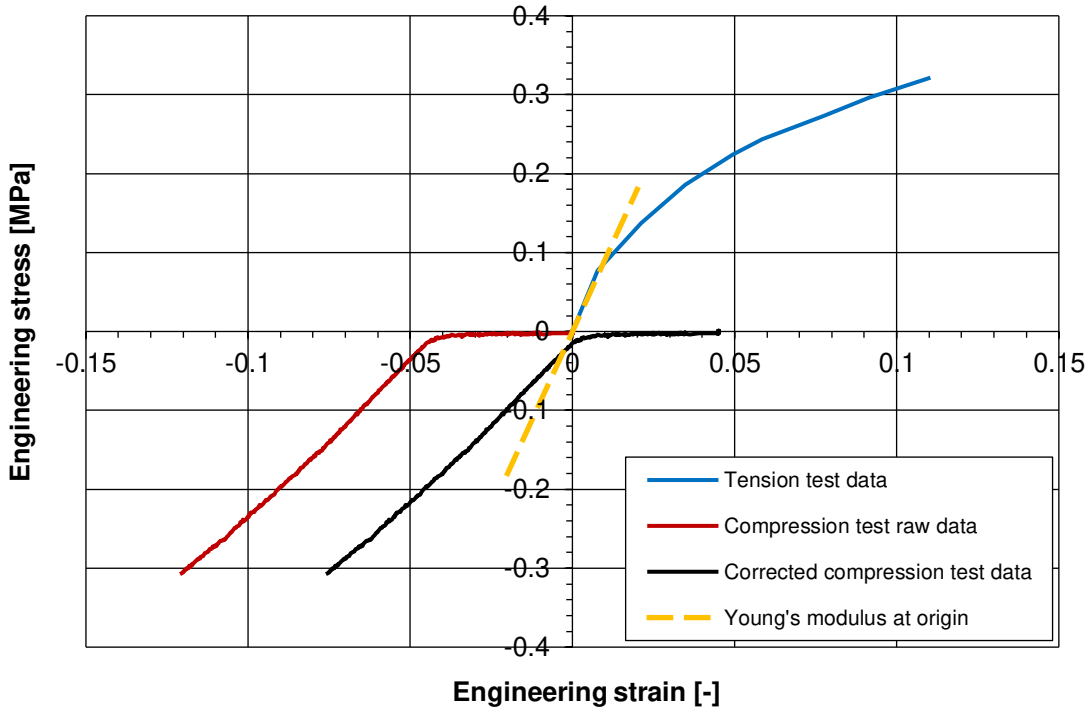

Figure 4.10: Comparison of the slopes at the origin of the engineering stress-strain curves in tension and compression

from almost horizontal to the real material response might be replaced by a linear connection with the origin.

ii Test results

The engineering stress-strain curves in compression of the test series UC-DC-17-1 are displayed in figure 4.11. The curves exhibit the typical asymptotic behaviour for strains approaching 100% engineering compression strain. The specimens were loaded up to 90% engineering compression strain. No failure in terms of rupture of the specimens was observed at this point.

Figure 4.12 gives the engineering stress-strain relationship for the specimen UC-DC-17-2.2, which was loaded in steps of 10% engineering compression strain. Additionally, the curve for a specimen loaded to 90% engineering compression strain in one step (referred to as *"compression test"*) is given in the same diagram. The specimen, which was unloaded for multiple times, clearly shows the *Mullins* effect, discussed in section 3.1. Once the specimen is compressed beyond the preloaded range, it follows the initial or *virgin* curve. For clarity reasons, the unloading paths are not displayed. The complete set of test data can be found in annex A.

After each load step, the specimens were unloaded and the dimensions measured, as described in the previous paragraph. Special focus was put on the specimens' height. For

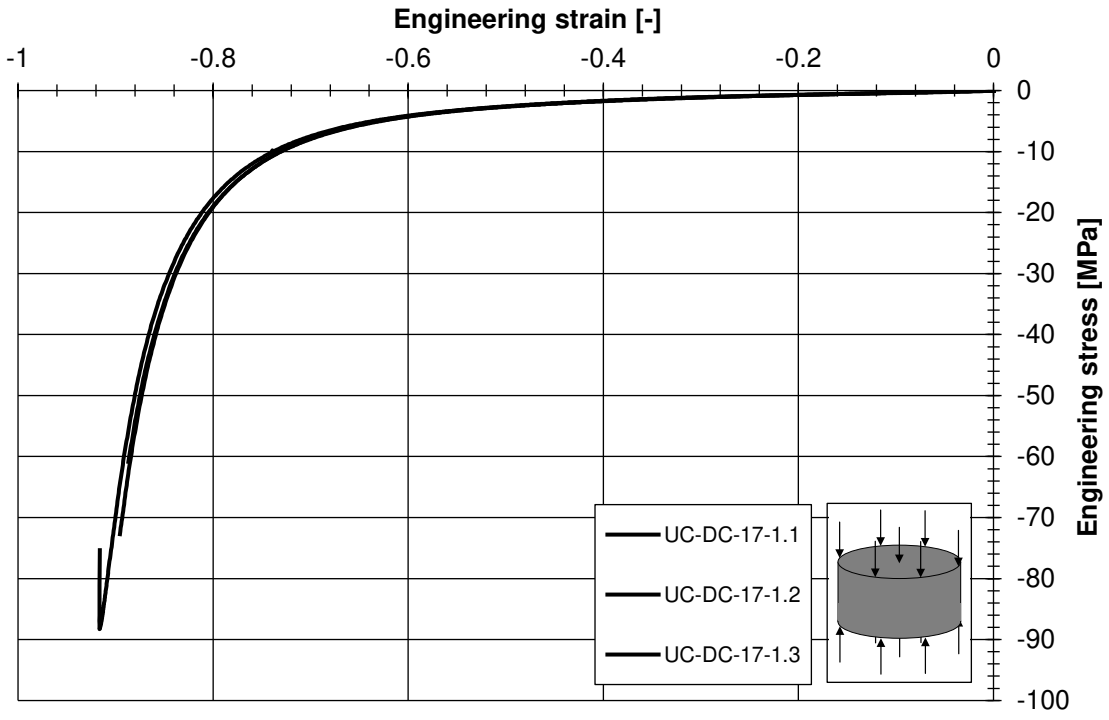

Figure 4.11: Results of the compression test series UC-DC-17-1

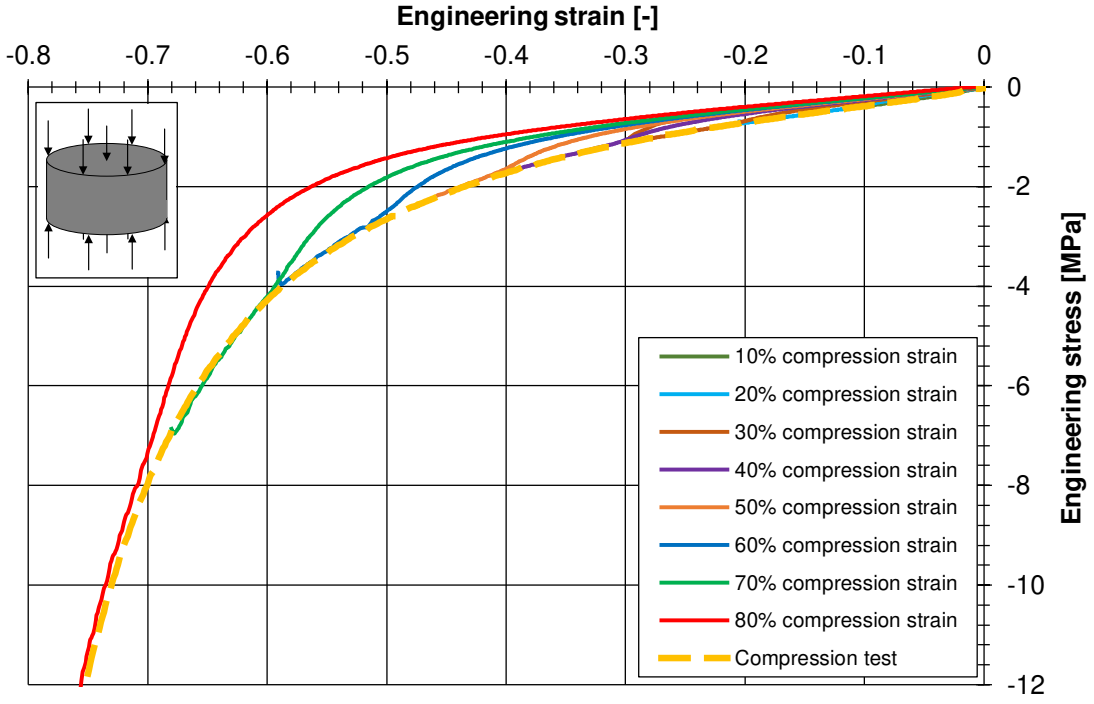

Figure 4.12: Engineering compression stress-strain curve

each load step, the remaining engineering compression strain, which is defined as

$$\varepsilon_{\mathrm{r,UC}} = \frac{\Delta h}{h_{\mathrm{UC,0}}} = \frac{h_{\mathrm{UC}} - h_{\mathrm{UC,0}}}{h_{\mathrm{UC,0}}}, \tag{4.4}$$

has been determined. In equation 4.4, $\varepsilon_{\mathrm{r,UC}}$ is the remaining engineering compression strain at a given applied compression strain, $h_{\mathrm{UC,0}}$ the initial height of the specimen and h_{UC} the residual height of the specimen after unloading.

In figure 4.13, the remaining compression strain is plotted against the applied compression strain. Even for small applied deformations, a remaining deformation is recorded. This observation is attributed to the *Mullins* effect. In Dorfmann and Ogden (2003), a particle-reinforced rubber was investigated regarding the *Mullins* effect. A residual strain was detected, which linearly increased with the applied tensile elongation. For the investigated structural silicone sealant, the curves of remaining strain versus applied compression strain exhibit a linear behaviour up to an applied engineering compression strain of 60%. The linear regression of the curves between 0% and 60% applied compression strains was plotted and a very good coefficient of determination of more than 98% was found. Starting from 60% imposed engineering compression strain, the remaining deformation was found to strongly increase. However, no failure in terms of visible cracks was observed. This strong increase of the remaining deformation of the specimens is interpreted as an onset of significant internal damage, occurring in parallel to the observed residual deformation due to the *Mullins* effect.

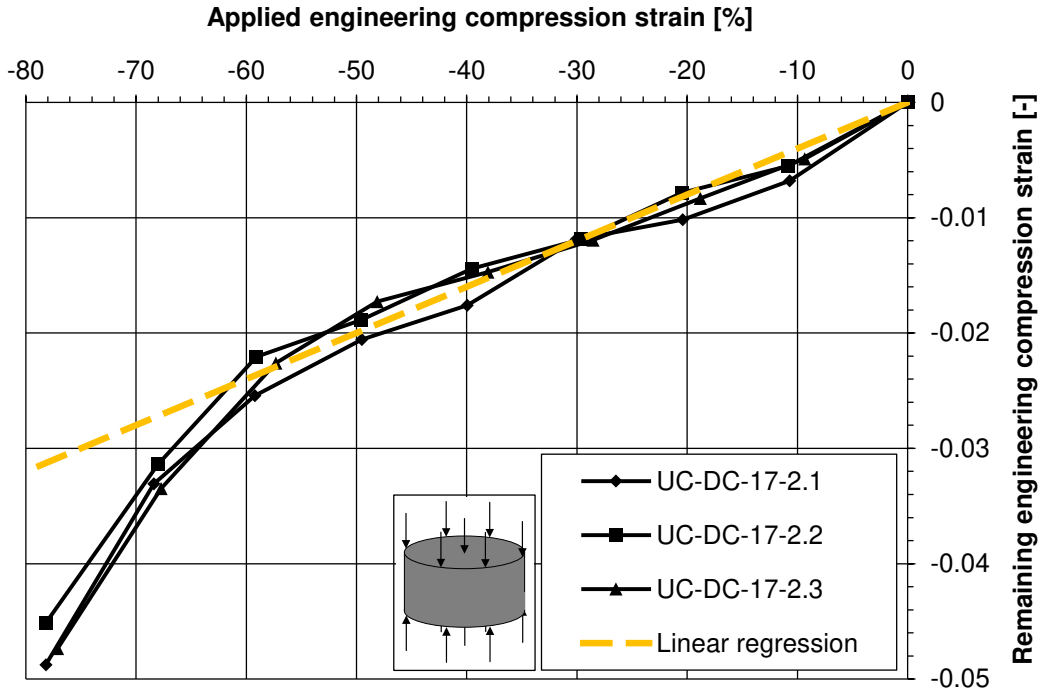

Figure 4.13: Remaining compression strain

Figure 4.14 shows a specimen before, during the test between the two compression plates and after unloading. The restrained lateral dilatation due to friction is clearly visible in figure 4.14b. The unloaded specimen has no longer a cylindrical shape, but the shape of a wine barrel, as the diameter of at mid-height is larger than the diameter at the top and bottom face (see figure 4.14c). Some specimens were cut along the vertical axis to check if cracks or cavities have developed, but no visible signs have been detected. Figure 4.14d shows specimen UC-DC-17-2.3 (loaded up to -85.9% engineering strain). The cut surface is smooth and free of visible defects.

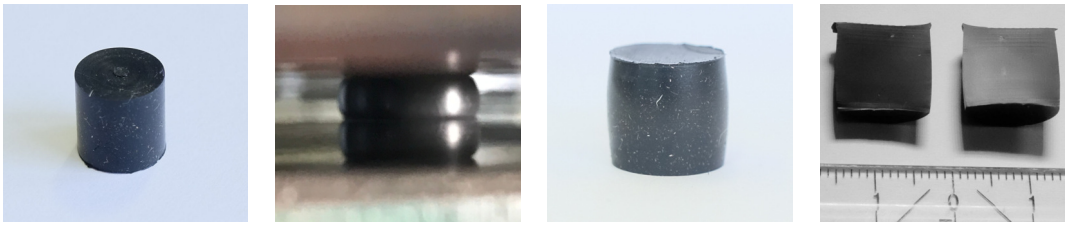

(a) Before test - initial shape

(b) During test - deformed shape

(c) After test

(d) Cut specimen

Figure 4.14: Shape of a compression test specimen

In order to check if the remaining deformation recovers after a certain time, the heights of the specimens of the test series UC-DC-17-2 and UC-DC-17-3 were measured once again 6 months after the test. Figure 4.15 shows the records of these measurements. The initial height of the unloaded specimens, the remaining height immediately after the test and after 6 months of storage at ambient conditions are given. At the horizontal axis of figure 4.15, the applied engineering compression strain is displayed.

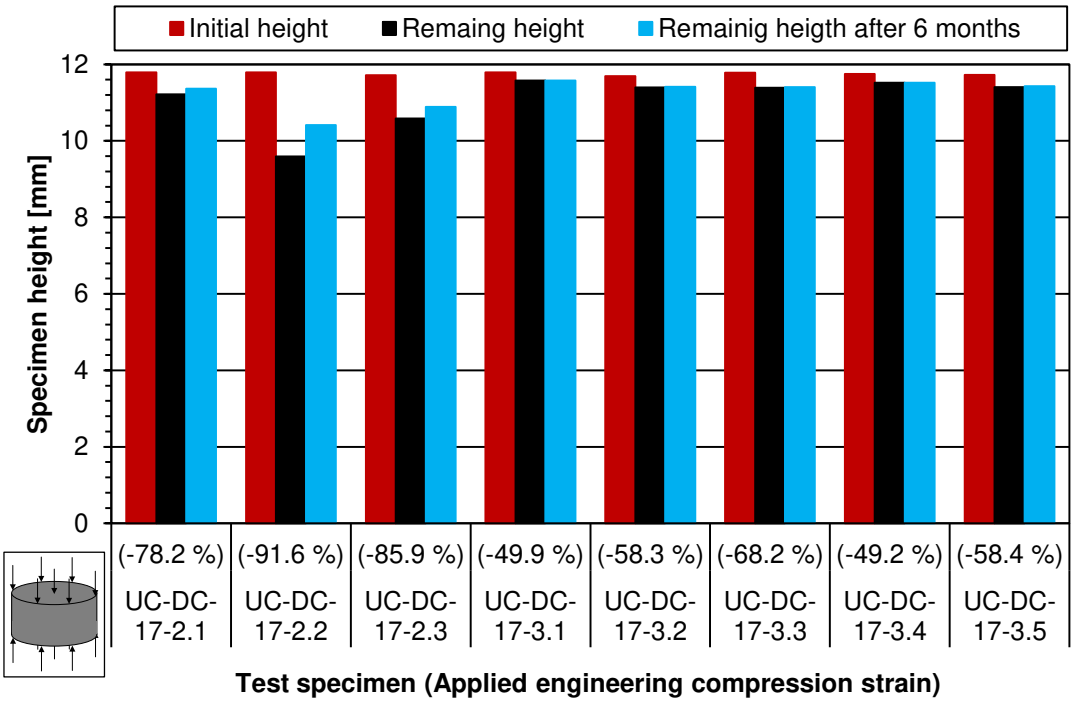

Figure 4.15: Remaining compression strain measured after 6 months

Only small recovery of the remaining deformation was recorded. For the specimens loaded up to 70% engineering compression strain, the residual height increased by less than 0.2%, compared to the measurement performed immediately after the test. For the specimens loaded beyond 80% engineering compression strain, the recovery was more pronounced, the residual height increased by 1.3% to 8.5% compared to the measurement, carried out immediately after the test. However, although the values for the residual strain slightly change considering the measurements carried out 6 months after the tests, the significant increase of the residual deformation, displayed in figure 4.13, can still be observed at 60% applied

engineering compression strain.

iii Analytical solution for the strain distribution of a solid under compression

In this section, the analytical solution for the strain distribution in a cylindrical solid, subjected to uniaxial compression is given. The material of the solid is assumed isotropic, fully elastic and incompressible. The boundary conditions are given in figure 4.16. The vertical deformation of the solid is supposed to be uniform. The solid is free to deform in horizontal directions, no restraining force as friction is considered. The considered solid in its initial and deformed shape is shown in figure 4.16.

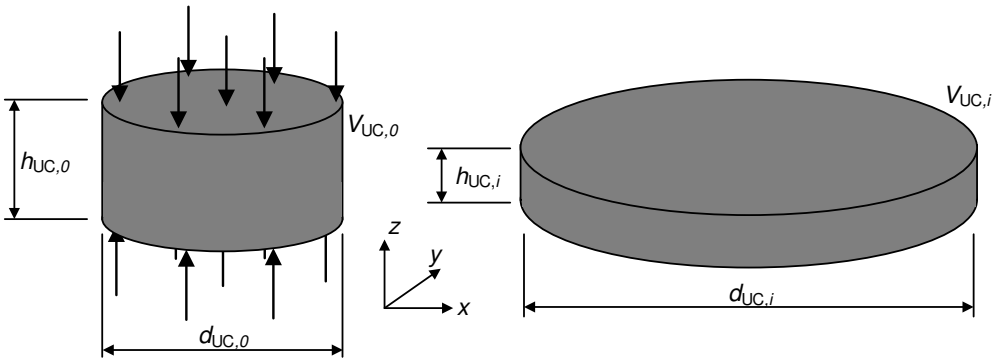

Figure 4.16: Initial and deformed shaped of a cylinder under uniform compression

The volumes of the solids in the initial shape ($V_{\mathrm{UC},0} = \pi/4\ d_{\mathrm{UC},0}^2\ h_{\mathrm{UC},0}$) and in the deformed shape ($V_{\mathrm{UC}} = \pi/4\ d_{\mathrm{UC}}^2\ h_{\mathrm{UC}}$) are considered. Since the material is assumed incompressible ($\nu = 0.5$), the volume of the cylinder stays constant. The deformed height of the solid is given as

$$h_{\mathrm{UC}} = h_{\mathrm{UC},0} + \Delta h_{\mathrm{UC}} = h_{\mathrm{UC},0} + h_{\mathrm{UC},0} \cdot \varepsilon_{\mathrm{e},z} = h_{\mathrm{UC},0} \cdot (1 + \varepsilon_{\mathrm{e},z})\,. \tag{4.5}$$

In equation 4.5, Δh_{UC} is the change of height of the cylinder between its initial and deformed shape and $\varepsilon_{\mathrm{e},z}$ is the engineering compression strain in vertical direction. Considering the equal volumes in the initial and deformed states and using equation 4.5 gives

$$\begin{aligned} &\pi\ \frac{d_{\mathrm{UC},0}^2}{4}\ h_{\mathrm{UC},0} = \pi\ \frac{d_{\mathrm{UC}}^2}{4}\ h_{\mathrm{UC},0}\ (1 + \varepsilon_{\mathrm{e},z}) \\ &\implies d_{\mathrm{UC}} = d_{\mathrm{UC},0}\ \sqrt{\frac{1}{1 + \varepsilon_{\mathrm{e},z}}}. \end{aligned} \tag{4.6}$$

The strains in x and y directions are equal due to the cylindrical shape of the solid. Considering the change of diameter and equation 4.6 gives

$$\varepsilon_{\mathrm{e},x} = \varepsilon_{e,y} = \frac{d_{\mathrm{UC}} - d_{\mathrm{UC},0}}{d_{\mathrm{UC},0}} = \sqrt{\frac{1}{1 + \varepsilon_{\mathrm{e},z}}} - 1. \tag{4.7}$$

For the evaluation of the strain magnitude (cf. equation 3.41 in section 3.4.4), the analytical expressions for the engineering strains have to be converted in true strains according equation 3.31. For the vertical strains

$$\begin{aligned}
\varepsilon_{\mathrm{e},z} &= \frac{\Delta h}{h_{\mathrm{UC},0}} \\
\varepsilon_z &= \ln\left[\frac{\Delta h}{h_{\mathrm{UC},0}} + 1\right] \\
&= \ln\left[\frac{h_{\mathrm{UC}} - h_{\mathrm{UC},0} + h_{\mathrm{UC},0}}{h_{\mathrm{UC},0}} + 1\right] \\
&= \ln\left[\frac{h_{\mathrm{UC}}}{h_{\mathrm{UC},0}}\right]
\end{aligned} \tag{4.8}$$

and for the horizontal strains

$$\begin{aligned}
\varepsilon_{\mathrm{e},x} &= \sqrt{\frac{1}{1+\varepsilon_{\mathrm{e},z}}} - 1 \\
\varepsilon_x &= \ln\left[\sqrt{\frac{1}{1+\varepsilon_{\mathrm{e},z}}} - 1 + 1\right] \\
&= \ln\left[\sqrt{\frac{1}{1+\varepsilon_{\mathrm{e},z}}}\right] \\
&= \ln\left[\sqrt{\frac{1}{1+\frac{h_{\mathrm{UC}}}{h_{\mathrm{UC},0}} - 1}}\right] \\
&= \ln\left[\sqrt{\frac{h_{\mathrm{UC},0}}{h_{\mathrm{UC}}}}\right].
\end{aligned} \tag{4.9}$$

The strains ε_x, ε_y, ε_z are at the same time the principal strains. Therefore, the strain magnitude can be computed as

$$\begin{aligned}
\varepsilon_{\mathrm{M}} &= \sqrt{\varepsilon_1^2 + \varepsilon_2^2 + \varepsilon_3^2} \\
&= \sqrt{\varepsilon_x^2 + \varepsilon_y^2 + \varepsilon_z^2} \\
&= \sqrt{2\,\varepsilon_x^2 + \varepsilon_z^2} \\
&= \sqrt{2\,\left[\ln\left(\sqrt{\frac{h_{\mathrm{UC},0}}{h_{\mathrm{UC}}}}\right)\right]^2 + \left[\ln\left(\frac{h_{\mathrm{UC}}}{h_{\mathrm{UC},0}}\right)\right]^2} \\
&= \sqrt{\frac{1}{2}\,\left[\ln\left(\frac{h_{\mathrm{UC},0}}{h_{\mathrm{UC}}}\right)\right]^2 + \left[\ln\left(\frac{h_{\mathrm{UC}}}{h_{\mathrm{UC},0}}\right)\right]^2}.
\end{aligned} \tag{4.10}$$

The relation given in equation 4.10 will be used in chapter 5.

iv Numerical simulation

The compression tests have been numerically reproduced using the commercial Finite Element software code ABAQUS® (Dassault Systèmes, 2014) in order to check, if the chosen material law, which was characterised using tensile test data, was able to describe the behaviour in compression. Moreover, the distribution of internal stresses and strains are investigated in chapter 5. The silicone sealant was modelled using the *Marlow* hyperelastic material law with the assumption of incompressible material behaviour, as described in section 3.3.3. The Finite Element model is shown in figure 4.17. 2D quadratic fully integrated hybrid CAX8H elements were used in the nonlinear axisymmetric analysis. In addition, symmetry in vertical direction was assumed. The compression plate was modelled as well and a reference point was connected with the plate using a kinematic coupling. Boundary conditions for the plate were defined on the reference point.

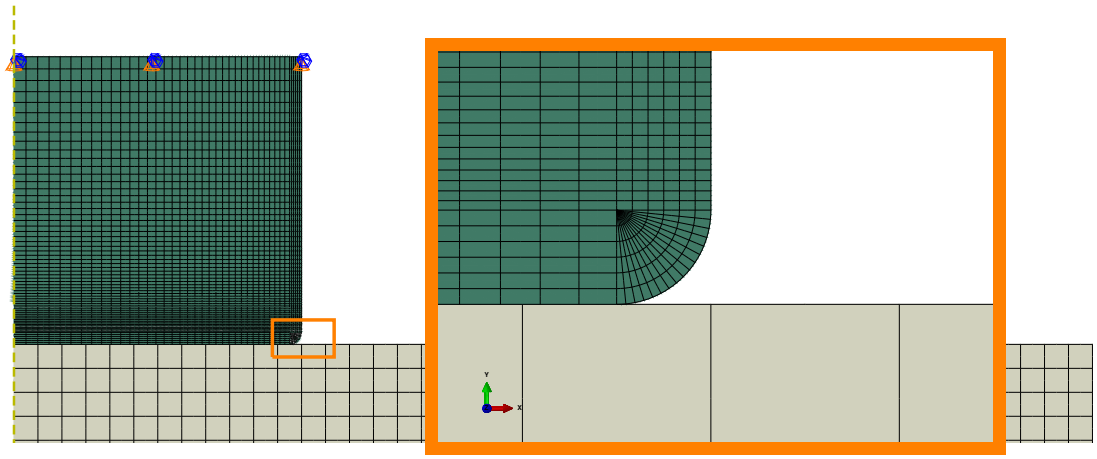

Figure 4.17: Finite Element model of the compression test specimen

Since large deformation were expected and as the lateral dilatation was restrained due to friction, the finite element at the corner between horizontal and lateral surface would be highly distorted, thus leading to an abort of the analysis. This effect was investigated in detail in the master thesis of Schwind (2016). Using a triangular mesh with special orientation or using a round were proposed as possible solutions to avoid excessive mesh distortion. For the simulation of the compression test, a rounding of 0.25 mm was inserted in the model. A preliminary numerical study showed that the size of the rounding had only minor influence on the results regarding the global force deformation behaviour. In the same way, a preliminary mesh study showed that the results concerning force deformation gave convergent results for the selected element size.

The friction formulation in tangential direction was penalty-based with the definition of a friction coefficient. In normal direction, hard contact was assumed. The friction coefficient μ was chosen between 0.05 and 0.2. In addition, frictionless and bonded behaviour between the bodies were considered. Figure 4.18 shows the comparison between the experimentally recorded engineering stress-strain curves and the results of the numerical simulation using different friction coefficients. A good agreement was found, especially for small strains. For

larger strains, a friction coefficient of 0.1 described well the experimentally recorded behaviour.

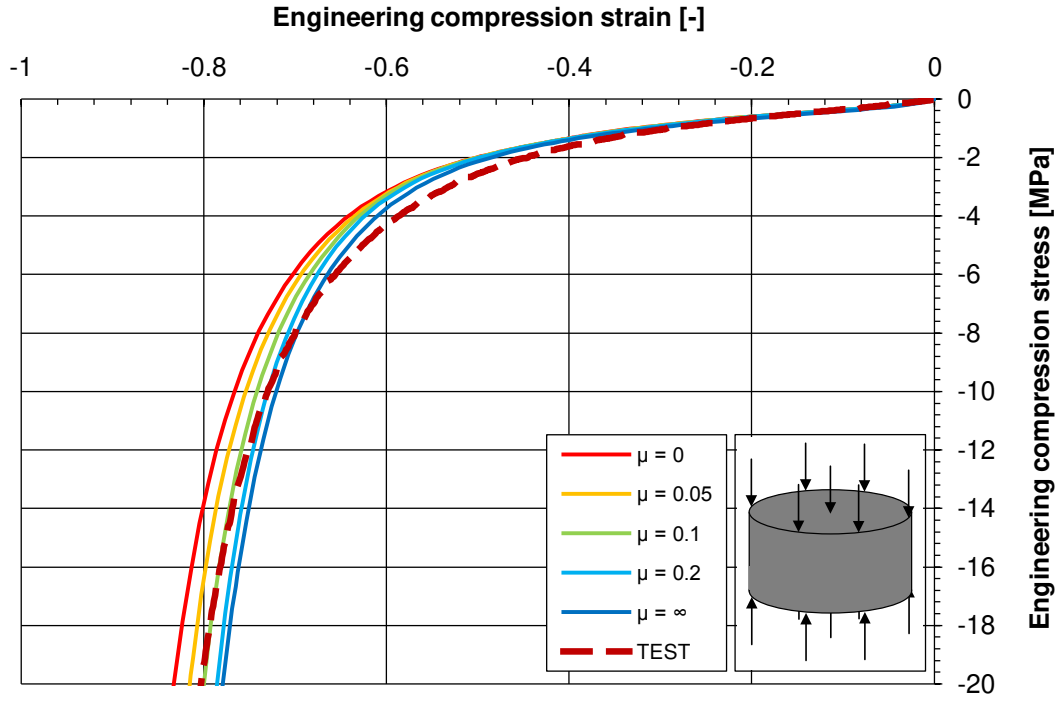

Figure 4.18: Engineering stress-strain curves from FEA for different friction coefficients

The distribution of the first principal strain is shown in figure 4.19 for an applied engineering compression strain of 60%. It is clearly visible that the lateral surfaces touch the compression plate. The maximum value for the first principal strain was found in the centre of the specimen. In figure 4.19, only one fourth of the specimen is shown due to symmetry boundary conditions in horizontal and vertical directions.

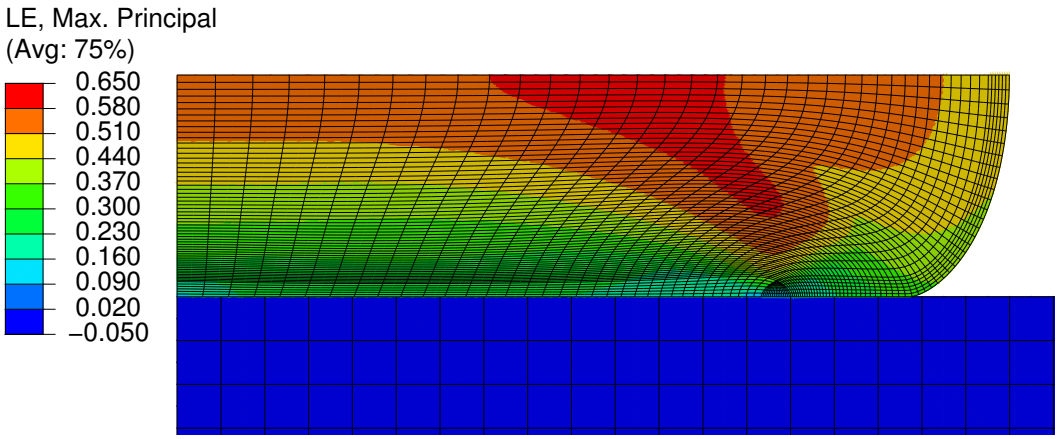

Figure 4.19: Plot of the first principal strain calculated using a Finite Element Analysis

4.2 Experimental investigations on adhesively bonded connections

4.2.1 Simple shear tests

Simple shear tests on bonded connections with Dow Corning 993® structural silicone sealant (Dow Corning Corporation, 2001) have been conducted to determine the influence of the adhesive thickness as well as the overlap length on the failure initiation load and on the force-deformation behaviour. Specimens similar to those detailed in ETAG 002 (2012) were used for these tests. Some results of this section have been published in Staudt et al. (2016).

i Specimens and investigated parameters

For the shear tests, specimens analogous to those defined in ETAG 002 (2012) and shown in figure 4.20 were chosen. These specimens consist of a linear and rectangular silicone bead between two adherends. Unlike prescribed by ETAG 002 (2012), steel adherends were used to allow a comparison with push out tests conducted in Dias (2013).

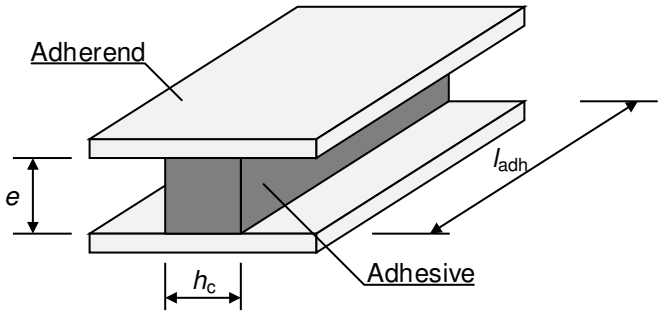

Figure 4.20: Definition of the dimensions of the simple shear specimens used - h_{c} is the bite or width, l_{adh} the length and e the thickness of the adhesive.

The definitions of length, thickness and width (or bite) are given in figure 4.20. The standard specimen as foreseen by ETAG 002 (2012) has an overlap length of 50 mm, an adhesive thickness of 12 mm and a bite of 12 mm. Apart from this geometry, specimens with half and double thickness (i.e. 6 mm and 24 mm) as well as specimens with a length of 100 mm and 200 mm were tested in addition. All the specimens show a constant bite dimension of 12 mm.

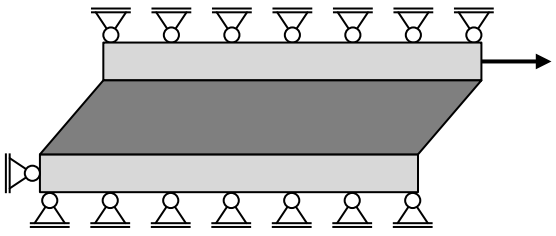

Figure 4.21: Boundary conditions of the simple shear tests

The specimens were loaded in displacement control, i.e. a constantly increasing shear displacement was applied with the boundary conditions according to figure 4.21. As a simple shear test is performed, the distance between the adherends is kept constant. Table 4.3

summarises the chosen parameter of influence in a test matrix. Two test series have been conducted. In 2015, specimens with 100 and 200 mm overlap length have been tested and in 2016, additional specimens with 100 mm overlap length and specimen with 50 mm overlap length.

Table 4.3: Investigated parameters, designation and number of specimens

Thickness e	Overlap length l_{adh}		
	50 mm	100 mm	200 mm
6 mm	-	100-6: 10	-
12 mm	50-12: 5	100-12: 14	200-12: 5
24 mm	-	100-24: 10	200-24: 5
Nomenclature: [overlap length-thickness]: number of specimens tested			

As mentioned before, the adherends were made of steel parts, which were sandblasted and ground. After these steps and close to the pouring of the silicone, the adherends were carefully cleaned using an appropriated solvent (Dow Corning® R40) and a primer (Dow Corning® 1200 OS) was applied with the two clothes method (cf. Dow Corning Corporation (2011b)). The silicone was poured within 3 hours after cleaning the adherends and applying the primer, thus respecting the requirements set by the silicone manufacturer (Dow Corning Corporation, 2011b).

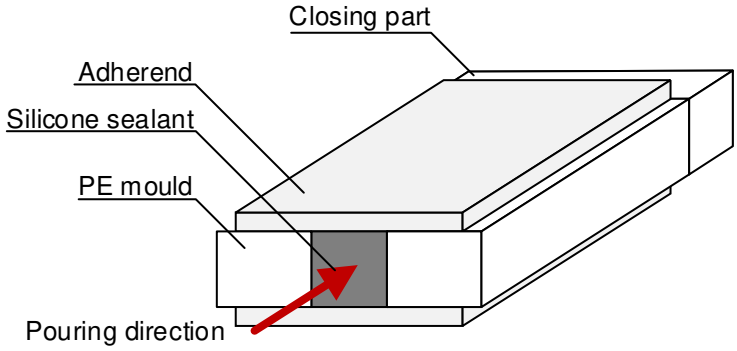

Figure 4.22: Production of the specimens for the shear tests

In the next step, the adherends were separated using a mould of polyethylene material as illustrated in figure 4.22. The adherends and the mould were fixed together with screws. The two components of the silicone sealant were mixed with a two component mixing plant. After the pouring of the silicone, the specimens were stored for 4 weeks at ambient temperature and humidity. In Staudt et al. (2016), results of 50-6 and 50-12 test series have been shown for which a different mould has been used. These specimens exhibited some flaws and defects. Therefore, in the following, these specimens are not taken into consideration for the failure load analysis.

Details about the manufacturing process can be found in annex B. In Comyn et al. (2002), the kinetics of cure and the crosslink density of a one-component silicone sealant have been investigated. The value of *Young's* modulus and the crosslink density were found to vary with the distance to the air surface. In the present investigations, the material behaviour is assumed to be homogeneous with a uniform distribution of the crosslink density and the

stiffness. Furthermore, the material is supposed to be isotropic and independent regarding the manufacturing conditions.

ii Test setup and measurement equipment

The test setup, which is shown in figure 4.23, was manufactured at the metalworking shop of the University of Luxembourg. It is composed of two parallel plates, with the left plate fixed to the 10 kN hydraulic jack and the right plate to the cross beam of the testing frame.

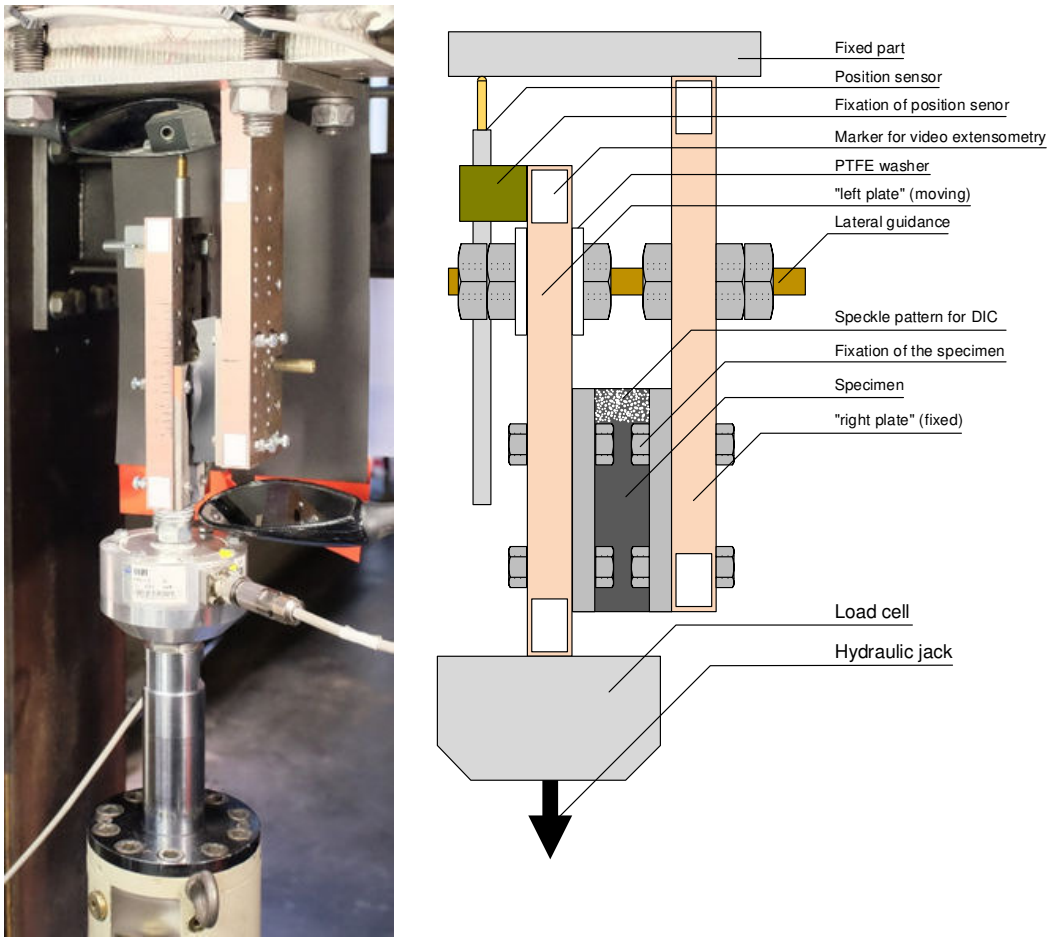

(a) Test setup

(b) Schematic view of the test setup

Figure 4.23: Test setup of the simple shear tests

In order to guarantee the boundary condition *simple shear* shown in figure 4.21, a lateral guidance consisting of a threaded rod was used. The right plate was equipped with a threaded hole and the left one with a slot. Nuts were placed at both sides of the moving plate. In order to avoid friction, washers made of PTFE were used in combination with grease. Prior and after each test series, the friction of the test setup was evaluated by running an empty test, i.e. without specimen, while measuring the force. A friction force less than 10 N was recorded, even when a horizontal force was manually applied on the moving plate. The condition of parallel movement of the two plates was checked using video-extensometry (see section 4.1.1 for further information on the method). A maximum lateral displacement of less than 0.1 mm was found for the tests.

The specimens were fixed on the plates using screws and nuts. The tests were carried out at ambient temperature. The loading rate was determined applying the principle of constant energy input, described in Scherer (2014). According to this, the shear displacement velocity can be determined as

$$\dot{\gamma}_{\mathrm{e}} = \frac{d\gamma_{\mathrm{e}}}{dt} = \frac{1}{e}\,\frac{du}{dt} = \frac{\dot{u}}{e} = \sqrt{3}\,\dot{\varepsilon}_{\mathrm{e,UT}}. \tag{4.11}$$

In equation 4.11, γ_{e} is the engineering shear strain, t the testing time, u the imposed displacement and e the thickness of the specimen. Taking into account the tensile tests at low velocity (cf. figure 4.3), a value of 1 mm/min was found for the 6 mm thickness specimens of the shear tests. According to equation 4.11, 2 mm/min are obtained for the 12 mm specimens and 4 mm/min for the 24 mm specimens.

(a) Test setup used for the simple shear tests

(b) Speckle pattern

Figure 4.24: 3D Digital Image Correlation System used for the simple shear tests

Concerning the measurement equipment, a 5 kN load cell was added between the hydraulic jack and the left plate. A displacement transducer was used to record the relative displacement between the two plates. In addition, a 3D Digital Image Correlation System consisting of two cameras was used to measure the deformations locally on the surface of the sealant. The measurement could not be performed continuously, i.e. recording one image per second for example, but for discrete steps. The cameras were placed in front of the specimen, in a way that both cameras captured the surface of interest, at which the deformations were evaluated. Figure 4.24 shows the test setup with the cameras. In addition, a strong light source was placed in front of the specimen. Prior to the measuring process, the cameras were calibrated using a chequered pattern. The relative position of the two cameras and the conversion factor from image to world units was determined with the calibration. The deformations at the surface of the specimens were measured by following the displacements of a characteristic speckle pattern on the surface of the specimens. In order to guarantee an accurate measurement, an arbitrary and stochastic black-white speckle pattern was applied on the surface of the specimens. The speckle pattern is shown as well in figure 4.24 and in

figure 4.23 for the area of interest. The speckle pattern should have a good contrast and a single speckle should be a bit larger than one pixel of the recorded image to obtain a good resolution. The speckle pattern was created using Gouache paint, mixed with water and applied using a toothbrush.

iii Test results

In total, two test series over two years have been performed. For each series, force-displacement curves were recorded for every specimen. In addition, some tests were recorded using a camera with high resolution. With these video-files, the displacement of the specimen, at which the first significant crack appeared, could be determined. For the second test series, a digital image correlation system was used to measure the displacements on a local scale.

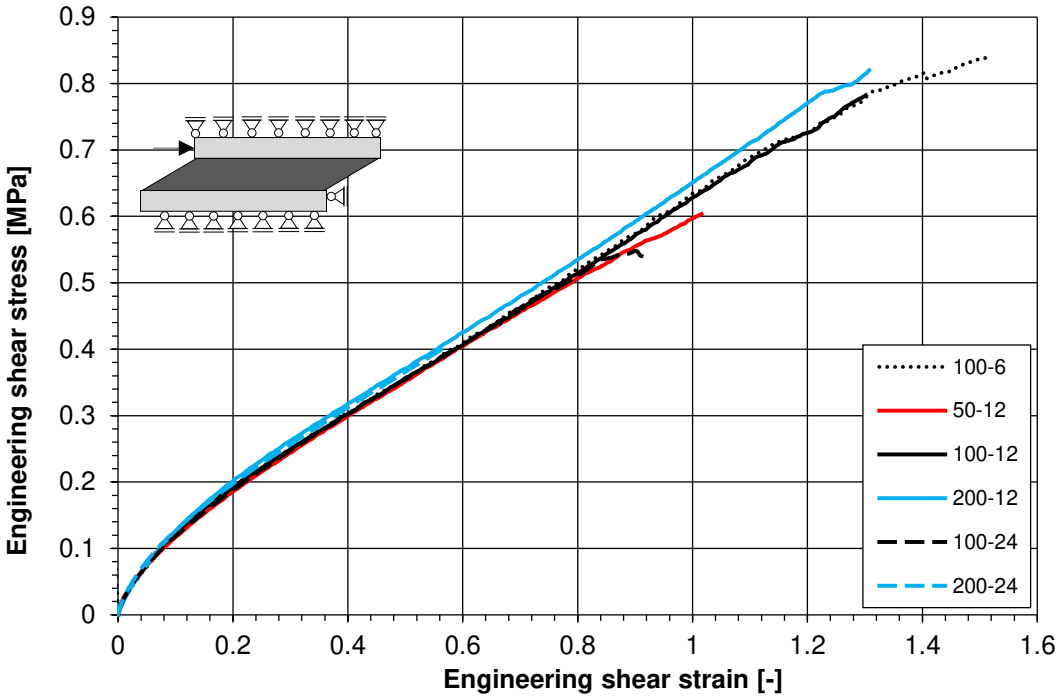

Figure 4.25: Engineering stress-strain curves of the considered test series - one average curve is shown per series.

The results of the shear tests are shown in figure 4.25, in form of engineering stress-strain curves for the first test series in 2015. The engineering shear stress is the recorded force divided by the initial cross sectional area (product of bite and overlap length) and the engineering shear strain is the ratio of applied displacement over adhesive thickness. For each specimen, the actual dimensions were measured before the test. In figure 4.25, an average curve is shown for each test series. The number of specimens for each series is given in table 4.3. The scattering of the results is in the order of magnitude of 5%-10%. The specimens tested in 2016 showed comparable behaviour. The engineering stress-strain curves in figure 4.25 are plotted until the average failure strain and failure stress observed for the respective series. All test data is given in appendix A. The failure point was defined as the appearance of a significant crack, which can be captured as a change of the slope or an offset of the force-deformation curve. The identification of the failure point will be discussed later.

As the experimental curves in figure 4.25 are coincident, it is concluded that the stress-strain relationship of the specimens is independent of the chosen overlap length and adhesive layer thickness, except for the failure point, which will be discussed later. The engineering shear stress strain relationship exhibits a pronounced nonlinear behaviour in the range of small deformations, followed by a linear behaviour for moderate to large strains.

The engineering shear stresses at failure are given in figure 4.26a and the corresponding engineering shear strains in figure 4.26b. The average value of all conducted tests and the standard deviation are shown for each geometry, with the number of specimens given in table 4.3. In addition, the average values for the engineering shear stresses and strains at failure of all conducted test series are summarised in table 4.4. The engineering failure stresses and strains are not influenced by the adhesive overlap length. However, the engineering shear stresses and strains at failure decrease with increasing adhesive thickness. This finding is referred to as *adhesive thickness effect*, which has been discussed in section 3.5. The failure initiation was located close to the corner edge of the interface between adhesive and adherend.

Table 4.4: Stresses and strains at failure of the simple shear test series

Test series 2015					
Test series	Number of specimens	Eng. shear stress [MPa]	Std. dev. [MPa]	Eng. shear strain [-]	Std. dev [-]
100-6	5	0.876	0.125	1.413	0.249
100-12	6	0.800	0.098	1.302	0.188
100-24	5	0.580	0.098	0.924	0.144
200-12	5	0.830	0.060	1.308	0.089
200-24	5	0.570	0.151	0.868	0.222
Test series 2016					
50-12	5	0.855	0.153	1.308	0.212
100-6	5	0.951	0.071	1.497	0.089
100-12	8	0.873	0.125	1.348	0.184
100-24	5	0.635	0.150	1.010	0.210
Average over all specimens					
100-6	10	0.914	0.104	1.455	0.182
50-12	5	0.855	0.153	1.308	0.212
100-12	14	0.841	0.116	1.328	0.180
200-12	5	0.830	0.060	1.308	0.089
100-24	10	0.608	0.123	0.967	0.176
200-24	5	0.570	0.151	0.868	0.222

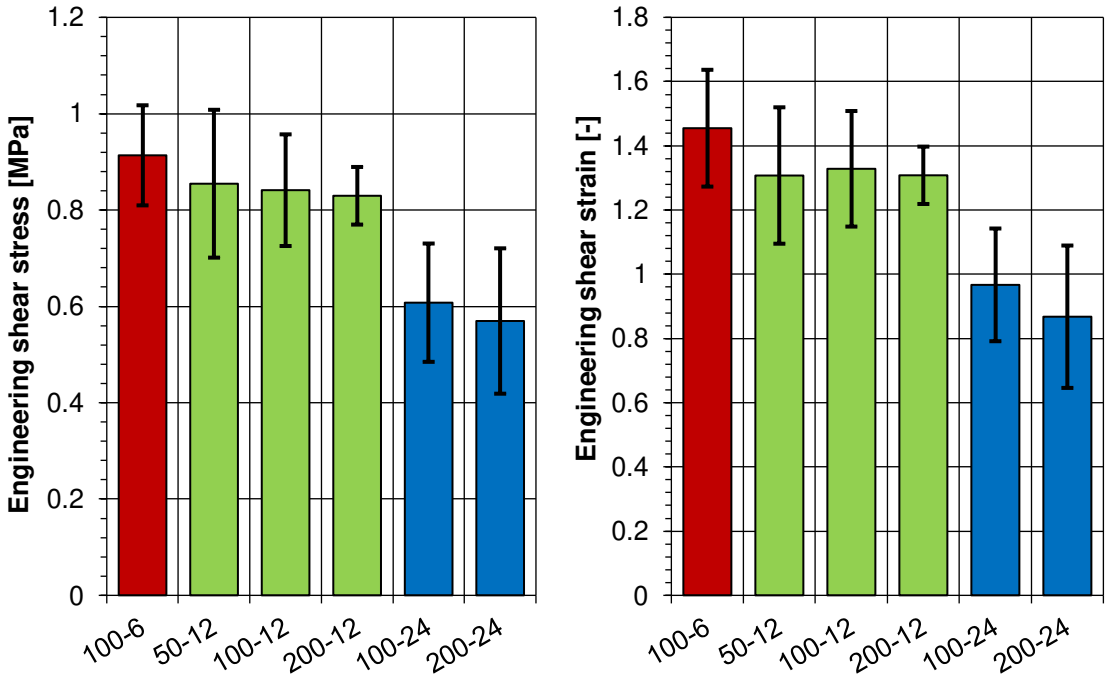

(a) Engineering shear stress at failure

(b) Engineering shear strain at failure

Figure 4.26: Engineering shear stresses and strains at failure

The failure pattern of a representative specimen (test series 100-12) is displayed in figure 4.27. The typical saw-tooth pattern was found with pure cohesive failure. Again, no voids or cavities are visible on the crack surfaces.

Figure 4.27: Typical failure pattern of a simple shear specimen

iv Identification of the crack initiation load

In this paragraph, the failure process is considered in detail and the failure point is defined. In order to define the failure load, two specimens showing a typical failure process were analysed. Failure is defined as the appearance of a significant crack, which can be identified in the stress-strain-diagram as a change of slope or an offset in the curve.

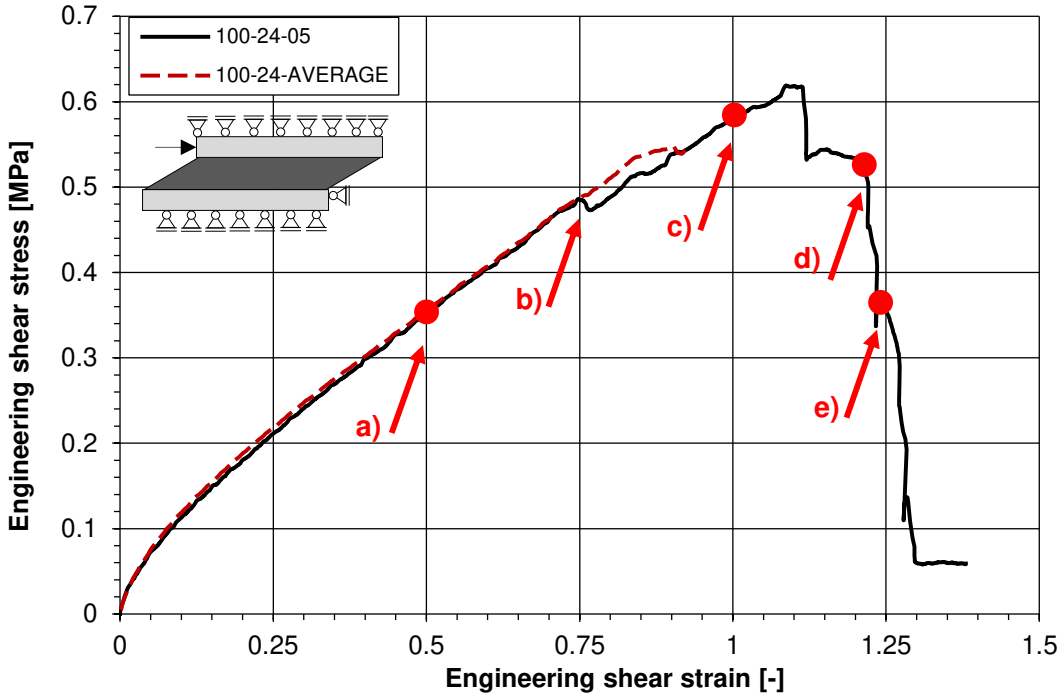

Engineering stress-strain curve for the 100-24-05 specimen and average curve for the 100-24 test series. The deformations corresponding to points a) to e) can be found below.

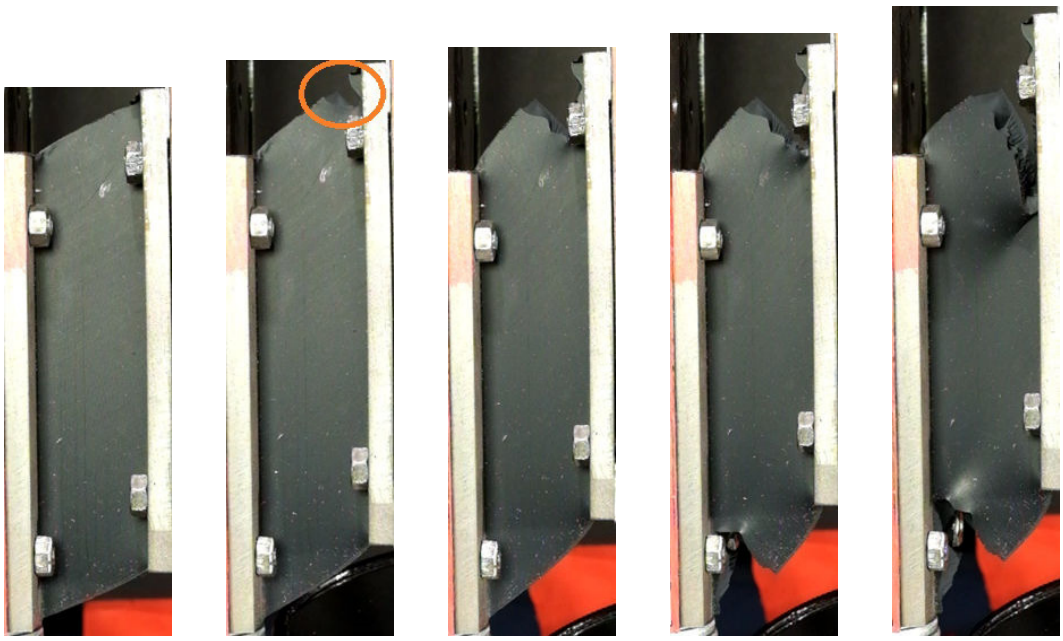

(a) $\gamma_e = 0.5$ (b) $\gamma_e = 0.75$ (c) $\gamma_e = 1.00$ (d) $\gamma_e = 1.13$ (e) $\gamma_e = 1.21$

Figure 4.28: Detailed evaluation of the test specimen 100-24-05

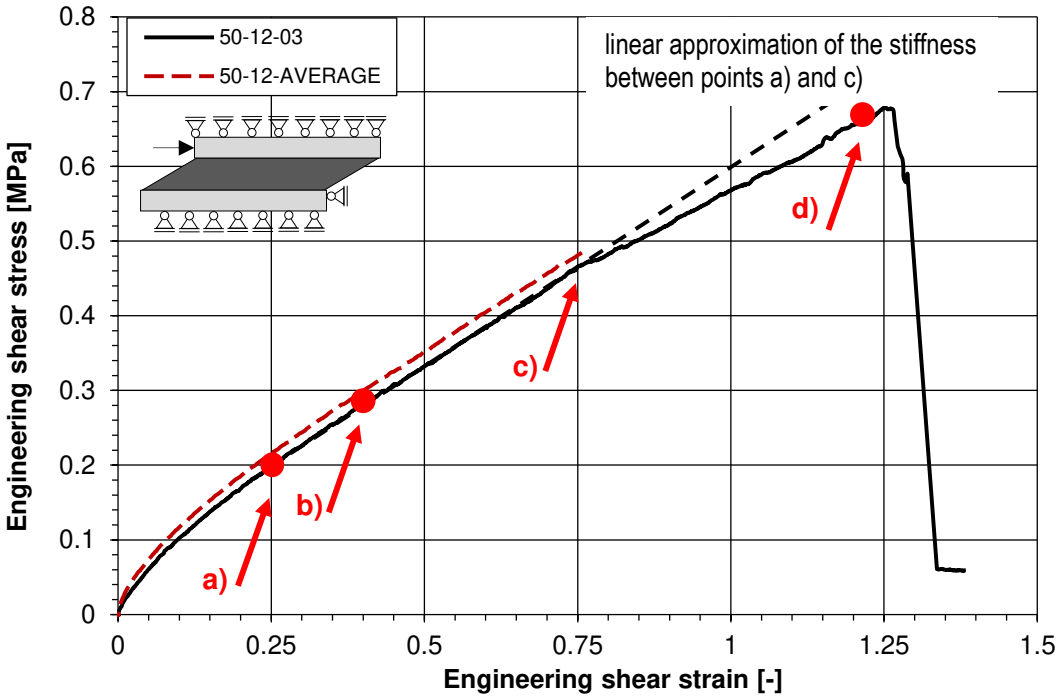

Engineering stress-strain curve for the 50-12-03 specimen and average curve for the 50-12 test series. The deformations corresponding to points a) to d) can be found below.

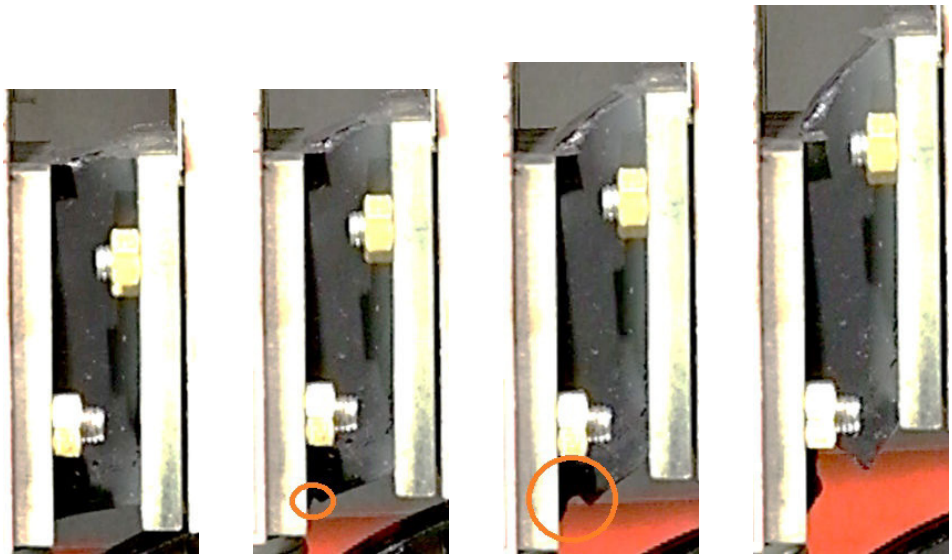

(a) $\gamma_e = 0.25$ (b) $\gamma_e = 0.40$ (c) $\gamma_e = 0.75$ (d) $\gamma_e = 1.20$

Figure 4.29: Detailed evaluation of the test specimen 50-12-03

In figure 4.28, the stress-strain relationship for the specimen 100-24-05 and the average curve for that series are given. Moreover, 5 points are selected with the corresponding video frames shown in figure 4.28 a) to e). For point a), no failure is observed. In point b), an offset in the stress-strain curve was recorded and a crack opening can be observed in figure 4.28 b) at the corner edge of the bonded connection. The transferred load increases after this offset in the engineering stress-strain curve. At point c), both the applied force and the crack length increased. At point d), a second crack at the opposite corner edge developed and force finally decreased. At the final point e), the specimen is close to complete failure. The

force did not drop to zero due to friction between the crack faces.

For the second example, shown in figure 4.29 b), a small crack was already visible for small displacements. However, the actual failure of this specimen was identified at the point of the stress-strain diagram in figure 4.29a, at which the slope of the stress-strain curve has changed. The extrapolation of the original stiffness of the curve is plotted as a dotted line.

It has been illustrated in this paragraph considering two representative specimens, that the failure initiation of the investigated bonded connections tested in simple shear correlates with an offset or a change of slope in the recorded stress-strain relationship and that this corresponds to the appearance of a first significant crack. After the initiation of failure, the applied load can still be increased as shown in these two examples. Generally speaking, the maximum load is 5%-25% higher than the failure load.

v Numerical simulation

The simple shear tests have been numerically simulated in order to check, if the chosen material law is able to reproduce the material behaviour observed in the shear tests. In addition, the numerical models are investigated in more detail in chapter 6. For the numerical simulation, the commercial Finite Element software code ABAQUS® (Dassault Systèmes, 2014) was employed. The *Marlow* hyperelastic material law was used to describe the sealant. Details about the material law employed can be found in section 3.3.3. 20-node quadratic fully integrated brick elements with hybrid formulation due to the incompressible material behaviour of the adhesive were chosen in the geometrical nonlinear analysis. A mesh size of 1 mm was selected, giving convergent results regarding the force-deformation behaviour. The boundary conditions are given in figure 4.30. Symmetry in bite direction was assumed and the adherends were not modelled since they are rigid compared to the soft silicone sealant.

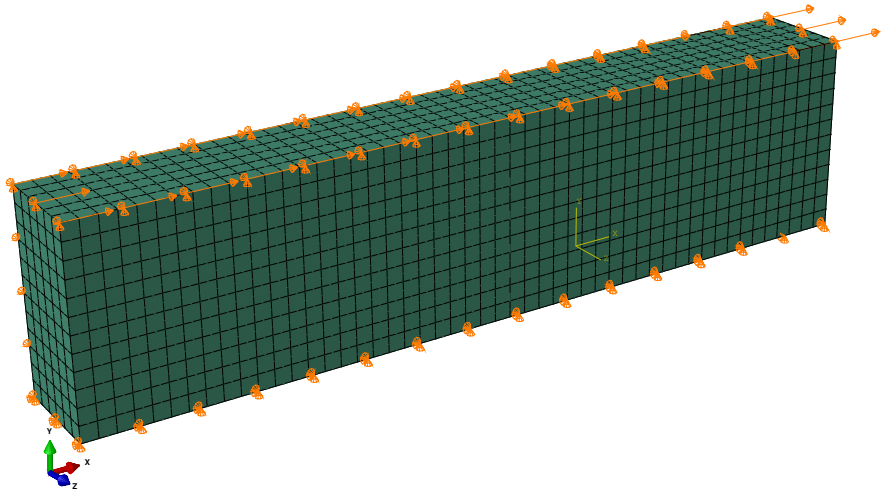

Figure 4.30: Boundary conditions assumed in the numerical simulation of the simple shear tests. The adherends were not modelled as they are rigid compared to the sealant.

A comparison between the experimentally obtained stress-strain curve and the numerical simulation is shown in figure 4.31. A very good agreement is obtained between the test results and their numerical simulation. Engineering shear stress-strain curves are shown. Since the stress-strain curves for the different test series are coincident, the results are shown

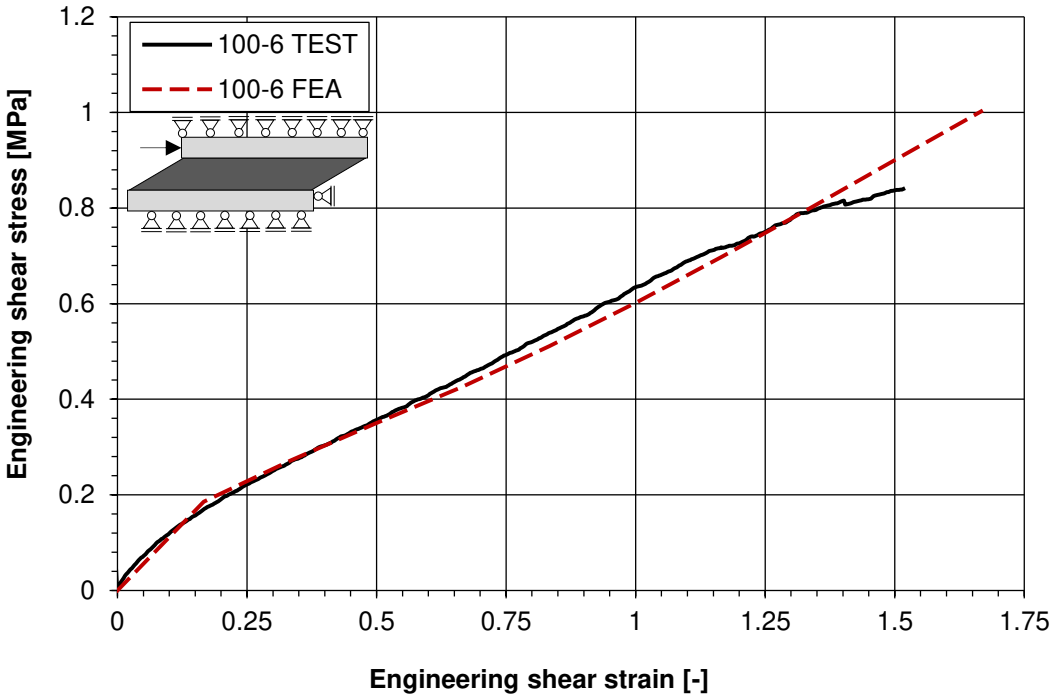

Figure 4.31: Experimentally obtained engineering shear stress-strain curve and numerical simulation of the 100-6 specimen

in an exemplary way for only one geometry.

Further results of numerical investigations were presented in Staudt et al. (2016). The stress distribution has been found to be independent of the overlap length. For a given imposed engineering shear strain and the same overlap length, the stresses obtained at the corner edge of the interface between adherends and adhesive were found to increase with the adhesive thickness. It was concluded, that the results of the Finite Element analysis qualitatively well describe the experimentally observed adhesive thickness effect. In sections 6.3 and 6.4.1, it will be shown that the FEA can also quantitatively describe the adhesive thickness effect.

vi Investigation of the displacement field at the surface of the sealant

In the previous paragraph, the global stress-strain behaviour of the simple shear tests was numerically reproduced. In this section, the local deformations at the corner edge, which have been determined using the digital image correlation system, are compared with the results of the previously described Finite Element Analysis. The region of measured surface displacements is given in figure 4.32. An applied displacement of $u_x = 3\,\text{mm}$ was considered for a specimen of the 50-12 test series and a specimen of the 100-12 test series. In order to obtain a high resolution, only a limited section of the specimens was considered.

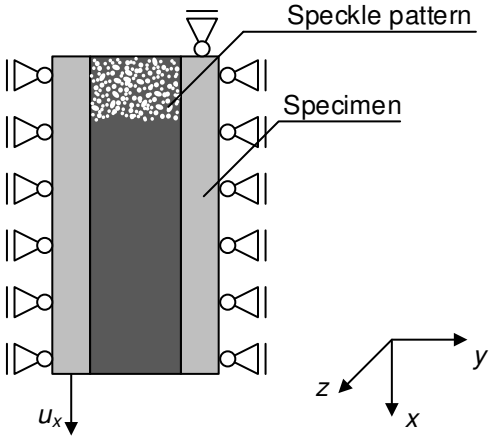

Figure 4.32: Region of measured surface displacements using DIC

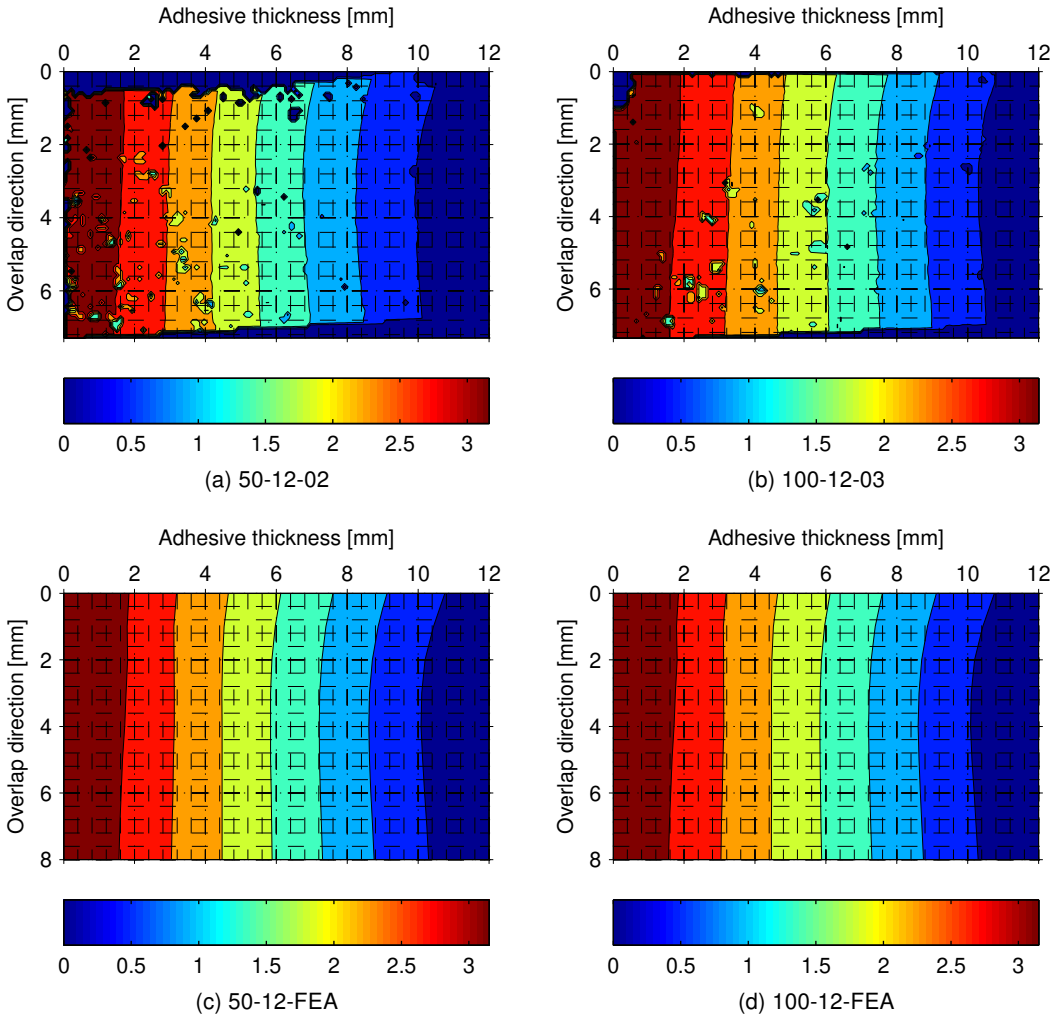

Figure 4.33: Plot of the deformation u_x for an applied deformation of $u_x = 3\,\text{mm}$, x is the load direction.

In the following, specimens 100-12-03 and 50-12-02 are compared for the same imposed displacement of 3 mm. In addition, the deformations measured in the tests on the surface of the sealant are compared with the results from the non-liner Finite Element Analysis, which was described in the previous chapter.

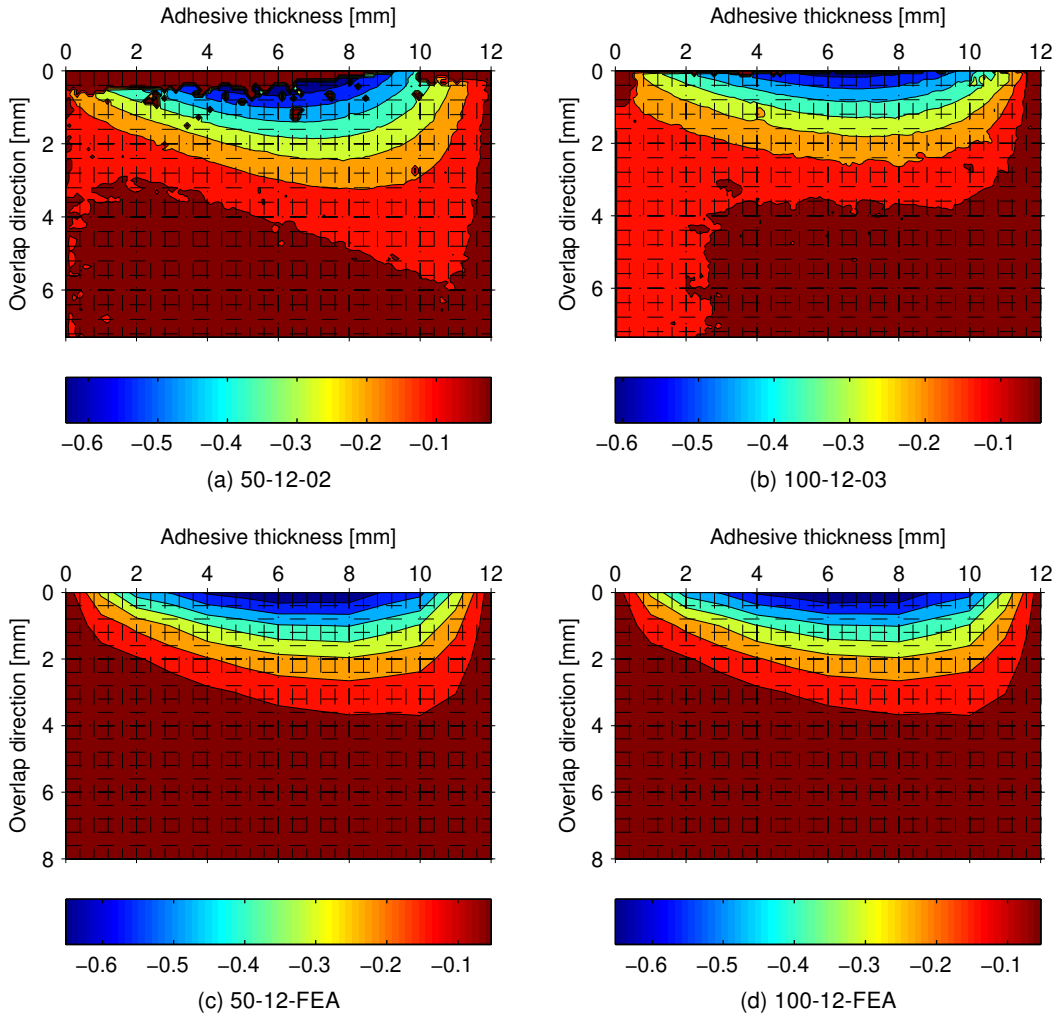

Figure 4.34: Plot of the deformation u_y for an applied deformation of $u_x = 3$ mm, y is the direction of thickness.

Figure 4.33 shows the displacement in x-direction. The chosen coordinate system is given in figure 4.32. x is the overlap direction, i.e. the direction of the applied displacement. The deformations perpendicular to the overlap direction (y-direction) are shown in figure 4.34. Finally, the out-of-plane deformations (z-direction) are given in figure 4.35. In these figures, subfigures (a) give the experimentally obtained values for the specimen 50-12-02 and (b) the values for the specimen 100-12-03. In subfigures (c) and (d), the respective results of the Finite Element Analysis are plotted.

A very good agreement in all considered directions is obtained, both qualitatively and quantitatively, between the experimentally measured deformations and the numerically predicted ones. Moreover, the displacement field at the corner edge is the same for different adhesive overlap lengths. This finding validates the working hypothesis formulated in Staudt et al. (2016) according to which the stress field at the corner edge is independent of the adhesive

overlap length for the considered geometries. The experimentally obtained deformation plots exhibit some defects, which correspond to areas, where the speckle pattern from the reference configuration could not be retrieved in the deformed shape. This is due to regions of speckle pattern, which were badly sized or which did not exhibit enough contrast.

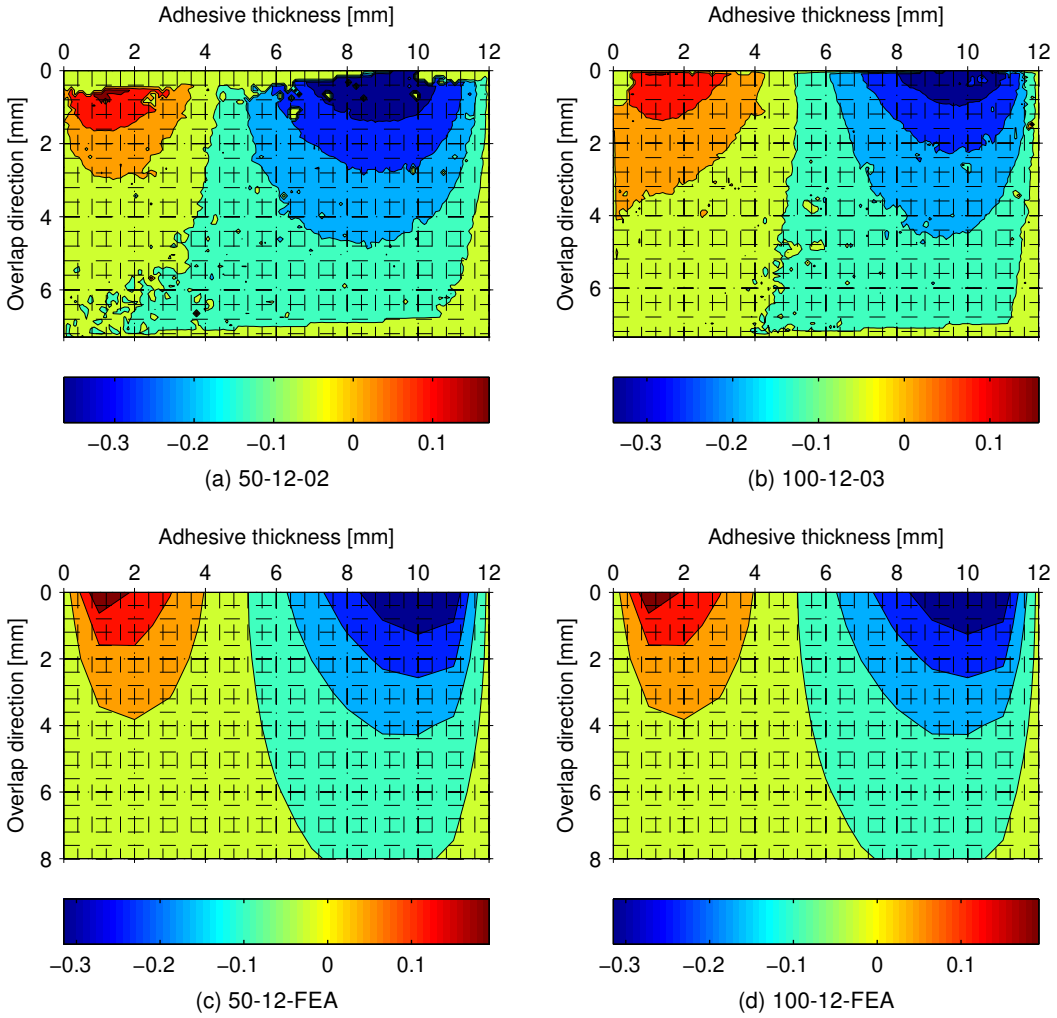

Figure 4.35: Plot of the deformation u_z for an applied deformation of $u_x = 3\,\text{mm}$, z is the bite direction.

4.2.2 Circular shear tests

Circular shear tests on bonded connection with Dow Corning® 993 structural silicone adhesive (Dow Corning Corporation, 2001) have been performed using two different types of specimens. For the first type, a continuous silicone bead was produced in order to investigate the material behaviour and the failure initiation of bulk material without being influenced by a significant singularity. The second type has a disrupted joint exhibiting the two-material wedge at the corner edge of the interface as shown in figure 4.36. The results of the specimens with continuous joints have already been published in Staudt et al. (2017). The basic idea of the circular shear test was to eliminate the corner edge areas of the standard H-shaped specimen as detailed in ETAG 002 (2012) by making the bonded connection circular. To obtain a shear loading, a torsional moment was applied on the circular bonded connection. Specimens

for circular shear tests can either be butt bonded or overlapping (Habenicht, 2009). In the present investigation, specimens with overlapping adherends, also known as tubular lap joints (cf. Adams and Peppiatt (1977) or Chen and Cheng (1992)) were used. The selected type of specimen is shown in figure 4.36. Inserting a fillet is another method to reduce the effect of the two-material wedge. This method has been applied in Cognard and Créac'hcadec (2009), where an improved thick adherend shear test was proposed. The complex adhesive geometry required to reduce the influence of the singularity is a disadvantage of this method.

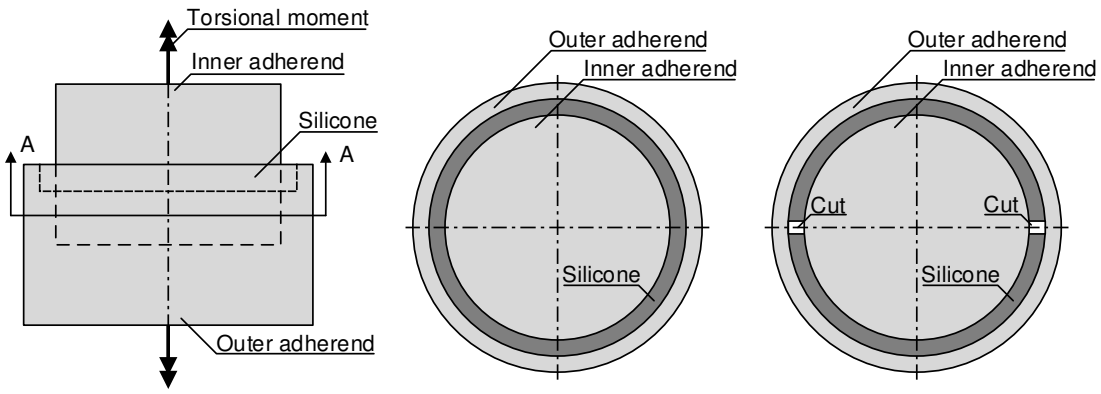

(a) Specimen (b) Cut A-A continuous joint (c) Cut A-A disrupted joint

Figure 4.36: Selected specimens for the circular shear tests on bonded connections with silicone

i Specimens and test setup

As mentioned before, specimens with cuts and specimens with continuous silicone bead have been used, with a number of 5 specimens produced for each type. The cross-section of a specimen is shown in figure 4.37.

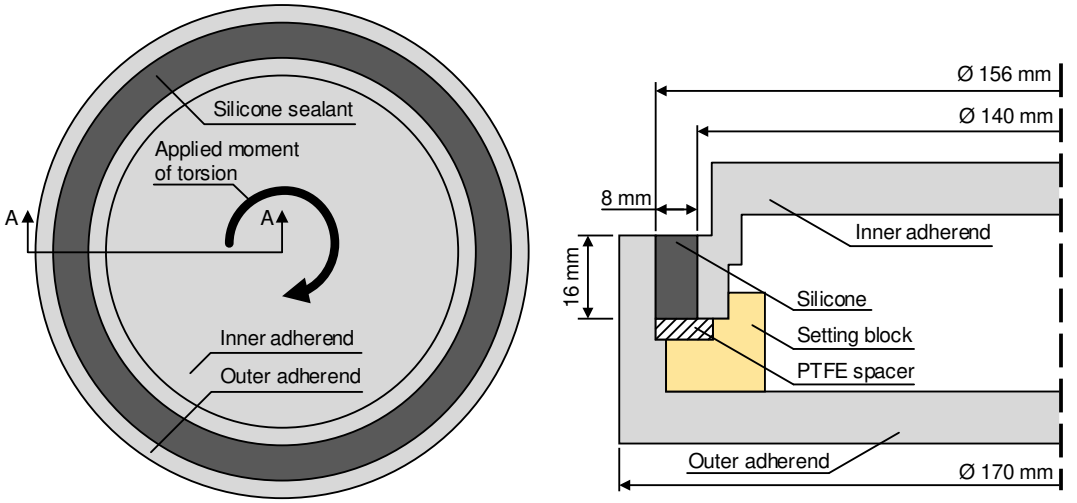

(a) Butt bonded adherends (b) Overlapping adherends

Figure 4.37: Specimen used for the circular shear test on a bonded connection with silicone

(a) Components of the specimen without cut

(b) Components of the specimen with cuts

Figure 4.38: Components of the specimens of the circular shear tests

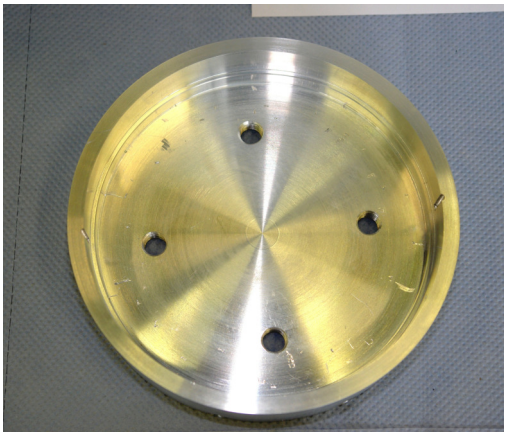

(a) Outer adherend

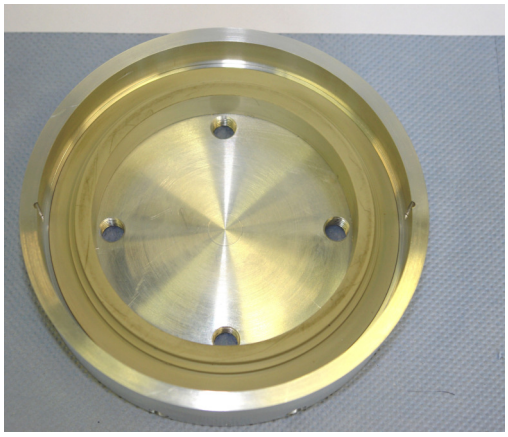

(b) Outer adherend with setting block

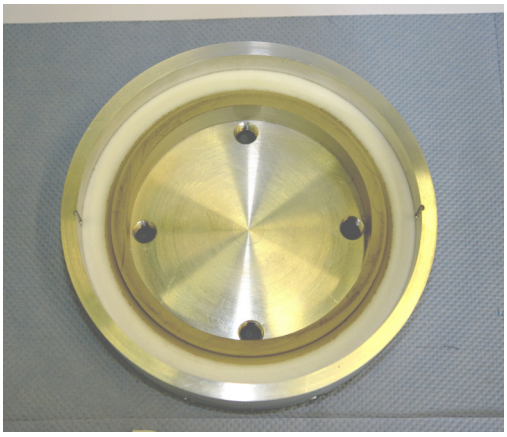

(c) PTFE ring added

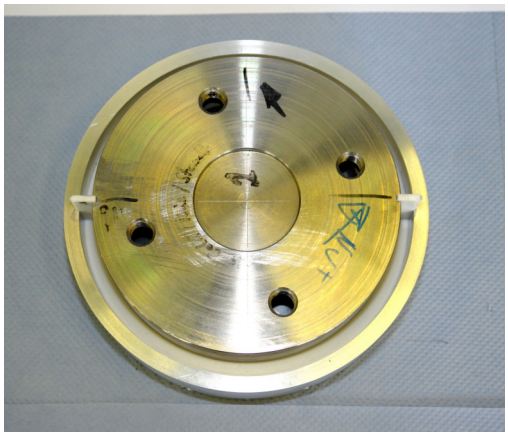

(d) Inner adherend and PTFE spacer for the cuts added

Figure 4.39: Assembly of a specimen with 2 cuts

The specimens are composed of two bowls, with one bowl placed into the other and bonded together with Dow Corning® 993 structural silicone adhesive (Dow Corning Corporation, 2001). The inner adherend has a diameter of 140 mm and is placed on a plastic setting block, which is placed inside the outer adherend, to avoid a dead load transfer through the adhesive. Between the setting block and the silicone bead, a PTFE ring was inserted to avoid adherence on three sides. PTFE was not used for the setting block because of its pronounced visco-elastic behaviour. For the specimens with cuts, two 3 mm PTFE plates were placed between the inner and outer ring. Two notches were milled at the inner side of the outer adherend and at the outer side of the inner adherend to create a guidance for the PTFE plates. The installed PTFE plates are shown in figure 4.39d. Once the sealant had cured, the plate were removed, thus creating the edge areas subject to the present investigations.

The adherends were made out of aluminium. Before the sealing of the specimens with silicone, the parts were carefully cleaned with a solvent (Dow Corning® R40) and prepared to the pouring of the silicone with an appropriated primer (Dow Corning® 1200 OS) (Dow Corning Corporation, 2011b). The silicone was poured using a professional mixing device. After the sealing, the specimens have been stored at controlled conditions. Details about the cure conditions can be found in annex B. Figure 4.38 shows the components of the specimens. The manufacturing process is illustrated in figure 4.39. Although the manufacturing conditions differ from those of the simple shear tests, for which the surface in contact with air was considerably smaller, the material behaviour is assumed to be independent of the manufacturing conditions.

(a) Torsion testing machine

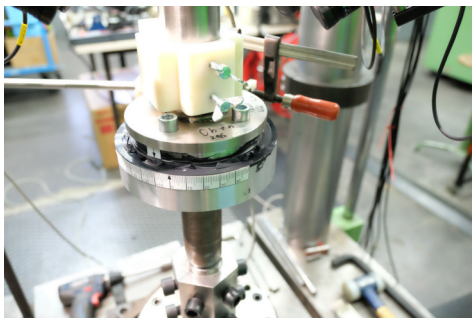

(b) Installation of the specimen inside the torsion testing machine

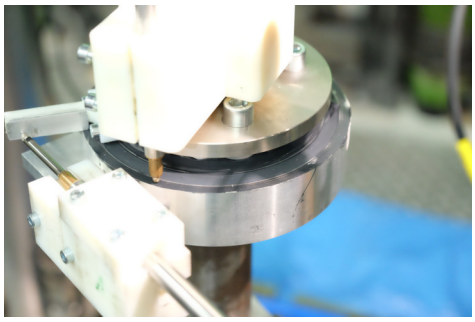

(c) Displacement transducers used

Figure 4.40: Test setup of the circular shear tests at TU Darmstadt

The test series have been performed using a tension-torsion testing machine with a maximum capacity of 4000 Nm in an air conditioned environment with 20°C and 50% relative humidity.

The testing machine is shown in figure 4.40a. Two adapters, consisting each one of a disk welded to a steel cylinder, were produced to clamp the specimens in the testing machine. The adapters were fixed to the specimens with screws. The cylindrical parts of the adapter were inserted in the clamp of the testing machine and fixed with screws as well. Two adapters, one for the top and one for the bottom side, were used. The connection detail is shown in figure 4.40b. Figure 4.40c shows the fixation devices, produced for the displacement transducers.

The applied torsional moment was measured using the load cell of the testing device. In addition, two displacement transducers were used to measure the angle of torsion and the relative axial displacement between the adherends. This displacement transducer was fixed in tangential direction of the specimen. Knowing the exact position from the displacement transducer to the centre of the specimen and measuring the relative displacement between the two adherends, the angle can be calculated using simple trigonometrical equations (see figure 4.41). The results of this measurement were in very good agreement with the travel recorded by the testing machine. A second displacement transducer was fixed in vertical direction to measure the vertical relative displacement between the two substrates.

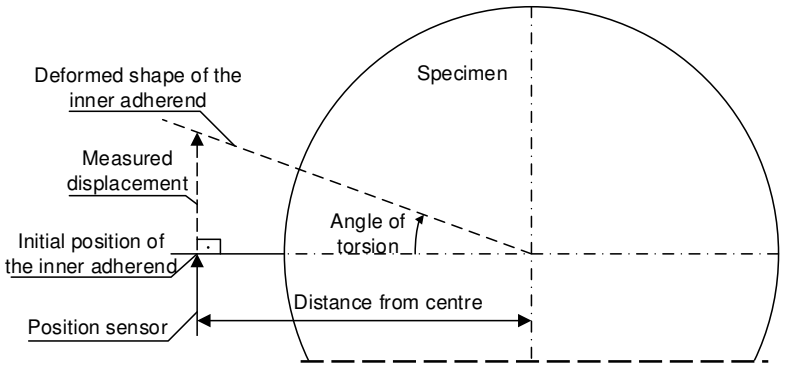

Figure 4.41: Relationship between the measured tangential displacement and the angle of torsion

The loading rate has been determined following the principle of constant energy input. A loading rate of 1.5°/min was determined. The test program was chosen to avoid any normal force in vertical direction.

For the failure load prediction in chapter 6, the shear stress distribution within the adhesive in the circular shear specimen is investigated. A small section of the circular silicone bead is considered in figure 4.42. From equilibrium, the applied moment of torsion can be computed as given in equation 4.12. The shear stresses are assumed constant in bite direction (h_c).

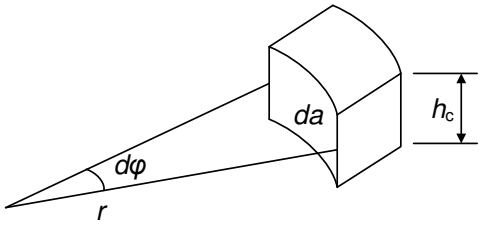

Figure 4.42: Small section of the adhesive joint

$$
\begin{aligned}
M &= \int_A \tau\,(r)\ r\ h_\mathrm{c}\ \mathrm{d}a \\
&= \int_0^{2\pi} \tau\,(r)\ r^2\ h_\mathrm{c}\ \mathrm{d}\varphi \\
&= \tau\ r^2\ h_\mathrm{c} \int_0^{2\pi} \mathrm{d}\varphi \\
&= 2\pi\ \tau\ r^2\ h_\mathrm{c}.
\end{aligned}
\tag{4.12}
$$

ii Test results

The torsional moment versus the angle of torsion for the two conducted test series is plotted in figure 4.43. The average curve is shown for each series. For the series without cuts (labelled T-NC), 5 specimens have been tested. For the series with two cuts (labelled T-2C) only 4 specimens were tested due to a problem encountered while testing one specimen. The scattering of the results is in the order of 10%. The specimens with 2 cuts show a lower stiffness than the specimens with continuous silicone bead.

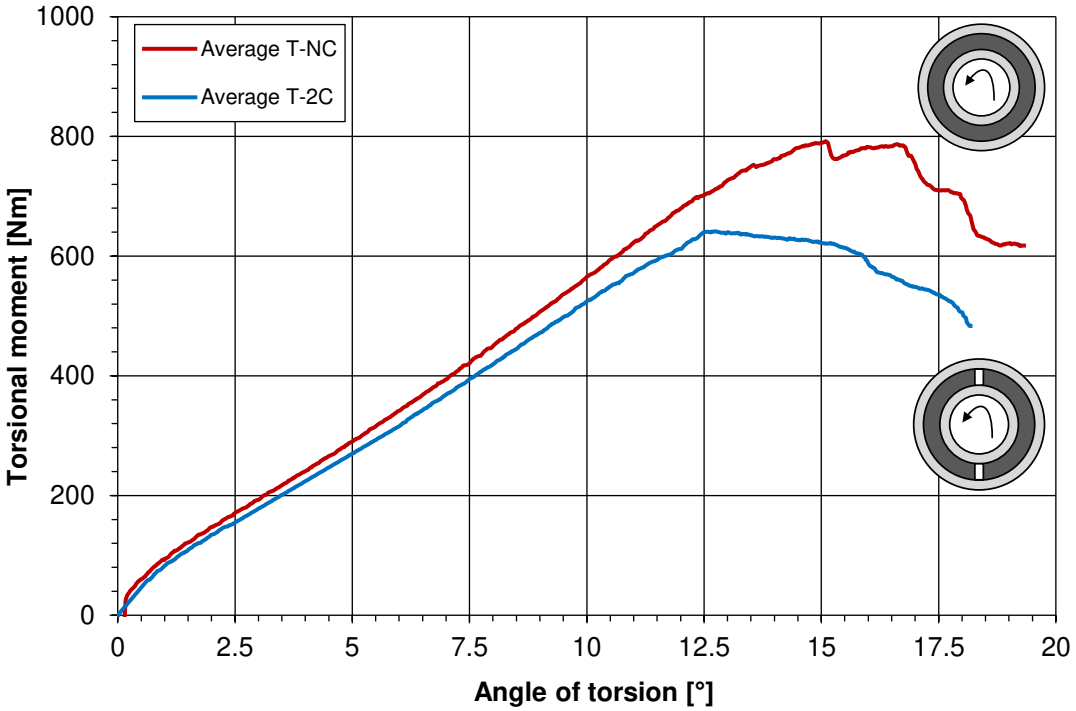

Figure 4.43: Results of the circular shear tests

Regarding the vertical displacement transducer, which was used to monitor the axial displacement, a maximum axial separation of 0.5 mm was found with an average value of 0.22 mm for all the tests. A maximum axial compression displacement of 0.1 mm was found with an average of 0.02 mm for all the specimens. Due to the small values, these displacements were neglected for the numerical analysis, which is discussed later.

The moment of torsion and the angle of torsion at failure initiation are given in figure 4.44. The identification of failure initiation was performed in the same way as discussed in section 4.2.1. A specimen has reached its failure point, if an offset or a significant change of slope is visible in its force-deformation curve. Considering figure 4.44, it can be concluded that the difference in the load bearing capacity between the specimens with cuts and without cuts is within the range of scattering. Whereas the average values for the angle of torsion at failure is almost equal, there is a small difference in the applied moment of torsion. It should be recalled here, that the total load transferring area of the specimens with cuts is smaller than for the specimens without cuts due to the presence of these cuts.

Considering the failure mechanism, for both series, 100% cohesive failure was observed. The

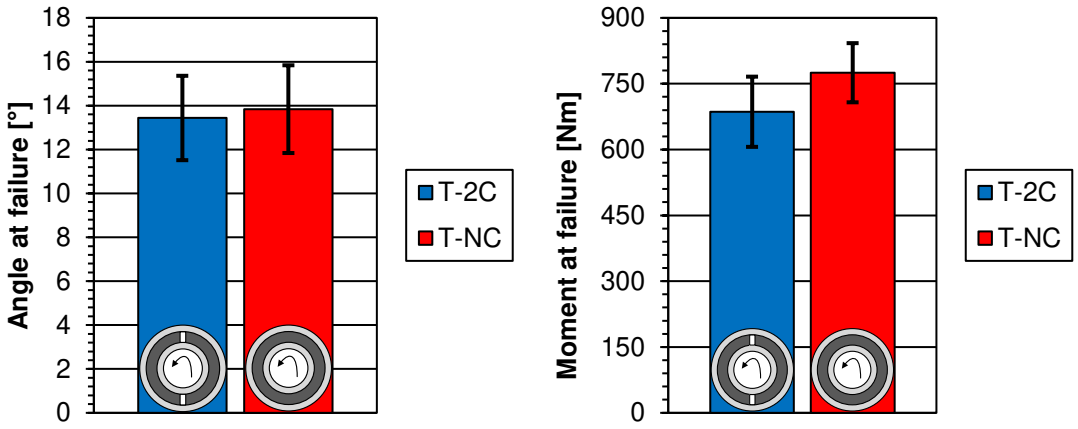

(a) Angle of torsion at failure

(b) Moment of torsion at failure

Figure 4.44: Evaluation of the failure loads of the circular shear tests - average value and standard deviation are displayed

failure pattern is shown in figure 4.45. It shows the typical sawtooth-shaped cohesive pattern of the adhesive layer. No permanent deformation after failure was observed. A detailed view on the crack surfaces of a representative specimen is given in figure 4.46. No voids or cavities are visible.

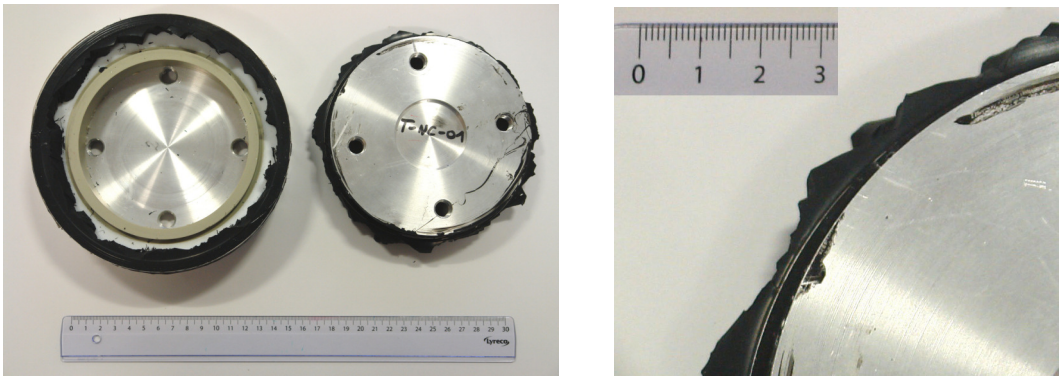

(a) Cohesively failed specimen

(b) Detailed view

Figure 4.45: Typical failure pattern of a circular shear test specimen

For the notched circular shear specimen, the silicone bead was disrupted. Prior to the pouring of the sealant, a small piece of PTFE with a thickness of 3 mm and covering the whole cross-section of the adhesive joint, was inserted to create the corner edges, similar to those found at the simple shear specimens. During the test, it was observed that for a certain applied rotation, the faces of the inserted gap came into contact. Figure 4.47 shows a picture of the specimen T-2C-05, for which the gap almost vanished and the corresponding numerical simulation. Details about the numerical model used are given below. The deformation of the sealant in bite direction is qualitatively well reproduced in the numerical simulation. The circular shear tests were performed to investigate the influence of the corner edge on the failure behaviour of the adhesive joint. The above mentioned observations should be considered for the following investigations.

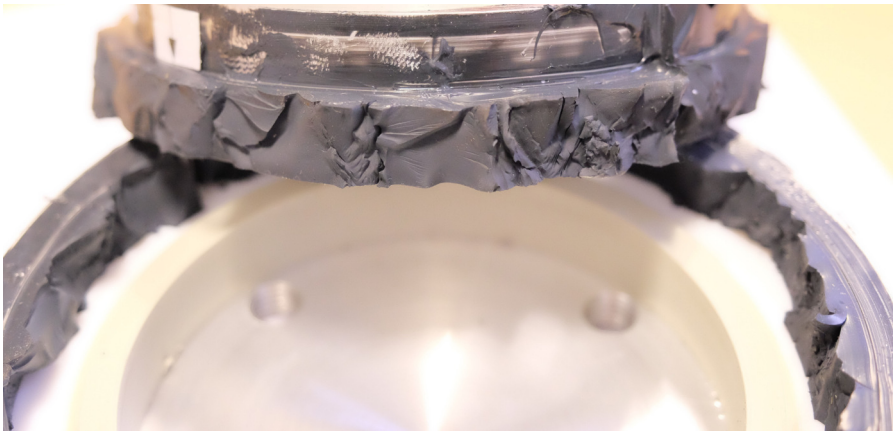

Figure 4.46: Detailed view on the failure pattern of a circular shear test specimen

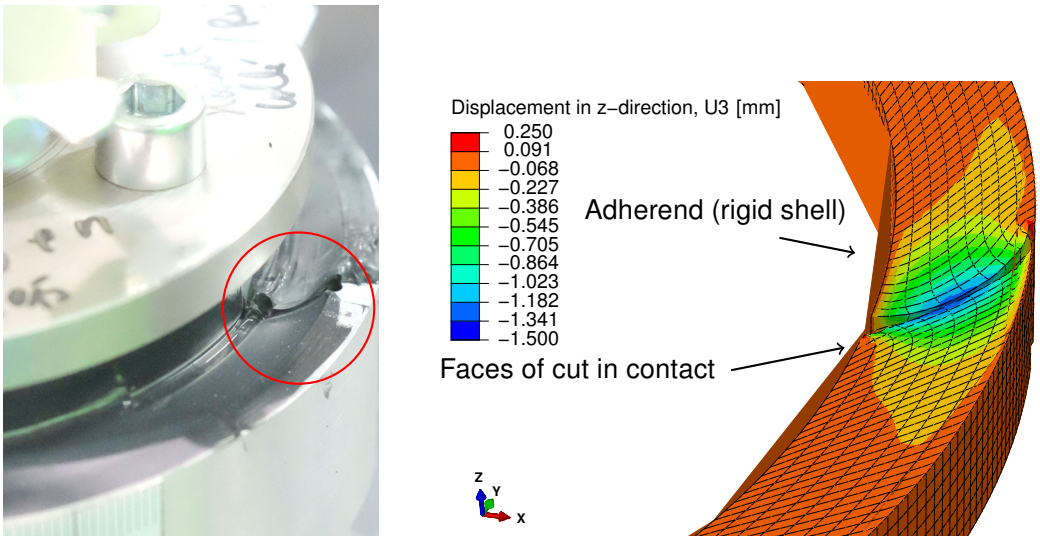

(a) Test

(b) Numerical simulation

Figure 4.47: Behaviour of the faces of the cut in the circular shear test - U3 is in z-direction

iii Numerical simulation

The circular shear tests have been numerically reproduced using the commercial Finite Element software code ABAQUS®(Dassault Systèmes, 2014). The results of these simulations will be investigated in more detail in chapters 5 and 6. For the silicone sealant, the *Marlow* hyperelastic material law has been used, as described in section 3.3.3. Symmetry in bite direction was used and the adherends were represented with analytically rigid shells bonded to the sealant with a *tie* constraint. 2 reference points have been defined to apply the boundary conditions for the adherends. The boundary conditions are given in figure 4.48.

The inner rigid shell was fully fixed at its reference point and the rotation was applied on the outer rigid shell. 20-node quadratic, fully integrated hybrid solid elements (C3D20H) have been used to represent the sealant. A preliminary mesh study showed that the results for the force-deformation behaviour give convergent results for a reasonably refined mesh with 2 mm element size.

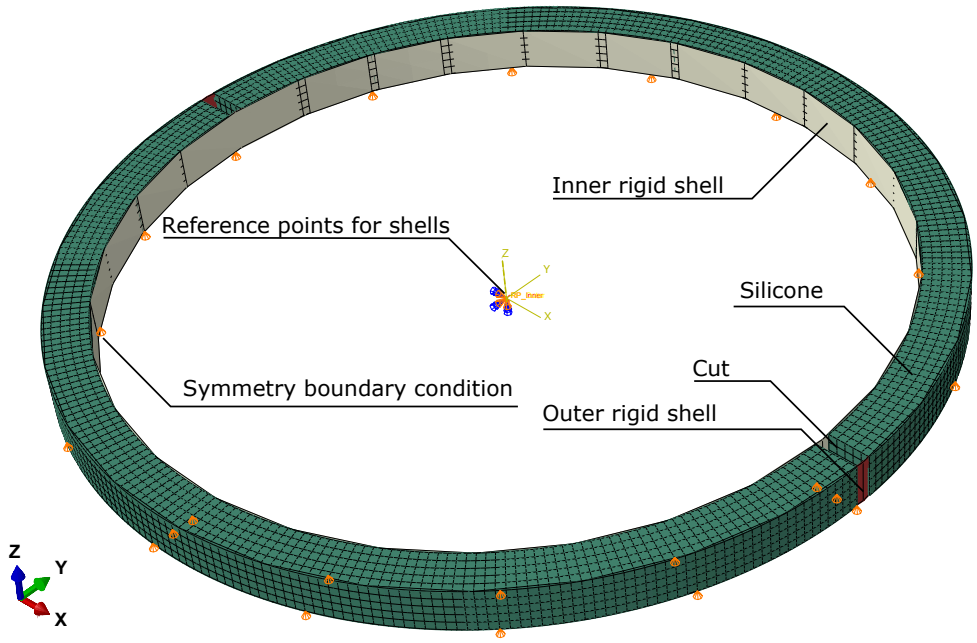

Figure 4.48: Boundary conditions of the numerical simulation of the circular shear test

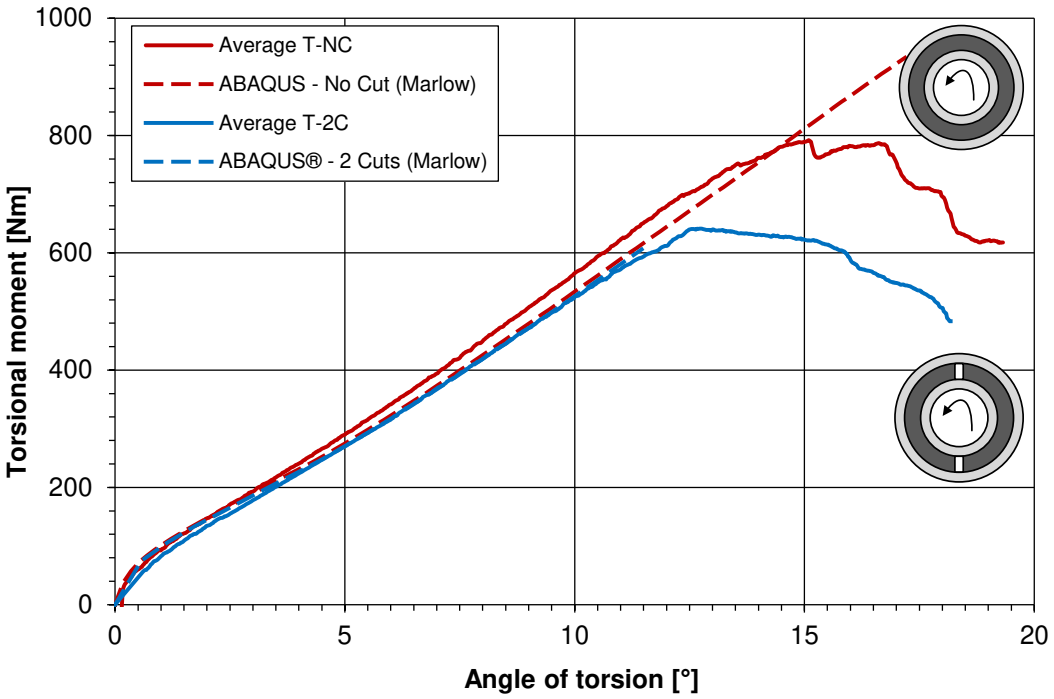

Figure 4.49: Comparison of the test results with the Finite Element Analysis

A comparison between the experimentally recorded moment-rotation curves and the numerical simulation for the two series is given in figure 4.49. A good agreement is obtained between the test data and the Finite Element Analysis. The nonlinear behaviour of the experimental curve is well represented. Since failure is not covered by the constitutive law, the numerical results do not cover the failure process. For both models, almost no difference can be seen

between the curves of the specimens with and cuts without cuts.

4.2.3 Tension tests

Tension tests on H-shaped specimens according to ETAG 002 (2012) have been performed on Dow Corning® 993 structural silicone sealant (Dow Corning Corporation, 2001). The objective of these tensile tests is to validate the chosen material law. Moreover, failure of these specimens will be investigated in chapter 6.

i Specimens and test setup

The specimen used is shown in figure 4.50. The dimensions of the silicone bead were selected according to the specifications given in ETAG 002 (2012) with an adhesive overlap length of $l_{\mathrm{adh}} = 50\,\mathrm{mm}$, an adhesive layer thickness of $e = 12\,\mathrm{mm}$ and a bite of $h_{\mathrm{c}} = 12\,\mathrm{mm}$. The adherends were made of anodized aluminium. The material behaviour is supposed to be homogeneous, isotropic and independent of the curing conditions. A number of 6 specimens was tested.

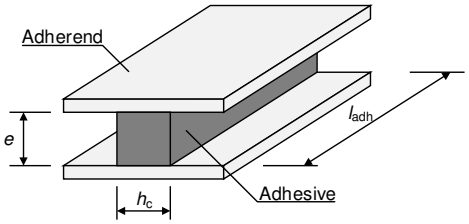

(a) H-shaped specimen

(b) Picture of a tensile specimen

Figure 4.50: Standard H-specimen as detailed by ETAG 002 (2012)

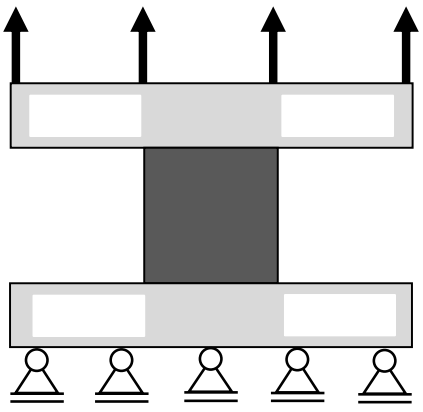

(a) Boundary conditions of the tension test

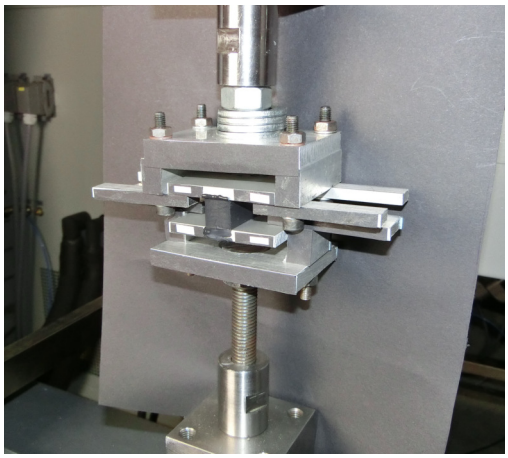

(b) Test setup of the ETAG tension test

Figure 4.51: Test setup and boundary conditions of the tensile tests on H-specimens

The tests were performed at ambient conditions (23 °C temperature and 50 % relative humidity). A tensile testing machine with a maximum capacity of 50 kN was used for the tests. A constant loading rate of 5 mm/min was applied, following the specifications according to ETAG 002 (2012). The tests were run in displacement control. The deformations were measured using video-extensometry, which has been detailed in section 4.1.1. Figure 4.51 illustrates the boundary conditions of the test and shows the white marks used for the evaluation of the displacements. The test setup is displayed in figure 4.51. Two specimens were not immediately loaded to failure, but to approximately 50 % of ultimate displacement, then unloaded to 10 % and reloaded to failure. The objective of this test procedure was to visualise the *Mullin's* effect.

ii Test results

The test results are given in figure 4.52. A quite low scattering of the results can be observed, especially for small deformations. For two specimens, a lower stiffness was recorded. As already described in Staudt (2013), an almost ideal *Mullins* effect can be observed with an almost coincident unloading and reloading path and a force-deformation curve, which follows the initial curve beyond the preloaded range.

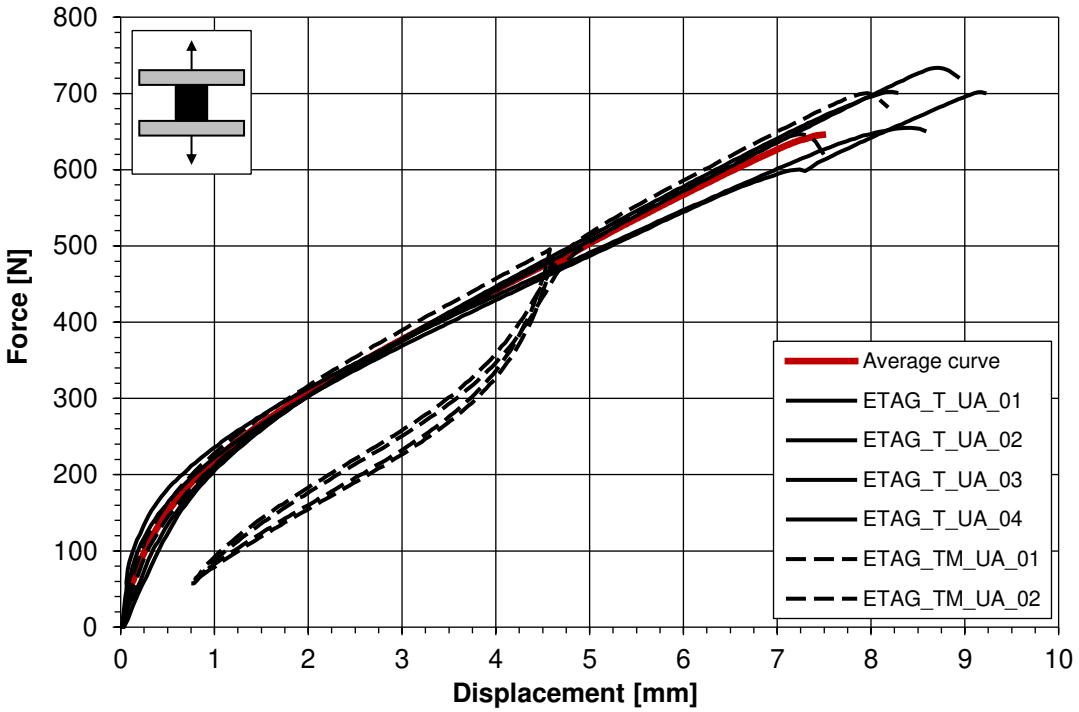

Figure 4.52: Results of the ETAG 002 tension tests, loading rate of 5 mm/min

A typical failure pattern is shown in figure 4.53. 100% cohesive failure was observed for all the specimens. No voids or cavities could be observed at the crack surfaces. The location of failure initiation is illustrated in figure 4.54. It is located at the corner edge of the interface between the adhesive and the adherend, where an inhomogeneous deformation due to the restrained lateral contraction can clearly be observed. For one specimen, the failure initiation point was not visible on the recorded video, but the failure pattern showed that the failure

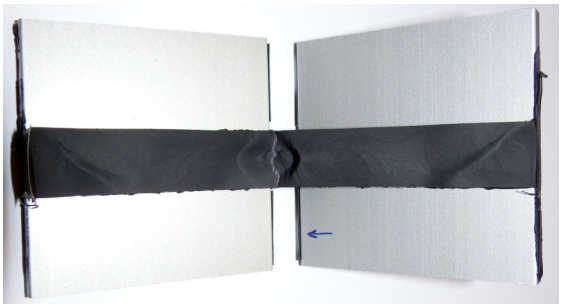

Figure 4.53: Cohesive failure of a H-specimen in tension (specimen ETAG-T-UA-03)

surface is located close to the interface, when considering the edge areas. An average failure displacement of 8.28 mm with a standard deviation of 0.66 mm was recorded.

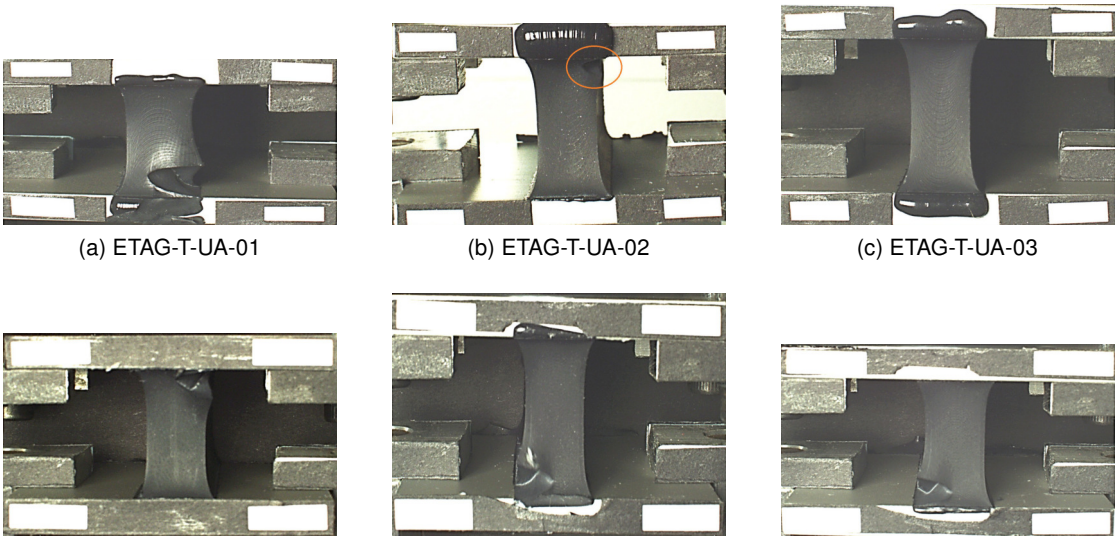

(a) ETAG-T-UA-01 (b) ETAG-T-UA-02 (c) ETAG-T-UA-03

(d) ETAG-T-UA-04 (e) ETAG-T-TM-UA-01 (f) ETAG-T-TM-UA-02

Figure 4.54: Failure initiation of the H-specimens in tension

iii Numerical simulation

The tensile tests on the H-specimens were numerically reproduced using the commercial Finite Element software code ABAQUS® (Dassault Systèmes, 2014). The results of the numerical model were compared with the test data and the results will be further investigated in chapter 6. 20-node quadratic fully integrated brick elements with hybrid formulation due to the incompressible material behaviour of the adhesive were chosen in the geometrical nonlinear analysis. The *Marlow* hyperelastic material law was used to represent the sealant. Details about the material law are discussed in section 3.3.3. An element size of 1 mm was chosen for the mesh. A preliminary mesh study showed that the results concerning force-deformation were convergent for this mesh size. The adherends were not modelled since they are rigid compared to the sealant and the failure of the adhesive was cohesive. One fourth of the specimen was modelled due to symmetry in all bite and overlap direction. The boundary conditions are displayed in figure 4.55.

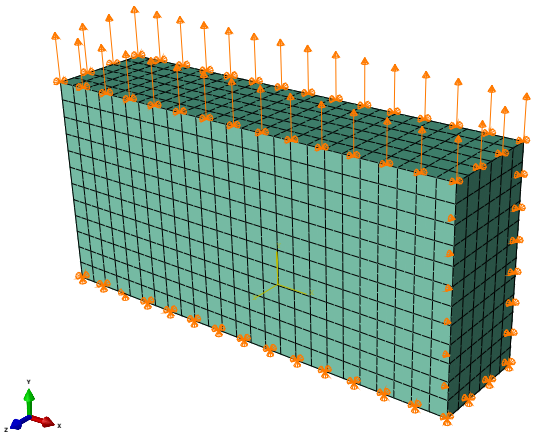

Figure 4.55: Numerical model of the H-specimen under a tensile load

In figure 4.56, the results of the numerical simulation regarding force-deformation are given. A good agreement between the experimental curve and the numerical simulation can be observed, especially for small to moderate deformations. For large deformations, the forces are underestimated for a given displacement.

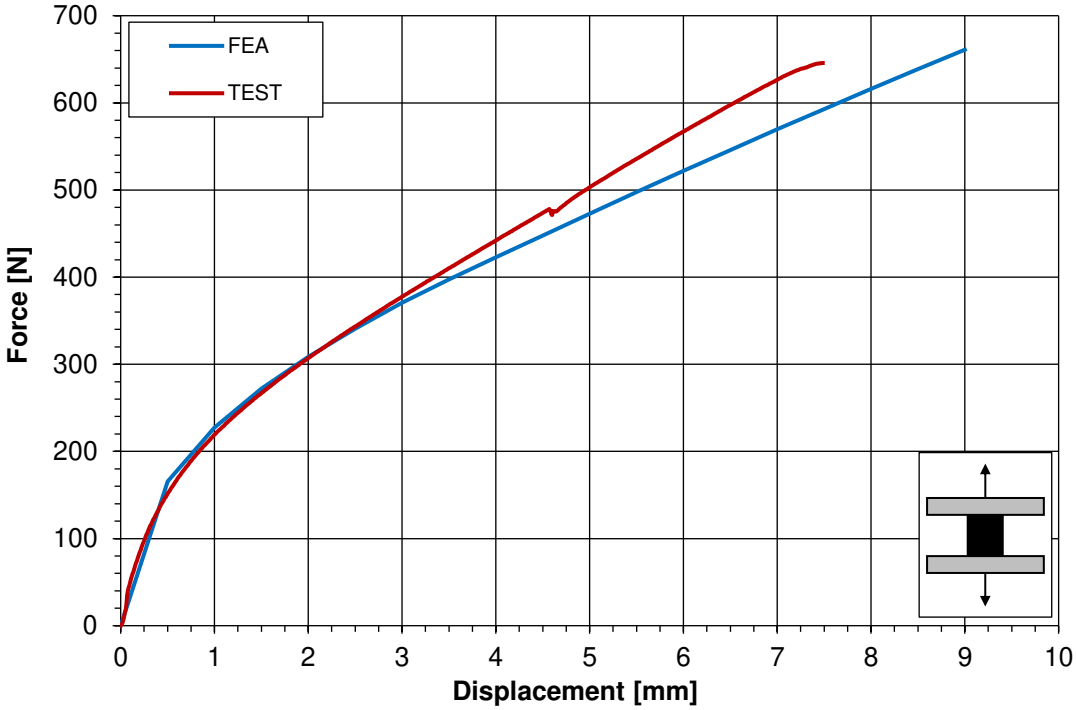

Figure 4.56: Comparison of the test results with the Finite Element Analysis

4.3 Fracture mechanics tests

4.3.1 DCB tests on Dow Corning® 993 structural silicone sealant

Double cantilever Beam (DCB) tests have been performed on Dow Corning 993® structural silicone adhesive (Dow Corning Corporation, 2001). The objective of these tests was the determination of the critical energy release rate for the silicone sealant considered.

i Specimens and test setup

The geometry and loading conditions are given in figure 4.57. Two different adhesive thicknesses were tested, one thick silicone bead with a thickness of $e = 12\,\text{mm}$ (series DCB-12) and a thin silicone bead with a thickness of $e = 6\,\text{mm}$ (series DCB-6). A total number of 7 specimens has been tested for both series. The adherends were made of high strength aluminium in order to avoid a plastic deformation of the adherends.

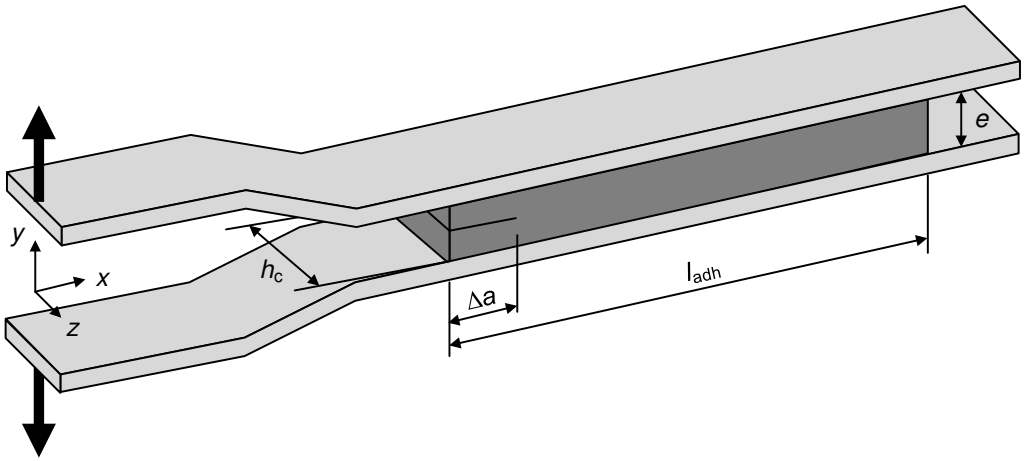

Figure 4.57: Double Cantilever Beam tests on silicone elastomer

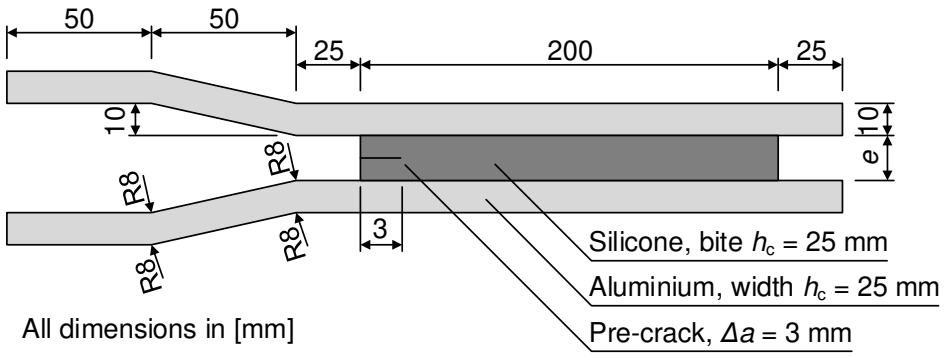

Figure 4.58: Dimensions of the Double Cantilever Beam specimens (drawing not to scale)

The objective of the DCB tests was to determine the critical energy release rate of the silicone sealant. Therefore, in order to avoid that the failure process is initiated at the interface between adhesive and adherend, where the lateral contraction of the sealant is retained due

to the high stiffness of the adherends, a pre-crack with a length Δa of 3 mm was created in the specimens with a razor blade. The crack was located at the half adhesive thickness. The crack length was the same for both test series.

For the manufacturing process, the aluminium adherends were placed on a plate of polyethylene material. At the beginning and at the end of the adhesive joint, a polyethylene spacer was used to adjust the nominal thickness of the sealant. Adherends and spacers were fixed using screw clamps. In addition, screw clamps have been used to avoid slipping on the ground plate. Before assembling the different parts, the adherends were carefully cleaned with Dow Corning® R40 solvent and Dow Corning® 1200 OS primer was used prior to the pouring of Dow Corning® 993 structural silicone sealant (Dow Corning Corporation, 2001), which was done using a professional mixing plant under controlled conditions. Details about the storage conditions can be found in annex B. The material properties are assumed to be homogeneous, isotropic and independent of the manufacturing conditions. The parts used for the manufacturing process and the produced specimens are shown in figure 4.59.

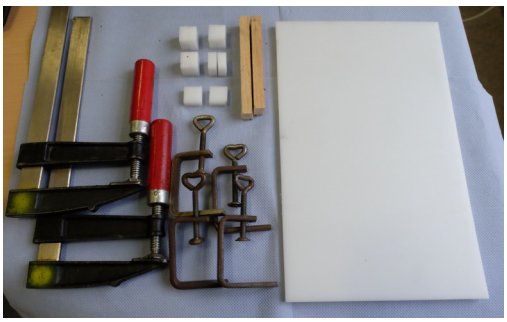

(a) Parts for the manufacturing of the specimens

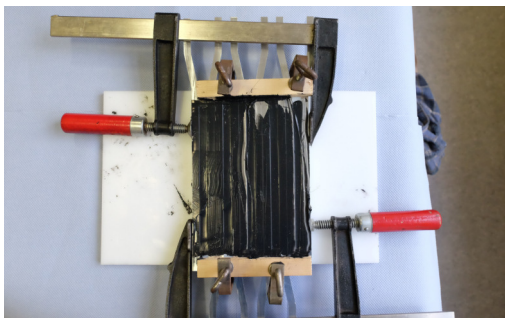

(b) Manufactured specimens

Figure 4.59: Manufacturing process of the Double Cantilever Beam specimens

Due to the manufacturing process, which consisted in pouring the silicone from the top in bite direction, air pockets were found on some specimens. For most of them, the air pockets were not critical, as they were located sufficiently far away from the region of interest. Specimen DCB-12-01 should not be evaluated since the air pocket was close to the beginning of the adhesive joint. Figure 4.60 shows specimen DCB-12-01 and a specimen with high quality.

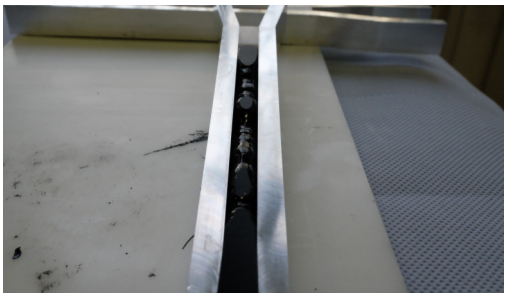

(a) Specimen DCB-12-01 with bad quality

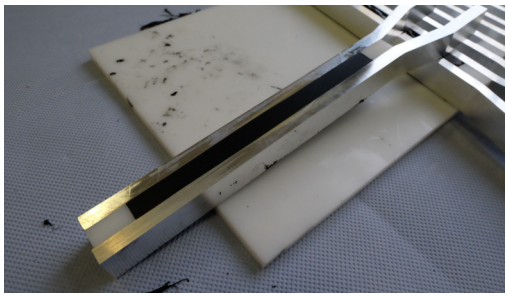

(b) Specimen with good quality

Figure 4.60: Quality of the produced DCB specimens

The Double Cantilever Beam tests have been performed using the tensile testing machine shown in figure 4.57. The specimens were loaded in tension with the tensile force applied in y-direction at the extremities of the specimens, as displayed in figure 4.57. The two cantilever

arms of the specimens were fixed in a device with unrestrained rotation about the specimens' z-axis.

The forces were recorded using a load cell and the rotation of the two loading points were measured using inclinometers. For the measurement of the crack opening displacement, a speckle pattern has been applied on the specimens as shown in figure 4.61b. With these speckle pattern, the displacements were recorded using a digital image correlation system. Before the tests, the specimens' dimensions were measured. The tests have been carried out in ambient conditions and in displacement control. A constant loading rate of 3 mm/min has been applied for the 12 mm specimens and a loading rate of 1.5 mm/min for the 6 mm specimens.

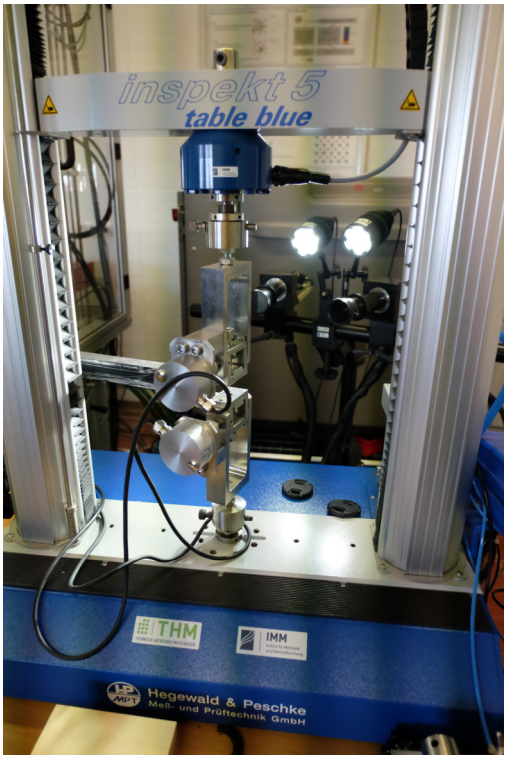

(a) Tensile testing machine with load cell

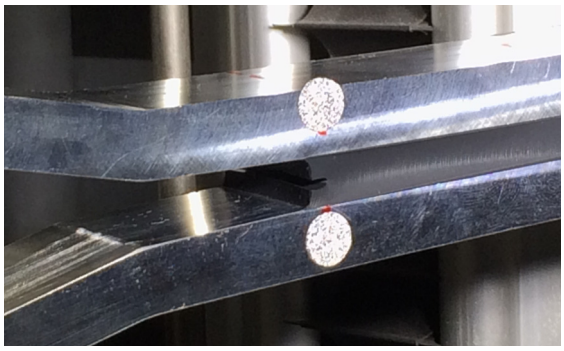

(b) Speckle pattern for displacement measurement

(c) Failure pattern of a DCB-6 specimen

Figure 4.61: Double Cantilever Beam test setup

ii Test results and evaluation

In this paragraph, the results of the Double Cantilever Beam tests are shown. In figure 4.62a, the J-integral is plotted against the crack opening displacement, i.e. the displacement measured on the adherends above the initial position of the crack tip using the digital image correlation system. The curves are almost linear. Figure 4.62b shows the J-integral plotted against the crack opening displacement for the 6 mm specimens. After an initial nonlinear part, the curves flattened. Measurements beyond 9 mm were not possible since the traced speckle pattern was moving out of the video frame.

The traction is potted against the crack opening displacement for the 6 mm specimens in figure 4.63a. These curves have been obtained applying equation 3.66 on the experimental

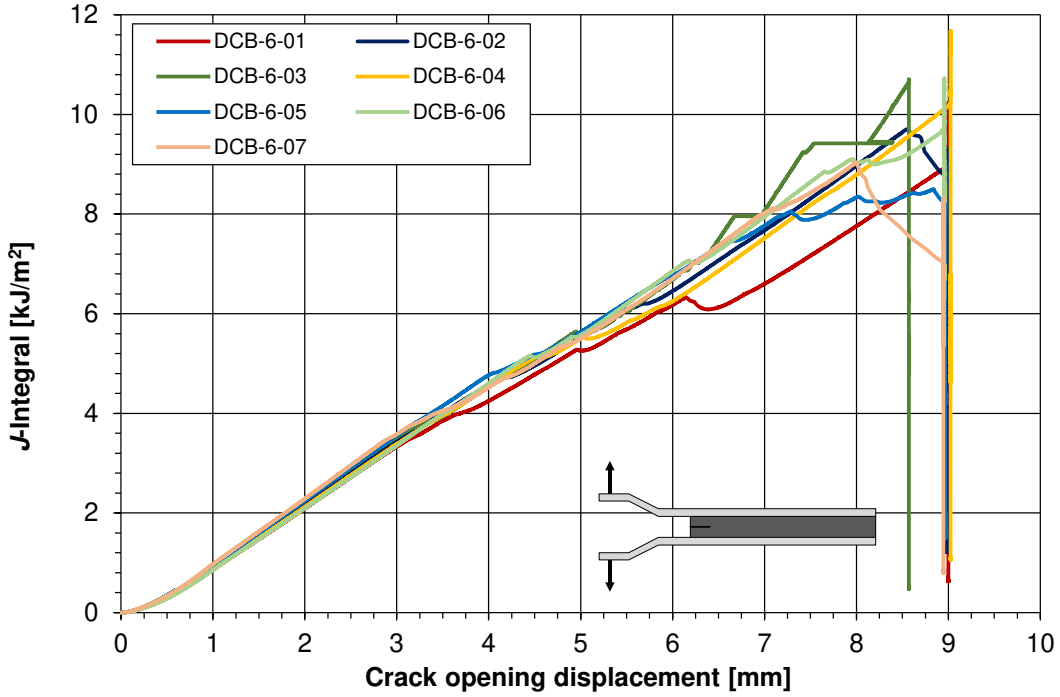

(a) J-integral plotted against the crack opening displacement for the Double Cantilever Beam tests with 6 mm adhesive thickness

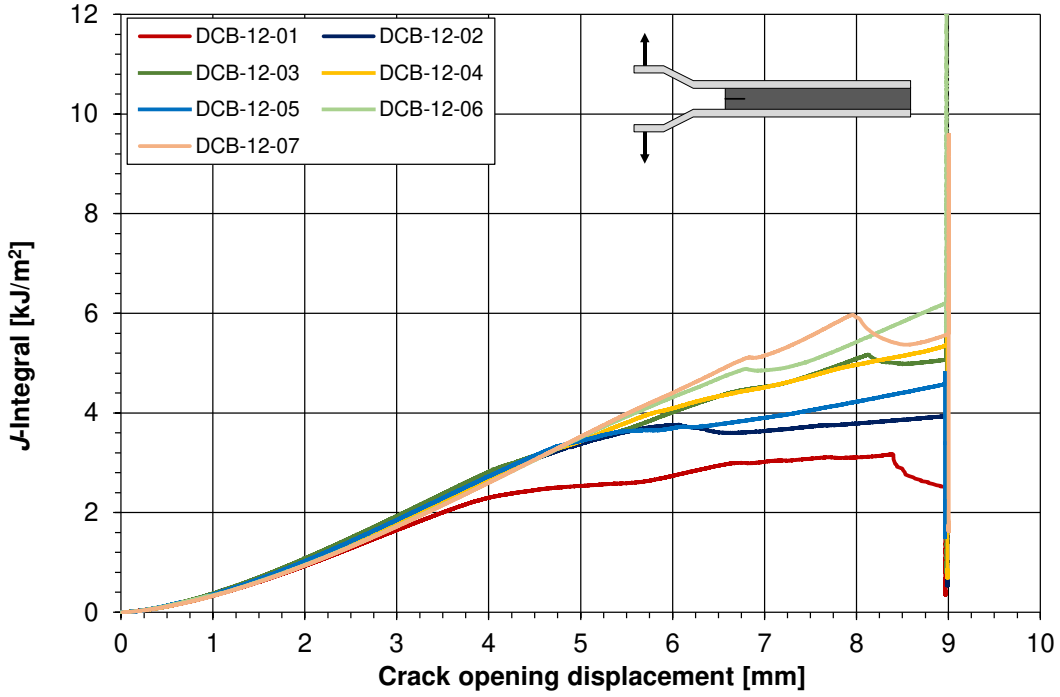

(b) J-integral plotted against the crack opening displacement for the Double Cantilever Beam tests with 12 mm adhesive thickness

Figure 4.62: J-integral plotted against the crack opening displacement for the Double Cantilever Beam tests

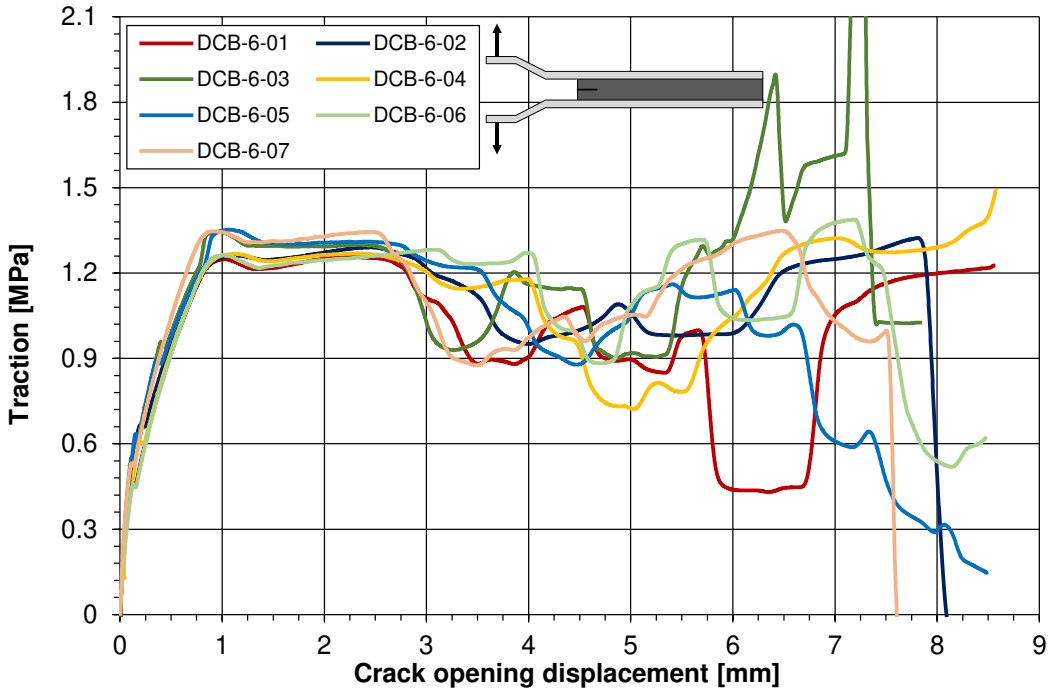

(a) Traction-separation law for the Double Cantilever Beam tests with 6 mm adhesive thickness

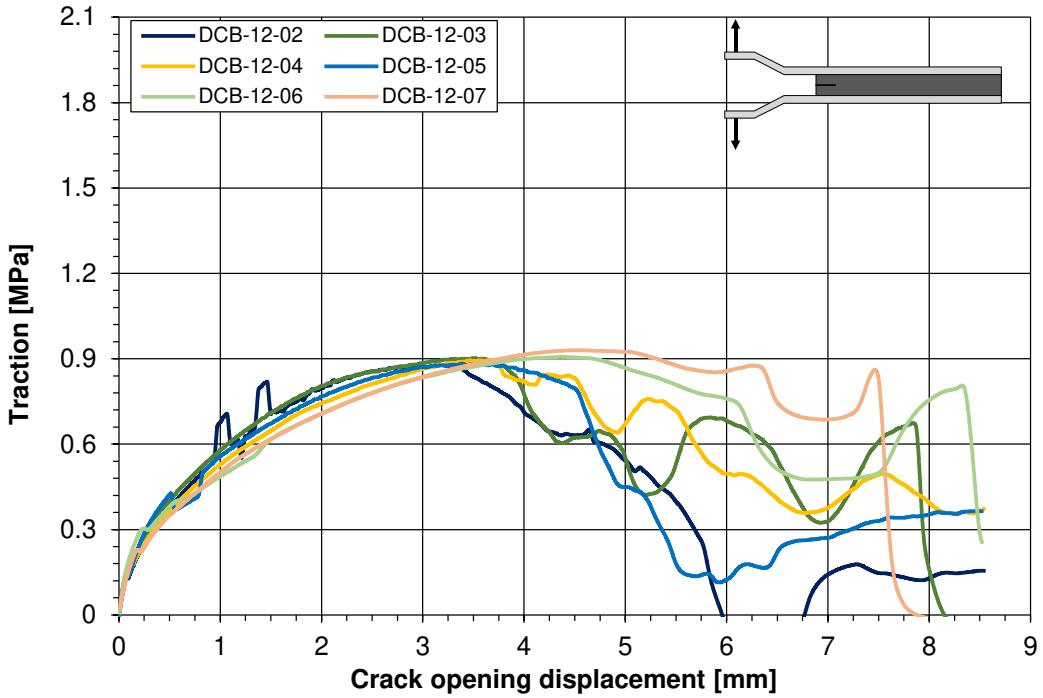

(b) Traction-separation law for the Double Cantilever Beam tests with 12 mm adhesive thickness

Figure 4.63: Traction-separation law for the Double Cantilever Beam tests

curves displayed in figure 4.62. The experimental curves have been approximated using a polynomial function of degree 6. Unlike as for the curves of the DCB-12 specimens, the values for the traction did not decrease to zero. Therefore, it is not a priori possible to determine

the critical energy release rate regarding this data. The evaluation will be further discussed in paragraph iv. Similar behaviour was observed for some specimens of the DCB-12 test series, but less pronounced. For these specimens, the evaluation has been carried out up to a point for which the stresses decrease below 5% of the maximum value or up to a point, at which the curve starts to show unstable behaviour.

The behaviour observed for the thin adhesive layers can be linked to unstable crack growth. In Leffler et al. (2007), unstable crack propagation was observed for a thin epoxy-based adhesive tested in shear. The unstable crack growth was explained with an insufficient initial crack length. Another explanatory approach is given in Biel and Stigh (2017). A thin incompressible adhesive tape has been investigated in a DCB test with transparent polymethlymethacrylate adherends in order to visualise the effects, which take place in the adhesive. Nucleation and growth of cavities have been observed in the adhesive. After the first peak stress in the traction-separation law, the decreasing curve is due to the growth of the cavities. A second stress peak was observed prior to final decrease of the traction-separation curve, which was related to the breakage of the walls between the cavities.

The failure pattern of a representative specimen is shown in figure 4.64. The typical sawtooth shaped failure pattern can be observed. Figure 4.65 shows the failure surfaces for a representative specimen. As for the previously described tests, no voids or cavities were detected.

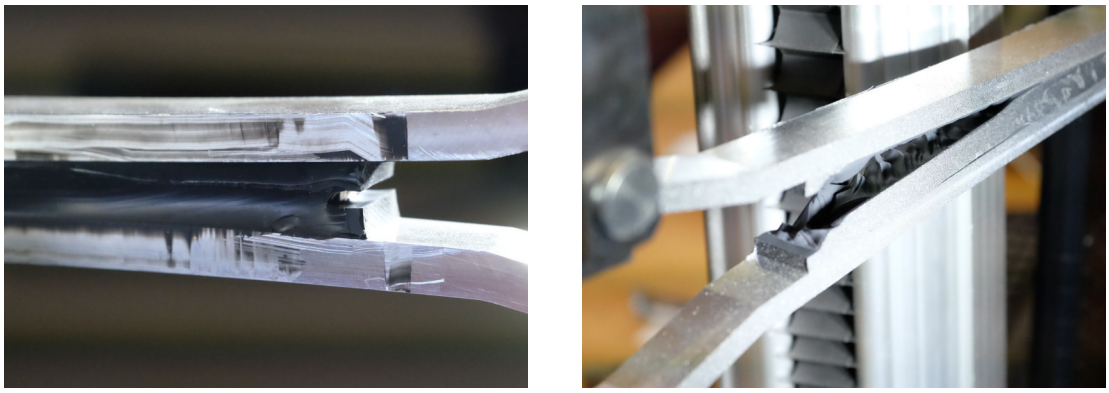

(a) Crack opening (b) Failure pattern

Figure 4.64: Failure process and failure pattern of specimen DCB-12-03

Figure 4.65: Typical failure pattern of a DCB specimen. The pre-crack corresponds to the smooth surface at the right-hand side of the photo.

iii Numerical simulation of the DCB test

The performed DCB tests have been numerically simulated using the commercial Finite Element software code ABAQUS® (Dassault Systèmes, 2014). Apart from the assessment of the material law to reproduce the behaviour of the specimen, the Finite Element Analysis was used to localise the displacement, at which the inserted crack started to propagate. A geometrical nonlinear analysis has been performed assuming a linear elastic material behaviour for the aluminium adherends and an incompressible hyperelastic material law for the silicone adhesive layer (model according to Marlow (2003)). Figure 4.66 shows the numerical model. Symmetries in global Y and Z directions have been used.

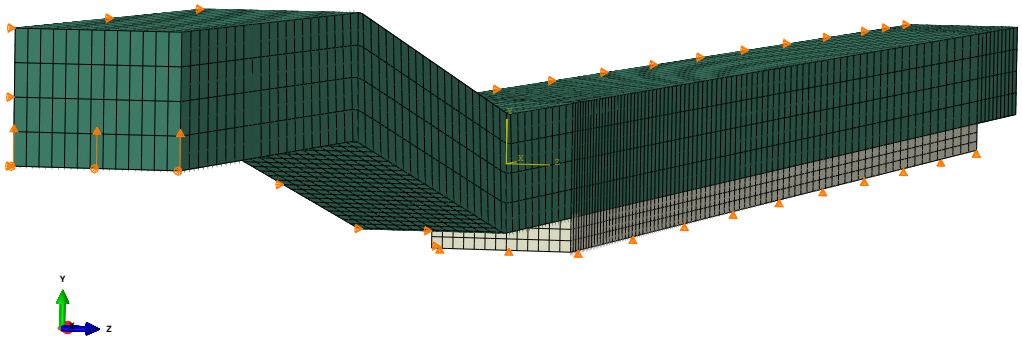

Figure 4.66: Finite Element model of the Double Cantilever Beam test on silicone

For both adhesive and adherends, second order fully integrated solid elements have been selected with hybrid formulation, due to the incompressible material behaviour of the silicone sealant. An element size of 1 mm has been defined in the vicinity of the inserted crack. For the remaining parts, a mesh size of 2.5 to 5 mm has been chosen for computational efficiency and since the results in terms of global force-crack opening displacement behaviour showed convergent behaviour for a rather coarse mesh. The symmetry boundary condition in Y direction has been applied on the whole surface on the symmetry plane except for the area of the initial crack.

The results of the numerical simulation in terms of force-displacement are given in figure 4.67 for both test series DCB-6 and DCB-12. The measured force is plotted against the crack opening displacement, which was tracked using the digital image correlation system as described in the paragraph i. Concerning the experimental data, one average curve is plotted per test series. For the DCB-6 test series, a very good agreement between the experimental data and the numerical simulation was obtained up to a crack opening displacement of 2.5 mm. A good agreement up to 6 mm crack opening displacement was found as well for the DCB-12 test series. Since the crack onset and propagation are not covered by the numerical simulation, the numerically reproduced curve deviated from the experimental results at crack propagation.

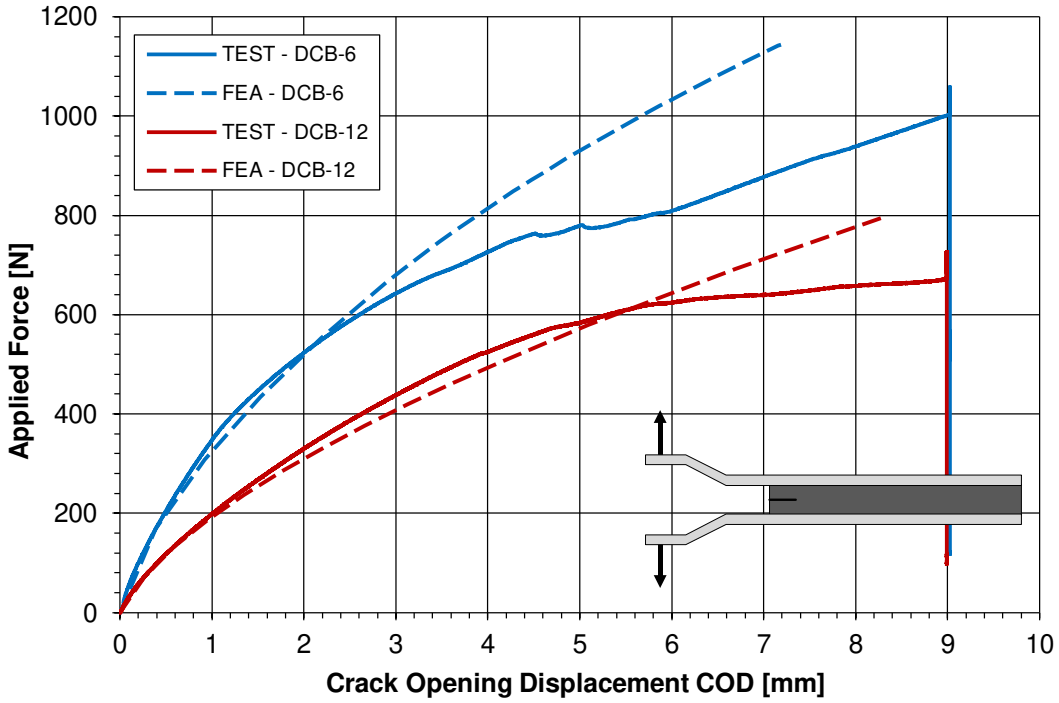

Figure 4.67: Simulation of the force-displacement behaviour of the DCB tests

iv Determination of the critical energy release rate

The critical energy release rate was calculated applying equation 3.63 to the experimentally obtained traction-separation laws, shown in figure 4.63. The numerical integration was carried out up to the crack opening displacement, for which the traction has decreased to zero or for which the traction-separation law exhibits unstable behaviour. The onset of this behaviour was taken as a limit for the computation of the critical energy release rate. Table 4.5 summarises the obtained values. The specimens of the test series DCB-6 have not been evaluated using this method since the discussed unstable behaviour already occurred for high traction values.

Table 4.5: Results of the DCB-12 test series

Specimen	$\mathcal{G}_c$ [kJ/m^2]	σ_{max} [MPa]	δ_{max} [mm]	Unstable behaviour?
DCB-12-01	2.56	0.73	5.19	yes
DCB-12-02	3.72	0.88	6.00	no
DCB-12-03	3.56	0.90	5.24	yes
DCB-12-04	3.40	0.90	4.94	yes
DCB-12-05	3.65	0.88	5.72	yes
DCB-12-06	4.77	0.91	6.78	yes
DCB-12-07	4.96	0.93	6.68	yes
Average (01-05)	3.38	0.86	5.42	-
Std. dev.	0.48	0.07	0.43	-
Average (02-07)	4.01	0.90	5.89	-
Std. dev.	0.67	0.02	0.75	-

Method based on linear extrapolation

In order to determine the critical energy release rate of the test specimens of the DCB-6 series, the descending branch of the traction-separation law was linearly extrapolated. The evaluation of a typical specimen is shown in figure 4.68. The traction-separation law, which was determined from the experimental data, is shown for the specimen DCB-6-01. Starting from the crack opening displacement δ_{ext}, unstable behaviour was detected. The descending branch of the curve was extrapolated considering the slope of the section between 2.75 mm and 3.5 mm crack opening displacement. The results for each specimen of the test series DCB-6 and DCB-12 using the extrapolation method for the determination of the critical energy release rate are given in table 4.6 for the DCB-6 series and table 4.7 for the DCB-12 test series.

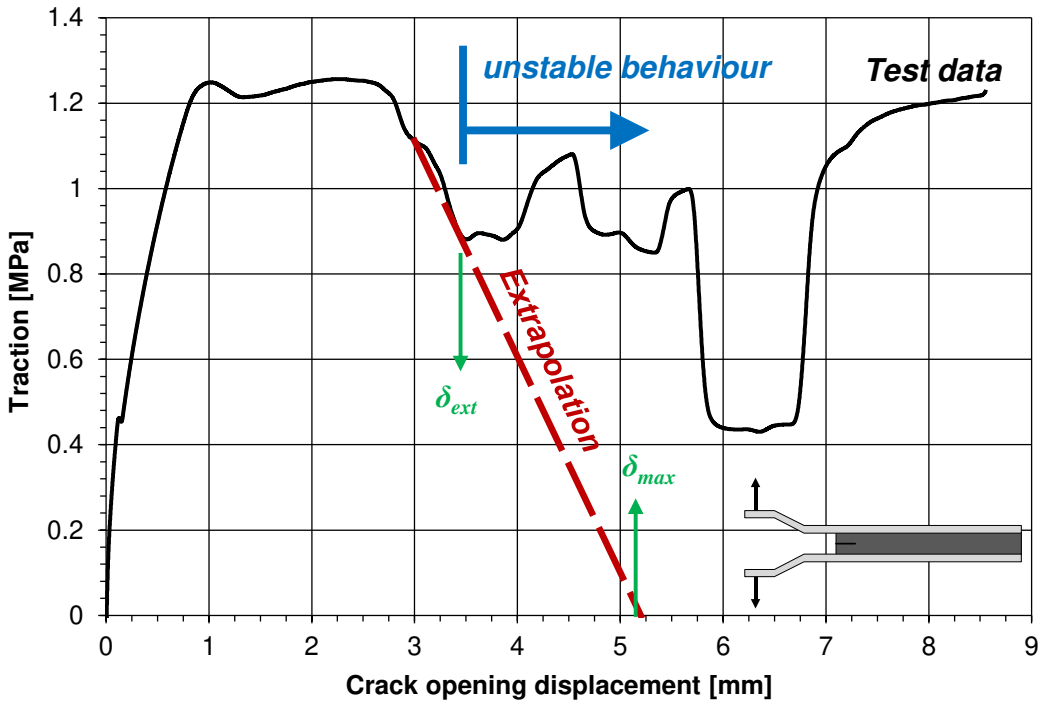

Figure 4.68: Extrapolation of the descending branch of the traction-separation law

Table 4.6: Results of the DCB-6 test series extrapolating the traction-separation law

Specimen	$\mathcal{G}_{\mathrm{c}}$ [kJ/m^2]	$\sigma_{\max}$ [MPa]	δ_{ext} [mm]	$\delta_{\max}$ [mm]
DCB-6-01	4.54	1.26	3.47	5.2
DCB-6-02	4.98	1.29	3.79	5.2
DCB-6-03	4.06	1.35	3.00	4.1
DCB-6-04	5.33	1.27	4.73	5.4
DCB-6-05	5.50	1.35	4.25	5.5
DCB-6-06	5.73	1.28	4.64	5.8
DCB-6-07	4.42	1.35	3.33	4.6
Average	4.94	1.31	3.89	5.1
Std. dev.	0.62	0.04	0.67	0.6

Table 4.7: Results of the DCB-12 test series extrapolating the traction-separation law

Specimen	$\mathcal{G}_\mathrm{c}$ [kJ/m^2]	σ_max [MPa]	δ_ext [mm]	δ_max [mm]
DCB-12-01	2.55	0.73	4.95	5.2
DCB-12-02	3.72	0.88	6.00	6.0
DCB-12-03	3.61	0.90	4.39	5.6
DCB-12-04	3.62	0.90	4.94	5.8
DCB-12-05	3.64	0.88	5.60	5.7
DCB-12-06	4.74	0.91	6.43	7.0
DCB-12-07	4.99	0.93	6.54	7.0
Average (02-07)	4.06	0.90	5.65	6.2
Std. dev.	0.63	0.02	0.85	0.7

Method based on Finite Element Analysis

The evaluation procedure described in section 3.9.3 is based on the idea illustrated in figure 3.35. The region in the vicinity of a crack is represented as a cohesive layer with the mechanical behaviour being defined in the traction-separation law. Prior to the onset of a crack, which can be seen as a rupture of material, the cohesive layer exhibits some damage initiation. This damage initiation is characterised by decreasing values in the traction-separation law. In the case of the test series DCB-6 however, the initially inserted crack grows before the traction decreases to zero. The key question therefore is to localise the onset of the crack, in order to determine the work performed by the material, before the crack propagates.

This question of fracture initiation of adhesive joints has been discussed by Dean et al. (2004), where failure of bonded connections with a rubber-toughened glassy polymer was investigated. The failure point was identified as the position of the force-deformation curve, where the numerically predicted values start to differ from the measured curves. Failure initiation was assumed as the reason for this observed deviation. This deviation was supposed to result from failure initiation due to crack onset. For this procedure, the accurate prediction of the material behaviour is a fundamental requirement.

Considering figure 4.67, the point, where the numerically predicted values start to differ from the experimentally recorded data is found at 6 mm for the DCB-12 test series. Considering figure 4.63b, this value is in good agreement with the crack opening displacement at crack onset. Applying this method to the DCB-6 test series, the crack initiation can be identified at a crack opening displacement of 2.5 mm. Recalling equation 3.63, the critical energy release rate can be determined as

$$J_\mathrm{c} = \int_0^{\delta_\mathrm{c}} \sigma\left(\delta\right) \mathrm{d}\delta \qquad \text{with } \delta_\mathrm{c} = 2.5\,\mathrm{mm}. \tag{4.13}$$

The results applying the FEA method are given in table 4.8.

Table 4.8: Results of the DCB tests using the FEA method

	Test series DCB-6		Test series DCB-12	
Specimen	$\mathcal{G}_{\mathrm{c}}$ [kJ/m^2]	$\sigma_{\max}$ [MPa]	$\mathcal{G}_{\mathrm{c}}$ [kJ/m^2]	$\sigma_{\max}$ [MPa]
01	2.72	1.26	N/A	N/A
02	2.80	1.29	3.72	0.88
03	2.90	1.35	4.01	0.90
04	2.75	1.27	4.10	0.90
05	2.90	1.35	3.69	0.88
06	2.50	1.28	4.31	0.91
07	2.50	1.35	4.41	0.93
Average	2.72	1.31	4.04	0.90
Std. dev.	0.17	0.04	0.29	0.02

Summary of the results

Table 4.9 summarises the results obtained for the critical energy release rate $\mathcal{G}_{\mathrm{c}}$, the mode I strength $\sigma_{\max}$ and the maximum crack opening displacement $\delta_{\max}$ using the above discussed evaluation methods.

Table 4.9: Summary of the parameters determined using the DCB tests

Specimen	$\mathcal{G}_{\mathrm{c}}$ [kJ/m^2]	$\sigma_{\max}$ [MPa]	$\delta_{\max}$ [mm]
"Classic method"			
DCB-6	evaluation not possible		
DCB-12	4.01$\pm$0.67	0.90$\pm$0.02	5.89$\pm$0.75
Method using linear extrapolation			
DCB-6	4.94$\pm$0.62	1.31$\pm$0.04	5.1$\pm$0.6
DCB-12	4.06$\pm$0.63	0.90$\pm$0.02	6.2$\pm$0.7
Method using Finite Element Analysis			
DCB-6	2.72$\pm$0.17	1.31$\pm$0.04	2.5
DCB-12	4.04$\pm$0.29	0.90$\pm$0.02	6.0

The critical energy release rate of Dow Corning® 993 structural silicone sealant has been determined in Double Cantilever Beam tests investigating two adhesive layers. The J-integral approach has been used to determine the cohesive properties (traction-separation law) and the critical energy release rate of the adhesive. Unlike as for the test series with an adhesive thickness of 12 mm, the traction-separation law determined for the thin adhesive layer with a thickness of 6 mm didn't allow for a direct calculation of the critical energy release rate. Therefore, two different engineering approaches have been used, one consisting in a linear extrapolation of the traction-separation law and one based on a Finite Element Analysis. For the method based on linear extrapolation, the critical energy release rate is found to decrease with the layer thickness. This finding is not in line with the behaviour observed for other types of adhesives and thus judged implausible. The method based on a Finite Element Analysis gives plausible results and the order of magnitude found is similar to DCB tests carried out

on a one-component room temperature vulcanising silicone, which was investigated in Banea et al. (2010).

5 Identification of a failure criterion for silicone bulk material

5.1 Introduction

5.1.1 Methodology

In this section, the failure criteria, which have been introduced in section 3.4, are investigated. In a first step, the tensile and circular shear tests were considered. These tests have been numerically reproduced using a commercial Finite Element software code. A good agreement has been found between the experimentally recorded and numerically reproduced force-deformation curves (cf. section 4.1.1 for the uniaxial tensile tests and section 4.2.2 for the circular shear tests). In this section, the loads or displacements at crack initiation were applied on the numerical models and the stress or strain distributions in the silicone sealant were investigated regarding the different failure criteria introduced in section 3.4. The numerical model of the uniaxial tension test was taken as a reference and was compared with the results of the unnotched circular shear test.

In a second step, the proposed failure criterion was validated using the compression test data. Since only tension, shear and compression test data were considered in the framework of this thesis, the proposed failure criterion has limited validity. On the one hand, bonded connections with high amount of hydrostatic tensile stresses, as found in thin butt bonded cylinders under axial tension, cannot be assessed assuming an incompressible material law. Moreover, failure of these configurations is governed by the so-called *cavitation*. On the other hand, complex geometries should not be assessed either, since no biaxial test data has been used to calibrate the failure criterion. The proposed failure criterion can be used for bonded connections with silicone in form of a linear bead, as found in façade applications, which were shown in section 3.2.

5.1.2 Preliminary considerations

As the failure criterion uses the results of numerical models, a fundamental requirement consists in two aspects. First of all, the behaviour of the considered components must be accurately reproduced. This has been checked for the tension, shear and compression specimens in the corresponding sections. A good agreement has been found between the experimentally recorded and the numerically reproduced global force-deformation behaviour. Moreover, convergence of the stresses and strains is essential for their assessment with a failure criterion. If the values of the acting stresses and strains depend on the chosen discretisation of the component, these values become into some extend arbitrary. The failure load prediction in case of non-converging stresses, as observed for the simple shear specimens, will be subject of chapter 6.

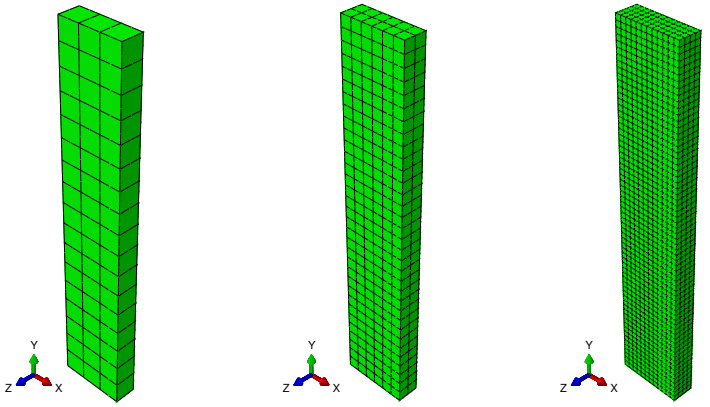

(a) Coarse mesh (b) Medium mesh (c) Fine mesh

Figure 5.1: Finite element mesh for the uniaxial tensile test specimen

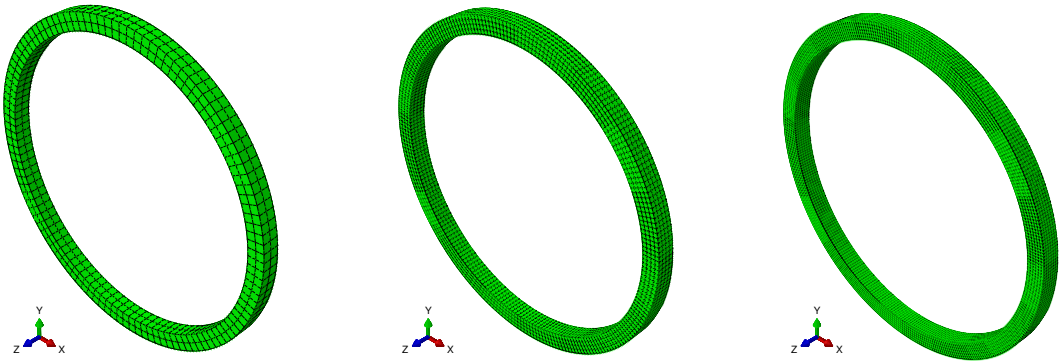

(a) Coarse mesh (b) Medium mesh (c) Fine mesh

Figure 5.2: Finite element mesh for the circular shear test specimen

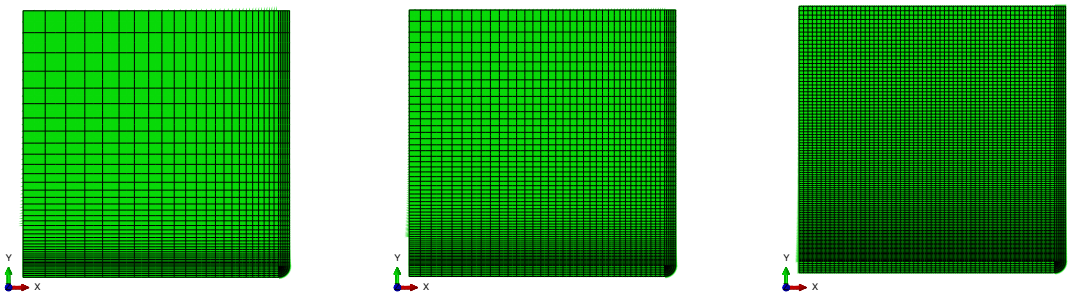

(a) Coarse mesh (b) Medium mesh (c) Fine mesh

Figure 5.3: Finite element mesh for the compression test specimen

In order to check the convergence of the results of the numerical simulations in terms of stresses and strains for the tensile, shear and compression specimens, three different numerical models have been built for each specimen. The investigated Finite Element models are visualised in figure 5.1, figure 5.2 and figure 5.3. A coarse, medium and fine mesh

were investigated for each specimen. The results are summarised in table 5.1. The values of the principal stress σ_1 and the strain magnitude ε_{M} are given for three different mesh sizes. A good convergence was found for the stresses and strains. For the compression test specimen, the numerical model assuming a friction coefficient of $\mu = 0.1$, which exhibited good agreement with the experimental data, was considered.

Table 5.1: Mesh study on the stresses and strains

Test	Number of elements	σ_1 [MPa]	ε_{M} [-]
Tension	51	8.290	1.607
	396	8.290	1.607
	3168	8.290	1.607
Circular shear	466	5.300	1.634
	3714	5.376	1.634
	12528	5.407	1.640
Compression	2103	1.328	1.730
($\mu = 0.1$)	3611	1.328	1.730
	8368	1.330	1.731

In section 3.4, different failure criteria have been introduced. A differentiation was made between stress-, strain- and energy-based criteria. For the stress-based criteria, the maximum principal stress (*Rankine*) criterion and the *von Mises* equivalent stress have been considered. For the strain-based criteria, the maximum principal strain criterion and the strain magnitude were investigated. Finally, the strain energy density was selected amongst the group of the energy-based failure criteria.

5.2 Calibration of a failure criterion

The tensile tests have been numerically reproduced as described in detail in section 4.1.1. Three load levels have been investigated: the average failure load, the average failure load with the standard deviation subtracted and added. For these load levels, the selected failure criteria were evaluated using the results of the conducted Finite Element Analysis.

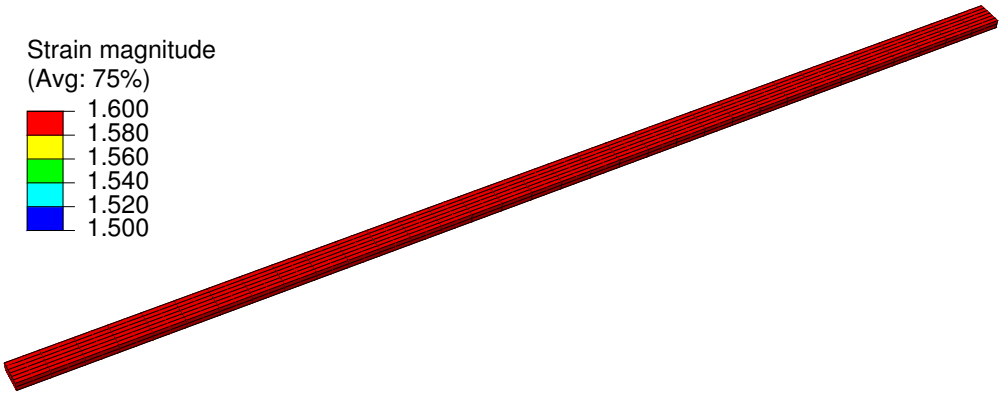

Figure 5.4: Plot of the strain magnitude for the uniaxial tensile test specimen at the average failure load

The distribution of the strain magnitude for the uniaxial tensile test, subjected to its experimentally determined average value for the failure strain, is given in figure 5.4. A uniform

distribution is obtained in the reproduced area of parallel edges. As mentioned in section 4.1.1, failure was observed in this region.

In the second step, the same procedure was applied for the circular shear tests on the unnotched specimens. Neither the notched circular specimens, nor the simple shear specimens have been considered, as they exhibit a stress singularity, thus not fulfilling the second requirement about converging stresses and strain, discussed in section 5.1.2. Moreover, crack onset was observed at the singularity for the simple shear specimens. For the unnotched circular shear specimens, the numerical model described in section 4.2.2 was employed and the resulting stress, strain and strain energy distributions have been investigated for the three previously described load levels (average failure load applied, failure load with added and subtracted standard deviation). Figure 5.5 shows the distribution of the strain magnitude for the circular shear test with the average failure rotation applied. The maximum value for the strain magnitude appears at the inner adherend. The same is true for the stress- and energy-based criteria. The value of the strain magnitude at the outer substrate is 20% lower than the maximum value.

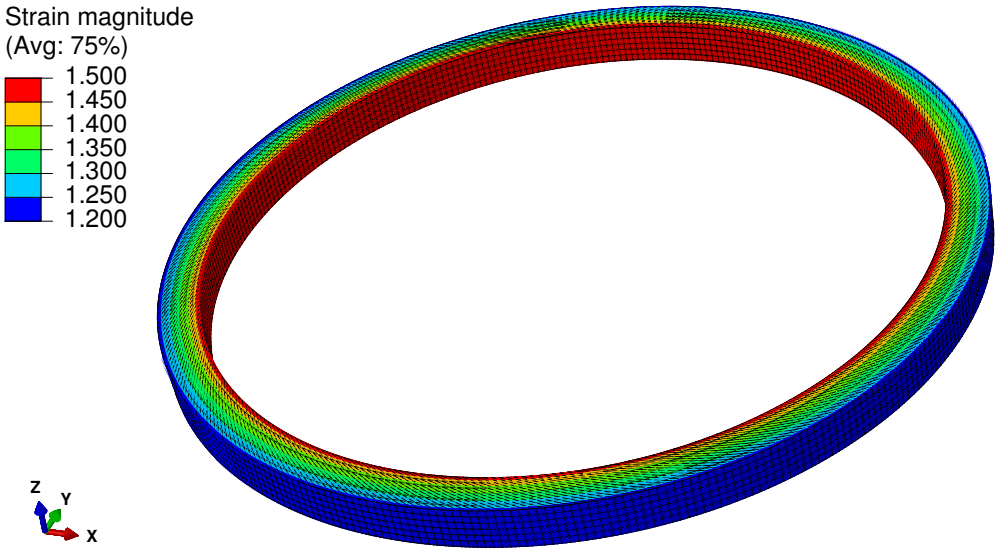

Figure 5.5: Plot of the strain magnitude for the circular shear test specimen at the average failure load

Table 5.2 summarises the values obtained for the different equivalent stresses and strains considering the stress and strain distributions of the tensile and circular shear specimens at their respective failure loads. Apart from the values at the average failure loads, the failure loads with the standard deviation added (referred to as *Max.*) and subtracted (referred to as *Min.*) are given as well. The values listed in table 5.2 are plotted in figure 5.6. The *relative strength* given on the vertical axis is the ratio of the obtained equivalent stress, strain or energy, found for the applied failure load in tension or shear, divided by the value obtained in the tensile test for its failure load. Consequently, as the uniaxial tensile test is the reference, its relative strength is 1 for each failure criterion.

Table 5.2: Comparison of the failure criteria considering the tensile and circular shear specimens

		Uniaxial tension			Circular shear		
Failure criterion		Min.	Average	Max.	Min.	Average	Max.
Hydrostatic pressure	[MPa]	-2.76	-2.67	-2.62	-1.43	-1.07	-0.79
Rankine	[MPa]	7.86	8.02	8.29	3.16	4.14	5.38
von Mises	[MPa]	7.86	8.02	8.29	3.58	4.66	5.94
Strain energy density	[N/mm]	3.32	3.41	3.49	1.43	1.94	2.57
Max. principal strain	[-]	1.29	1.3	1.32	0.92	1.04	1.15
Strain magnitude	[-]	1.58	1.59	1.61	1.31	1.47	1.63

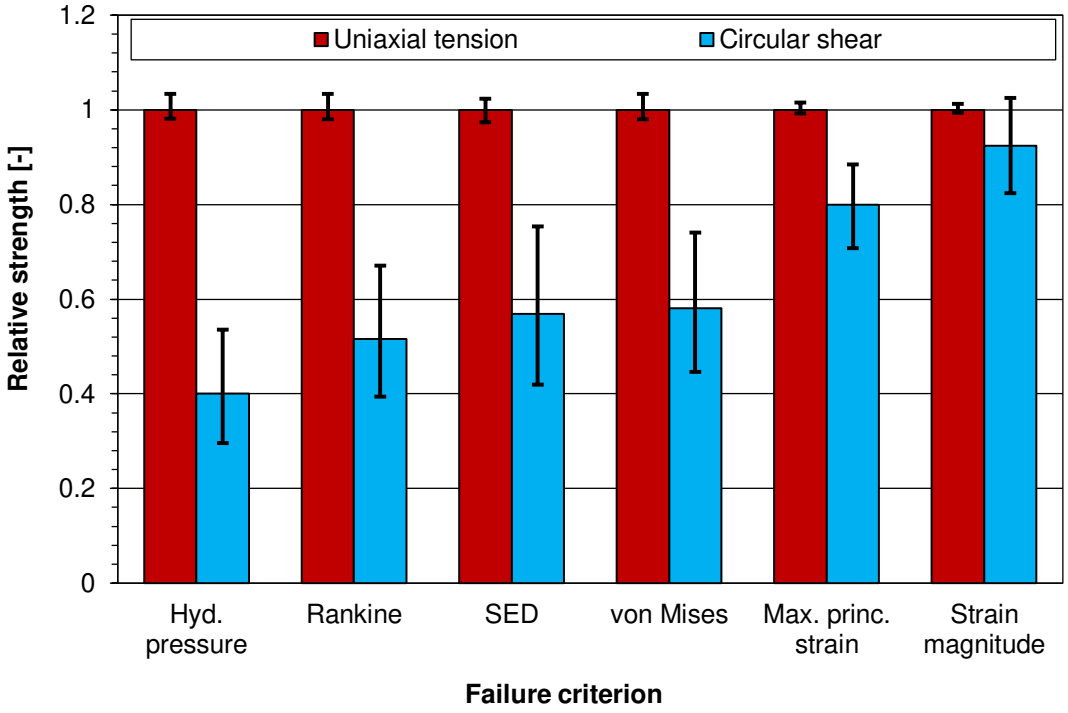

Figure 5.6: Comparison of the results regarding different failure criteria

At their respective failure loads, the values found for the hydrostatic pressure, the maximum principal stress, the strain energy density and the equivalent stress according to *von Mises* show poor agreement between the tensile and circular shear specimens. The threshold values at failure initiation regarding these failure criteria are significantly lower in the circular shear specimen, compared to the tensile test specimen. A different situation can be observed for the strain-based failure criteria. The values obtained for the maximum principal strain are in a comparable order of magnitude comparing the two considered stress states. Finally, at their respective failure displacements, the values for the strain magnitude found in the tensile and circular shear numerical models show a good agreement. Therefore, the strain magnitude will be investigated in more detail in the following sections.

5.3 Validation of the proposed failure criterion

The previous section has shown that the strain magnitude is a suitable failure criterion for the silicone bulk material considering tension and shear stress states. In this section, the failure criterion is validated using the compression test data. In section 4.1.2, the failure point for compression has been identified as the load level, for which the residual deformation strongly increased. This strong increase was referred to internal damage of the material and has been experimentally recorded at 60% applied engineering compression strain.

The compression test specimen has been numerically reproduced taking into account for the friction occurring between the specimen and the compression plates (cf. section 4.1.2). Good agreement was obtained between the experimental stress-strain curves and their numerical simulation. The obtained distribution of the strain magnitude for the compression test specimen is given in figure 5.7 for an applied engineering compression strain of 60%, which was identified as the threshold level for damage onset. Figure 5.7 shows that due to friction, the lateral surface comes into contact with the compression plates. In order to avoid excessive mesh distortion at the edge, a rounding of 0.25 mm was inserted. The maximum values for the strain magnitude are found at the centre of the specimen. It is pointed out that only one fourth of the specimen's section is shown, since a 2D axisymmetric analysis was performed with symmetry in vertical direction assumed.

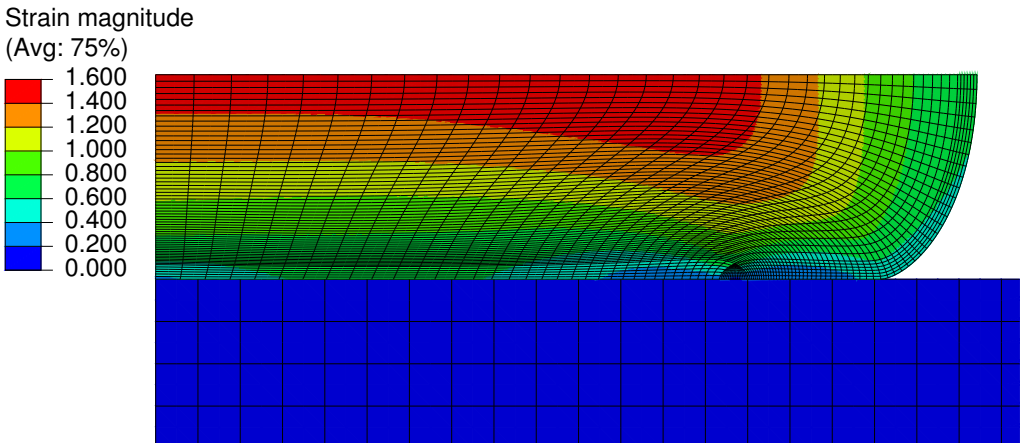

Figure 5.7: Plot of the strain magnitude for the compression test specimen at failure initiation

In figure 5.8, the maximum value for the strain magnitude in the compression specimen is plotted against the applied engineering compression strain. Since the influence of friction cannot be clearly assessed, the curves for different friction coefficients are given. Considering the results for a friction coefficient of $\mu = 0.1$, which gave a good estimation of the force-deformation behaviour, a maximum strain magnitude of $\varepsilon_{\mathrm{M}} = 1.5$ has been obtained for an engineering compression strain $\varepsilon_{\mathrm{e,UC}} = -0.6$. The location of the maximum value of the strain magnitude is in the centre of the compression test specimen, as shown in figure 5.7.

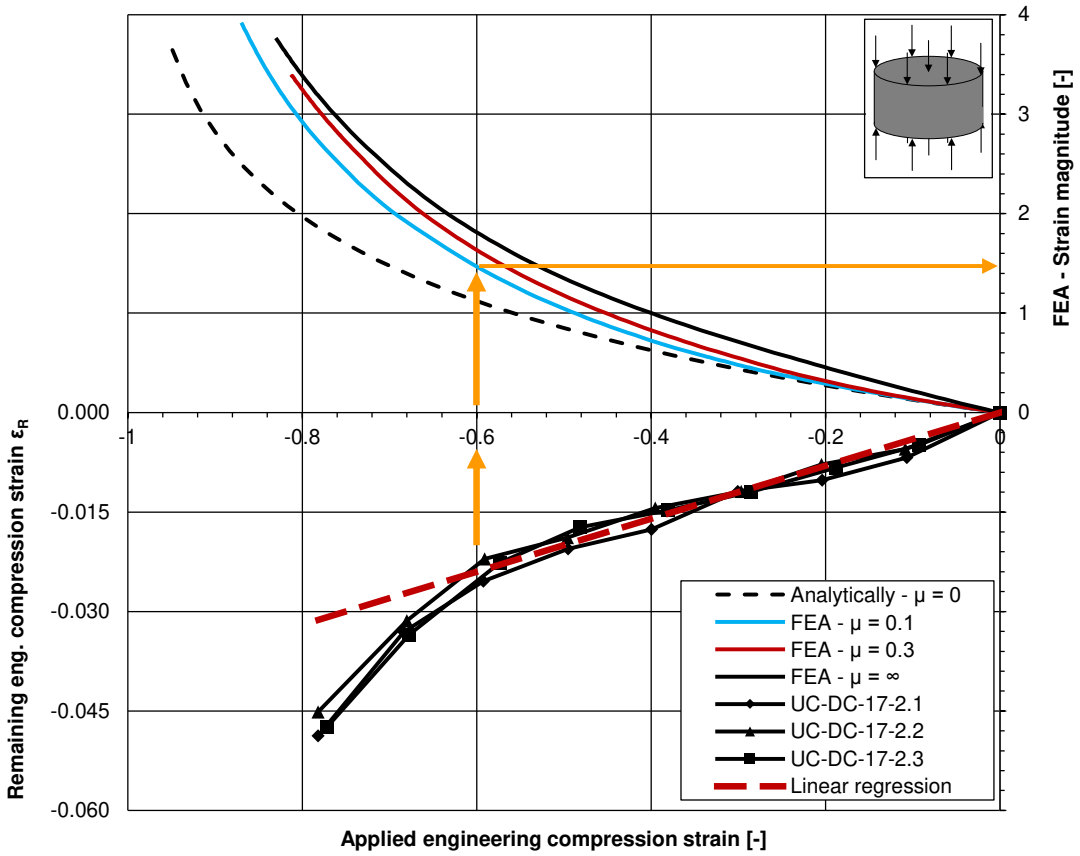

Figure 5.8: Maximum value of the strain magnitude in the compression test specimen

The strain magnitude is a failure criterion based on true (logarithmic) strains. Physically, it can be seen as a measure for the stretch of the molecular chains. Considering equation 3.41, it describes a sphere centred at the origin of the space of true principal strains, as shown in figure 5.9. Unlike as for the maximum principal strain criterion, the contribution of all strain components are taken into account. Thus, failure does not only occur, when the material is stretched in tension, but also when it is highly compressed.

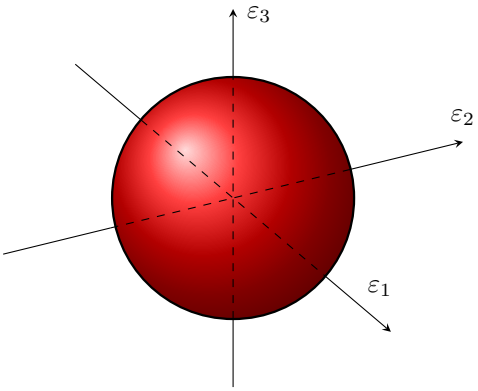

Figure 5.9: Representation of the strain magnitude as a failure surface in the space of true principal strains

5.4 Summary

Failure of bulk material has been investigated considering the experimental results obtained for the tests described in chapter 4.1 (uniaxial tension and compression) as well as the unnotched circular shear tests described in section 4.2.2. With the nonlinear numerical simulations of the tensile and circular shear tests, the strain magnitude has been identified as a suitable failure criterion for these tests. The proposed failure criterion has been validated with the results of the compression tests. In fact, for the identified failure initiation point at 60% engineering compression strain, a value for the strain magnitude close to $\varepsilon_{\mathrm{M}} = 1.6$, which was calibrated in the uniaxial tensile test, has been obtained in the centre of the compression specimen using a Finite Element Analysis.

The proposed failure criterion has been validated on bulk material with no stress singularities. Therefore, neither the simple shear, nor the notched circular shear, nor the tensile tests on the H-shaped specimens, have been considered. In addition, as only tension, compression and shear were investigated assuming incompressible hyperelastic material behaviour, the proposed failure criterion should not be used for silicone bonded connections with high amount of hydrostatic tensile stresses, as found in butt bonded cylinders with small adhesive layer thickness or for complex geometries.

6 Failure load discussion of bonded connections

6.1 Introduction

In chapter 5, failure of defect-free bulk material has been investigated and the strain magnitude has been identified as a suitable strain-based failure criterion. The performed investigations were based on Finite Element Analysis and the stress solutions gave convergent results, which was considered as a fundamental requirement for assessing the different characteristic stress states. This convergent behaviour is no longer given, when bonded connections with edge areas are considered. Due to the sharp change of the geometry and the elastic constants, a singularity is found, the so-called *two-material wedge*. When the stress or strain distributions are analysed with the Finite Element Method, the values of stresses or strains depend on the size of the elements and on their formulation. A direct assessment of the stresses is therefore not possible. The stress distribution in bonded connections has been intensively discussed in section 3.5. Methods have been presented, which take into account for the stress singularity at the interface between adhesive and substrate.

In this chapter, the test results given in chapter 4.2 are investigated regarding the failure initiation. The performed investigations are based on Finite Element models, which have been presented in the respective sections, describing the numerical simulation of the considered test series. The simple shear tests, the notched circular shear test and the tension test according to ETAG 002 (2012) have been considered for the subsequent investigations.

In section 6.2, the load bearing capacity of the different tests is predicted using the design equations given in ETAG 002 (2012) and using the analytical solution for the shear and peel stress distributions in single-lap shear joints proposed by Allman (1977).

In section 6.3, a concept from Finite Fracture Mechanics has been applied on the simple shear test data. The so-called *coupled stress and energy criterion*, proposed by Leguillon (2002) and successfully employed by Weißgraeber (2014) to predict crack initiation of single-lap shear joints with linear elastic adhesive, has been extended to nonlinear elastic material behaviour.

Section 6.4 gives some results using the Theory of Critical Distances, following three different approaches: choosing a constant element size and formulation for the description of the stresses in the vicinity of the notch, averaging the strain energy density in a control volume around the notch and evaluating the stresses or strains at a certain distance from the singularity.

6.2 Analytical models

6.2.1 Failure load prediction according ETAG 002 (2012)

The design concept according to ETAG 002 (2012) has been presented in section 3.2.5. It is based on the assumption of a uniform stress distribution inside the sealant. In this section, the set of test data is analysed following the design approach given in ETAG 002 (2012). For the engineering shear strength τ_{des} and tensile strength σ_{des}, the engineering stresses of the 50-12 specimen in simple shear and tension are taken respectively. Considering table 4.4, $\tau_{\mathrm{des}} = 0.855\,\mathrm{MPa}$ and from section 4.2.3, $\sigma_{\mathrm{des}} = 1.150\,\mathrm{MPa}$. In contrast to ETAG 002 (2012), τ_{des} and σ_{des} are not fractile values divided by a design factor, but average values.

According to ETAG 002 (2012), the acting shear stress is independent of the adhesive overlap length and thickness. Therefore, for all the simple shear test series, the predicted engineering shear stress at failure equals τ_{des}. The same is true for the circular shear specimen. Figure 6.1 summarises the failure load prediction for the different test series. Very good agreement is found for the simple shear test series with 12 mm adhesive thickness, since the shear strength was calibrated using this test series and since failure does not depend on the overlap length for the considered dimensions. Very good agreement can also be found for the ETAG-Tension series, since the strength was calibrated using this test data.

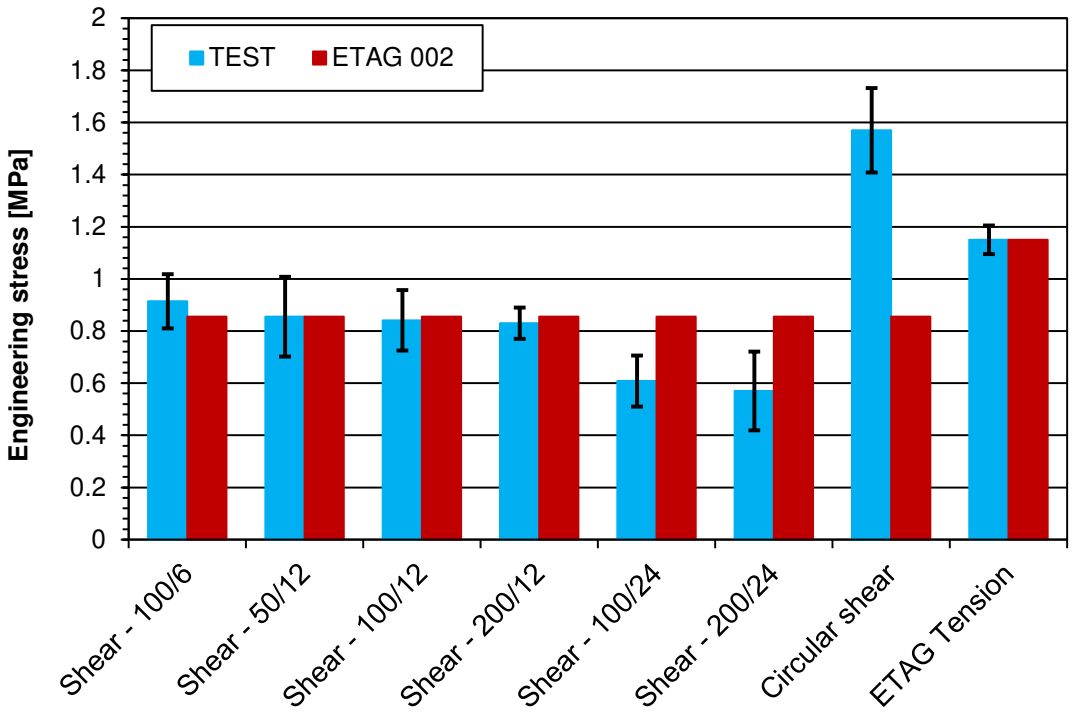

Figure 6.1: Results of the failure load prediction using the design concept given in ETAG 002 (2012)

The design equations proposed by ETAG 002 (2012) or ASTM C1401 (2002) only consider average shear stresses, which can be observed in the plane at mid-height of the adhesive joint. The failure process however is dominated by the two-material wedge, which is located at the interface between adhesive and adherend. Therefore, the design approach cannot reproduce the adhesive thickness effect, which has been experimentally observed.

6.2.2 Failure load prediction according *Allman*

In section 3.5.1, the stress distribution in a single-lap shear joint proposed by Allman (1977) has been presented. Unlike as for the Volkersen equation, the stress distribution according to Allman fulfils the stress-free edge condition. As only single-lap shear joints are covered by the analytical approach, this section focus on the simple shear test series. The equations for the stress distribution in the single-lap shear joint for the *Allman* approach are given in section 3.5.1, equation 3.45. The adherends have been assumed as rigid and the sealant as incompressible. The Volkersen equation has not been considered subsequently, since it predicts a constant shear stress distribution for the combination of rigid adherends with a soft adhesive.

According to the *Allman* equation, the maximum stress values are found for the peel stresses at the free edge of the adhesive interface. Regarding the peel strength, the 100-12 test series is taken as a reference with the adhesive assumed as incompressible and the adherends as rigid compared to the sealant. Figure 6.2 gives the summary of the failure load prediction according to the *Allman* solution.

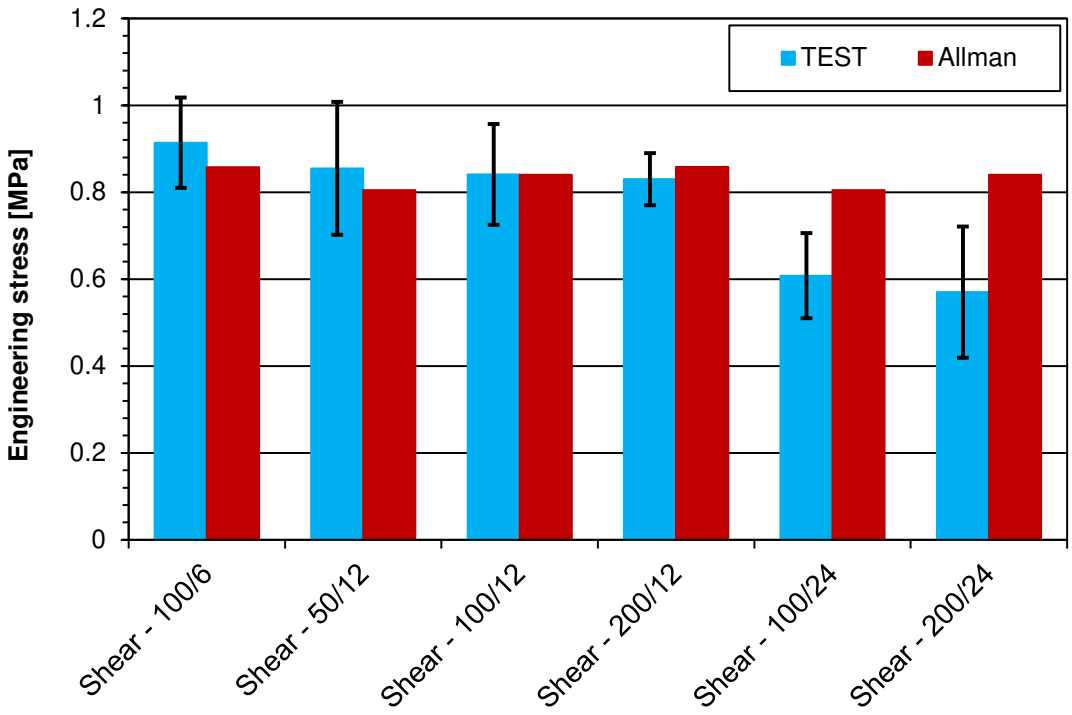

Figure 6.2: Results of the failure load prediction using the *Allman* solution

Considering the results given in figure 6.2, the failure loads are found to decrease with the adhesive thickness. This trend is observed as well in the tests, but to a much larger extend. Concerning the adhesive overlap length, the failure engineering shear stresses are found to increase slightly. This trend however has not been observed in the tests. Although the *Allman* equations consider the peel stresses at the interface, they cannot reproduce the experimentally observed findings.

6.3 Finite Fracture Mechanics

6.3.1 Introduction

The simple shear tests have been numerically reproduced and the concepts described in section 3.7 have been employed to predict the crack onset, referred to as failure initiation points, which were experimentally determined and presented in section 4.2.1. The results given in this section have been presented at the 14th International Conference on Fracture on Rhodos in 2017 (Rosendahl et al., 2017).

The coupled criterion has been described in section 3.7. It is based on two partial criteria - the stress criterion and the energy criterion. For a given structure, the applied load or displacement at crack onset and the initiated crack length are unknown. If the acting stresses exceed the strength of the bulk material over the whole area of the predicted crack and if this crack releases enough energy for its onset (i.e. if the incremental energy release rate exceeds the critical energy release rate of the material), the two partial criteria are fulfilled and the load at crack onset is found. As mentioned in section 3.7, this leads to an optimisation problem, in which the load at crack onset and the crack length need to be determined. In order to solve this problem, the strength of the bulk material and the critical energy release rate must be known.

6.3.2 Basic assumptions and numerical model

In the original work of Leguillon (2002), a stress failure criterion was adopted to assess whether the strength of the bulk material was exceeded. In Weißgraeber (2014), the maximum principal stress was selected to evaluate the stress criterion for the single-lap shear joint connection investigated. In the following, the stress criterion is modified to a strain-based criterion. As shown in section 5, the strain magnitude, defined as

$$\varepsilon_{\mathrm{M}} = \sqrt{\varepsilon_1^2 + \varepsilon_2^2 + \varepsilon_3^2}, \tag{6.1}$$

with ε_1, ε_2, ε_3 the three true principal strains, has been identified as a suitable failure criterion for the silicone bulk material. Apart from the strain magnitude, the mode I strength, as determined in the DCB tests in section 4.3, has been selected as well in preliminary studies.

Apart from the failure criterion, the critical energy release rate must be known to assess the energy partial criterion. For the subsequent analysis, the critical energy release rate, as determined in section 4.3 for the specimens with an adhesive layer thickness of 12 mm, has been adopted.

The simple shear tests, presented in section 4.2.1 have been numerically reproduced in a nonlinear 2D Finite Element analysis, using the commercial Finite Element software code ABAQUS® (Dassault Systèmes, 2014). Bonded connections are often modelled assuming plane strain conditions (e.g. Da Silva and Campilho (2012)), since the thickness is small compared to the bite dimension. Typically, for these assemblies, the adhesive thickness is much smaller than the bite dimension. For the investigated bonded connections with silicone however, the bite dimension is in the same order of magnitude than the thickness. Therefore, plane stress conditions were assumed.

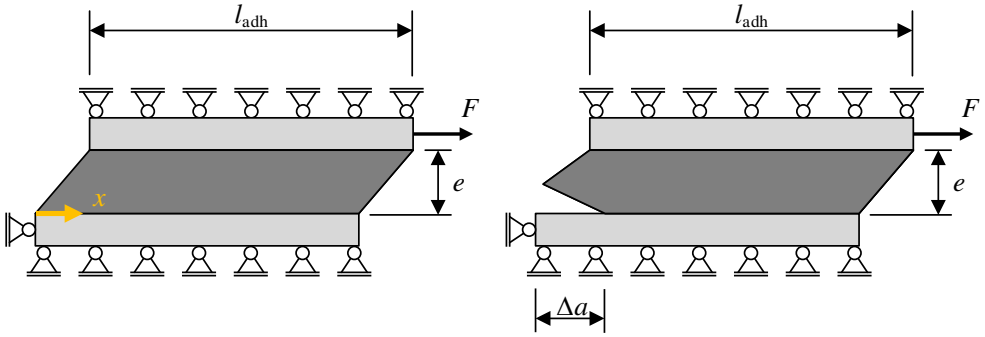

(a) Model for the stress criterion (b) Model for the energy criterion

Figure 6.3: Numerical models of the simple shear test specimen for the coupled criterion

The silicone sealant was modelled assuming an incompressible material behaviour with the hyperelastic material law according to Marlow (2003). The stress-strain curve of the uniaxial tensile tests presented in section 4.1.1 was used to characterise the chosen material law. The boundary conditions of the specimens are given in figure 6.3. Simple shear conditions were assumed, since the distance between the adherends was kept constant during the tests. The adherends have been assumed as rigid.

For the evaluation of the stress partial criterion, the model given in figure 6.3a was employed. The stresses or strains were evaluated on the horizontal interface path indicated. For the energy partial criterion, the numerical model shown in figure 6.3b was employed. Straight interface cracks were investigated. For a given applied load, the energy release rate was determined considering the difference of potential energies prior and after initiation of a crack with finite length Δa.

Concerning the critical energy release rate, the values given in table 4.5 (Average 01-05) have been employed. For the failure criterion, the mode I strength determined from the DCB test was used in first step as a stress-based failure criterion (independently of the findings of chapter 5). In a second step, the strain magnitude was adopted as a strain-based failure criterion.

6.3.3 Results

The results of the evaluation of the crack initiation loads of the simple shear tests using the coupled criterion are given in figure 6.4. The experimentally recorded engineering shear stress at crack initiation (cf. section 4.2.1) are compared with the results from the coupled criterion. As aforementioned, two different failure criteria were adopted, one stress-based, the mode I strength as determined in the DCB test and the strain magnitude as a strain-based failure criterion for silicone bulk material.

A good agreement was found between the experimental data and the predictions made using the coupled criterion, especially for the specimens with a layer thickness of 12 mm, since the critical energy release rate was determined on specimens with this adhesive layer thickness. For the specimens with 6 mm layer thickness, the crack initiation load is overestimated. The results of section 4.3 showed that the critical energy release rate of the thin specimens (6 mm

layer thickness) were considerably lower. Consequently, the energy criterion is fulfilled for smaller cracks or at a lower load level. The difference observed for the specimens with 24 mm layer thickness could be due to the presence of defects. The number of defects in thick adhesive joints is generally estimated higher than in thin layers, as discussed in section 3.5.1.

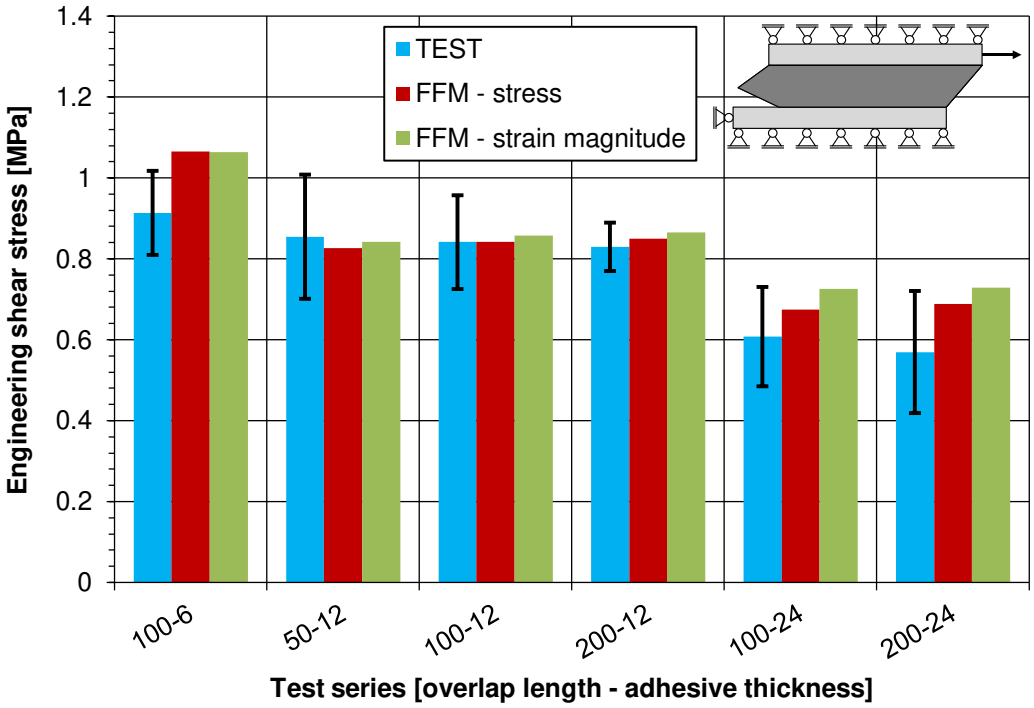

Figure 6.4: Results of the failure load prediction using Finite Fracture Mechanics. The standard deviation is shown for the test results

Concerning the results assuming the strain magnitude as a failure criterion, the predicted finite crack length at crack onset was found almost constant with a value of 2.5 mm for all the considered specimens.

6.3.4 Summary and outlook

In the present investigations, the coupled stress and energy criterion, initially developed by Leguillon (2002) and applied for the failure load prediction of adhesively bonded joints with linear elastic material behaviour by Weißgraeber and Becker (2013), has been applied for the first time on hyperelastic materials. Furthermore, a strain-based failure criterion was employed instead of a stress-based one. With the two material parameters strength and critical energy release rate of the silicone bulk material, the adhesive thickness effect was well predicted, based on a physically sound model. For the investigated simple shear geometries, a constant crack length was found.

In a next step, the circular shear tests will be analysed with the coupled criterion. For these specimens, the difference between the notched and unnotched specimens was very small. This means that the notched specimens failed, when the bulk strength has been reached in the bulk material. Regarding the two-material wedge, the stress criterion is largely fulfilled.

However, if failure does not occur, the energy criterion cannot be met. A predominant mode II could be a possible explanation for this behaviour.

6.4 Theory of Critical Distances

6.4.1 Choosing a constant element size and formulation

In a first approach, a very simple procedure has been employed to predict the failure loads or displacements for the different test series. As described in section 3.8 in the framework of the Theory of Critical Distances, a constant element size and element formulation has been used to represent the sealant in the vicinity of the respective notch. The simple shear tests with different adhesive layer thicknesses, the notched circular shear test, the tensile test on the H-specimens as detailed in ETAG 002 (2012) and the DCB test specimens have been numerically reproduced using the commercial Finite Element software code ABAQUS® (Dassault Systèmes, 2014). Details about the different numerical models can be found in the respective sections. For all these models, the same element type, a second order, hybrid and fully integrated solid element (C3D20H), has been chosen. The size of the elements in these numerical models was fixed to 1 mm in the vicinity of the notch. The following investigations focus on the distribution of the strain magnitude, since it has been identified as a suitable failure criterion in chapter 5.

In the first step, the numerical model of the simple shear specimen with 12 mm layer thickness was considered at the crack initiation displacement with the above mentioned element size and formulation. At the experimentally determined crack initiation displacement, a value for the strain magnitude of $\varepsilon_{\mathrm{M}} = 1.6$ was found at the two-material wedge. This value is considered as a threshold value and corresponds to the bulk material strength. However, for a different element size, a different threshold value would be obtained.

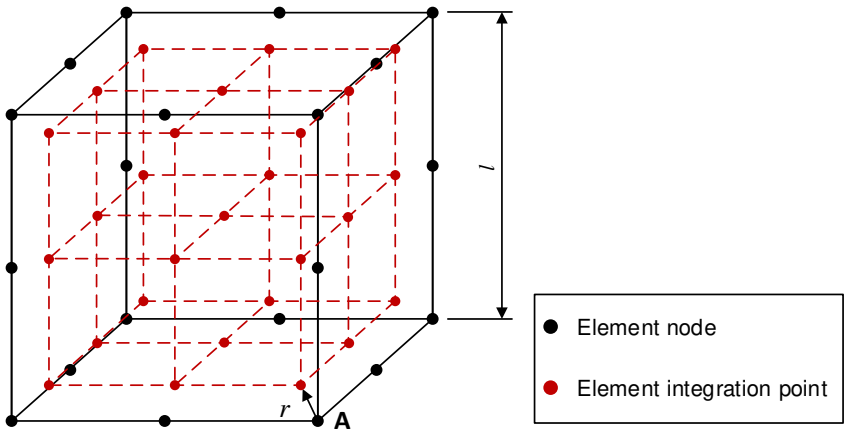

Figure 6.5: Location of the element's nodes and integration points

Figure 6.5 shows schematically the location of the nodes and integration points of a second order element, like C3D20H. The element is composed of 20 nodes and 27 integration points, where the stresses and strains are actually computed. The values at the nodes are extrapolated and averaged with the values of neighbouring nodes. If the notch tip is located at

point **A** in figure 6.5, the distance r for an element with equal corner length l can be computed knowing the location of the integration points as $r = \frac{l}{2}\sqrt{3\ \left(1-\sqrt{0.6}\right)^2}$. Consequently, for an element size of 1 mm, a distance $r = 0.195$ mm is obtained. This distance is considered as the characteristic material dimension for the silicone sealant. Since the stress values are most accurate at the integration points, the strain magnitude is evaluated as well on the integration point, which is closest to the notch tip. Considering the values of the strain magnitude at the integration point corresponds to the *point method* as described in section 3.8. Taking into consideration the values at the integration point for a 1 mm second order fully integrated element, the length scale parameter L gives 0.39 mm. Again, the same numerical model of the simple shear specimen with 12 mm adhesive thickness has been considered with the experimentally determined crack initiation displacement applied. For the integration point closest to the maximum nodal value of the strain magnitude, a threshold value for the strain magnitude of $\varepsilon_{\mathrm{M}} = 1.45$ was obtained.

Simple shear specimen

Figure 6.6 shows the plot of the strain magnitude for the applied failure displacement of the simple shear test series 50-12. Two areas showing high values of the strain magnitude can be identified. The first area is located in a region of highly distorted elements, which are compressed against the adherend. As the results of these highly distorted elements are questionable, the region at the lower corner edge has been considered for evaluating the strain magnitude.

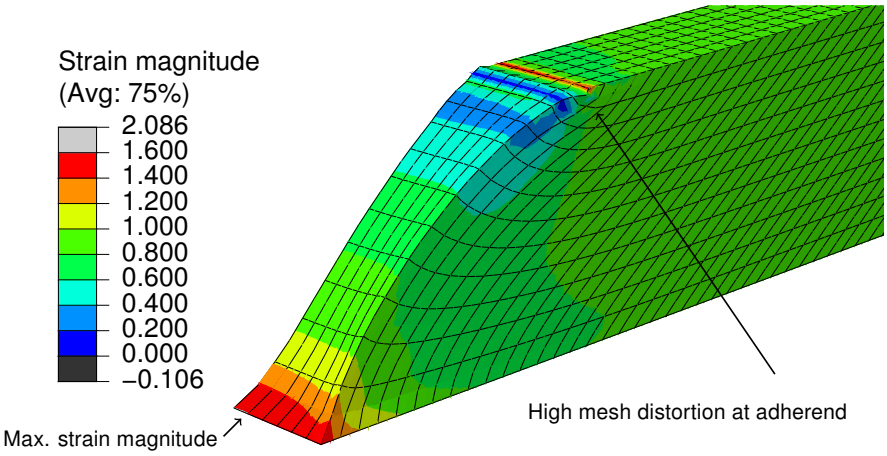

Figure 6.6: Plot of the strain magnitude in the simple shear specimen

The maximum value of the strain magnitude (at the bottom corner edge) is plotted against the applied engineering shear strain in figure 6.7 for the three considered adhesive layers. Both the values at the element's node and the corresponding integration point are given. For each layer thickness, the intersection of the material strength with the calibrated threshold values gives the predicted crack initiation strain. For the selected element size of 1 mm, the threshold value for the strain magnitude was found 1.6 for the nodal solution and 1.45, when the values at the integration point were considered. Figure 6.7 shows that the engineering shear strain obtained at the intersection of the threshold value with the strain magnitude decreases with increasing layer thickness. The values, shown in figure 6.14, are in a very good agreement with the experimentally recorded crack initiation strains.

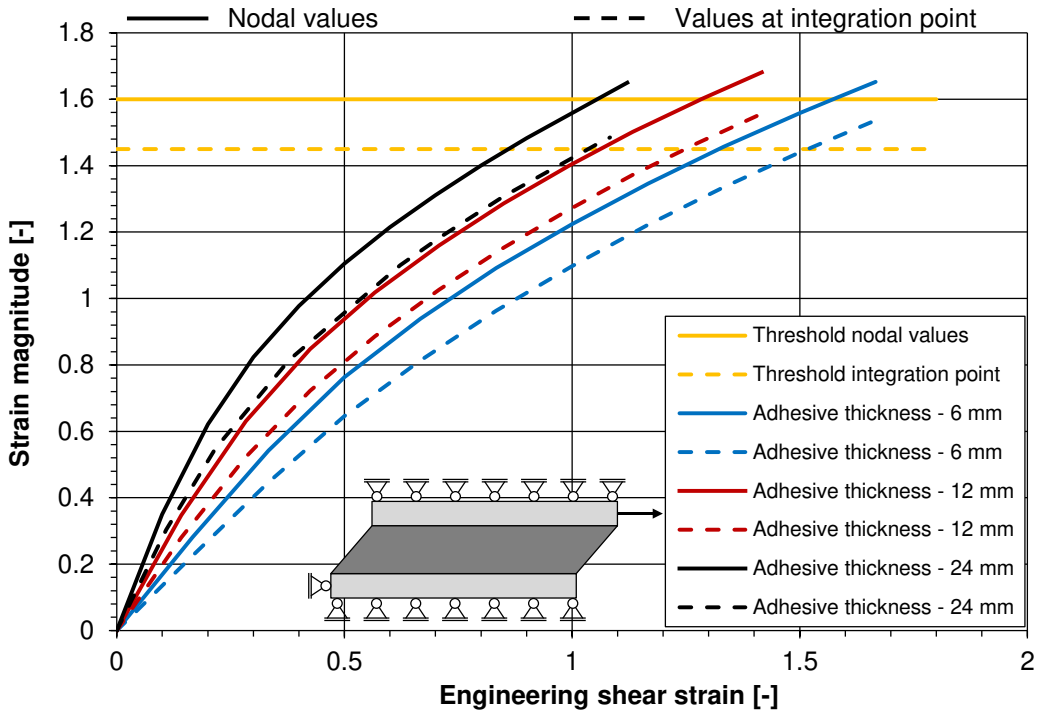

Figure 6.7: Maximum value of the strain magnitude in the simple shear specimen for a given applied engineering shear strain

Notched circular shear specimen

In the second step, the notched circular shear specimen has been numerically reproduced using the above mentioned element size and formulation, as well as adopting the threshold values for the strain magnitude at crack initiation, as calibrated on the simple shear specimen with an adhesive thickness of 12 mm. Figure 6.8 shows the distribution of the strain magnitude, when the threshold value is obtained.

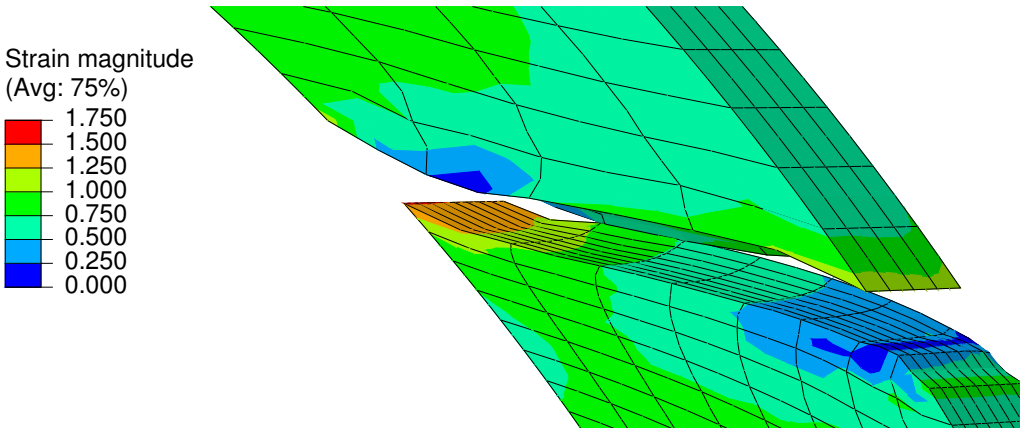

Figure 6.8: Plot of the strain magnitude in the notched circular shear specimen (only a part of the specimen is shown)

The maximum values for the strain magnitude at the element node and the integration point

are plotted against the applied torsional rotation in figure 6.9. Again, the intersection of the strain magnitude with the threshold value gives the predicted crack initiation rotation. The rotations recorded for a maximum strain magnitude of 1.6 at the node and of 1.45 at the integration point are given in figure 6.14. For this case, the strain magnitude is a very conservative approach, since the failure load is largely underestimated.

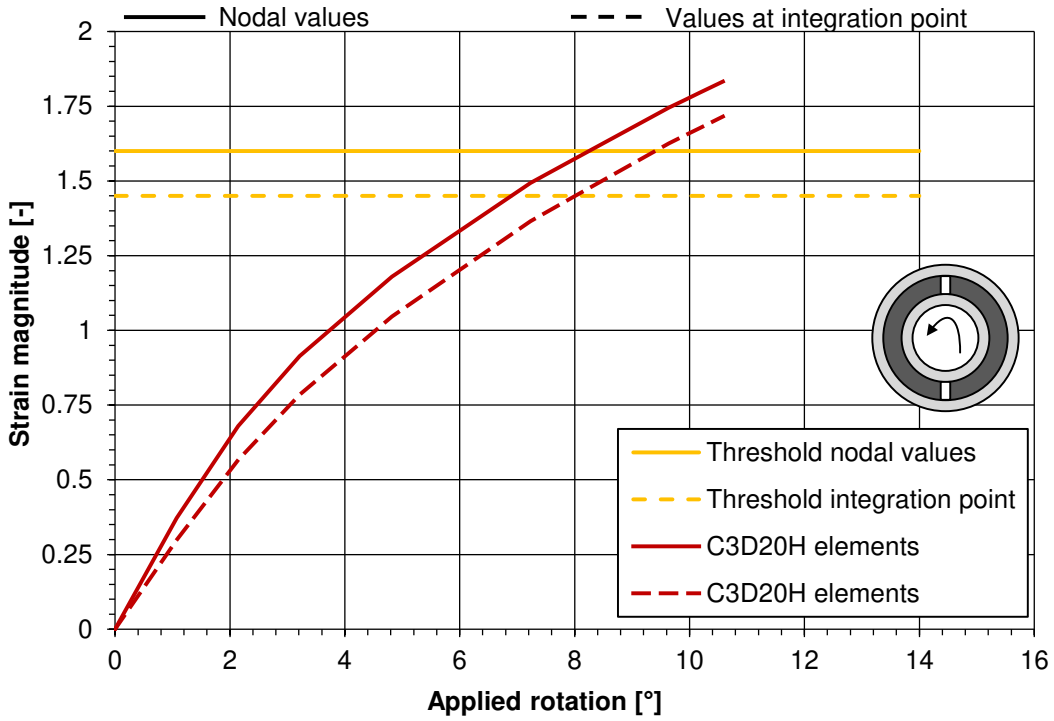

Figure 6.9: Maximum value of the strain magnitude in the notched circular shear specimen for a given applied rotation

Tensile specimen according ETAG 002 (2012)

After consideration of shear loaded bonded connection, the H-shaped tensile specimen according to ETAG 002 (2012) was investigated regarding the strain magnitude distribution. Figure 6.10 gives the distribution of the strain magnitude in the tensile specimen. At the interface between substrate and adhesive, three highly stressed regions could be identified, referred to as "FRONT", "CORNER" and "MIDDLE". Considering the values of the strain magnitude at these three locations, as shown in figure 6.11, the "MIDDLE" region gave the highest values. However, in section 4.2.3, figure 4.54, failure initiation was observed along the short edge. The values at the different locations are in the same order of magnitude, but due to the manufacturing process, the short edge exhibits more defects than the centre area of the long edge.

The failure load prediction is given in figure 6.14. The failure displacement corresponds to the displacement for which, a maximum nodal value for the strain magnitude of 1.6 was reached in the "MIDDLE" region. The same procedure was performed for the value at the integration point with a threshold value of 1.45. Unlike for the circular shear specimen, the failure load is overestimated.

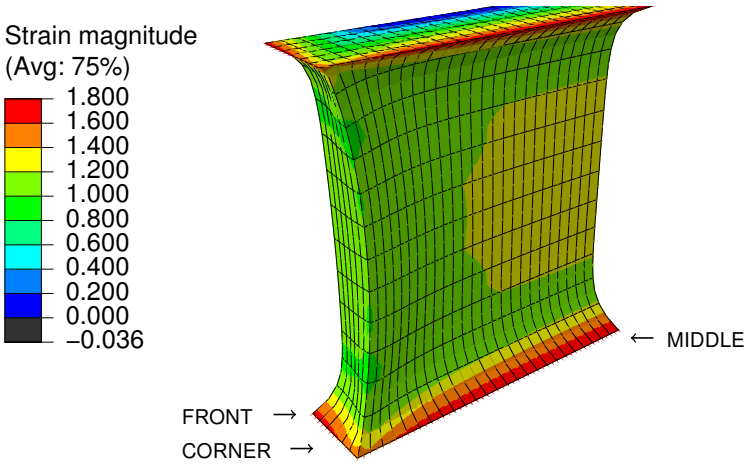

Figure 6.10: Plot of the strain magnitude in the tensile specimen as detailed in ETAG 002

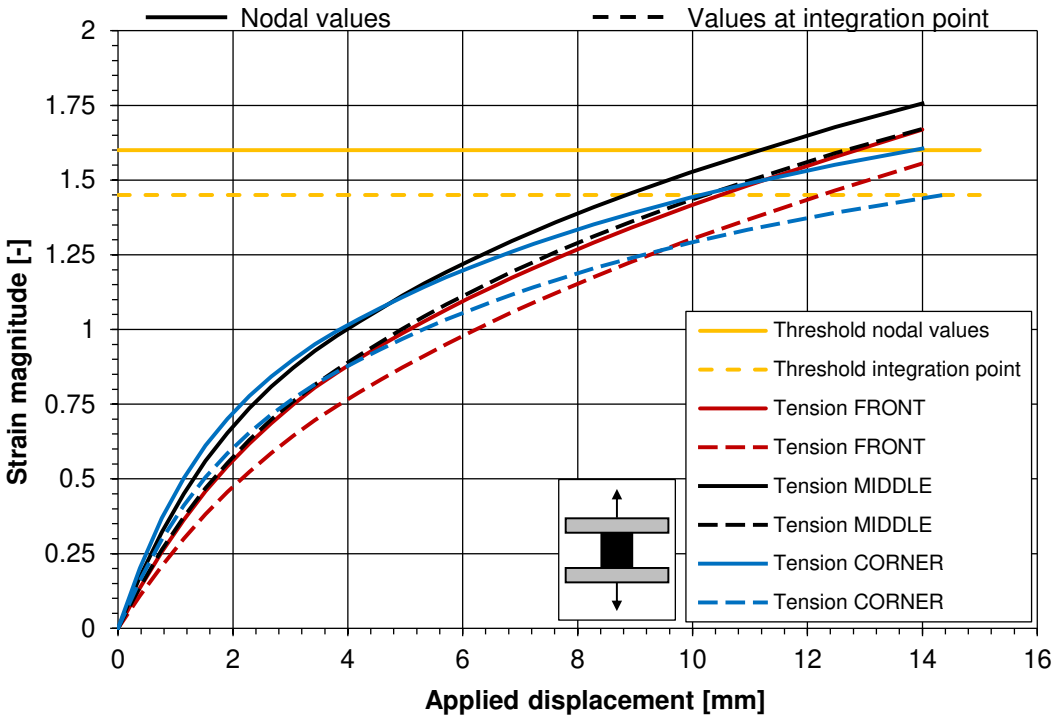

Figure 6.11: Maximum value of the strain magnitude in the tensile specimen according to ETAG 002 (2012) at different locations for a given applied displacement

Double Cantilever Beam specimen

Finally, the Double Cantilever Beam specimen is considered. In section 4.3, crack onset, i.e. macroscopic failure initiation, has been identified as the point at which the numerical prediction starts to deviate from the experimentally obtained force-deformation curve. In the following, the distributions of the strain magnitude at these points has been investigated.

Figure 6.12 gives the distribution of the strain magnitude for the DCB-6 specimen at its crack propagation displacement. The maximum values were found at the crack tip. Figure 6.13 gives the maximum values of the strain magnitude for both specimens and both evaluation

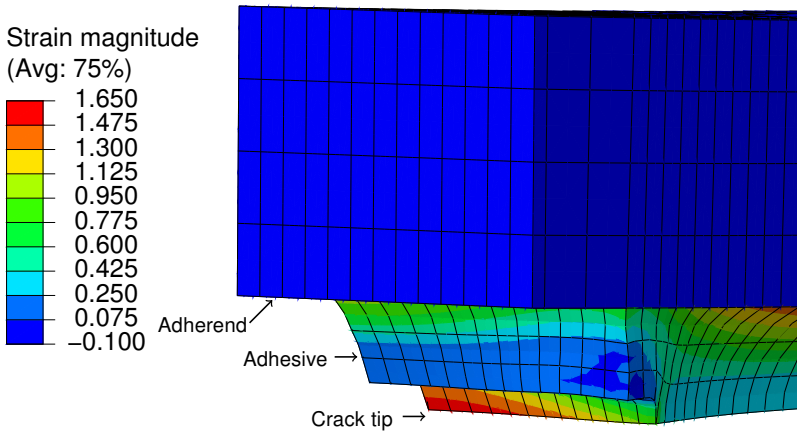

Figure 6.12: Plot of the strain magnitude in the DCB specimen (only a part of the specimen in the vicinity of the initial crack is shown)

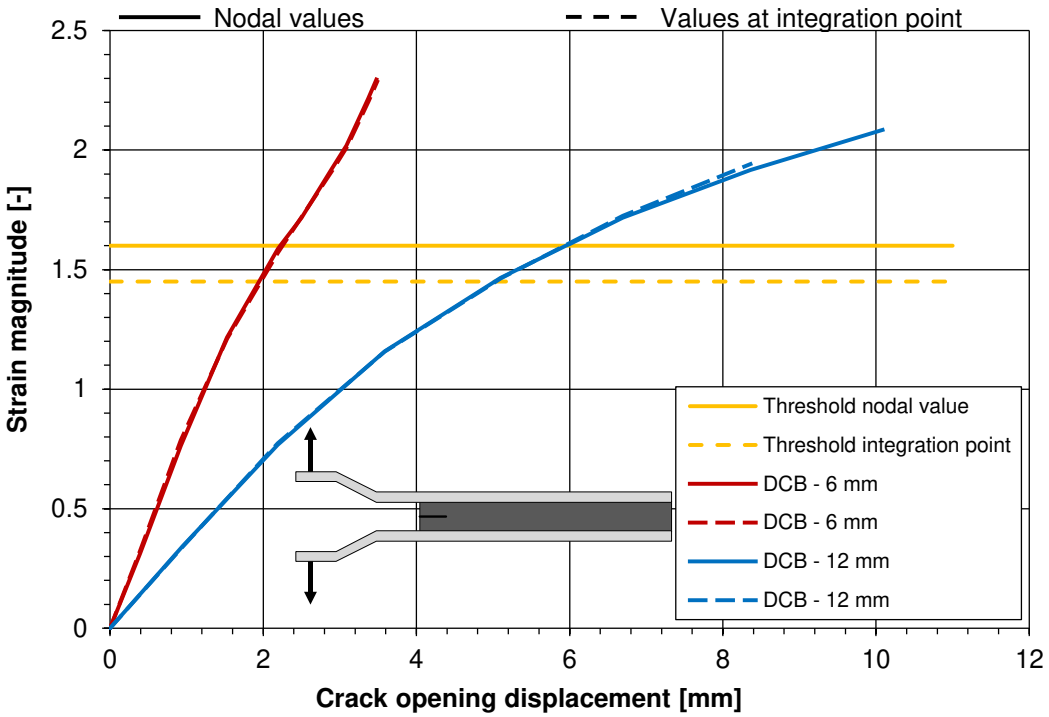

Figure 6.13: Maximum value of the strain magnitude in the DCB specimen for a given crack opening displacement

locations (nodal and integration point) as a function of the crack opening displacement. Again, the failure load prediction is given in figure 6.14 and a good agreement was found compared to the experimental data.

Summary

A comparison of the predicted crack initiation displacements with the experimentally determined values is given in figure 6.14. For clarity reasons, engineering failure strains have

been plotted, i.e. the recorded displacements have been divided by the respective adhesive thicknesses. The predicted values were determined using the C3D20H element, a second-order fully integrated hybrid solid element, in the commercial Finite Element software code ABAQUS® (Dassault Systèmes, 2014). A common element size of 1 mm at the critical points (in the vicinity of the considered notch) has been chosen. For the experimental data, the average values of each considered test series are given, including the standard deviation. For the DCB specimen, no standard deviation is given, since the failure point could not be experimentally identified.

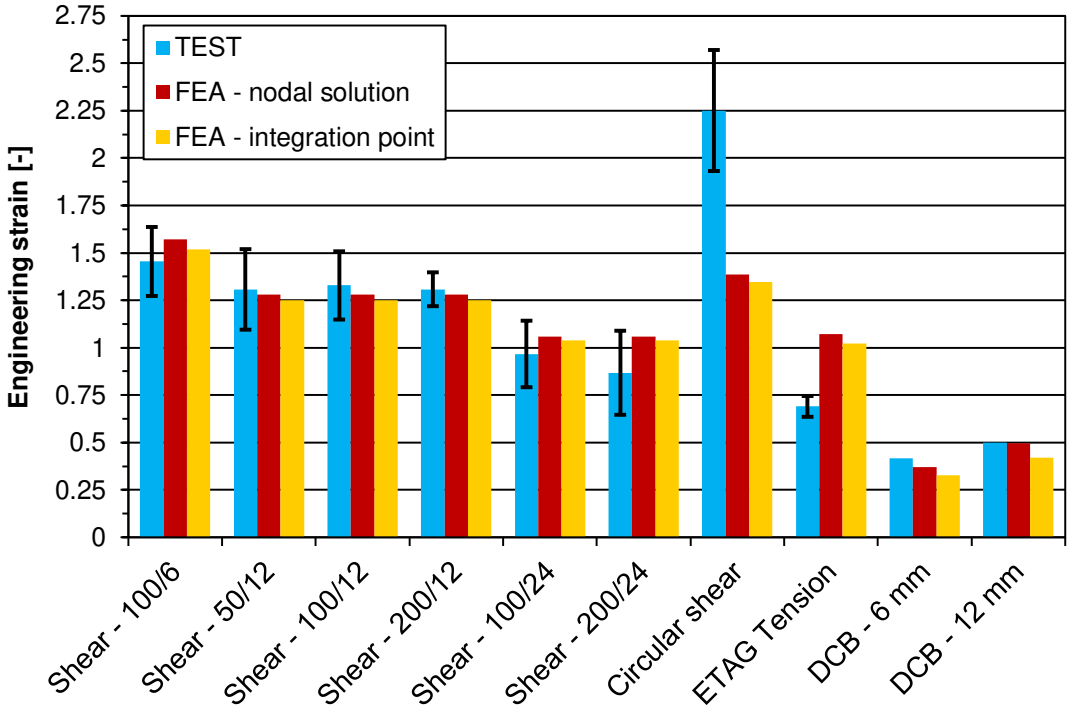

Figure 6.14: Failure load prediction using the Theory of Critical Distances - the standard deviation is shown for the test data

For the simple shear specimens, the predicted failure displacements are in a good agreement with the experimental data. The strains have been determined at the same distance from the origin of the singularity, since a common element size and formulation has been used. Whereas the crack initiation displacement of the notched circular shear specimen has been underestimated, the crack initiation displacement of the H-shaped tensile specimen was overestimated. For the DCB specimens, good agreement was found again.

The advantage of the adopted design procedure is its simplicity. If the global force-deformation behaviour is accurately reproduced, the stresses or strains can directly be determined in a simple post-processing, provided that a calibrated mesh (element formulation and element size) was used. A drawback of the method is that it fails in the failure load prediction for the tensile and the notched circular shear specimens. Nevertheless, this consideration can give a first order of magnitude for the stress state in the adhesive. The singularities are taken into account with this approach.

Regarding figure 6.14, there is no significant difference between the predictions of the crack initiation loads using the nodal values or the values at the integration point. Depending on

the Finite Element software code used, nodal values are more convenient to evaluate. The values at the integration points however are more accurate, since they are not extrapolated or averaged with values from neighbouring elements.

6.4.2 Control volume

The control volume approach has been successfully employed in Berto (2015) to assess fracture of cracked components made of an incompressible hyperelastic material. The proposed method consisted in averaging the strain energy density within a control volume, defined in the vicinity of a singular point. In a first step, the size of the control volume needs to be calibrated using two different test specimens. Berto (2015) showed with a mesh sensitivity study that the value of the strain energy density averaged over the control volume, yield convergent results even when a coarse mesh was used.

Calibration of the control volume

For the calibration of the control volume size and the value of the strain energy density at failure, the simple shear test series 100-6 and 100-12 were considered. Details about the numerical models, the chosen element types, the boundary conditions and the analysis settings can be found in section 4.2.1. Figure 6.15 displays the numerical model of the 100-12 specimen with the defined cylindrical control volume enclosing the two-material wedge. For both test specimens, the respective failure displacements were applied as a boundary condition and the average strain energy densities were evaluated for both specimens as a function of the control volume's radius.

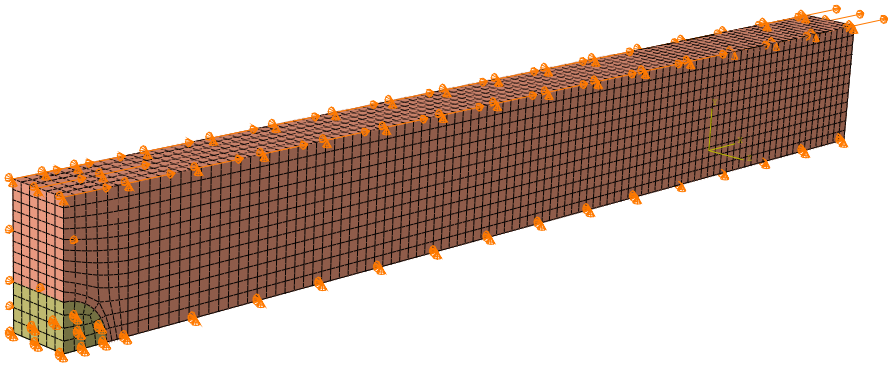

Figure 6.15: Numerical model for the simple shear specimens with a defined control volume

A small mesh sensitivity study was performed on the 50-12 specimen loaded in simple shear. For a given control volume and the failure load applied, two different mesh configurations were investigated. With the number of elements increased by a factor of 4, the strain energy density averaged within the control volume exhibited a change of 0.1%. Figure 6.16 shows the average strain energy density plotted against the radius of the control volume for the two considered test series at their respective failure loads. For a radius of 6 mm, the average strain energy density at failure $\overline{W_c}$ is equal for both specimens, with $\overline{W_c} = 0.61$ N/mm. Consequently, this radius was selected for the subsequent investigations.

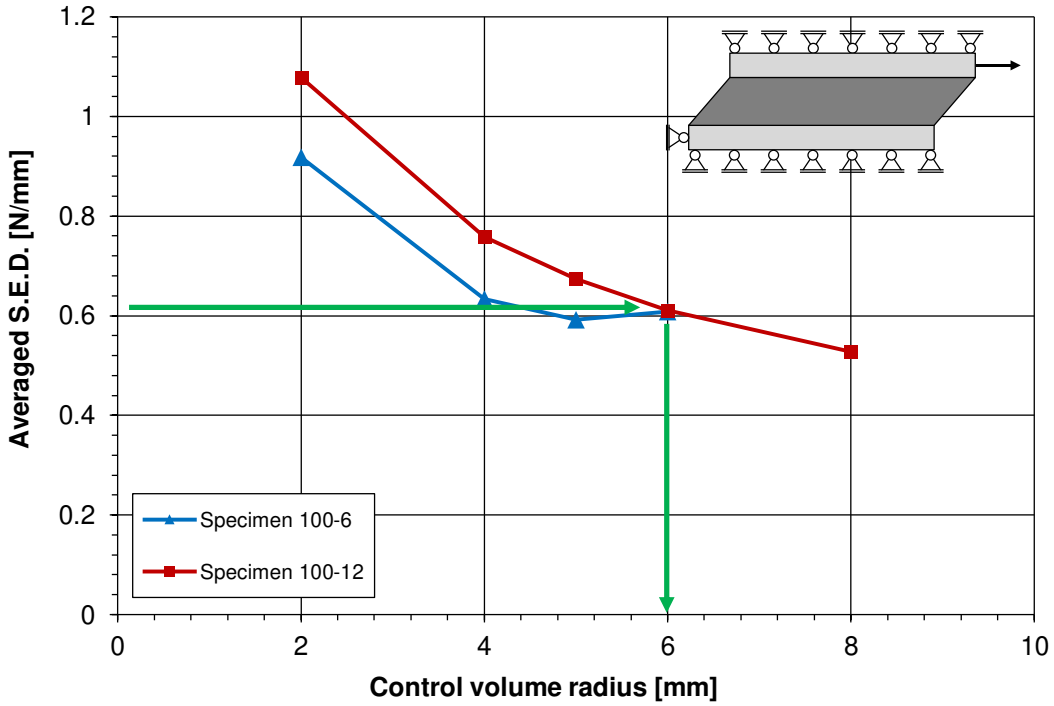

Figure 6.16: Calibration of the radius of the control volume - S.E.D. is the strain energy density.

Evaluation of the failure load

The control volume approach has been used to assess failure of the experimental data basis on bonded connections. For each test specimen, a control volume with the previously calibrated radius has been inserted in the respective numerical model and the average strain energy density has been evaluated as

$$\overline{W} = \frac{1}{V_\mathrm{c}} \int_{V_\mathrm{c}} W dV. \tag{6.2}$$

In equation 6.2, $\overline{W}$ is the strain energy density averaged within a control volume with a radius r_c and a volume V_c. The cylindrical control volume is given as $V_\mathrm{c} = 1/8\ \pi\ r_\mathrm{c}^2\ h_\mathrm{c}$. h_c is the bite of the adhesive joint.

Figure 6.17 summarises the results for the failure load prediction on the selected test series. For the experimental results, the standard deviation is given. The control volume approach based on the strain energy density can reproduce the adhesive thickness effect. For the simple shear specimens with 6 mm and 12 mm adhesive thickness, very good agreement is found as the control volume has been calibrated using these test series. The load bearing capacity of the notched circular shear specimen is largely underestimated, whereas the failure load for the H-shaped specimen under tension is overestimated.

Consequently, the results of the failure load prediction using the control volume approach are in line with the previous method consisting in choosing a constant element size and formulation for all numerical models. Both methods rely on the local stress and strain distributions,

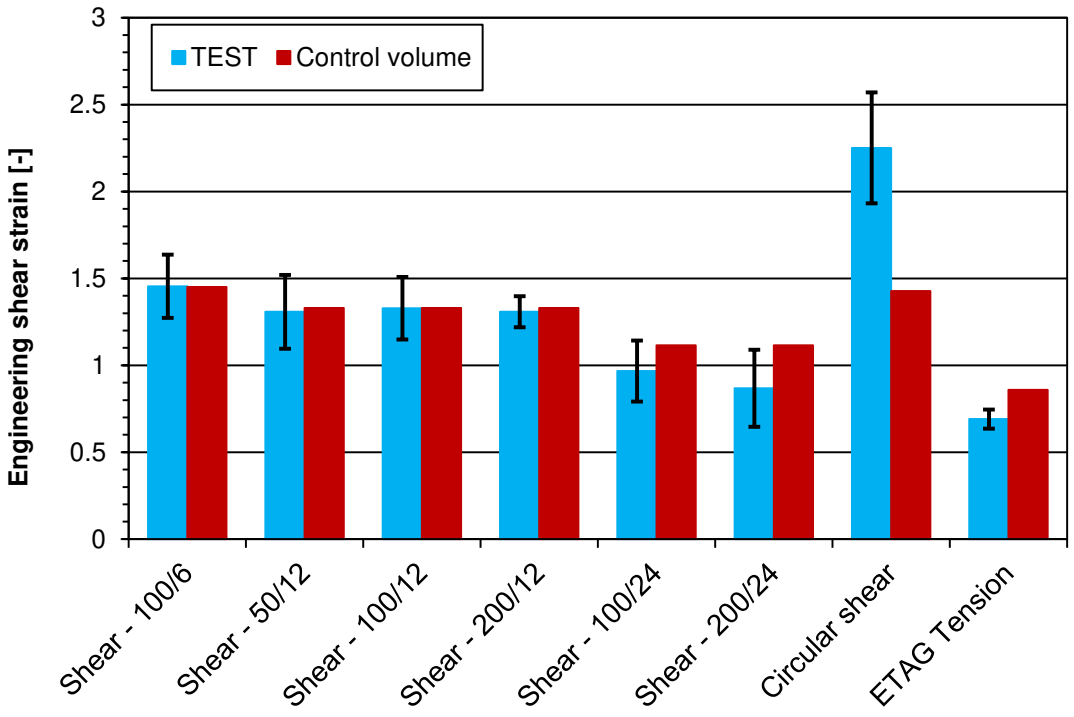

Figure 6.17: Failure load prediction using the control volume approach

which are dominated by the singularity of the two-material wedge. Both methods can reproduced the adhesive thickness effect, underestimate the failure load for the notched circular shear specimens and overestimate the failure load for the H-shaped tensile specimens.

6.4.3 Point method

Preliminary considerations

In section 6.3, the coupled stress and energy criterion, proposed by Leguillon (2002), has been used for the failure load prediction of the simple shear specimens. Good agreement was obtained with the experimental data. The initiated crack length has been found to be almost independent on the investigated geometries. A value of $\Delta a = 2.5\,\text{mm}$ has been found. Consequently, the design approach can be simplified. Knowing the length of the finite crack, the coupled criterion can be reduced to the evaluation of the stress partial criteria. The crack length can thus be seen as the characteristic length parameter, which has been discussed in the framework of the Theory of Critical Distances.

Experimental database and numerical models

The simple shear tests, the notched circular shear test and the H-shaped tensile tests have been numerically reproduced. For computational efficiency, a quite coarse mesh of 1.5 mm element edge size has been chosen. In the vicinity of the corner edge, a part with a refined mesh of 1/8 mm has been connected to the coarse part with a tie constraint. Figure 6.18 shows the numerical model for the 50-12 specimen and the path at which the strain magnitude distribution has been evaluated.

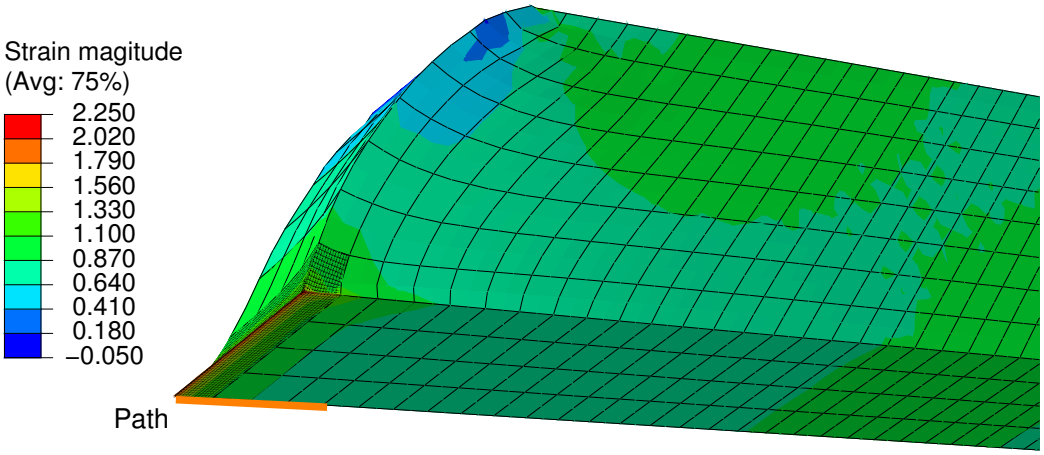

Figure 6.18: Numerical model for the failure load prediction using the point method

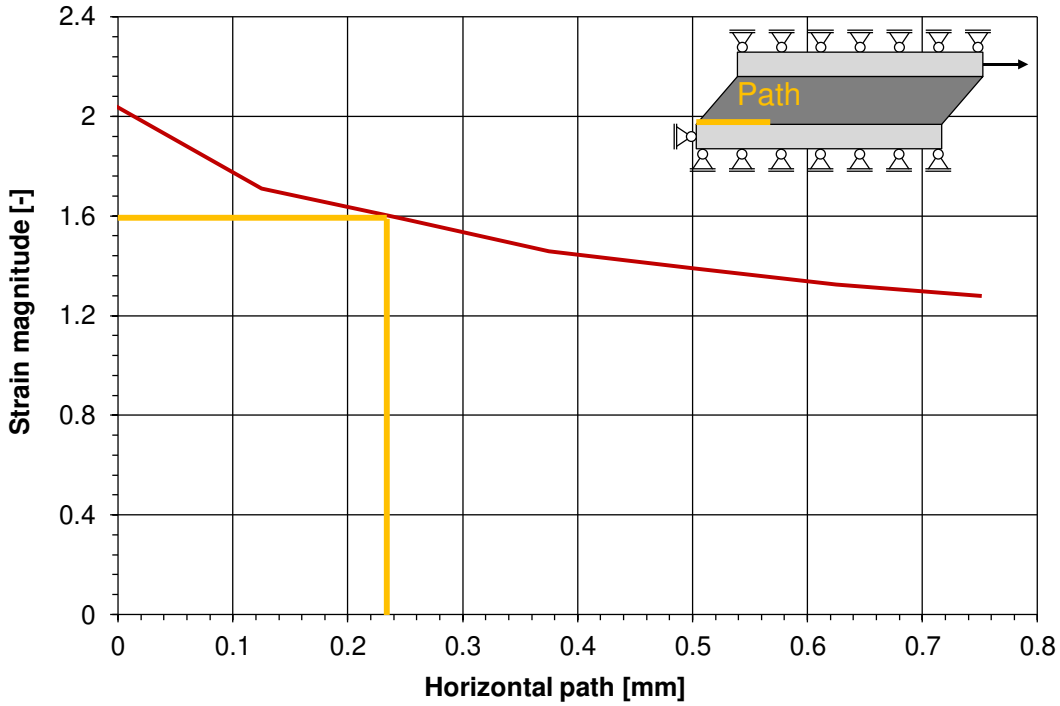

Figure 6.19: Distribution of the strain magnitude in the 50-12 specimen for the failure load applied

In figure 6.19, the strain magnitude distribution is plotted against the centreline path on the level of the interface layer (cf. figure 6.18). A path along the edge in overlap direction has not been considered, since the stresses are mesh dependent there as well. Details about the Finite Element models and the analysis settings can be found in the respective sections about the numerical simulations of the tests.

Figure 6.19 shows that the strain magnitude is far below the critical value of 1.6 at the end of a finite crack with a length of 2.5 mm. Since this crack length has been determined using a 2D plane stress model, the 50-12 test series is used to determine a new crack length. Again, it is assumed that the crack length is constant. From figure 6.19, a crack length of

0.23 mm is found. In the following, the strain magnitude is considered at the centre of the interface between the adhesive and the adherend at a distance of 0.23 mm from the origin of the two-material wedge.

Failure load evaluation

Figure 6.20 shows the results for the failure load prediction using the point method with a distance of 0.23 mm from the origin of the singularity. As already observed previously, the failure load predictions of the simple shear specimens are in good agreement with the experimental data. The load bearing capacity of the notched circular shear specimen is underestimated, whereas the load bearing capacity of the tensile specimen according to ETAG 002 (2012) is overestimated.

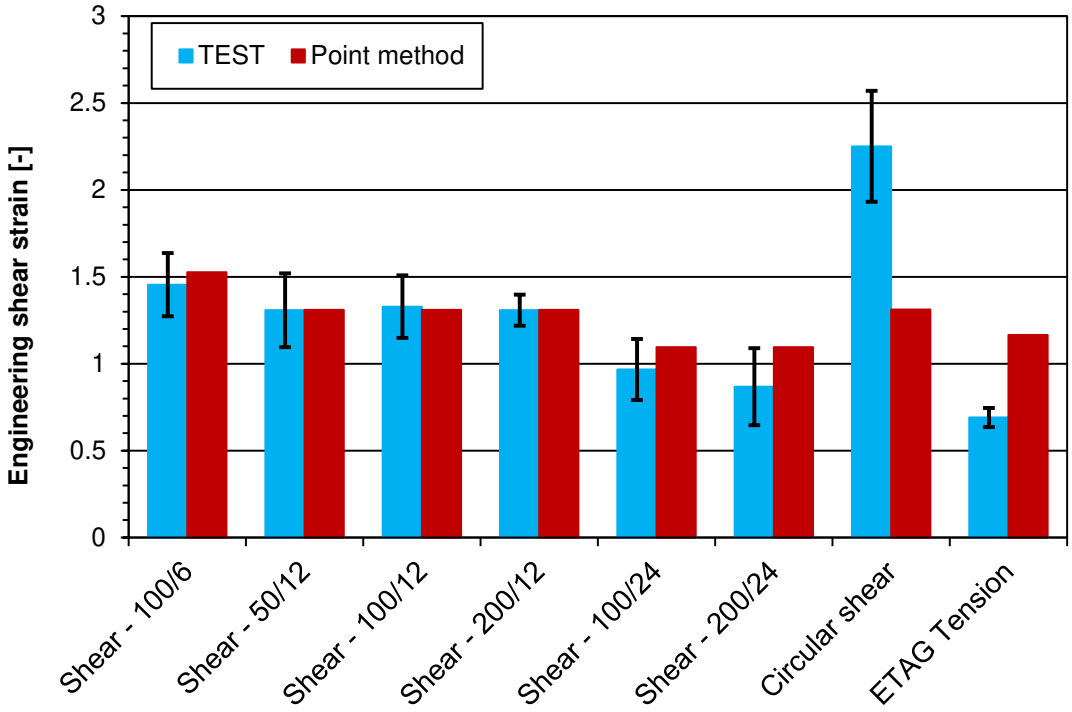

Figure 6.20: Failure load prediction using the point method

The failure load prediction given in this section is based on the results of the Finite Fracture Mechanics approach, the coupled stress and energy criterion. For the simple shear specimens, which have been investigated in the section 6.3, the finite crack length has been found to be a constant value. Assuming that this crack length is a material parameter, the energy partial criterion can be omitted and the stress partial criterion reduces to evaluating the stresses (or more generally the failure criterion) at the tip of an imaginary crack with constant length.

From the consideration of the 50-12 specimen, it has been found that the strain magnitude at a distance of 2.5 mm is much lower than the critical value for failure of bulk material. Therefore, the distance has been adapted to fit the experimentally recorded failure displacement of the 50-12 specimen and a value of 0.23 mm has been found. The difference can be explained by the different assumptions for the model. In section 6.3, a 2D plane stress model has been

assumed, whereas the present results are based on a 3D model.

The point method fails in predicting the notched circular shear test data and the results of the tension test on H-specimen. Consequently, the crack length cannot be considered as a constant value. Considering the notched circular shear test, the failure load is comparable to the failure load of the unnotched, i.e. the bulk material. This means that the stress partial criterion is fulfilled, but the energy partial criterion is not fulfilled and that failure occurs, when the strain magnitude in the bulk material exceed the critical value.

6.5 Summary

The failure load prediction of a set of experimental data on bonded connections presented in chapter 4.2 has been investigated using various approaches. The design concept given by ETAG 002 (2012) has failed in reproducing the adhesive thickness effect, as it does not consider the stresses at the interface, where failure initiation actually takes place, but average stresses at the adhesive mid-height. The analytical solution according to Allman (1977) predicted qualitatively the influence of the adhesive thickness on the failure load, but it also failed in the quantitative prediction.

The simple shear test data has been analysed using concepts from Finite Fracture Mechanics. The so-called coupled *stress and energy criterion*, originally proposed by Leguillon (2002) and applied for single-lap shear joints with linear elastic adhesive by Weißgraeber (2014), was successfully extended to nonlinear elastic materials. With the strain-based failure criterion derived in chapter 5 and the critical energy release rate, determined using Double Cantilever Beam specimens in section 4.3, the crack initiation loads of the simple shear test series were predicted in good agreement with the experimental results. Furthermore, the crack length was found to have constant value. Finite Fracture Mechanics has thus proven to be an adequate tool to describe failure initiation with regard to the two-material wedge and has a strong physical basis. Up to this moment, only two-dimensional models have been investigated. In addition, further investigation, e.g. on the notched circular shear specimen, need to be performed to validate the proposed method.

The coupled stress and energy criterion is an optimisation problem and thus needs some computational effort. Therefore, methods from the Theory of Critical Distances have been considered based on Finite Element Analysis to assess failure of the adhesively bonded connections. In a first approach, since the stresses and strains depend on the Finite Element mesh used, the same element size and formulation has been chosen to describe the silicone in the vicinity of the notch. This method is very easy to implement and gives good results for the simple shear specimens, but fails in predicting the circular shear and tensile specimens. Similar results were obtained, when the strain energy density has been averaged within a control volume. Since the results from the Finite Fracture Mechanics approach predicted a constant crack length, the strain magnitude was, in a third approach, evaluated at the distance of the crack length away from the singularity. Similar results were found as for the two proceeding methods. Consequently, a constant crack length cannot be assumed. Especially regarding the notched circular shear specimens, which exhibited almost the same failure load as for the unnotched specimens, it is assumed that the energy partial criterion is not fulfilled for the small crack lengths as determined previously.

7 Conclusions and recommendations

7.1 Conclusions

The present work focus on two aspects concerning the failure analysis of adhesively bonded connections with silicone described using the Finite Element Method. Apart from the definition of a failure criterion for defect-free silicone bulk material, the failure initiation in bonded connections was investigated in detail.

Experimental investigations:

In order to analyse failure of bulk material, standard experimental investigations on bulk material, uniaxial tension and compression tests, have been performed on silicone bulk material. The uniaxial tensile test data has been chosen subsequently for the characterisation of the chosen nonlinear elastic material law. Although no real macroscopic failure was observed for the compression specimens, the consideration of the inelastic deformations gave a strong evidence on significant damage onset in the material.

Apart from the standard experimental investigations, tests on bonded connections were performed to create an experimental database for the failure load analysis of adhesive joints. Simple shear, circular shear and tensile tests on small-scale bonded connections have been carried out. The simple shear specimens clearly exhibited the adhesive thickness effect, i.e. a decreasing strength with increasing layer thickness. The failure initiation was analysed in detail and it was located at the edge area. For the circular shear specimens, two types of specimens were produced, one type with a circular continuous silicone bead and one type with inserted cuts to investigate the influence of the edge area on the load bearing capacity. The circular shear specimens with continuous silicone bead have been used to assess failure of bulk material, as the adhesive was less influenced by edge effects, compared to the simple shear specimens. Despite the absence of the edge area, the failure loads and displacements were almost identical for both series.

Finally, since the edge area of bonded connections can be seen as a two-material wedge, the fracture mechanics properties, namely the mode I cohesive properties and the mode I critical energy release rate have been investigated in Double Cantilever Beam tests. The J-integral method has been used to determine the fracture mechanics parameters and an engineering approach based on a Finite Element Analysis has been developed to determine the critical energy release rate of the adhesive.

In the experimental investigations, the silicone sealant exhibited a *brittle* failure behaviour, following the definition given in Gross and Seelig (2011) and discussed in section 3.4.2. Crack initiation occurred without any visible sign of preannouncement, like necking. In contrast to brittle materials, like glass, crack initiation was observed at very large deformations. Except for the uniaxial compression test specimens, elastic behaviour with no significant remaining

deformations after failure was observed for the investigated specimens. For all tests on bonded connections, 100% cohesive failure was observed.

The previously described tests have been numerically simulated using the Finite Element Method. The highly nonlinear material behaviour has been described with the hyperelastic material law according to Marlow (2003). The material behaviour has been assumed as incompressible in the geometrical nonlinear analysis. Very good agreement was found with the experimental data, since the stress distributions of the investigated structural components, mainly linear silicone beads, were dominated by deviatoric stresses.

Failure of bulk material:

The strain magnitude has been identified as a suitable failure criterion for the defect-free bulk material. The strain magnitude can be seen as a sphere in the space of true principal strains. The criterion has been calibrated on the uniaxial tension tests and the circular shear tests with continuous silicone bead. The compression test results have been used to confirm the chosen failure criterion. Strain-based failure criteria are often assumed for rubber-like materials, but mainly focussing on the maximum principal strain criterion. The strain magnitude additionally incorporates the second and third principal strains, imposed to the material. Physically, the strain magnitude can be seen as a measure for the distortion of the material.

Failure of rubber-like material is often associated with cavitation. For thin adhesive layers under tensile forces, a stress state close to hydrostatic tension is observed, which leads to the onset of small cavities. Cavitation leads to a characteristic failure pattern in which, the small bubbles are clearly distinguishable. The fracture behaviour of the specimens considered in this work however was not governed by cavitation.

Stress peak:

Bonded connections with silicone are increasingly analysed using the Finite Element Method. In the case of bonded connections however, certain regions, especially at the interface between the adhesive and the substrate, exhibit high stresses and strains, which depend on the size and formulation of the Finite Elements used. Consequently, the stresses and strains in that region are into some extend arbitrary. The mesh dependence of these stresses is due to a singularity. In the case of the edge area of the interface of bonded connections, the stress singularity is referred to as *two-material wedge*. Considering analytical models, like *Volkersen* or *Goland-Reissner*, the stress singularities are not covered, as these models generally describe average stresses, which occur in the centreline of the adhesive layer.

Failure load prediction:

The failure load prediction of bonded connections has been performed following three different concepts. In a first step, the design equations according to ETAG 002 (2012) and the analytical solution according to Allman (1977) were analysed. Whereas the adhesive thickness effect was not covered by the design equations defined in the current standards, the effect was qualitatively, but not quantitatively reproduced by the *Allman* solution.

In a next step, the coupled stress and energy criterion, originally proposed by Leguillon (2002)

and applied to adhesively bonded connections with a linear elastic adhesive by Weißgraeber (2014), was extended for the first time to nonlinear elastic materials. The coupled criterion is a crack initiation criterion for weak singularities such as notches. It is an optimisation problem, which consists in determining the crack initiation load and the length of the initiated crack. Crack onset is not considered as a continuous process, but in discrete steps with the onset of crack with finite length. The coupled stress and energy criterion is a concept from Finite Fracture Mechanics. The criterion is based on a stress criterion, which gives an upper bound for the crack length and a fracture mechanics criterion, which gives a lower bound for the crack length. The crack initiation load is determined, if both criteria are met for the same crack length. Very good agreement between the experimental data of the simple shear tests and the Finite Fracture Mechanics approach has been found. The model investigated was based on a 2D plane stress model with the strain magnitude as failure criterion and the critical energy release rate, as determined in the DCB test. The crack length was found independent of the geometry of the simple shear specimens. The coupled stress and energy criterion is a physically sound model, which does not evaluate the stresses or strains at the origin of the singularity, but at a certain distance, where the results of a Finite Element Analysis give convergent values, provided that a reasonably refined mesh is used.

Finally, concepts of the Theory of Critical Distances have been applied on the test data base. When describing the sealant with the same element size and formulation for all the models, a good agreement is found for simple shear tests, but the failure loads of the notched circular shear tests are underestimated and those of the tension test on H-shaped specimens overestimated. Similar results were found when the strain energy density was averaged within a control volume. Since the crack length in the Finite Fracture Mechanics approach was constant, the method can be simplified to evaluating the stresses or strains at the distance of the crack length away from the singularity. However, similar results were found as for the method with the constant element size, indicating that the crack length cannot be considered as a characteristic length, as it is assumed in the framework of the Theory of Critical Distances.

7.2 Recommendations

One of the starting points of this research work has been the occurrence of stress peaks in the Finite Element numerical simulation. It has been shown that these stresses arise from a singularity, which is due to the two-material wedge. Although infinite stresses, as predicted by the theory of elasticity, do not exist in reality, these regions are highly stressed areas, where failure is prone to occur. Therefore, the local stress concentrations should not be neglected. In addition, in order to guarantee a certain comparability between different structural components, the element size and the element formulation should be chosen consistently between different models. The simple shear test data provide an easy and clear test result, which can be used to "calibrate" a Finite Element mesh in the vicinity of a singular point. Finally, an accurate reproduction of the material behaviour of the sealant is a fundamental requirement.

In the field of Finite Fracture Mechanics, promising results have been generated. The failure loads of the simple shear specimens have been successfully predicted with a model, based on only two essential parameters of the bulk material: material strength and critical energy release rate. Further research work is currently done, analysing additional specimens. The

results of this research could lead to some engineering approach for the use in design offices.

A number of tests has been performed in this research project. A failure criterion has been identified for the bulk material. It is recommended to perform additional tests on specimens, like biaxial tests, to confirm the results of this work. Moreover, a number of interesting observations have been documented. Analysing these observations regarding the microstructure of the material (polymer chains and filler) would promote the understanding of silicone.

7.3 Outlook and further research required

In this research work, the strain magnitude has been identified as a suitable failure criterion for silicone adhesives. Since the failure criterion has only been determined using three different characteristic stress states, additional tests, like biaxial tension tests, e.g. bulge test as performed in Drass et al. (2017a), or pure shear tests, should be carried out to confirm the presented research results.

Regarding the critical energy release rate of the material, the DCB tests have shown some drawbacks. Although the results are in line with published test results on a different silicone sealant, additional tests on a different specimen or with optimised boundary conditions (increase of the initial crack length) could be useful to confirm the results generated within this project.

Finite Fracture Mechanics has proven being a suitable tool to assess failure initiation, taking into account the stress peak at the two-material wedge. In the framework of this project, only a first set of simulations was performed on simple shear test data. Therefore, additional models, e.g. on the notched circular shear test, are currently developed to validate the method using additional test data. With this powerful and physically sound method, the large database, which is available on the standard H-specimen, as defined by ETAG 002 (2012), can be thoroughly investigated regarding the influence of parameters, like temperature, water, or UV radiation. For this however, the bulk strength and the critical energy release rate should be determined under the influence of water, temperature and UV radiation as well. Up to now, the strength of these specimens were quantified with engineering stresses or strains, knowing that these engineering values were strongly depending on the geometry. The coupled criterion however, is based on the material constants strength and critical energy release rate.

The coupled stress and energy criterion is an optimisation problem. In order to determine the failure load, a number of Finite Element models needs to be solved, since both the failure load and the crack length are unknown. Regarding the use of this method in engineering offices, some simplifications could be implemented to reduce the computational effort. In addition, the method should be applied on three-dimensional models, which cannot be approximated by plane stress or plane strain conditions.

Failure initiation of adhesively bonded connections under quasi-static loading has been investigated in this research project. Since the material behaviour of silicone sealants is time and load-history dependent, these two parameter of influence should be considered as well in future research works. Here again, the promising results of Finite Fracture Mechanics

could be used to evaluate failure on the standard H-specimen, provided that the influence of time and load history on the bulk strength and critical energy release rate is known. The visco-elastic behaviour as well as fatigue also need to be better understood in the vision of omitting the mechanical load transfer devices, which are currently prescribed.

The performed tests were based on the assumption that the material properties, i.e. the distributions of the crosslink density and *Young's* modulus, are homogeneous and independent regarding the manufacturing conditions, like the geometry of the mould used or the demoulding time. Considering these assumptions, further research works should investigate the influence of the cure conditions and clarify, if the assumption of homogeneous material properties is valid.

Bibliography

AAMA (2014). *Structural Silicone Glazing (SSG) Design Guidelines*. American Architectural Manufacturers Association.

Ackermann, J. and Damrath, V. (1989). Chemie und Technologie der Silicone II. Herstellung und Verwendung von Siliconpolymeren. *Chemie in unserer Zeit*, 23(3):86–99.

Adams, R. and Peppiatt, N. (1977). Stress analysis of adhesive bonded tubular lap joints. *The Journal of Adhesion*, 9(1):1–18.

Aït-Hocine, N., Hamdi, A., Naït-Abdelaziz, M., Heuillet, P., and Zaïri, F. (2011). Experimental and finite element investigation of void nucleation in rubber-like materials. *International Journal of Solids and Structures*, 48(9):1248–1254.

Alfredsson, K. (2003). On the determination of constitutive properties of adhesive layers loaded in shear–an inverse solution. *International Journal of Fracture*, 123(1):49–62.

Allman, D. (1977). A theory for elastic stresses in adhesive bonded lap joints. *The Quarterly Journal of Mechanics & Applied Mathematics*, 30(4):415–436.

Altenbach, H. (2012). *Kontinuumsmechanik - Einführung in die materialunabhänigen und materialabhänigen Gleichungen*, volume 2. Springer.

Altus, E., Haber, O., and Tirosh, J. (1986). An Engineering Failure Envelope for Adhesive Joints. *Experimental Mechanics*, 26(3):267–274.

Andersson, T. and Stigh, U. (2004). The stress-elongation relation for an adhesive layer loaded in peel using equilibrium of energetic forces. *International Journal of Solids and Structures*, 41:413–434.

Andriot, M., Chao, S., Colas, A., Cray, S., de Buyl, F., DeGroot, J. J., Dupont, A., Easton, T., Garaud, J., Gerlach, E., Gubbels, F., Jungk, M., Leadley, S., Lecomte, J., Lenoble, B., Meeks, R., Mountney, A., Shearer, G., Stassen, S., Stevens, C., Thomas, X., and Wolf, A. (2007). *Silicones in Industrial Applications*. Inorganic Polymers. Nova Sciences.

Anthony, J. and Paris, P. (1988). Instantaneous evaluation of J and C. *International Journal of Fracture*, 38(1):R19–R21.

ASTM C1401 (2002). *Standard Guide for Structural Sealant Glazing*. ASTM International.

ASTM D412 (2013). *Standard Test Methods for Vulcanized Rubber and Thermoplastic Elastomers - Tension*. ASTM International.

Awerbuch, J. and Madhukar, M. (1985). Notched Strength of Composite Laminates: Predictions and Experiments – A Review. *Journal of Reinforced Plastics and Composites*, 4(1):3–159.

Ayoub, G., Naït-Abdelaziz, M., Zaïri, F., and Gloaguen, J. (2010). Multiaxial fatigue life prediction of rubber-like materials using the continuum damage mechanics approach. *Procedia Engineering*, 2(1):985–993.

Banea, M. and da Silva, L. (2010). Static and fatigue behaviour of room temperature vulcanising silicone adhesives for high temperature aerospace applications. *Materialwissenschaft und Werkstofftechnik*, 41(5):325–335.

Banea, M., Da Silva, L., and Campilho, R. (2015). The Effect of Adhesive Thickness on the

Mechanical Behaviour of a Structural Polyurethane Adhesive. *The Journal of Adhesion*, 91(5):331–346.

Banea, M. and da Silva, L. F. (2009). Adhesively bonded joints in composite materials: An overview. *Proceedings of the Institution of Mechanical Engineers, Part L: Journal of Materials Design and Applications*, 223(1):1–18.

Banea, M., Da Silva, L. F., and Campilho, R. (2010). Temperature dependence of the fracture toughness of adhesively bonded joints. *Journal of Adhesion Science and Technology*, 24(11-12):2011–2026.

Barenblatt, G. (1962). The Mathematical Theory of Equilibrium Cracks in Brittle Fracture. *Advances in Applied Mechanics*, 7:55–129.

Beer, F., Johnston, E., DeWolf, J., and Mazurek, D. (2009). *Mechanics of Materials*, volume 5. McGraw-Hill higher Education.

Beers, M. D. and Klosowski, J. M. (1990). *Silicones*, volume 1 of *Engineered Materials Handbook - Adhesives and Sealants*. ASM International.

Berto, F. (2015). A criterion based on the local strain energy density for the fracture assessment of cracked and V-notched components made of incompressible hyperelastic materials. *Theoretical and Applied Fracture Mechanics*, 76:17–26.

Biel, A. (2005). Cohesive behaviour and fracture toughness of an adhesive layer. Master's thesis, Chalmers University of Technology, Göteborg, Sweden.

Biel, A. and Stigh, U. (2017). Cohesive zone modelling of nucleation, growth and coalesce of cavities. *International Journal of Fracture*, 204(2):159–174.

Biel, A., Stigh, U., and Walander, T. (2012a). A critical study of an alternative method to measure cohesive properties of adhesive layers. In *Proceedings of the 19th European Conference on Fracture ECF19, Kazan, Russia*. ESIS.

Biel, A., Walander, T., and Stigh, U. (2012b). Influence of edge-boundaries on the cohesive behaviour of an adheisve layer. In *Proceedings of the ASME 2012 International Mechanical Engineering Congress & Exposition IMECE2012*. ASME.

Blackman, B., Dear, J., Kinloch, A., and Osiyemi, S. (1991). The calculation of adhesive fracture energies from double-cantilever beam test specimens. *Journal of Materials Science Letters*, 10:253–256.

Bogy, D. (1968). Edge-Bonded Dissimilar Orthogonal Elastic Wedges Under Normal and Shear Loading. *Journal of Applied Mechanics*, pages 460–466.

Bormann, A. (2005). *Elastomerringe zur Schwingungsberuhigung in der Rotordynamik - Theorie, Messungen und optimierte Auslegung*. Disseration, Technische Universtät Berlin.

Boué, T. G., Harpaz, R., Fineberg, J., and Bouchbinder, E. (2015). Failing softly: a fracture theory of highly-deformable materials. *Soft matter*, 11(19):3812–3821.

Brendler, S. and Haufe, A. (2007). Zur Versagensvorhersage von Silikon-Glas-Klebeverbindungen mit LS-DYNA: Identifizierung von geeigneten Materialmodellen und -parametern. In *6. LS-DYNA Anwenderforum, Frankenthal*.

Brighenti, R., Carpinteri, A., and Artoni, F. (2017). Fracture toughness of highly deformable polymeric materials. *Procedia Structural Integrity*, 3:18–24.

Brockmann, W., Geiß, P., Klingen, K., and Schröder, B. (2005). *Klebtechnik*. Wiley-VCH Verlag GmbH & Co. KGaA.

Brostow, W. and Lobland, H. (2010). Brittleness of materials: implications for composites and a relation to impact strength. *Journal of Materials Science*, 45(1):242.

Campilho, R., Banea, M., and Da Silva, L. (2012). Innovative Finite Element techniques for

strength prediction of bonded joints. In Scutelnicu, E., editor, *The annals of "Dunarea de Jos" University of Galati - Welding equipment and technology*, volume 23, pages 26–33. Galati University Press.

Campilho, R., Banea, M., Pinto, A., da Silva, L., and De Jesus, A. (2011). Strength prediction of single-and double-lap joints by standard and extended finite element modelling. *International Journal of Adhesion and Adhesives*, 31(5):363–372.

Campilho, R., Moura, D., Banea, M., and Da Silva, L. (2015). Adhesive thickness effects of a ductile adhesive by optical measurement techniques. *International Journal of Adhesion and Adhesives*, 57:125–132.

Chaves, F. J., Da Silva, L., De Moura, M., Dillard, D., and Esteves, V. (2014). Fracture mechanics tests in adhesively bonded joints: a literature review. *The Journal of Adhesion*, 90(12):955–992.

Chen, D. and Cheng, S. (1992). Torsional stress in tubular lap joints. *International Journal of Solids and Structures*, 29(7):845–853.

Chen, Z., Adams, R., and Da Silva, L. (2011). The use of the J-integral vector to analyse adhesive bonds with and without a crack. *International Journal of Adhesion and Adhesives*, 31(1):48–55.

Clift, C., Carbary, L., Hutley, P., and Kimberlain, J. (2014). Next generation structural silicone glazing. *Journal of Facade Design and Engineering*, 2(3-4):137–161.

Cognard, J.-Y. and Créac'hcadec, R. (2009). Analysis of the Non-linear Behavior of an Adhesive in Bonded Assemblies Under Shear Loadings. Proposal of an Improved TAST. *Journal of Adhesion Science and Technology*, 23(10-11):1333–1355.

Comyn, J., De Buyl, F., Shephard, N., and Subramaniam, C. (2002). Kinetics of cure, crosslink density and adhesion of water-reactive alkoxysilicone sealants. *International Journal of Adhesion and Adhesives*, 22(5):385–393.

Cook, R., Malkus, D., Plesha, M., and Witt, R. (2002). *Concepts and applications of finite element analysis*, volume 4. John Wiley & Sons, Inc.

Cornec, A., Schneider, I., and Schwalbe, K.-H. (2003). On the practical application of the cohesive model. *Engineering Fracture Mechanics*, 70(14):1963–1987.

Cornetti, P., Pugno, N., Carpinteri, A., and Taylor, D. (2006). Finite fracture mechanics: A coupled stress and energy failure criterion. *Engineering Fracture Mechanics*, 73(14):2021–2033.

Da Silva, L. and Campilho, R. (2012). *Advances in numerical modelling of adhesive joints*. Springer.

Da Silva, L., das Neves, P., Adams, R., and Spelt, J. (2009a). Analytical models of adhesively bonded joints - Part I: Literature survey. *International Journal of Adhesion and Adhesives*, 29(3):319–330.

Da Silva, L., das Neves, P., Adams, R., and Spelt, J. (2009b). Analytical models of adhesively bonded joints - Part II: Comparative study. *International Journal of Adhesion and Adhesives*, 29(3):331–341.

Da Silva, L. and Öchsner, A. (2008). *Modeling of adhesively bonded joints*. Springer.

Dassault Systèmes (2014). *ABAQUS® 6.14 Documentation*.

De Buyl, F. (2001). Silicone sealants and structural adhesives. *International Journal of Adhesion and Adhesives*, 21(5):411–422.

Dean, G., Crocker, L., Read, B., and Wright, L. (2004). Prediction of deformation and failure of rubber-toughened adhesive joints. *International Journal of Adhesion and Adhesives*,

24(4):295–306.

Descamps, P., Hayez, V., and Chabih, M. (2017). Next generation calculation method for structural silicone joint dimensioning. *Glass Structures & Engineering*, pages 1–14.

Descamps, P., Iker, J., and Wolf, A. T. (1996). Effects of anodized aluminium surface parameters on the long-term adhesion of silicone structural glazing sealants. *Construction and Building Materials*, 10(7):527–538.

Diani, J., Fayolle, B., and Gilormini, P. (2009). A review on the Mullins effect. *European Polymer Journal*, 45(3):601 – 612.

Dias, V. (2013). *Development of adhesives constitutive material laws for the assessment of bonded steel to glass partial composite beams*. PhD thesis, University of Luxembourg.

Dispersyn, J., Santarsiero, M., Belis, J., and Louter, C. (2014). A preliminary study of the nonlinearity of adhesive point-fixings in structural glass facades. *Journal of Facade Design and Engineering*, 2(1-2):85–107.

Domininghaus, H., Elsner, P., Eyerer, P., and Hirth, T. (2008). *Kunststoffe - Eigenschaften und Anwendungen*, volume 7. Springer-Verlag, Berlin, Heidelberg.

Dorfmann, A. (2009). Modelling of rubberlike materials. In *Advances in Constitutive Relations Applied in Computer Codes*, pages 147–202. Springer.

Dorfmann, A. and Ogden, R. (2003). A pseudo–elastic model for loading, partial unloading and reloading of particle–reinforced rubber. *International Journal of Solids and Structures*, 40(11):2699–2714.

Dow Corning Corporation (2001). *Dow Corning® 993 Structural Glazing Sealant - Product sheet*. Dow Corning Corporation. Ref. no. 62-0918H-01.

Dow Corning Corporation (2006). *Lasting Innovation: 20 Years of Structural Silicone Glazing Success*. Dow Corning Corporation. Form number: 62-1465-01.

Dow Corning Corporation (2010a). *Case study: Forum Hochhaus Frankfurt am Main, Germany*. Dow Corning Corporation. Form number 62-1298C-01.

Dow Corning Corporation (2010b). *Case study: Zeppelin University, Friedrichshafen, Germany*. Dow Corning Corporation. Form number: 62-1535C-01.

Dow Corning Corporation (2011a). *Dow Corning® 993 Structural Glazing Sealant*. Dow Corning Corporation. Form number 62-1267D-01.

Dow Corning Corporation (2011b). *Silicone Structural Glazing Manual*. Dow Corning Corporation. Form number: 62-0979H-01.

Dow Corning Corporation (2013). *Dow Corning®TSSA - Transparent Structural Silicone Adhesives*. Dow Corning Corporation. Form number: 62-1709A-01.

Drass, M. and Schneider, J. (2016). On the mechanical behavior of transparent structural silicone adhesive - TSSA. In Zingoni, A., editor, *Insights and Innovations in Structural Engineering, Mechanics and Computation: SEMC 2016 - Sixth International Conference on Structural Engineering, Mechanics and Computation*. Elsevier B.V.

Drass, M., Schneider, J., Kelleter, C., Sobek, W., and Haase, W. (2016). Aspekte experimenteller und numerischer Untersuchungen von Klemmhalterungen im Glasbau. In Weller, B. and Tasche, S., editors, *Glasbau 2016*. Ernst & Sohn.

Drass, M., Schwind, G., Schneider, J., and Kolling, S. (2017a). Adhesive Connections in Glass Structures - Part I: Experiments and Analytics on Thin Structural Silicone. *Glass Structures & Engineering*.

Drass, M., Schwind, G., Schneider, J., and Kolling, S. (2017b). Adhesive Connections in Glass Structures - Part II: Material Parameter Identification on Thin Structural Silicone.

Glass Structures & Engineering.

Dugdale, D. (1960). Yielding of steel sheets containing slits. *Journal of the Mechanics and Physics of Solids*, 8(2):100–104.

ETAG 002 (2012). *Guideline for European Technical Approval for Structural Sealant Glazing Kits*. European Organisation for Technical Approvals.

Eyerer, P., Hirth, T., and Elsner, P. (2008). *Polymer Engineering - Technologie und Praxis*. Springer-Verlag, Berlin, Heidelberg.

Franz, J. (2015). *Untersuchungen zur Resttragfähigkeit von gebrochenen Verglasungen: Investigation of the residual load-bearing behaviour of fractured glazing*. PhD thesis, Technische Universität Darmstadt.

Gaul, L. and Fiedler, C. (2013). *Methode der Randelemente in Statik und Dynamik*, volume 2. Springer.

Gent, A. N. and Lindley, P. B. (1959). Internal rupture of bonded rubber cylinders in tension. *Proceedings of the Royal Society of London. Series A, Mathematical and Physical Sciences*, 249(1257):195–205.

Gleich, D. (2002). *Stress Analysis of Structural Bonded Joints*. PhD thesis, Technical University of Delft.

Goland, M. and Reissner, E. (1944). The Stresses in Cemented Joints. *Journal of Applied Mechanics*, 11(1):A17–A27.

Grandcoin, J., Boukamel, A., and Lejeunes, S. (2014). A micro-mechanically based continuum damage model for fatigue life prediction of filled rubbers. *International Journal of Solids and Structures*, 51(6):1274–1286.

Griffith, A. (1921). The Phenomena of Rupture and Flow in Solids. *Philosophical Transactions of the Royal Society of London. Series A, Containing Papers of a Mathematical or Physical Character*, 221:163–198.

Gross, B. and Mendelson, A. (1970). Plane elastostatic analysis of V-notched plates. Technical report, National Aeronautics and Space Administration.

Gross, D. and Seelig, T. (2011). *Fracture Mechanics: With an Introduction to Micromechanics*, volume 2. Springer.

Groth, H. (1988). Stress singularities and fracture at interface corners in bonded joints. *International Journal of Adhesion and Adhesives*, 8(2):107–113.

Gutowski, V. W., Russell, L., and Cerra, A. (1993). New tests for adhesion of silicone sealants. *Construction and Building Materials*, 7(1):19 – 25.

Habenicht, G. (2009). *Kleben - Grundlagen, Technologien, Anwendungen*, volume 6. Springer.

Hagl, A. (2006). Die Innovation - Kleben. *Stahlbau*, 75(6):508–520.

Hagl, A. (2007). Bemessung von strukturellen Silikon-Klebungen. *Stahlbau*, 76(11):569–581.

Hagl, A. (2008a). Punktuelles Kleben mit Silikonen. *Stahlbau*, 77(11):791–801.

Hagl, A. (2008b). Understanding complex adhesive behaviour: case study u-type bonding geometry. In *Challenging Glass Conference 1 - May 2008 - Delft, The Netherlands*, pages 227–240.

Hagl, A. (2009). Durability by Design: New Results on Load Carrying Silicone Bonding. In *Third Symposium on Durability of Building and Construction Sealants and Adhesives, Denver CO, June 25-26, 2008*.

Hagl, A. (2016). Development and test logics for structural silicone bonding design and sizing.

Glass Structures and Engineering, 1(1):131–151.

Hart-Smith, L. (1973). Adhesive-bonded single-lap joints. Technical report, National Aeronautics and Space Administration.

Hashin, Z. (1996). Finite Thermoelastic Fracture Criterion with Application to Laminate Cracking Analysis. *Journal of the Mechanics and Physics of Solids*, 44(7):1129–1145.

Hein, V. and Erdogan, F. (1971). Stress singularities in a two-material wedge. *International Journal of Fracture Mechanics*, 7(3):317–330.

Holzapfel, G. (1996). On large strain viscoelasticity: continuum formulation and finite element applications to elastomeric structures. *International Journal for Numerical Methods in Engineering*, 39:3903–3926.

Ihara, T., Gustavsen, A., and Jelle, B. (2014). Sealant ageing and its correlation with façade reflectance. *Construction and Building Materials*, 69:390–402.

ISO 7743 (2008). *Rubber, vulcanized or thermoplastic - Determination of compression stress-strain properties*. International Organization for Standardization.

Kawabata, S. (1973). Fracture and mechanical behaviour of rubber-like polymers under finite deformation in biaxial stress field. *Journal of Macromolecular Science*, pages 605–630.

Klein, B. (2007). *FEM: Grundlagen und Anwendungen der Finite-Elemente-Methode im Maschinen- und Fahrzeugbau*, volume 2. Vieweg.

Klosowski, J. and Wolf, A. (2016). *Sealants in construction*. CRC Press.

Kolupaev, V., Moneke, M., and Kraatz, A. (2003). Kombinierte Anstrengungsbedingungen zur Beschreibung des mehraxialen Kriechverhaltens von unverstärkten Kunststoffen. *KGK Kautschuk Gummi Kunstsoffe*, 56(11):600–608.

Kurzweil, P. and Scheipers, P. (2012). *Chemie - Grundlagen, Aufbauwissen, Anwendungen und Experimente*. Springer-Verlag.

Lazzarin, P. and Berto, F. (2005). Some expressions for the strain energy in a finite volume surrounding the root of blunt v-notches. *International Journal of Fracture*, 135(1-4):161–185.

Leffler, K., Alfredsson, K., and Stigh, U. (2007). Shear behaviour of adhesive layers. *International Journal of Solids and Structures*, 44(2):530–545.

Leguillon, D. (2002). Strength or toughness? A criterion for crack onset at a notch. *European Journal of Mechanics A/Solids*, 21(1):61–72.

Li, V. and Ward, R. (1989). A novel testing technique for post-peak tensile behaviour of cementitious materials. *Fracture Toughness and Fracture Energy*, pages 183–195.

Machado, G., Chagnon, G., and Favier, D. (2010). Analysis of the isotropic models of the Mullins effect based on filled silicone rubber experimental results. *Mechanics of Materials*, 42(9):841–851.

Mang, H. and Hofstetter, G. (2013). *Festigkeitslehre*, volume 4. Springer-Verlag Berlin Heidelberg.

Marckmann, G. and Verron, E. (2006). Comparison of hyperelastic models for rubber-like materials. *Rubber chemistry and technology*, 79(5):835–858.

Marlow, R. (2003). A general first-invariant hyperelastic constitutive model. In Busfield, J. and Muhr, A., editors, *Constitutive models for rubber III - Proceedings of the third european conference on constitutive models for rubber, London*, pages 157–160. Swets & Zeitlinger, Lisse.

Marzi, S., Biel, A., and Stigh, U. (2011). On experimental methods to investigate the effect of

layer thickness on the fracture behaviour of adhesively bonded joints. *International Journal of Adhesion and Adhesives*, 31(8):840–850.

Molls, M. (2013). *Experimentelle und numerische Untersuchung ein- und mehrachsig belasteter Elastomerbuchsen unter besonderer Berücksichtigung des Reihenfolgeeinflusses*. PhD thesis, Universität Duisburg-Essen.

Mullins, L. (1948). Effect of stretching on the properties of rubber. *Rubber Chemistry and Technology*, 21(2):281–300.

Naït-Abdelaziz, M., Zaïri, F., Qu, Z., Hamdi, A., and Aït-Hocine, N. (2012). J integral as a fracture criterion of rubber-like materials using the intrinsic defect concept. *Mechanics of Materials*, 53:80–90.

Neuber, H. (1936). Theorie der technischen Formzahl. *Forschung im Ingenieurwesen*, 7(6):271–274.

Neuber, H. (1958). *Kerbspannungslehre*, volume 2. Springer-Verlag, Berlin.

Ogden, R. W. (2005). Mechanics of rubberlike solids. In *Mechanics of the 21st Century*, pages 263–274. Springer.

Olsson, P. and Stigh, U. (1989). On the determination of the constitutive properties of thin interphase layers - an exact inverse solution. *International Journal of Fracture*, 41:R71–R76.

Overend, M., Jin, Q., and Watson, J. (2011). The selection and performance of adhesives for a steel–glass connection. *International Journal of Adhesion and Adhesives*, 31(7):587–597.

Penado, F. (2000). Analysis of singular regions in bonded connections. *International Journal of Fracture*, 105:1–25.

Piculin, S., Nicklisch, F., and Brank, B. (2016). Numerical and experimental tests on adhesive bond behaviour in timber-glass walls. *International Journal of Adhesion and Adhesives*, 70:204–217.

Pipes, R. B., Wetherhold, R. C., and Gillespie Jr, J. W. (1979). Notched Strength of Composite Materials. *Journal of Composite Materials*, 13(2):148–160.

Reedy, E. (1993). Free-edge stress intensity factor for a bonded ductile layer subjected to shear. *Journal of Applied Mechanics*, 60:715–720.

Reller, A., Braungart, M., Soth, J., and von Uexküll, O. (2000). Silicone - eine vollsynthetische Materiaklasse macht Geschichte(n). *GAIA*, 9(1):13–24.

Rice, J. R. (1968). A path independent integral and the approximate analysis of strain concentration by notches and cracks. *Journal of Applied Mechanics*, 35:379–386.

Richter, C., Abeln, B., Geßler, A., and Feldmann, M. (2014). Structural steel-glass facade panels with multi-side bonding - Nonlinear stress-strain behaviour under complex loading situations. *International Journal of Adhesion and Adhesives*, 55:18–28.

Rinnbauer, M. (2006). *Technische Elastomerwerkstoffe - Basis für Hightech-Lösungen in der Dichtungs- und Schwingungstechnik*. Die Bibliothek der Technik. Verlag Moderne Industrie.

Rosendahl, P., Staudt, Y., Odenbreit, C., Schneider, J., and Becker, W. (2017). Silicone sealants: A Finite Fracture Mechanics model for non-linear materials. In *14th International Conference on Fracture ICF*.

Schaaf, A., De Monte, M., Moosbrugger, E., Vormwald, M., and Quaresimin, M. (2015). Life estimation methodology for short fiber reinforced polymers under thermo-mechanical loading in automotive applications. *Materialwissenschaft und Werkstofftechnik*, 46(2):214–228.

Scherer, T. (2014). *Werkstoffspezifisches Spannungs–Dehnungs–Verhalten und Grenzen*

der Beanspruchbarkeit elastischer Klebungen. PhD thesis, Technische Universität Kaiserslautern.

Schliebs, R. and Ackermann, J. (1987). Chemie und Technologie der Silicone I. *Chemie in unserer Zeit*, 21(4):121–127.

Schneider, J., Kuntsche, J., Schula, S., Schneider, F., and Wörner, J.-D. (2016). *Glasbau: Grundlagen, Berechnung, Konstruktion*. Springer-Verlag.

Schneider, J., Schula, S., and Weinhold, W. (2012). Characterisation of the scratch resistance of annealed and tempered architectural glass. *Thin Solid Films*, 520(12):4190–4198. 8th International Conference on Coatings on Glass and Plastics - ICCG8.

Schwind, G. (2016). Inverse, numerical investigations for the materialparameteridentification on rubberlike-materials. Master's thesis, Technische Universität Darmstadt, Germany.

Sedlacek, G., Wellershoff, F., and Kasper, R. (1999). *Glas im konstruktiven Ingenieurbau*. Ernst & Sohn.

Sinclair, G. (2004). Stress singularities in classical elasticity-I: Removal, interpretation, and analysis. *Applied Mechanics Reviews*, 57(4):251–298.

Sorensen, B. and Jacobsen, T. (2003). Determination of cohesive laws by the *J* integral approach. *Engineering Fracture Mechanics*, 70(14):1841–1858.

Staudt, Y. (2013). Investigation of the material behavior of glued connections with silicones. Master's thesis, Technische Universität Darmstadt, Germany.

Staudt, Y., Odenbreit, C., and Schneider, J. (2016). Investigation of bonded connections with silicone under shear loading. In Bos, F., Louter, C., and Belis, J., editors, *Challenging Glass 5 - Conference on Architectural and Structural Applications of Glass*.

Staudt, Y., Odenbreit, C., and Schneider, J. (2017). Failure Behaviour of Silicone Adhesive in Bonded Connections with Simple Geometry. *International Journal of Adhesion and Adhesives*. in press.

Stein, N., Dölling, S., Chalkiadaki, K., Becker, W., and Weißgraeber, P. (2017a). Enhanced XFEM for crack deflection in multi-material joints. *International Journal of Fracture*, pages 1–18.

Stein, N., Rosendahl, P., and Becker, W. (2017b). Modelling load transfer and mixed-mode fracture of ductile adhesive composite joints. *International Journal of Adhesion and Adhesives*. under review.

Stommel, M. and Korte, W. (2011). *FEM zur Berechnung von Kunststoff- und Elastomerbauteilen*. Hanser.

Tan, S. (1987). Fracture Strength of Composite Laminates with an Elliptical Opening. *Composites Science and technology*, 29(2):133–152.

Taylor, D. (2008). The theory of critical distances. *Engineering Fracture Mechanics*, 75(7):1969–1705.

Taylor, D. (2013). Applications of the theory of critical distances to the prediction of brittle fracture in metals and non-metals. In *ECF15, Stockolm 2004*.

Thomas, N. (2010). Frederic Stanley Kipping - Pioneer in Silicon Chemistry: His Life & Legacy. *Silicon*, 2(4):187–193.

Thrower, J. (1986). *Technical statics and strength of materials*, volume 2. Breton Publishers.

Tibolt, M. and Odenbreit, C. (2014). The stress peak at the borehole of point-fitted IGU with undercut anchors. *Journal of Facade Design and Engineering*, 2(1-2):33–66.

Tock, W., Dinivahi, M., and Chew, C. (1988). Viscoelastic properties of structural silicone

rubber sealants. *Advances in Polymer Technology*, 8(3):317–324.

Trapper, P. and Volokh, K. (2008). Cracks in rubber. *International Journal of Solids and Structures*, 45(24):6034–6044.

Vable, M. (2008). Stress Analysis of Bonded Joints by Boundary Element Method. In *Modeling of adhesively bonded joints*. Springer.

Van Tooren, M. and Krakers, L. (2006). A generalized stress singularity approach for material failure prediction and its application to adhesive joint strength analysis. *Journal of Adhesion Science and Technology*, 20(9):981–995.

Volkersen, O. (1938). Die Nietkraftverteilung in zugbeanspruchten Nietverbindungen mit konstanten Laschenquerschnitten. *Luftfahrtforschung*, 15(1/2):41–47.

Volokh, K. (2010). On modeling failure of rubber-like materials. *Mechanics Research Communications*, 37(8):684 – 689.

Wacker Chemie AG (2007). *Silicone sealants manual - perfect joints made easy*. Wacker Chemie AG.

Waddoups, M., Eisenmann, J., and Kaminski, B. (1971). Macroscopic Fracture Mechanics of Advanced Composite Materials. *Journal of composite materials*, 5(4):446–454.

Wang, C. and Rose, L. (2000). Compact solutions for the corner singularity in bonded lap shear joints. *International Journal of Adhesion and Adhesives*, 20(2):145–154.

Weißgraeber, P. (2014). *Neue Ansätze zur Analyse der Lastübertragung und Initiierung finiter Risse in Klebverbindungen*. PhD thesis, Technische Universität Darmstadt.

Weißgraeber, P. and Becker, W. (2013). Finite fracture mechanics model for mixed mode fracture in adhesive joints. *International Journal of Adhesion and Adhesives*, 50(14):2383–2394.

Weißgraeber, P., Leguillon, D., and Becker, W. (2016). A review of Finite Fracture Mechanics: crack initiation at singular and non-singular stress raisers. *Archive of Applied Mechanics*, 86(1-2):375–401.

Weißgraeber, P., Stein, N., and Becker, W. (2014). A general sandwich-type model for adhesive joints with composite adherends. *International Journal of Adhesion and Adhesives*, 55:56–63.

Weller, B., Kothe, M., Nicklisch, F., Schadow, T., Tasche, S., Vogt, I., and Wünsch, J. (2011). Kleben im konstruktiven Glasbau. In Kuhlmann, U., editor, *Stahlbau-Kalender 2011*. Wilhelm Ernst & Sohn, Berlin.

Whitney, J. and Nuismer, R. (1974). Stress Fracture Criteria for Laminated Composites Containing Stress Concentrations. *Journal of composite materials*, 8(3):253–265.

Williams, J. G. (1984). *Fracture mechanics of polymers*. Horwood.

Williams, M. (1952). Stress Singularities Resulting From Various Boundary Conditions in Angular Corners of Plates in Extension. *Journal of applied mechanics*, 19(4):526–528.

Wolf, A. (2010). *Contributions of Silicone Technology to Sustainable Architecture*. Dow Corning Corporation. Form number: 63-1177-01.

Wolf, A. and Cleland-Host, H. (2004). Material Properties for Use in FEA Modelling: Sealant Behavior with Ambient Laboratory Climate Ageing. In Wolf, A., editor, *Durability of Building and Construction Sealants and Adhesives, ASTM STP 1453*. ASTM International, West Conshohocken, PA.

Wolf, A. and Descamps, P. (2002). Determination of Poisson's Ratio of Silicone Sealant from Ultrasonic and Tensile Measurements. In Johnson, P., editor, *Performance of Exterior Building Walls, ASTM STP 1422*. American Society for Testing and Materials, West

Conshohocken, PA.

Zienkiewicz, O. and Taylor, R. (2000). *The Finite Element Method - Volume 1: The Basis*, volume 5. Elsevier/Butterworth-Heinemann.

Zine, A., Benseddiq, N., and Naït-Abdelaziz, M. (2011). Rubber fatigue life under multiaxial loading: Numerical and experimental investigations. *International Journal of Fatigue*, 33(10):1360–1368.

Zine, A., Benseddiq, N., Naït-Abdelaziz, M., Aït-Hocine, N., and Bouami, D. (2006). Prediction of rubber fatigue life under multiaxial loading. *Fatigue & Fracture of Engineering Materials & Structures*, 29(3):267–278.

Appendices

A Test data

A.1 Compression tests

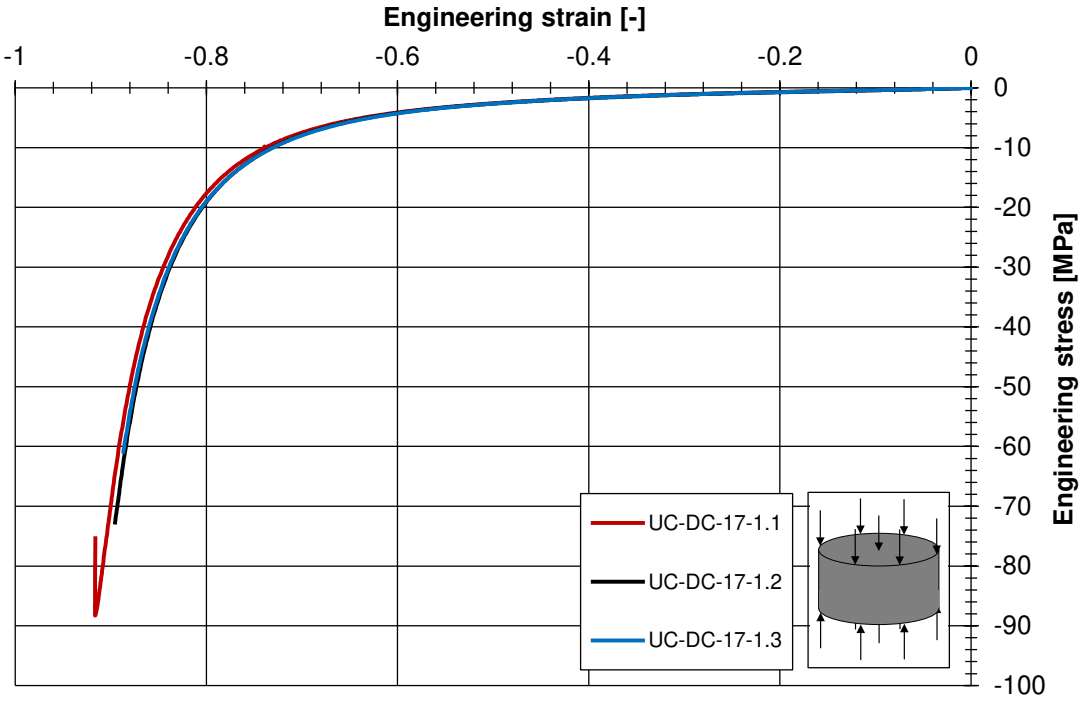

Figure A.1: Compression test data, series UC-DC-17-1

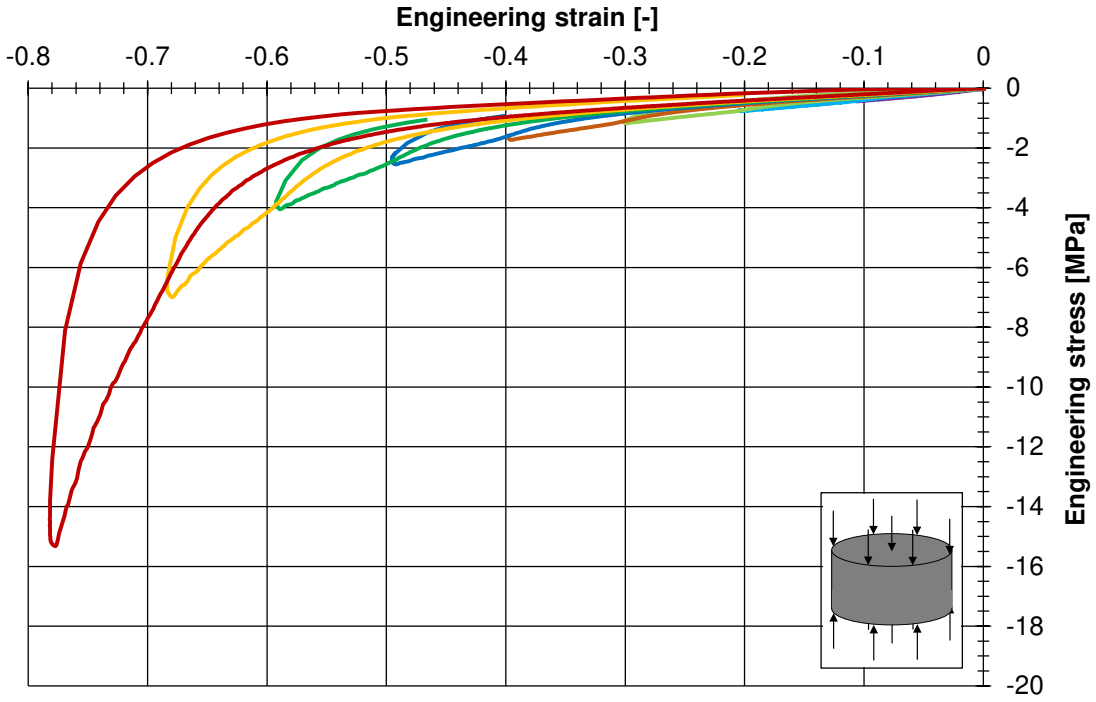

Figure A.2: Compression test data, specimen UC-DC-17-2.1

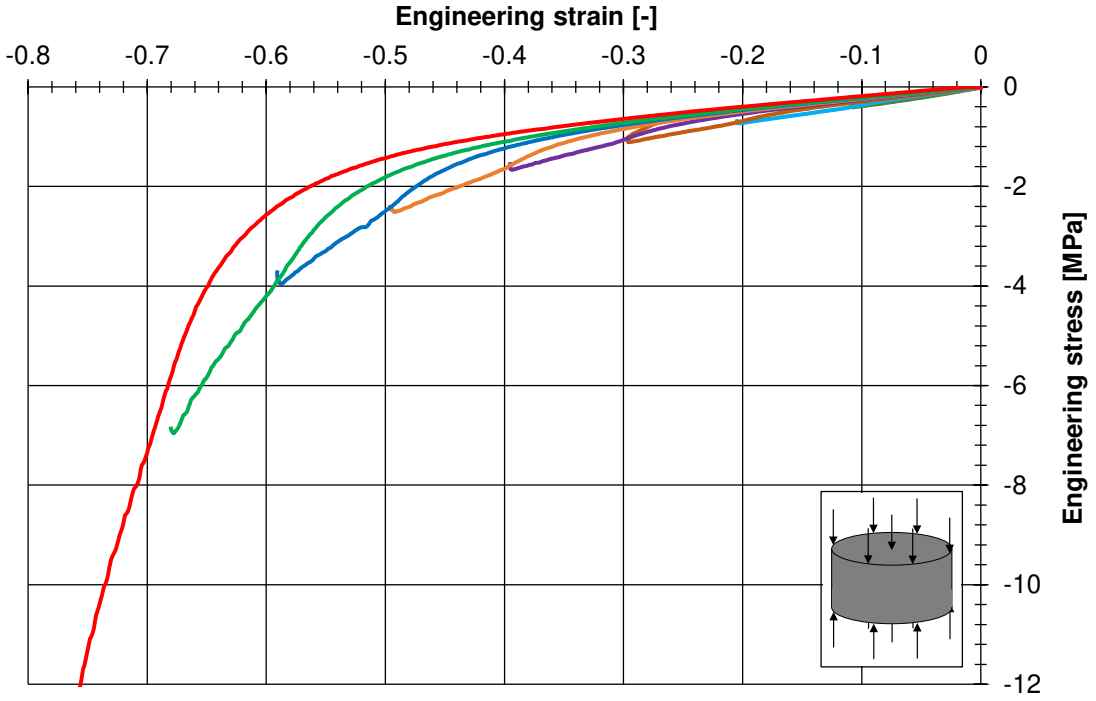

Figure A.3: Compression test data, specimen UC-DC-17-2.2

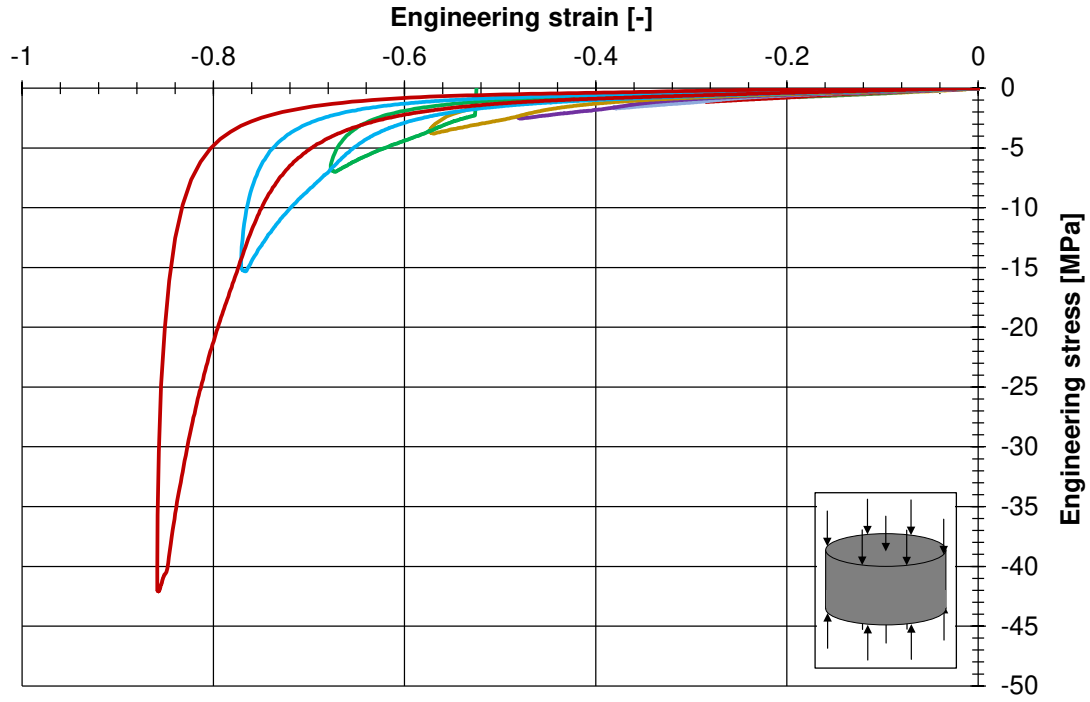

Figure A.4: Compression test data, specimen UC-DC-17-2.3

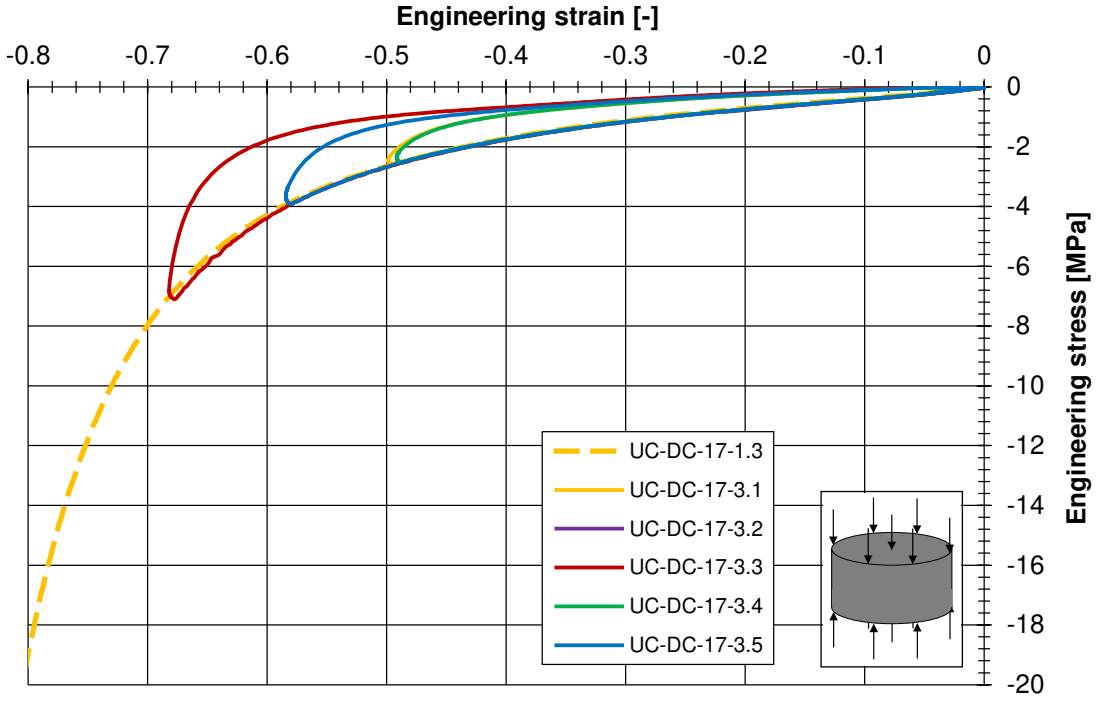

Figure A.5: Compression test data, series UC-DC-17-3

A.2 Simple shear tests

A.2.1 Test series 2015

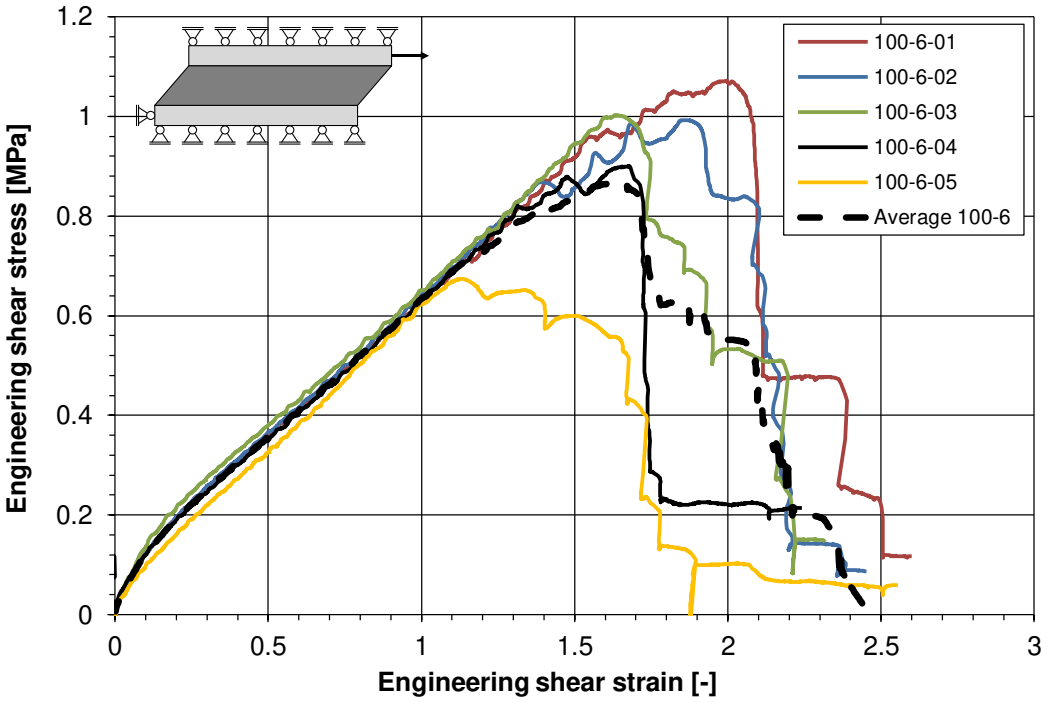

Figure A.6: Simple shear test data, series 100-6, 2015

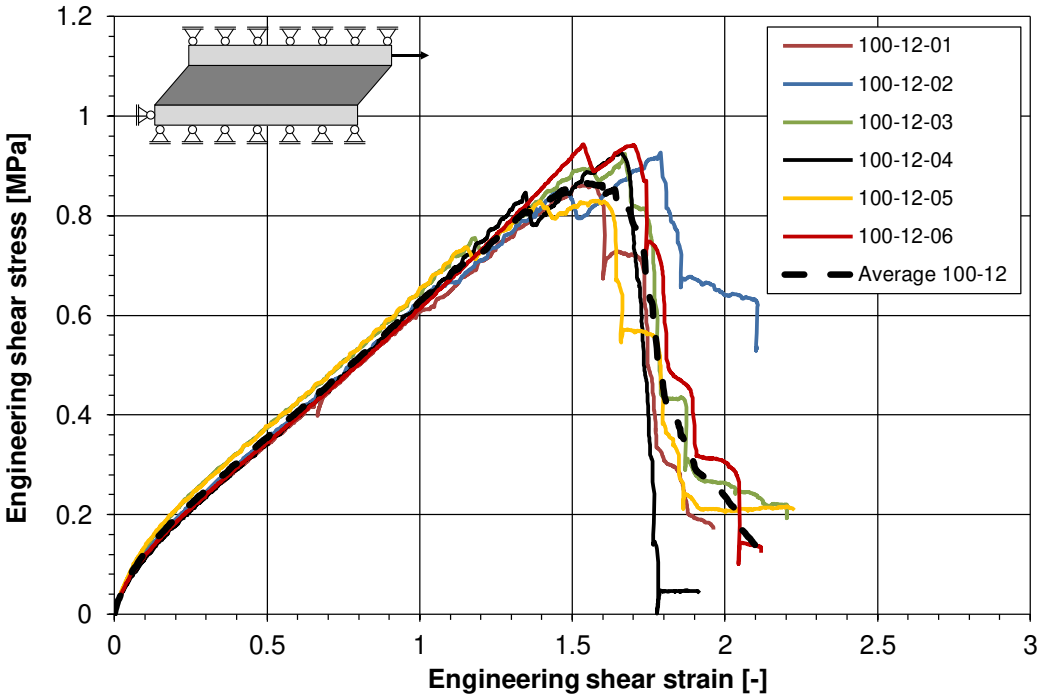

Figure A.7: Simple shear test data, series 100-12, 2015

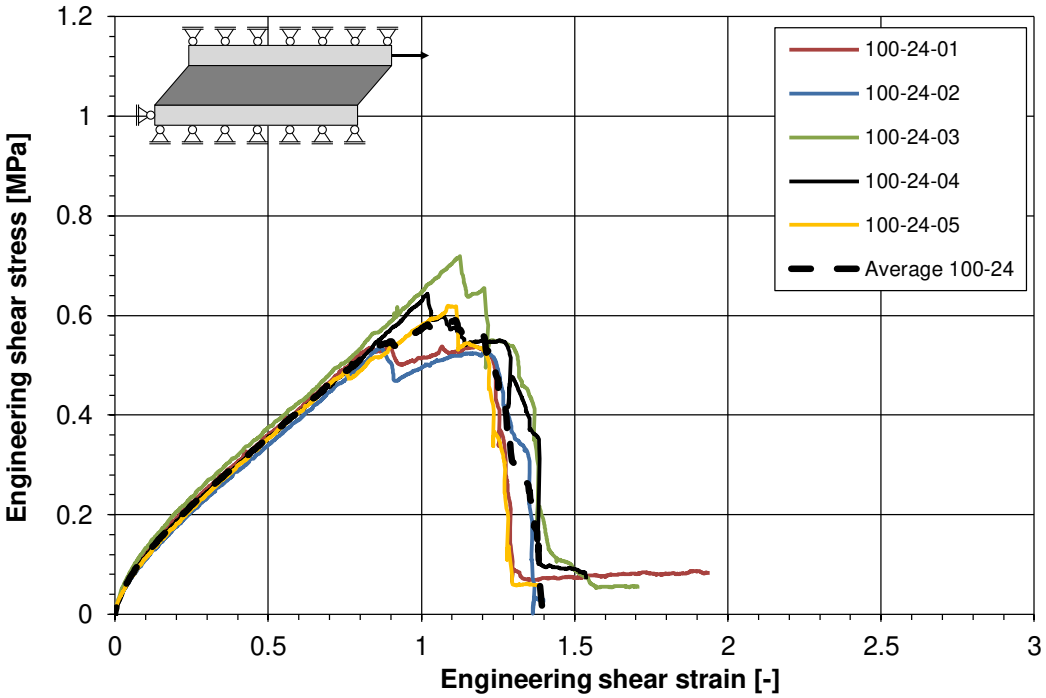

Figure A.8: Simple shear test data, series 100-24, 2015

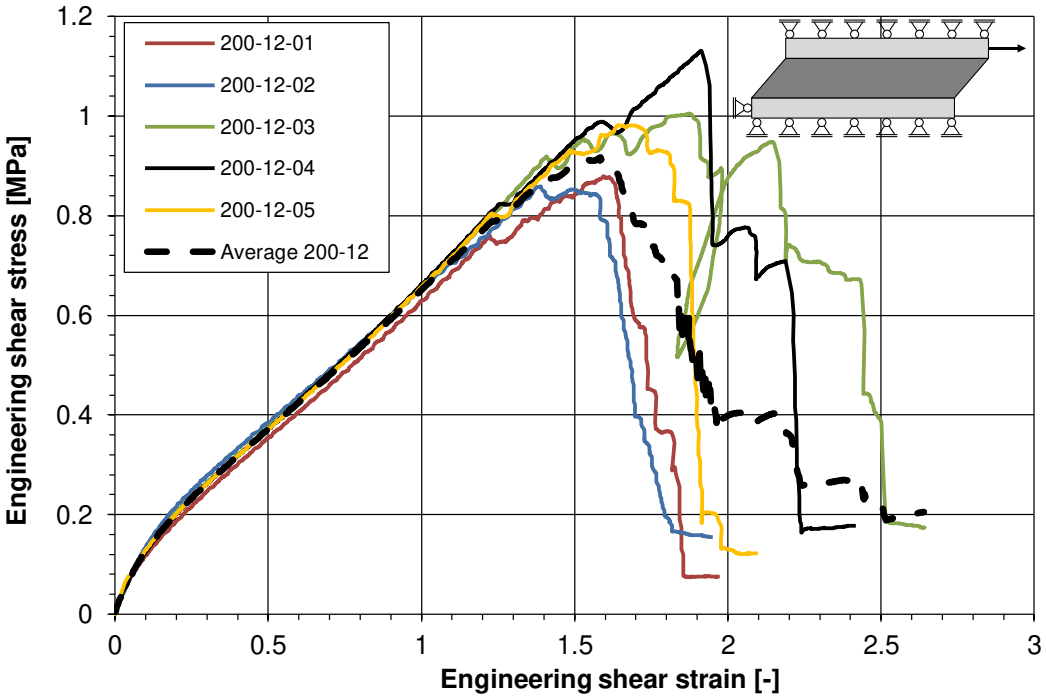

Figure A.9: Simple shear test data, series 200-12, 2015

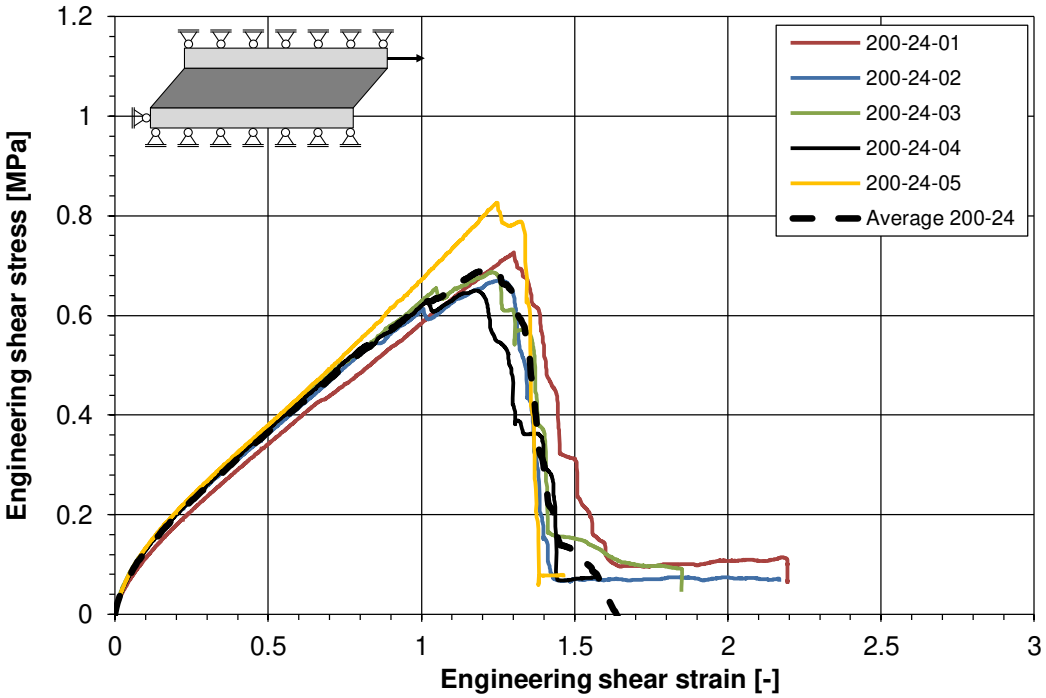

Figure A.10: Simple shear test data, series 200-24, 2015

A.2.2 Test series 2016

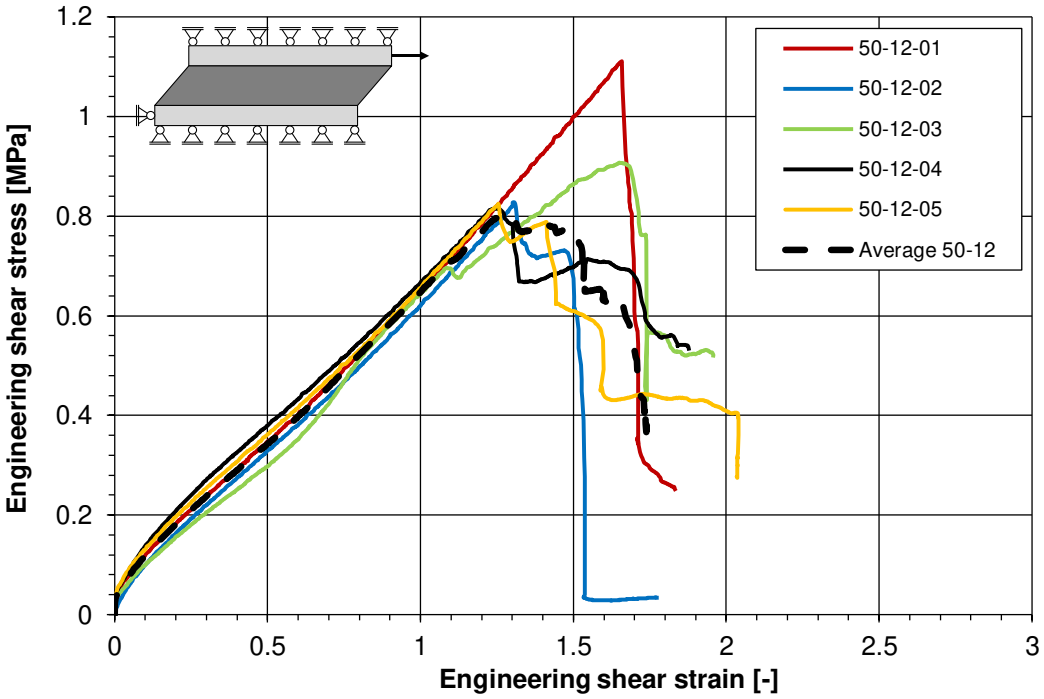

Figure A.11: Simple shear test data, series 50-12, 2016

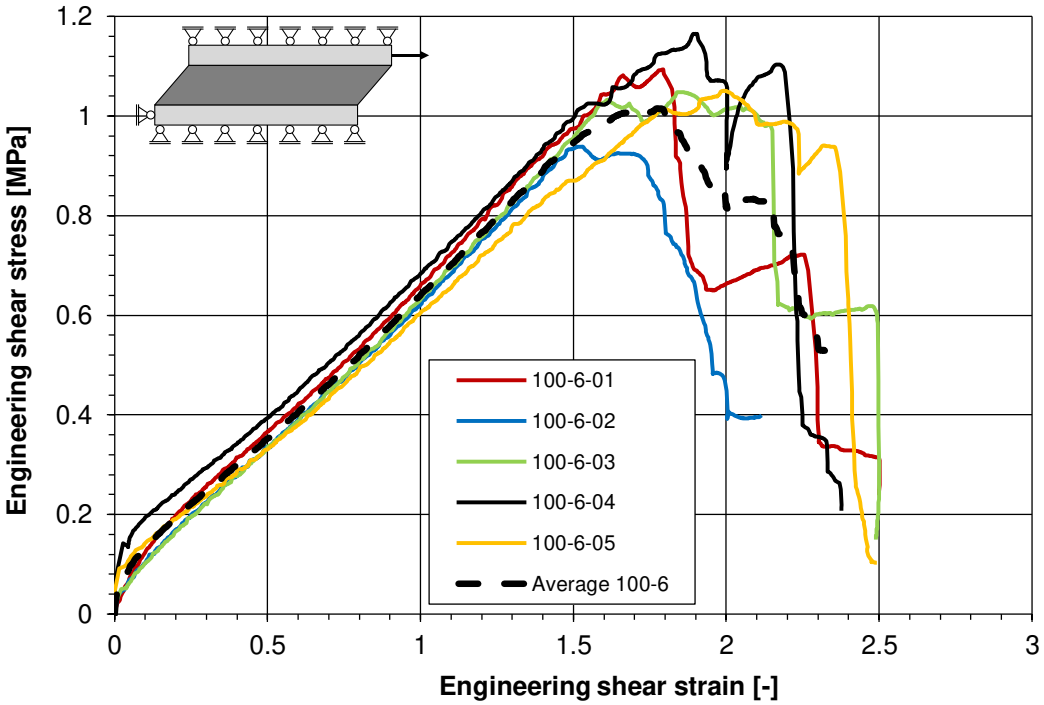

Figure A.12: Simple shear test data, series 100-6, 2016

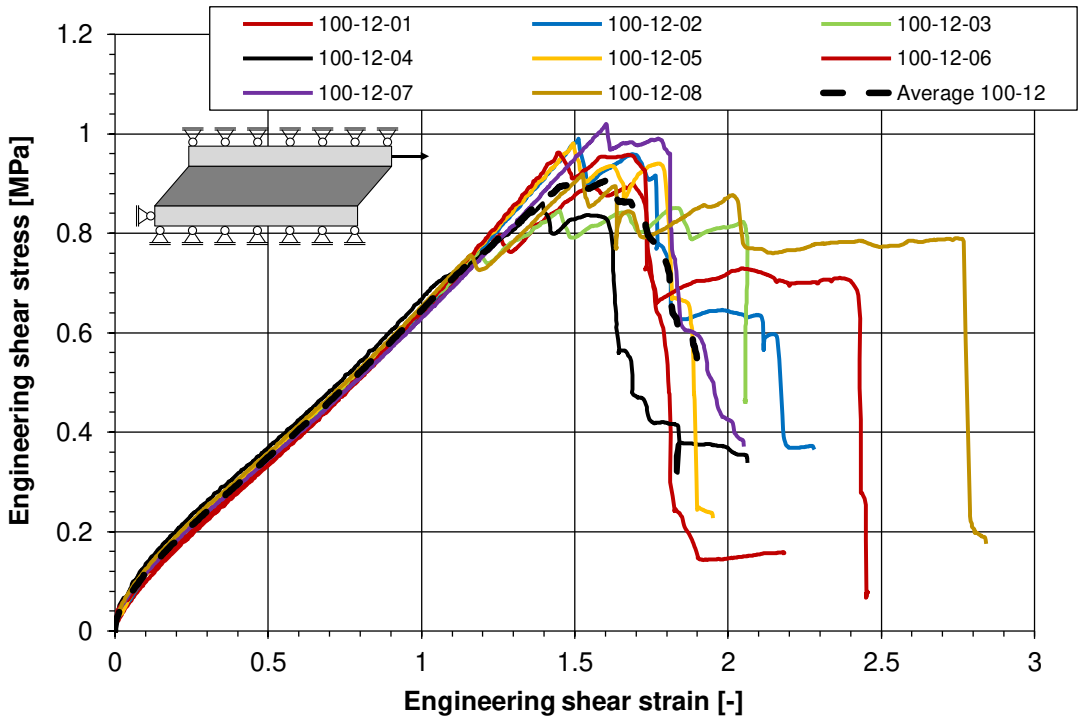

Figure A.13: Simple shear test data, series 100-12, 2016

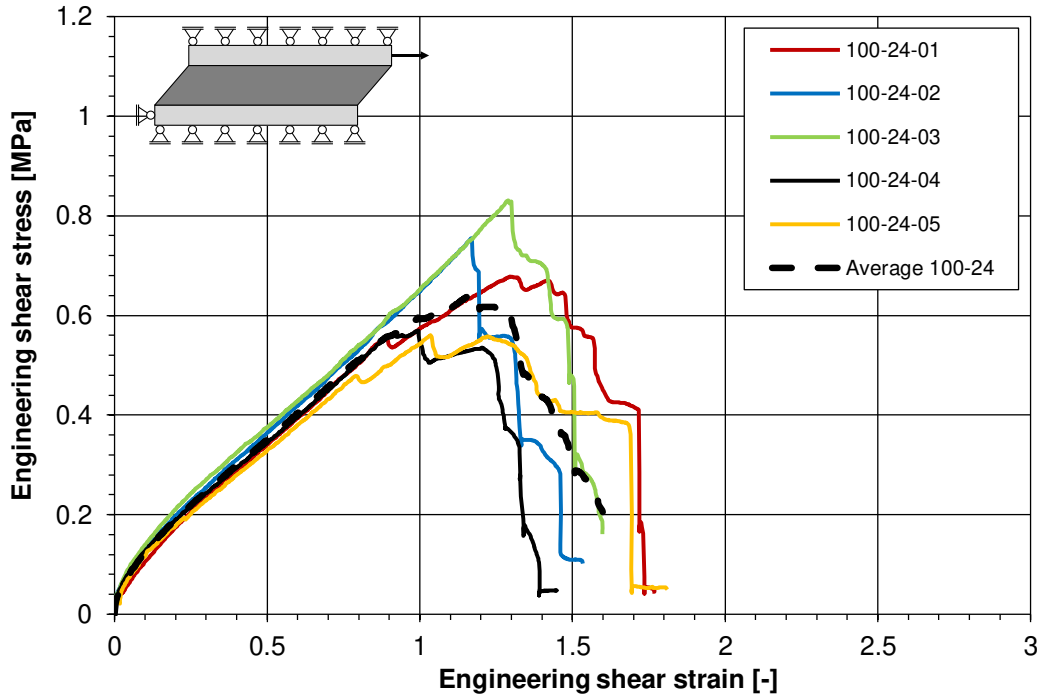

Figure A.14: Simple shear test data, series 100-24, 2016

A.3 Circular shear tests

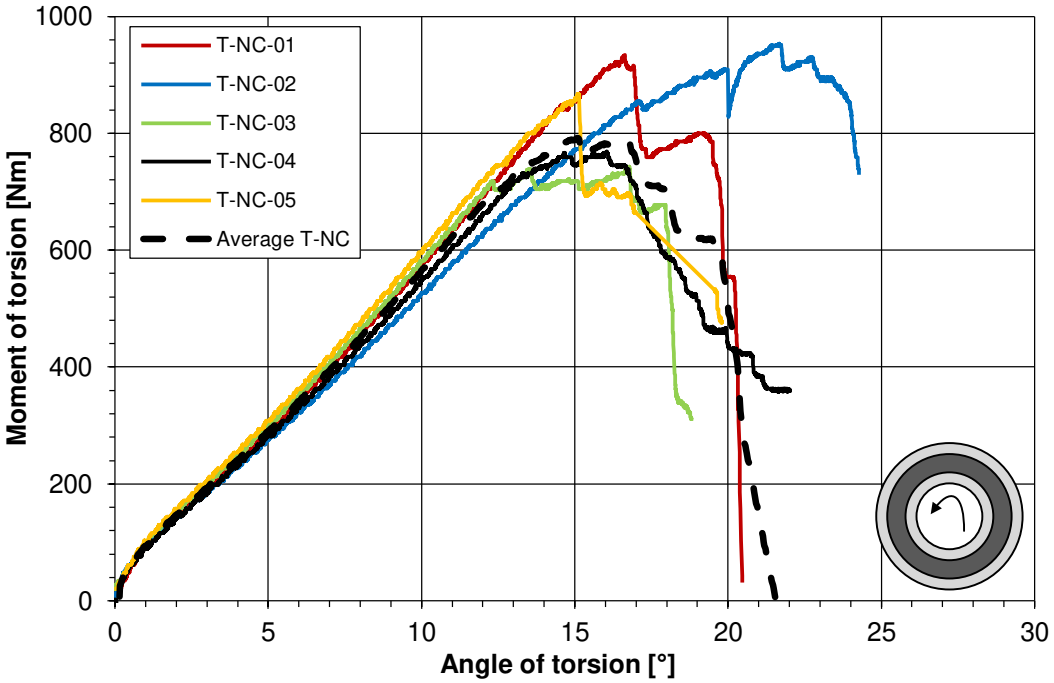

Figure A.15: Circular shear test data, series T-NC

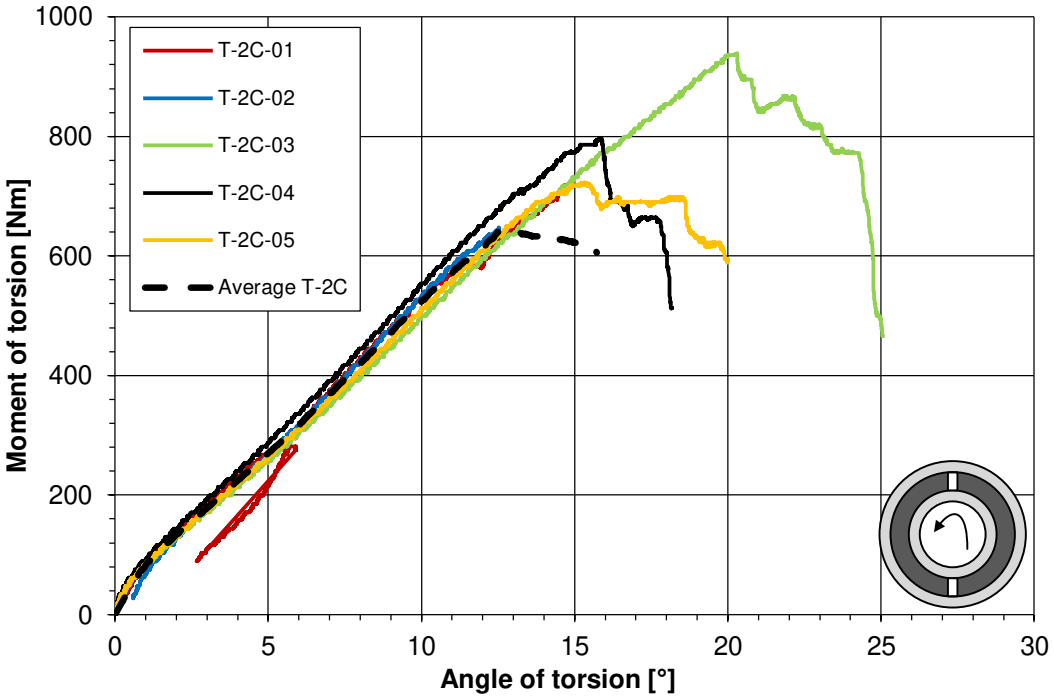

Figure A.16: Circular shear test data, series T-2C

B Details about the test series

B.1 Production of the specimens

B.1.1 Preliminary remarks

In the present chapter, details about the manufacturing process are listed in a condensed way. This includes information about the mixing process, the cure conditions and time, the demoulding time and the tooling.

B.1.2 Tensile specimens

Table B.1: Details about the production of the tensile specimens

Specimen:	Uniaxial tensile specimens
Series:	Z.AG.6
Production date:	26.07.2013
Location:	European headquarters of the Dow Corning Company in Seneffe (Belgium)
Mixing process:	Professional two parts mixing machine
Assessment of mixing quality:	Two plates test
Tooling:	Surface modelling with a dry spatula
Mould:	Poured on a PE foil
Cure conditions:	Controlled condition, 23°C, 50% relative humidity
Cure time at manufacturer:	14 days
Demoulding date:	06.08.2013
Testing date:	Period from 26.08. to 06.09.2013
Storage conditions prior to test:	Ambient conditions

B.1.3 Compression specimens

Table B.2: Details about the production of the compression test specimens

Specimen:	Compression test specimens
Series:	UC-DC-17-1 to 3
Production date:	27.01.2017
Location:	Hunsrücker Glasveredelung Wagner in Kirchberg, Germany
Mixing process:	Professional two parts mixing machine
Assessment of mixing quality:	Two plates test
Tooling:	-
Mould:	Poured in a closed PTFE mould
Cure conditions:	Ambient conditions
Cure time at manufacturer:	7 days
Demoulding date:	07.02.2017
Testing date:	Period from 27.02. to 03.03.2017
Storage conditions prior to test:	Ambient conditions

B.1.4 Simple shear test specimens

Table B.3: Details about the production of the simple shear test specimens - test series 2015

Specimen:	Simple shear test specimens
Series:	Test series 2015
Production date:	06.10.2015
Location:	Hunsrücker Glasveredelung Wagner in Kirchberg, Germany
Mixing process:	Professional two parts mixing machine
Assessment of mixing quality:	Two plates test
Tooling:	Surface modelling with a dry spatula
Mould:	U-shaped PE mould
Cure conditions:	Ambient conditions
Cure time at manufacturer:	3 days
Demoulding date:	14.10.2015
Testing date:	Period from 02.11. to 06.11.2015
Storage conditions prior to test:	Ambient conditions

Table B.4: Details about the production of the simple shear test specimens - test series 2016

Specimen:	Simple shear test specimens
Series:	Test series 2016
Production date:	24.03.2016
Location:	Hunsrücker Glasveredelung Wagner in Kirchberg, Germany
Mixing process:	Professional two parts mixing machine
Assessment of mixing quality:	Two plates test
Tooling:	Surface modelling with a dry spatula
Mould:	U-shaped PE mould
Cure conditions:	Ambient conditions
Cure time at manufacturer:	15 days
Demoulding date:	10.04.2016
Testing date:	Period from 13.05. to 31.05.2016
Storage conditions prior to test:	Ambient conditions

B.1.5 Circular shear test specimens

Table B.5: Details about the production of the circular shear test specimens

Specimen:	Circular shear test specimens
Series:	T-NC and T-2C
Production date:	19.05.2016
Location:	Hunsrücker Glasveredelung Wagner in Kirchberg, Germany
Mixing process:	Professional two parts mixing machine
Assessment of mixing quality:	Two plates test
Tooling:	Surface modelling with a dry spatula
Mould:	One surface in bite direction in contact with air Second surface in contact with PTFE ring
Cure conditions:	Ambient conditions
Cure time at manufacturer:	15 days
Demoulding date:	-
Testing date:	15.09. and 16.09.2016
Storage conditions prior to test:	Ambient conditions

B.1.6 Tensile test specimens

The H-shaped tensile test specimens have been produced under the same conditions as the dog-bone shaped tensile specimen. A U-shaped PTFE mould has been used.

B.1.7 Double Cantilever Beam test specimens

Table B.6: Details about the production of the DCB test specimens - series 2016

Specimen:	DCB test specimens
Series:	DCB-12-01..05
Production date:	24.03.2016
Location:	Hunsrücker Glasveredelung Wagner in Kirchberg, Germany
Mixing process:	Professional two parts mixing machine
Assessment of mixing quality:	Two plates test
Tooling:	Surface modelling with a dry spatula
Mould:	One surface in bite direction in contact with air Second surface in contact with PE plate
Cure conditions:	Ambient conditions
Cure time at manufacturer:	15 days
Demoulding date:	11.04.2016
Testing date:	21.04.2016
Storage conditions prior to test:	Ambient conditions

Table B.7: Details about the production of the DCB test specimens - series 2016-2

Specimen:	DCB test specimens
Series:	DCB-12-06..07, DCB-6.01..07
Production date:	19.05.2016
Location:	Hunsrücker Glasveredelung Wagner in Kirchberg, Germany
Mixing process:	Professional two parts mixing machine
Assessment of mixing quality:	Two plates test
Tooling:	Surface modelling with a dry spatula
Mould:	One surface in bite direction in contact with air Second surface in contact with PE plate
Cure conditions:	Ambient conditions
Cure time at manufacturer:	15 days
Demoulding date:	06.06.2016
Testing date:	09.09.2016
Storage conditions prior to test:	Ambient conditions

B.2 Failure of the simple shear test specimens

In this section, the locations of crack initiation of the different simple shear test specimens are given. Two locations are differentiated: area from which the silicone was poured (during curing in contact with the air), labelled *AIR* and the closed surface at the opposite side, labelled *PE*, since it was in contact with the polymer. It should be noted that the identification of the location of failure initiation could not be identified for all specimens.

Table B.8: Location of crack initiation for the simple shear and tensile test series

Test series:	Number of specimens with crack initiation at AIR side	Number of specimens with crack initiation at PE side
Simple shear tests		
100-6	2	3
100-12	1	7
100-24	2	3
200-12	2	3
200-24	2	3
Tension tests on H-shaped specimens		
ETAG-T	1	5 (PTFE side)